Technical Report
TR-19-06
September 2019

Radionuclide transport and dose calculations for the safety evaluation SE-SFL

SVENSK KÄRNBRÄNSLEHANTERING AB

SWEDISH NUCLEAR FUEL
AND WASTE MANAGEMENT CO

Box 3091, SE-169 03 Solna
Phone +46 8 459 84 00
skb.se

ISSN 1404-0344
SKB TR-19-06
ID 1721740
September 2019

Radionuclide transport and dose calculations for the safety evaluation SE-SFL

Svensk Kärnbränslehantering AB

Keywords: SFL, Long-lived low- and intermediate-level waste, Safety evaluation, Post-closure safety, Radionuclides, Transport modelling, Near-field, Geosphere, Biosphere, Activity release, Effective dose, Radiological consequences.

A pdf version of this document can be downloaded from www.skb.se.

Preface

This report is one of the main references for the evaluation of post-closure safety for a proposed repository concept for the repository for long-lived waste (SFL) in Sweden. The report describes the calculations of the release and transport of radionuclides from the deposited waste, via the repository near-field, the geosphere, and through the biosphere, over an analysis period of one million years after repository closure. The resulting effective radiation doses to humans are also assessed.

Jenny Brandefelt has been the project leader for SE-SFL and is responsible for the safety evaluation. The main contributing authors for this report have been Jenny Brandefelt, Per-Anders Ekström (Kvot AB), Svante Hedström, Olle Hjerne, Georg Lindgren (Kemakta Konsult AB), Peter Saetre, Pirouz Shahkarami (Kemakta Konsult AB) and Ola Wessely (SKB unless otherwise stated). Elizabeth Polido Legaria and Miranda Keith-Roach (Kemakta Konsult AB) also contributed to the work on an early draft stage. Additionally, several experts at SKB have contributed at various stages of the preparation of this report. An initial review of this report was performed by Russel Alexander (Bedrock Geosciences GmbH, Switzerland), Rodolfo Avila (ÅF Pöyry AB), Jordi Bruno (Amphos^{21} Consulting S.L, Spain), Michael Thorne (Mike Thorne and Associates Ltd, United Kingdom), and Per-Gustav Åstrand (ÅF Pöyry AB). A formal review was subsequently carried out by Jordi Bruno and Michael Thorne.

Solna, September 2019

Jenny Brandefelt
Project leader SE-SFL

Summary

SKB is planning to construct a repository for long-lived low- and intermediate-level radioactive waste, SFL. The present repository design proposes two waste vaults: BHA with a bentonite clay backfill for legacy waste, and BHK with a concrete backfill for reactor internal components. No site has yet been chosen for SFL, and only a first estimate of the initial inventory of radionuclides and other materials in SFL is available. The safety evaluation SE-SFL is the first analysis of post-closure safety for the SFL repository concept proposed by Elfwing et al. (2013). Its purpose is to assess under what conditions, in the repository and its environs, that the proposed design concept has the potential to meet the regulatory requirements for post-closure safety. This document is one of the main references for SE-SFL and describes the radionuclide transport modelling and dose calculations, crucial for the assessment of the repository's radiological consequences and its potential to meet the regulatory requirements on doses to humans.

The modelling methodology (Chapter 2) is based on the experiences from SKB's previous safety assessment SR-PSU, but the representation of the repository has intentionally been simplified. The transport modelling reported here relies on the reference evolution of the **Main report**, on the other four main SE-SFL references (**Biosphere synthesis**, **Climate report**, **FEP report**, **Initial state report**), as well as on many underlying reports specifically addressing various SFL system components. These include the hydrogeological properties around the repository, the properties and degradation of the bentonite and concrete engineered barriers, and methods and input data for the transport modelling in the various domains.

The prioritisation and selection of radionuclides to consider are described in Chapter 3. A one-million-year period is analysed, and Laxemar in south-eastern Sweden is used as a relevant example of a site for geological disposal of radioactive waste. Chapter 4 describes the modelling tools for calculation of the radionuclide releases from the repository (near-field), the transport from the repository to the surface system (geosphere), the transport and accumulation in the biosphere, and the resulting doses to members of the most exposed group (biosphere). The near-field and biosphere radionuclide transport models are implemented in the Ecolego software and build upon the same principles as the corresponding SR-PSU models. The geosphere transport is modelled with the code FARFCOMP, a new implementation of the same conceptual model that underlies FARF31 used in SKB's previous safety assessments (Appendix B). Thus, SE-SFL's geosphere and biosphere models are similar to those in SR-PSU and/or SR-Site, whereas the near-field model is less detailed in some aspects due to the partly preliminary nature of SE-SFL.

Most of the assumptions made in the radionuclide transport and dose modelling in SE-SFL are based on corresponding assumptions in SR-PSU and/or SR-Site. The maximum radiological consequences are likely overestimated due to several simplifying assumptions. These include that all radionuclides are unaffected by solubility limitations, that no radionuclide is affected by the presence of others (except ingrowth from parent radionuclides), that waste containers provide no transport resistance, that dissolved radionuclides do not reprecipitate, and that all radionuclides that reach the biosphere are discharged into a geographically limited area. Further, the uncertainty in the initial inventory of radionuclides and other materials in BHA is larger than for BHK, and thus some near-field model assumptions are more simplified and pessimistic. For instance, no account is taken of the potential delayed release of radionuclides from materials in BHA, even though part of the activity is likely contained in solid materials such as metals.

The calculations are performed for a set of evaluation cases that have been chosen based on the reference evolution (Chapter 6 in the **Main report**) or designed to evaluate the sensitivity of the release and dose results to different repository and site-specific conditions. The *present-day evaluation case* (Section 5.2) constitutes the base case for the radionuclide transport and dose calculations in SE-SFL and assumes a constant present-day climate. It serves as a simplified, highly stylized base case that in a straightforward way can be compared with cases with alternative assumptions and different temporal evolutions; it is not intended to establish a main scenario as defined by the regulations. Most evaluation cases, including the reference evolution cases, assume that the repository is located at the example location in Laxemar, and that it is constructed as per the proposed design concept. Material component

properties are taken from previous safety assessments. For instance, it is assumed that the BHA backfill is constructed with bentonite similar to that planned for the buffer in the Spent Fuel Repository, and the BHK backfill uses concrete similar to the construction concrete employed in the SFR repository.

The safety principle of SFL is retardation in the near-field (and geosphere). Effective retardation ensures that annual near-field releases are only small fractions of the total activity inventory at repository closure for all radionuclides. The release and resulting dose are further decreased by retention and radioactive decay, which is most effective for radionuclides with short half-lives relative to their retention time in the near-field (or geosphere). The total annual activity release from the BHA and BHK near-fields is dominated by the radionuclides that are most abundant in the initial inventory and have half-lives longer than a few thousand years, i.e. Tc-99, C-14 and Cl-36 from BHA and C-14 and Ni-59 from BHK. Several radionuclides that contribute significantly to the initial inventories, e.g. Ni-63 and Co-60, show a negligible release from the near-field due to their short half-lives and strong sorption onto cement and bentonite. Further, the slow release by corrosion, assumed for the metal in BHK, significantly reduces the annual near-field activity releases, including for non-sorbing radionuclides such as C-14.

Although near-field retardation of the non-sorbing C-14 is primarily due to retardation in the bentonite backfill in BHA and to slow corrosion release in BHK, it is similarly effective in the two vaults. I.e., in the base case, 93 % of the initial inventory in BHA, and 98 % in BHK, decay while retained in the near-field. Retention is more efficient for Mo-93 thanks to a low but non-zero sorption coefficient in cement and a half-life somewhat shorter than C-14; more than 99 % of the Mo-93 decays in the near-field. Of the radionuclides that contribute significantly to the near-field release and dose, retention is least efficient for the long-lived and low-sorbing Cl-36. Only about 40 % of the initial inventory in either waste vault decays in the near-field. The maximum Cl-36 near-field release is about two orders of magnitude lower from BHK than from BHA, directly correlating with the difference in initial inventory. Tc-99 has a similar half-life to Cl-36 but stronger sorption, improving retention in the BHA and BHK near-fields, albeit less in BHA since sorption there is assumed to be strongly inhibited (by a factor of 10 000) due to formation of non-sorbing complexes with cellulose-degradation products in the BHA waste.

Compared with the near-field, retention and decay in the geosphere have a marginal effect on the release of non-sorbing radionuclides in the base case, and an even more limited effect on long-lived, non-sorbing radionuclides. The translation from activity release to dose is highly radionuclide-specific; for a given release to the biosphere, the resulting dose varies by up to three orders of magnitude between substantially releasing radionuclides. Mo-93 gives large doses relative to its release compared to e.g. Ni-59. In the biosphere modelling, leaching from cultivated soil, plant uptake, and toxicity are relatively insensitive to discharge-area properties, so patterns from the base case are valid more generally. Conversely, the degree of radioactive decay occurring during retention and accumulation is discharge-area dependent, e.g. its size, soil depth and groundwater discharge. Thus, the trends among radionuclides in the base case are not readily generalisable to other discharge areas.

In the base case, the total annual doses from each of the two waste vaults exceed the dose corresponding to the risk criterion, 14 μSv. This is the dose limit according to the regulatory risk criterion, but SFL doses cannot be directly interpreted in relation to this limit, since the base case does not constitute a main scenario in a regulatory context. The annual doses from several individual radionuclides are within an order of magnitude of 14 μSv: C-14 and Mo-93 for both vaults, and Tc-99, Cl-36 and the uranium series for BHA. Draining and cultivation of a mire in the discharge area is the land use that causes the highest dose, primarily because radionuclides can accumulate in peat over a long period of time prior to exposure, and they yield dose primarily through ingestion of food. Well water contributes to the dose from Tc-99 early in the assessment and from decay products in the uranium series towards the end.

Complementing the base case, thirteen evaluation cases are analysed to study the effect of altered conditions with respect to climate (Chapter 5), the repository (Chapter 6), or the site (Chapter 7). They furthermore illustrate under what conditions sub-14 μSv doses may be achieved. The maximum doses in the *increased greenhouse effect* and the *simplified glacial cycle* cases are similar to those in the base case. The *simplified glacial cycle* case is a first evaluation of sensitivity to the large-scale landscape evolution related to future climate developments. The *alternative discharge area evaluation case* shows that the biosphere-object characteristics are important. For example, discharge into the sea can result in

doses that are orders of magnitude lower than if radionuclides are discharged to a mire. For sorbing radionuclides, this reduction is partly due to an increased effect of radioactive decay in the regolith, caused by low groundwater discharge under the sea.

Several evaluation cases lead to significantly lower doses than in the base case for BHK. These include *alternative concrete backfill in BHK*, *lower steel corrosion rate in BHK*, and *lower groundwater flow*. These three cases are potentially realistic; the first because a corresponding, new improved concrete formula is under development for SR-PSU. The second because the base-case corrosion rate is conservatively chosen and recent studies report very low long-term corrosion rates of stainless steel. Finally, better hydrological properties could, according to preliminary data, be found at other locations in Laxemar (e.g. at greater depths) and elsewhere in Sweden. In the *alternative geosphere retention properties* case, Mo-93 is modelled as weakly rather than non-sorbing in the geosphere, which decreases its annual dose contribution to about half of the maximum in the base case.

Several evaluation cases also lead to lower doses than in the base case for BHA. These include *no effect of complexing agents in BHA* and *lower groundwater flow*. BHA is less sensitive to groundwater flow rate than BHK since transport in BHA is driven by diffusion, so about hundredfold lower flow is required for significant dose reduction from BHA. Such conditions could, according to preliminary data, be found elsewhere in Sweden. The sorption-reduction effect of complexing agents is likely overestimated in the calculations, due to conservative assumptions regarding the abundance and longevity of complexing agents in BHA. It should moreover be noted that the annual dose is dominated by the radionuclides that are most abundant in the initial inventory and have half-lives longer than a few thousand years (i.e. Mo-93, Cl-36, Tc-99 and C-14). Also, nuclides in the U-238 decay chain contribute significantly towards the end of the one-million-year analysis period. Since the initial inventory for BHA is subject to substantial uncertainties, better knowledge of the inventory will influence the resulting doses.

Waste from the European Spallation Source will be placed in SFL. To assess if BHA or BHK is most appropriate, transport modelling of the corresponding radionuclides was performed. Both vaults appear promising, but definite conclusions cannot yet be drawn, due to highly uncertain inventory estimates.

Sammanfattning

SKB planerar att bygga ett slutförvar för långlivat låg- och medelaktivt radioaktivt avfall (SFL). Den föreslagna utformningen består av två förvarsdelar: BHA (bergssal för historiskt avfall) som återfylls med bentonitlera och BHK (bergssal för härdkomponenter) som återfylls med betong. Anläggningsplats för SFL har ännu inte valts, och endast en preliminär uppskattning av inventariet av radionuklider och andra material finns tillgänglig. Säkerhetsvärderingen SE-SFL är den första analysen av säkerhet efter förslutning för det förvarskoncept som Elfwing et al. (2013) föreslog. Syftet är att utreda under vilka omständigheter, i förvaret och i dess omgivningar, som det föreslagna utformningskonceptet har potential att uppfylla myndighetskraven kopplade till säkerhet efter förslutning. Denna rapport är en av huvudreferenserna till SE-SFL. Här beskrivs radionuklidtransport-modellering och dosberäkningar, som är avgörande för att utvärdera förvarets radiologiska konsekvenser och dess potential att uppfylla myndighetskraven kopplade till effektiv stråldos till människor.

Modelleringsmetodiken (kapitel 2) baseras på erfarenheter från SKB:s tidigare säkerhetsanalys SR-PSU. Dock är representationen av förvaret här avsiktligt förenklad jämfört med SR-PSU. Den häri beskrivna transportmodelleringen bygger på förvarets referensutveckling (**Huvudrapporten**), på SE-SFL:s fyra övriga huvudreferenser (**Biosfärssyntesen**, **Klimatrapporten**, **FEP-rapporten**, **Initialtillståndsrapporten**), och på de många underlagsrapporter som behandlar olika aspekter av systemkomponenter i SFL. Dessa innefattar bland annat de hydrogeologiska egenskaperna kring förvaret, bentonit- och betongbarriärernas degraderings- och andra egenskaper, samt metoder och indata för transportmodelleringen i de olika domänerna.

Urvalet av relevanta radionuklider som inkluderats i analysen beskrivs i kapitel 3. Analysperioden sträcker sig över en miljon år, och Laxemar i sydöstra Sverige används som ett relevant exempel på en anläggningsplats för ett geologiskt slutförvar. Kapitel 4 beskriver modelleringsverktygen som använts för beräkningar av radionuklidutsläpp från förvaret (närfält), för transport från förvaret till ytan genom berggrunden (geosfär), transport och ackumulation i ytsystemen, och resulterande stråldoser till människor i den mest exponerade gruppen (biosfär). Radionuklidtransportmodellerna för närfält och biosfär är implementerade i mjukvaran Ecolego, och bygger på samma principer som motsvarande modeller i SR-PSU. Geosfärstransporten har modellerats med koden FARFCOMP som är en ny implementering av samma konceptuella modell som ligger till grund för FARF31 som använts i SKB:s tidigare säkerhetsanalyser (Appendix B). Geosfärs- och biosfärsmodellerna liknar alltså de som använts i SR-PSU och/eller SR-Site, medan närfältsmodellen har en lägre detaljnivå i vissa hänseenden, på grund av SE-SFL:s delvis preliminära karaktär.

Radionuklidtransport- och dosmodelleringen bygger på ett antal antaganden, som i de flesta fall baseras på motsvarande antaganden i SR-PSU och/eller SR-Site. Förvarets maximala radiologiska konsekvenser är sannolikt överskattade, som följd av ett flertal förenklande antaganden. Bland annat antas att alla radionuklider har oändlig löslighet i grundvattnet, att ingen radionuklid påverkas av närvaron av andra radionuklider (förutom inväxt från modernuklider), att avfallsbehållare inte ger något transportmotstånd, att upplösta radionuklider inte fäller ut igen, och att alla radionuklider som når biosfären släpps ut till ett geografiskt begränsat område. Dessutom råder större osäkerheter kring BHA-avfallets radionuklid- och materialinventarium än för BHK-avfallet, varför vissa ytterligare förenklande och pessimistiska antaganden har gjorts i närfältsmodellen för BHA. Till exempel har ingen hänsyn tagits till möjlig fördröjning av utsläpp från fasta material, trots att en del av aktiviteten i BHA-avfallet sannolikt sitter bundet i fasta material såsom metaller.

Transportberäkningarna har utförts för en uppsättning utvärderingsfall, som har valts ut antingen baserat på referensutvecklingen (kapitel 6 i **Huvudrapporten**) eller för att utvärdera hur förändrade förhållanden i förvaret eller plats-specifika förhållanden påverkar utsläpps- och dosresultaten. Utvärderingsfallet *dagens förhållanden* (*present-day evaluation case*, avsnitt 5.2) utgör basfallet för radionuklidtransport och dosberäkningar i SE-SFL och antar ett konstant klimat motsvarande dagens. Fallet är alltså förenklat och stiliserat, en utgångspunkt som enkelt kan jämföras med andra fall med andra antaganden och annan tidsutveckling. Det är inte avsett som ett huvudscenario såsom avses i myndigheternas föreskrifter. De flesta utvärderingsfallen, inklusive de tre fall som utgår från referensutvecklingens tre varianter, antar att förvaret är beläget på exempelplatsen i Laxemar, och att det är

konstruerat enligt det föreslagna förvarskonceptet. Materialen i förvaret antas ha samma egenskaper som i tidigare säkerhetsanalyser. BHA-återfyllnaden antas till exempel bestå av en bentonitlera liknande den som planeras som buffert i Kärnbränsleförvaret, och BHK-återfyllnaden antas bestå av betong som liknar den konstruktionsbetong som använts i befintligt SFR.

SFL:s säkerhetsprincip är *fördröjning* i närfältet (och geosfären). En effektiv fördröjning säkerställer att de årliga utsläppen från närfältet endast utgör en mycket liten del av förvarets totala aktivitet vid förslutning för alla radionuklider. Utsläppet av radioaktivitet och resulterande doser minskar ytterligare tack vare retention och sönderfall, vilket är mest effektivt för radionuklider med kort halveringstid jämfört med deras retentionstid i närfältet (eller geosfären). De årliga aktivitetsutsläppen från närfältet i BHA och BHK domineras av de radionuklider som dominerar respektive förvarsdels inventarium vid förslutning och har halveringstider längre än några tusen år, alltså Tc-99, C-14 och Cl-36 från BHA, och C-14 och Ni-59 från BHK. Många radionuklider som förekommer i stora mängder vid förslutning, till exempel Ni-63 och Co-60, släpps ut i försumbara mängder från närfältet tack vare sin korta halveringstid och starka sorption på cement och bentonit. De årliga utsläppen från BHK minskar ytterligare tack vare långsam frigörelse av den inducerade radioaktiviteten i det metalliska avfallet via korrosion, vilket även påverkar icke-sorberande radionuklider såsom C-14.

Fördröjning av utsläppet av den icke-sorberande radionukliden C-14 från BHA beror framförallt på fördröjning i bentonitåterfyllnaden, medan det i BHK framförallt beror på den långsamma frigörelsen via korrosion. Effekten av fördröjningen av utsläppet av C-14 är dock liknande för de båda bergssalarna; 93 % av det initiala C-14-inventariet i närfältet sönderfaller i förvaret i BHA, och i BHK är motsvarande andel 98 %. Retention av Mo-93 är ännu effektivare tack vare att den sorberar (om än svagt) på cement, och har kortare halveringstid än C-14. Mer än 99 % av all Mo-93 sönderfaller i närfältet. Bland de radionuklider som ger signifikanta utsläpp och doser är retentionen sämst för Cl-36, på grund av lång halveringstid och låg sorption. Endast runt 40 % av det initiala inventariet sönderfaller i närfältet för respektive bergssal. Som en direkt effekt av skillnaden i det initiala inventariet, är det högsta årliga närfältsutsläppet av Cl-36 omkring två storleksordningar lägre från BHA än BHK. Tc-99 har liknande halveringstid som Cl-36 men högre sorption, vilket förbättrar retentionen i båda bergssalarnas närfält jämfört med Cl-36. Effekten av sorptionen är dock mindre i BHA eftersom sorptionen för Tc-99 antas vara kraftigt begränsad (med en faktor 10 000) av att cellulosa i avfallet bryts ner till komplexbildande molekyler, vilka antas bilda icke-sorberande komplex med radionuklider.

Jämfört med närfältet har retention och sönderfall i geosfären en marginell påverkan på basfallets utsläpp av icke-sorberande radionuklider. Påverkan är ännu mindre för icke-sorberande långlivade radionuklider. Sambandet mellan aktivitetsutsläpp och effektiv stråldos är högst radionuklidspecifikt. För ett givet utsläpp till biosfären kan den resulterande dosen skilja sig upp till tre storleksordningar mellan de olika radionuklider som ger högst utsläpp. Exempelvis ger Mo-93 höga doser relativt dess aktivitetsutsläpp jämfört med Ni-59. I biosfärsmodelleringen är vissa processer, såsom lakning från odlad jord, växtupptag och toxicitet, relativt okänsliga för utsläppsområdets egenskaper; basfallets slutsatser relaterade till dessa processer är därför giltiga mer generellt. De två processerna sönderfall till följd av retention och ackumulation varierar däremot mellan utsläppsområden, exempelvis med dess storlek, jorddjup och grundvattenutströmning. För dessa processer kan inte resultaten för olika radionuklider i basfallet generaliseras till andra utsläppsområden.

I basfallet överskrider BHA och BHK, var för sig, den årliga dos som motsvarar föreskriftens riskkriterium, 14 μSv. Det är dock viktigt att påpeka att basfallet inte är ett huvudscenario i föreskrifternas mening, varför den beräknade dosen inte direkt kan användas för att utvärdera om föreskriftens riskkriterium är uppfyllt. De årliga dosbidragen från ett flertal radionuklider är var för sig inom en storleksordning från 14 μSv: C-14 och Mo-93 från båda salarna, och dessutom Tc-99, Cl-36, och uranserien för BHA. Den typ av markanvändning som ger högst dos är dikning och uppodling av en myr i utsläppsområdet, vilket huvudsakligen beror på att radionuklider kan ackumulera i torv över lång tid innan människor exponeras, samt att dosen framförallt kommer från intag av mat. Brunnsvatten bidrar till dosen från Tc-99 under analysperiodens tidiga skede, och från sönderfallsprodukter ur uranserien mot slutet.

Som komplement till basfallet har ytterligare tretton utvärderingsfall analyserats. Dessa undersöker effekten av förändrade förhållanden gällande klimatet (kapitel 5), förvaret (kapitel 6) eller platsen (kapitel 7), och illustrerar under vilka förhållanden som doser under 14 μSv kan erhållas. Fallen *ökad växthuseffekt* (*increased greenhouse effect*) och *förenklad glacialcykel* (*simplified glacial cycle*) ger

maximala doser liknande de i basfallet. Utvärderingsfallet *förenklad glacialcykel* är en första utvärdering av känslighet för storskalig landskapsutveckling som är kopplad till framtida klimatutveckling. Utvärderingsfallet *anternativt utsläppsområde* (*alternative discharge area*) visar att biosfärsobjektsegenskaper är viktiga; exempelvis kan aktivitetsutsläpp i havet ge flera storleksordningar lägre doser än utsläpp till en myr. För sorberande radionuklider beror denna minskning delvis på ökat sönderfall i regoliten, vilket i sin tur orsakas av lågt grundvattenutsläpp under havet.

Flera utvärderingsfall ger betydligt lägre doser från BHK än i basfallet, däribland *alternativ betongåterfyllnad i BHK* (*alternative concrete backfill in BHK*), *lägre stålkorrosionshastighet i BHK* (*lower steel corrosion rate in BHK*) och *lägre grundvattenflöde* (*lower groundwater flow*). Dessa tre fall är potentiellt realistiska; den förstnämnda eftersom motsvarande betong med bättre egenskaper håller på att utvecklas inom SR-PSU. Den andra eftersom basfallets korrosionshastighet är konservativt vald, och aktuella forskningsstudier pekar på mycket långsam korrosion av rostfritt stål på lång sikt. Slutligen indikerar preliminära data att bättre hydrologiska egenskaper skulle kunna hittas på andra platser i Laxemarområdet (exempelvis på större djup), eller i andra områden i Sverige. I fallet *alternativa retentionsegenskaper i geosfären* (*alternative geosphere retention*) antas Mo-93 sorbera svagt i berggrunden, vilket sänker dess årliga dosbidrag till ungefär hälften jämfört med i basfallet där den är icke-sorberande i geosfären.

Flera utvärderingsfall ger också lägre doser från BHA än i basfallet, däribland *ingen effekt av komplexbildare i BHA* (*no effect of complexing agents in BHA*) och *lägre grundvattenflöde* (*lower groundwater flow*). BHA är mindre känsligt än BHK för grundvattenflödet eftersom diffusiv transport dominerar i bergssalen. Därför krävs ungefär en hundrafaldig sänkning av flödet för att märkbart minska dosen från BHA. Sådana flödesförhållanden skulle enligt preliminära data kunna hittas på andra ställen i Sverige. Den sorptionshämmande effekten av komplexbildare överskattas förmodligen i beräkningarna, på grund av försiktiga antaganden om komplexbildarnas livslängd och mängd i BHA. Viktigt att betänka är att dosen domineras av de radionuklider som förekommer i störst mängd vid förslutning (Mo-93, Cl-36, Tc-99 och C-14). Mot slutet av den en miljon år långa analystiden ger också radionuklider i sönderfallskedjan för U-238 betydande bidrag till dosen. Eftersom det råder betydande osäkerhet kring det initiala inventariet i BHA så kan beräknade doser komma att ändras i ljuset av bättre kunskap om inventariet.

Avfall från European Spallation Source kommer att deponeras i SFL. För att utvärdera vilken förvarsdel som är mest lämpad för detta avfall gjordes transportberäkningar från BHK respektive BHA för ESS-radionukliderna. Båda förvarsdelarna verkar lovande, men några definitiva slutsatser kan ännu inte dras på grund av högst osäkra uppskattningar av det initiala inventariet.

Contents

1 Introduction

This report constitutes one of the main references supporting the safety evaluation for a proposed repository concept for the repository for long-lived waste (SFL) in Sweden. The purpose of the SFL safety evaluation (SE-SFL) is to provide input to the subsequent, consecutive steps in the development of SFL. These consecutive steps include further development of the design of the engineered barriers and the site-selection process for SFL. Further, the outcomes of SE-SFL can be used to prioritize areas in which the level of knowledge must be improved in order to perform a subsequent, full safety assessment for SFL. This chapter gives the background to the project and an overview of the safety evaluation. Moreover, the role of this report is described in the context of the evaluation.

1.1 Background

The Swedish power industry has been generating electricity by means of nuclear power for more than 40 years. The Swedish system for managing and disposal of the waste from operation of the reactors has been developed over that period. When finalised, this system will comprise three repositories: the repository for short-lived radioactive waste (SFR), the repository for long-lived (SFL), and the Spent Fuel Repository.

The system for managing radioactive waste is schematically depicted in Figure 1-1. SKB currently operates SFR at Forsmark in Östhammar municipality to dispose of low- and intermediate-level waste produced during operation of the various nuclear power plants, as well as to dispose waste generated during applications of radioisotopes in medicine, industry, and research. Further, SFR is planned to be extended to permit the disposal of waste from decommissioning of nuclear facilities in Sweden. The spent nuclear fuel is presently stored in the interim storage facility for spent nuclear fuel (Clab) in Oskarshamn municipality. Clab will be complemented by the Encapsulation Plant, together forming Clink. SKB has also applied to construct, possess and operate the Spent Fuel Repository at Forsmark in Östhammar municipality. The current Swedish radioactive waste management system also includes a ship and different types of casks for transport of spent nuclear fuel and other radioactive waste.

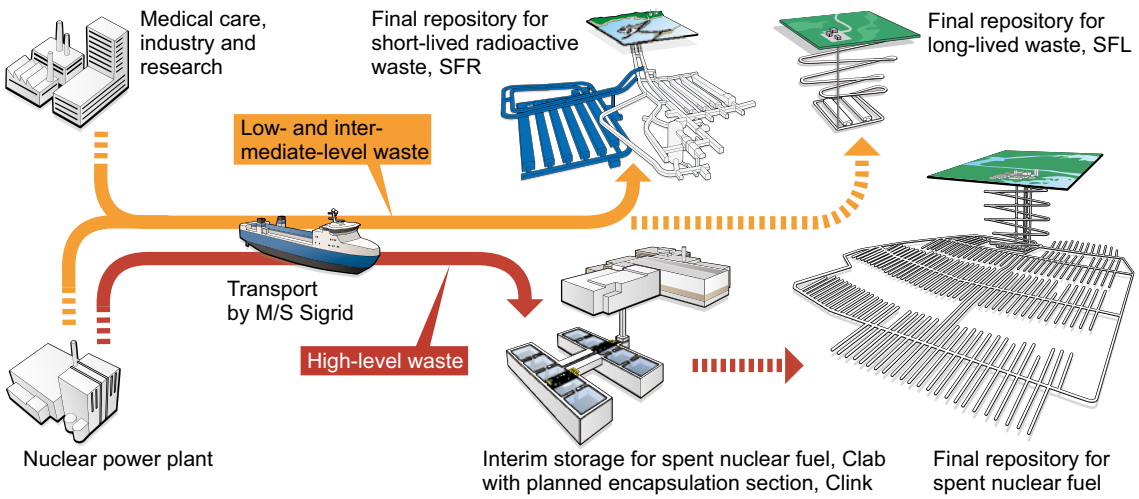

Figure 1-1. *The Swedish system for radioactive-waste management. Dashed arrows indicate future waste streams to facilities planned for construction.*

SFL will be used for disposal of the Swedish long-lived low- and intermediate-level waste. This comprises long-lived waste from the operation and decommissioning of the Swedish nuclear power plants, from early research in the Swedish nuclear programmes (legacy waste), from medicine, industry, and from research which includes the European Spallation Source (ESS) research facility. The long-lived low- and intermediate-level waste from the nuclear power plants consists of neutron-activated components and control rods and constitutes about one third of the waste planned for SFL. The rest originates mainly from the Studsvik site, where Studsvik Nuclear AB and Cyclife Sweden AB both produce and manage radioactive waste from medicine, industry and research. The legacy waste to be disposed of in SFL is currently managed by the company AB SVAFO.

In 1999, a preliminary safety assessment for SFL was presented that focussed on a quantitative analysis of the environmental impact for a reference scenario (SKB 1999). Reflecting the comments from the authorities on the preliminary safety assessment, possible solutions for management and disposal of the Swedish long-lived low- and intermediate-level waste were examined in the SFL concept study (Elfwing et al. 2013). Among the considered alternatives a system was proposed as a basis for further assessment of post-closure safety. According to this concept, SFL is designed as a deep geological repository with two different sections:

- One waste vault, designed with a concrete barrier, BHK, for metallic waste from the nuclear power plants, and
- one waste vault, designed with a bentonite barrier, BHA, for the waste from Studsvik Nuclear AB, Cyclife Sweden AB and AB SVAFO.

A schematic illustration of SFL is displayed in Figure 1-2. In SE-SFL, it is assumed that the waste vaults are located at 500 m depth. BHK is approximately 135 m long and BHA is approximately 170 m long. Both vaults have a cross sectional area of approximately 20 × 20 m^2 (see further Section 4.3 in the **Main report**).

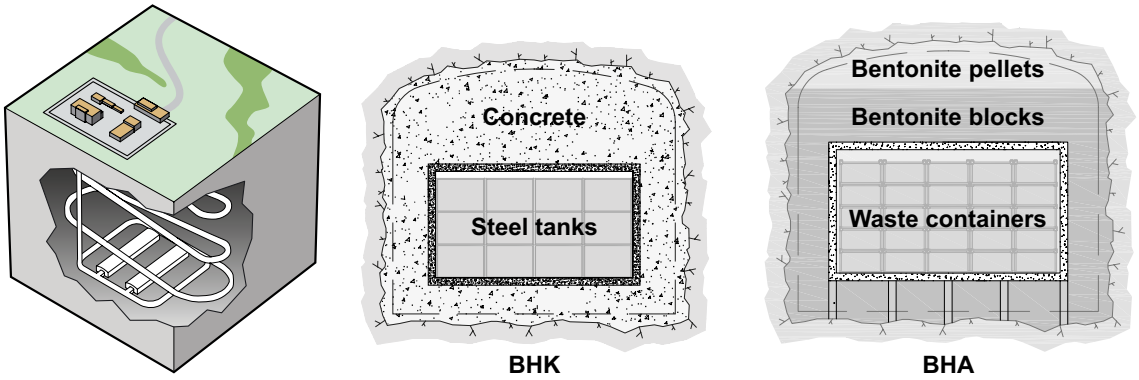

Figure 1-2. *Preliminary facility layout and the proposed repository concept for SFL (left), one waste vault for metallic waste from the nuclear power plants (BHK, centre) and one waste vault for waste from Studsvik Nuclear AB, Cyclife Sweden AB and AB SVAFO (BHA, right).*

1.2 The SFL safety evaluation

There are two main objectives for SE-SFL. The first is to evaluate conditions in the waste, the barriers, and the repository environs under which the repository concept has the potential to fulfil the regulatory requirements for post-closure safety. The second is to provide SKB with a basis for prioritizing areas in which the level of knowledge and adequacy of methods must be improved in order to perform a full safety assessment for SFL. This is in line with the iterative safety analysis process that the SFL repository program follows, in which the results from post-closure safety analyses and related activities (e.g. information from a site selection process and development of numerical methods) are used to successively inform and improve the analysis. In accordance with the Nuclear Activities Act (1984:3), important research needs for the SFL programme that emerge as a result of SE-SFL will be reported in the research development and demonstration (RD&D) programme. An important aspect of this is to ensure that the industry has well founded information to support long-term planning.

The safety analysis methodology as applied in SE-SFL is a first evaluation of post-closure safety for the repository concept proposed by Elfwing et al. (2013) and is not part of a license application. As such, the methodology has been adapted to suit the needs of SE-SFL and thus differs from the methodology established by SKB for the most recent safety assessments for the extended SFR (SR-PSU; SKB 2015a) and for the Spent Fuel repository (SR-Site; SKB 2011a). This also implies that the regulatory requirements on the methodology have not been applied rigorously, which would be needed for a safety analysis that is part of a license application. The evaluation is intentionally simplified as compared with SR-Site and SR-PSU, and more focus is given to aspects connected to the further development of the repository concept and related analyses. This is also reflected in using the term safety evaluation in contrast to safety assessment. The differences between SE-SFL and a full safety assessment are described in more detail in Section 2.1 of the **Main report**. The adaption of the methodology for the purposes of SE-SFL is described in Section 2.5 of the **Main report**.

To the extent applicable, SE-SFL builds on knowledge from SR-PSU and SR-Site. There are communalities regarding the waste, engineered barriers, bedrock, surface ecosystems and external conditions relevant to post-closure safety. For instance, SE-SFL and SR-Site both address timescales of one million years (see Section 2.3 in the **Main report**). A further similarity is the proposed depth of 300−500 m. There are similarities between SFR and SFL regarding the waste and waste packaging and the proposed engineered barriers.

In SE-SFL, a first evaluation of a suitable repository design for disposal of the ESS waste is carried out. Since the information regarding the ESS inventory is not yet as well defined as for the other waste streams, the protective capability of the different waste vaults in relation to this waste is analysed separately.

No site has yet been selected for SFL and therefore data from SKB's site investigation programmes for the Spent Fuel Repository and for the extension of SFR have been utilized in SE-SFL. In order to have a realistic and consistent description of a site for geological disposal of radioactive waste, data from the Laxemar site in Oskarshamn municipality (see Figure 1-3), for which a detailed and coherent dataset exists, are used. Based on an initial hydrogeological analysis for SE-SFL, the example location for the SFL repository was selected to be a part of the rock volume that was earlier found most suitable for a potential Spent Fuel Repository within the Laxemar site (SKB 2011b).

SE-SFL is further developed in comparison to the previous assessments, which were mentioned in Section 1.1. Important improvements are an updated inventory and more realistic account of internal and external processes. Moreover, the biosphere was in the preliminary assessment handled in a simplified manner, whereas it is handled in an elaborate way in SE-SFL. The availability of data from the Spent Fuel Repository site investigations also allows for more detailed representations of the geosphere. In general, SKB's experiences with safety analysis work have led to many developments since the late 1990s.

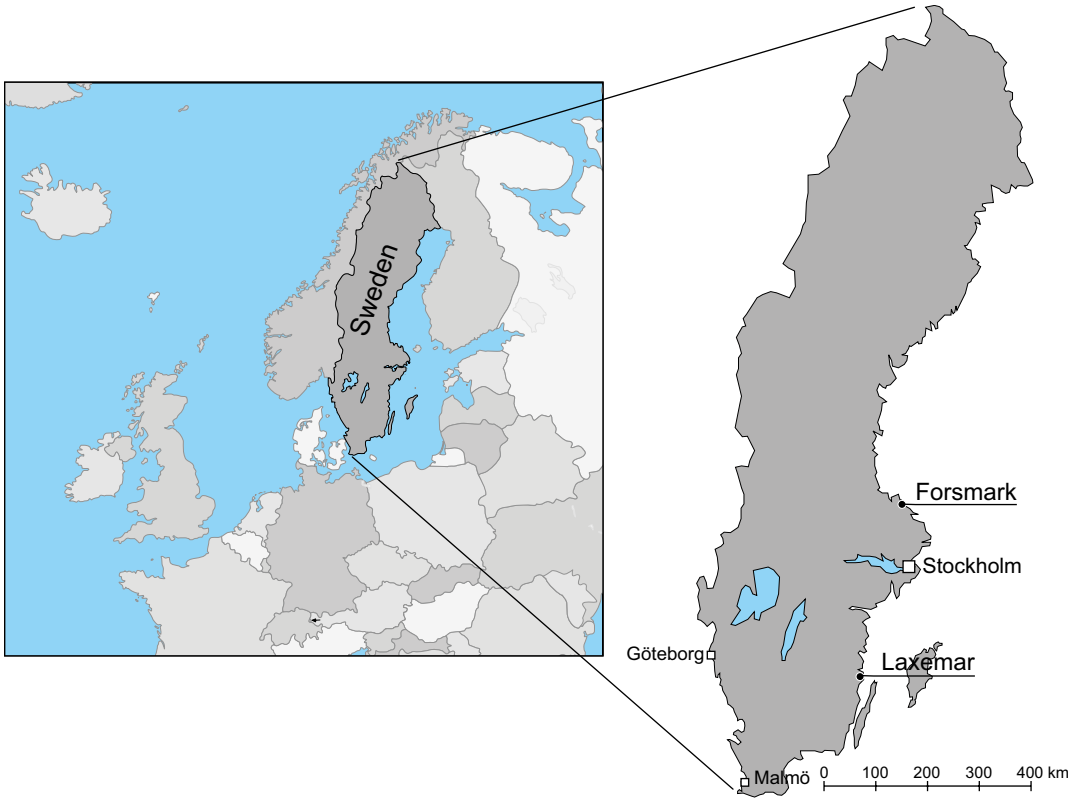

Figure 1-3. *Map showing the location of Laxemar and Forsmark. Data from the site investigations in Laxemar, along with the data from the SR-Site and SFR assessments from Forsmark, are used in SE-SFL in order to have a realistic and consistent description of a site for geological disposal of radioactive waste, for which a detailed and coherent dataset exists.*

1.3 The SE-SFL report hierarchy

The **Main report** and main references in SE-SFL are listed in Table 1-1, also including the abbreviations by which they are identified in the text (abbreviated names in bold text). It can be noted that there are no dedicated process reports for SE-SFL. The SFR and SFL waste and repository concepts have many similarities, for instance the use of similar barrier materials and thus similar process interactions with the surrounding bedrock environment (Section 2.5.4 in the **Main report**). Therefore, the descriptions of internal processes for the waste (SKB 2014a) and the barriers (SKB 2014b) in SR-PSU are used in SE-SFL. For the bedrock system, the descriptions of internal processes for the geosphere in SR-Site (SKB 2010a) and SR-PSU (SKB 2014c) are used. There are also several additional references, which include documents compiled within SE-SFL, for instance input data reports for the radionuclide transport and dose calculations (Shahkarami 2019, Grolander and Jaeschke 2019). But there are also references to documents that have been compiled outside of the project, either by SKB or other similar organisations, or are available in the scientific literature. In Figure 1-4, the hierarchy of the **Main report**, main references and additional references within SE-SFL is shown.

Table 1-1. Main references in SE-SFL and the abbreviations by which they are identified in the text, where they are bolded.

Abbreviation used when referenced in this report	Text in reference list
Main report	**Main report, 2019.** Post-closure safety for a proposed repository concept for SFL. Main report for the safety evaluation SE-SFL. SKB TR-19-01, Svensk Kärnbränslehantering AB.
Biosphere synthesis	**Biosphere synthesis, 2019.** Biosphere synthesis for the safety evaluation SE-SFL. SKB TR-19-05, Svensk Kärnbränslehantering AB.
Climate report	**Climate report, 2019.** Climate and climate-related issues for the safety evaluation SE-SFL. SKB TR-19-04, Svensk Kärnbränslehantering AB.
FEP report	**FEP report, 2019.** Features, events and processes for the safety evaluation SE-SFL. SKB TR-19-02, Svensk Kärnbränslehantering AB.
Initial state report	**Initial state report, 2019.** Initial state for the repository for the safety evaluation SE-SFL. SKB TR-19-03, Svensk Kärnbränslehantering AB.
Radionuclide transport report	**Radionuclide transport report, 2019.** Radionuclide transport and dose calculations for the safety evaluation SE-SFL. SKB TR-19-06, Svensk Kärnbränslehantering AB.

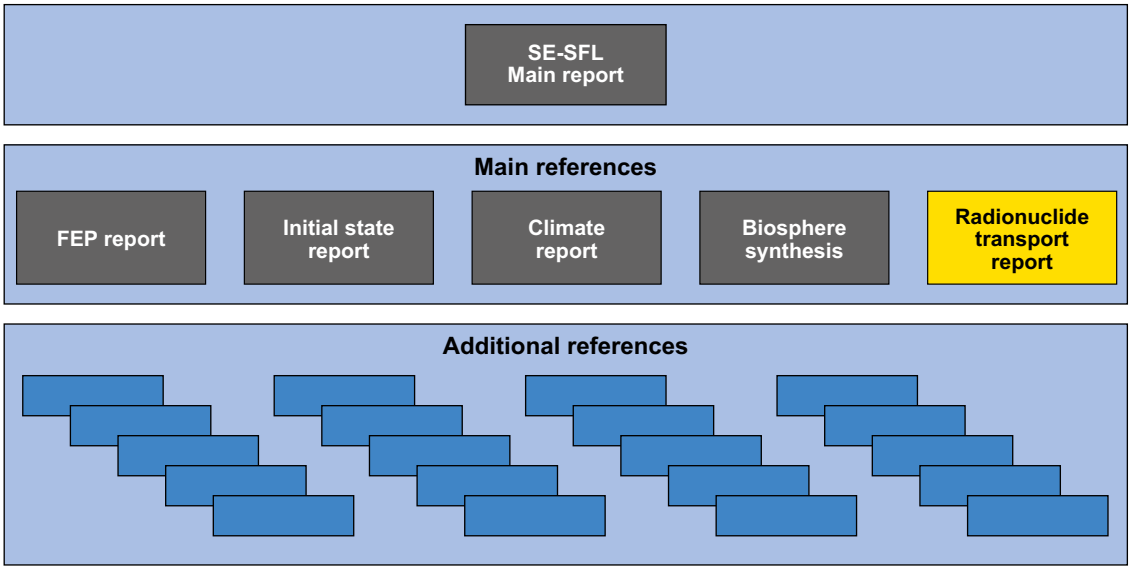

Figure 1-4. *The hierarchy of the Main report, main references and additional references in the safety evaluation of post-closure safety SE-SFL. The additional references either support the Main report or one or more of the main references.*

1.4 The role of this report in SE-SFL

This report documents developments and calculations undertaken in relation to the transport of radionuclides in the repository near-field, the geosphere, and the biosphere, which is a central part of the evaluation of post-closure safety for the proposed repository concept for SFL. The developed calculation tools have been used to provide support to, or to carry out, dose calculations. The radionuclide transport and dose calculations are performed with different models representing different parts of the disposal system; the near-field (repository), the geosphere and the biosphere. A description of the modelling tools used is given in Chapter 4. A detailed account of radionuclide transport in the surface ecosystem and the dose calculations is given in the **Biosphere synthesis**.

Radionuclide transport and dose calculations have been undertaken to provide a basis for estimation of the doses arising from the proposed calculation cases in SE-SFL (Chapters 5−7). The results are essential information to assess whether the proposed repository concept has the potential to provide an acceptable level of radiological safety over time. They should also provide SKB with a basis to assess under what conditions, including the repository environs, the disposed waste and the barriers, the proposed concept has the potential to meet applicable criteria. Moreover, the results can be used as a basis for the future development of the repository concept and the site selection process. The conclusions of the overall safety evaluation are presented in Chapters 9 and 10 of the **Main report**.

1.5 Structure of this report

This report contains descriptions of modelling tool developments, established models, calculation cases and results from the radionuclide transport and dose calculations. The following is a brief description of the contents by chapter.

Chapter 1 – Introduction: This chapter gives the background and discusses the role of this report within SE-SFL.

Chapter 2 – Methodology and modelling approach: This chapter describes the part of the safety analysis methodology that is directly related to radionuclide transport modelling and the approach used in the modelling and also discusses basic assumptions and the approach adopted for handling uncertainties.

Chapter 3 – Radionuclide inventory and selection of radionuclides for transport modelling: This chapter presents the radionuclide inventory used in the calculations and the initial selection performed to identify radionuclides potentially relevant to long-term safety and hence requiring consideration in the modelling.

Chapter 4 – Modelling concepts and tools: This chapter presents conceptual and mathematical models for the assessment of radionuclide transport in the near-field, geosphere and the biosphere as well as the calculation of doses.

Chapter 5 – Radionuclide transport and dose calculations for the reference evolution: This chapter presents the results, i.e. radionuclide releases from the near-field, from the geosphere, and annual effective doses to humans for the evaluation cases corresponding to the reference evolution.

Chapter 6 – Sensitivity of the safety evaluation to conditions in the repository near-field: This chapter presents the results for the evaluation cases that analyse the sensitivity of resulting doses to different properties and conditions in the repository near-field. Moreover, the performance of the barrier system for radionuclides that are expected to be part of the ESS waste is analysed.

Chapter 7 – Sensitivity of the safety evaluation to site-specific conditions: This chapter presents the results for the evaluation cases that analyse the sensitivity of resulting doses to different aspects of the site characteristics.

Chapter 8 – Discussion: This chapter discusses the results from the evaluation cases and draws conclusions regarding the main features of the proposed SFL concept that affect the radionuclide transport and dose calculations. This includes the impact of uncertainties from the used methodology and how the experience gained from this evaluation will be used in future assessments.

Appendix A – Glossary: Explanation of terms and abbreviations used in this report.

Appendix B – Description of the implementation of FARFCOMP, a compartment model for geosphere transport.

Appendix C – Groundwater flow scaling factors for the near-field and geosphere in the simplified glacial cycle evaluation case.

2 Methodology and modelling approach

2.1 Introduction

Chapter 2 in the **Main report** describes the methodology used for the safety evaluation. In this chapter, we present the part of the methodology that is directly related to radionuclide transport modelling. In Section 2.2, the role of the radionuclide transport and dose calculations in the safety evaluation methodology is described. In Section 2.3, the methodology used in SE-SFL for the radionuclide transport calculations is discussed with a focus on a description of the conceptual models adopted. In Section 2.4, methodological aspects of the modelling approach, the evaluation cases, input data and uncertainties are discussed.

2.2 Radionuclide transport and dose calculations in the context of the safety evaluation methodology

The safety evaluation methodology includes ten main steps, see Figure 2-1. Step 9 is the evaluation of post-closure safety. Within this step, models are used to calculate radionuclide releases from the repository, transport from the repository to the surface system, uptakes and transfers in the biosphere, and the resulting effective doses to humans. The present report constitutes the main account for step 9.

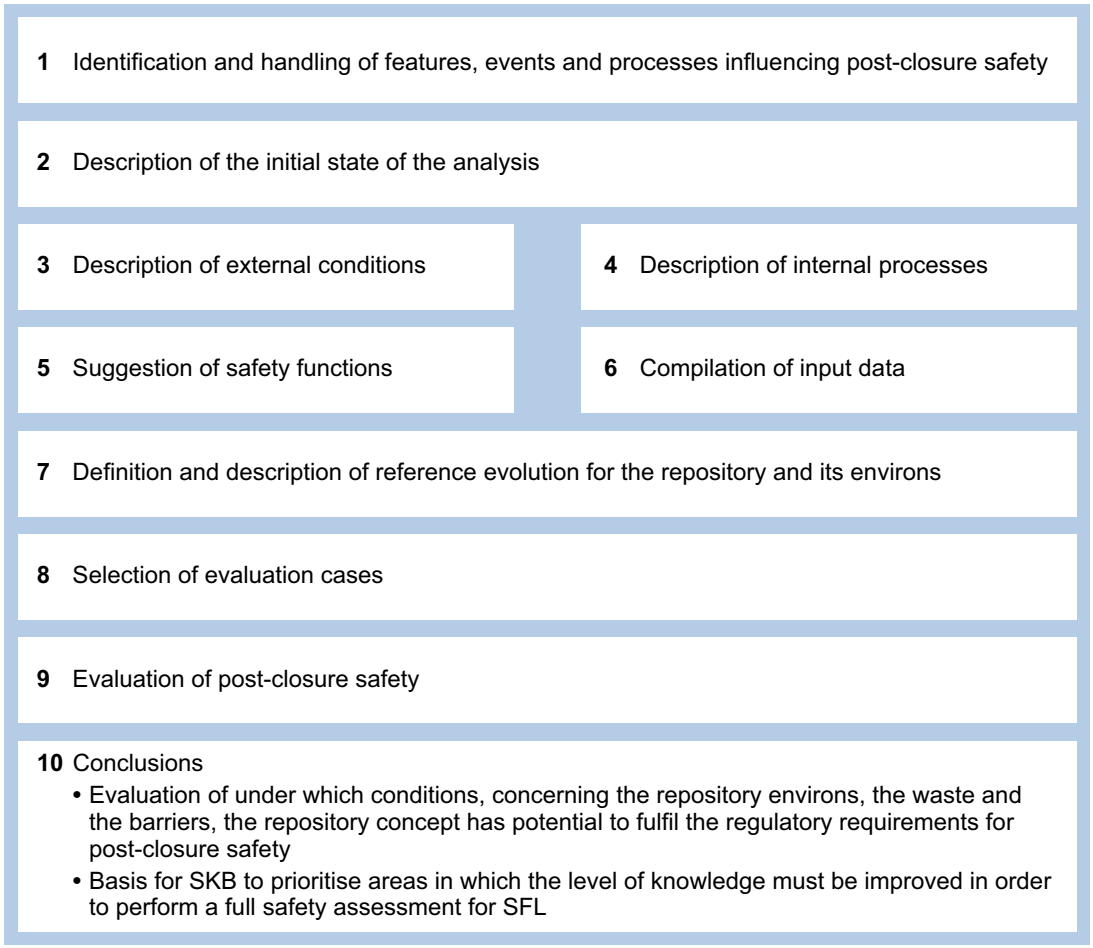

Figure 2-1. *Overview of the methodology applied for the evaluation of post-closure safety for the proposed repository concept for SFL. For a description of the steps, see the Main report, Section 2.5.*

A prerequisite for the transport and dose modelling is that the future evolution of the system is defined. The evolution, therefore, needs to be deduced from an assumed initial state of the repository and the important external and internal processes affecting the repository, together with related data. This is accomplished in step 7 of the methodology that describes the reference evolution that builds on the analysis in the preceding steps 1-6 of the methodology. To account for different possible future climate developments, three variants of the reference evolution are defined (see further Chapter 5).

The reference evolution defines the evolution of the repository and its environs. However, it does not quantify the effects of the evolution on the release and transport of radionuclides. To link the evolution of the system to the fate of the radionuclides contained in the system, evaluation cases are defined in step 8 of the safety evaluation methodology. Within these cases, the detailed assumptions and associated parameterisation that are used in the radionuclide transport and dose calculations are defined. The methodology underlying the selection of evaluation cases is described in Section 2.5.8 in the **Main report**, and they are briefly presented in Section 2.4.1. The input data are documented and described in Shahkarami (2019) and Grolander and Jaeschke (2019).

In step 8 of the methodology, evaluation cases are selected for which the radionuclide transport and dose calculations are performed, as documented in the present report. In SE-SFL, the term evaluation case is used rather than scenario, since a broader approach is applied in the selection of the cases than proposed in SSM's regulatory guidance for scenario selection (SSM 2008a). The evaluation cases are based on the three variants of the reference evolution (step 7) as well as several sensitivity cases evaluating different conditions in the near-field or relating to conditions at the repository site.

The results of the evaluation cases together with the results of the analysis of the evolution of the system, e.g. regarding barrier degradation, are used in the 10th step of the safety evaluation methodology to discuss and draw conclusions relating to the objectives of SE-SFL.

2.3 Conceptual models of radionuclide transport

Radionuclide transport and dose modelling is performed with a set of models representing different parts of the repository and its environs: the near-field, the geosphere, and the biosphere (Figure 2-2). The conceptual models for the geosphere and biosphere are the same as those used in SR-PSU and SR-Site. The near-field conceptual model is similar to that of SR-PSU. However, since this is a first evaluation of a proposed repository concept with a first estimate of the inventory of radionuclides and other materials, the near-field model is less detailed in some aspects than the corresponding SR-PSU model.

The development of the radionuclide transport modelling for the near-field is described in Wessely and Shahkarami (2019) and its detailed implementation and parameterization in SE-SFL in Shahkarami (2019), whereas the methodology of the geosphere modelling is described in detail in this report (Appendix B). The methodology of radionuclide transport in the surface system and the associated dose calculations are described in detail in the **Biosphere synthesis**. The implementation of these models for the evaluation cases is described in the present report.

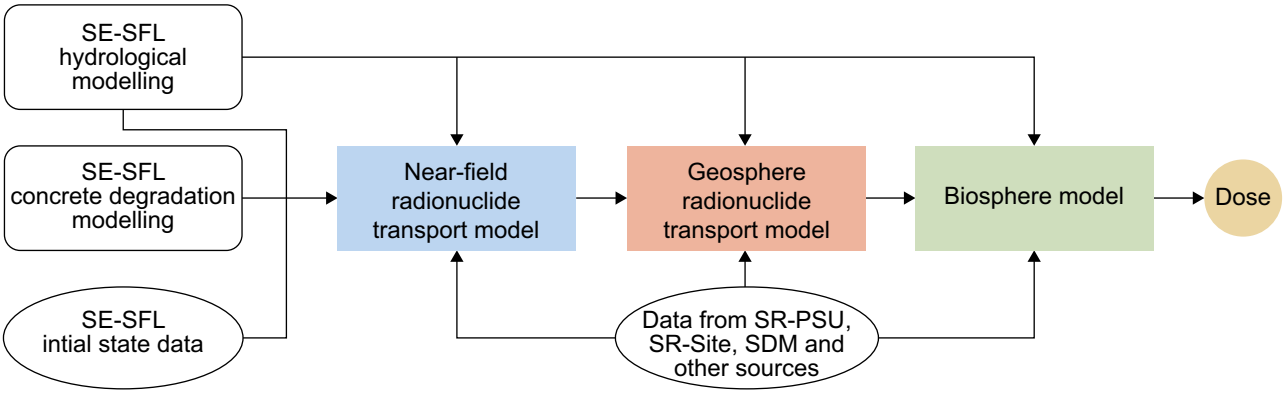

Figure 2-2. *Schematic representation of the SE-SFL radionuclide transport model chain and main sources of input for the respective models.*

The radionuclide transport calculations in SE-SFL for the geosphere are based on the hydrogeological model conceptualisation and data from Laxemar, i.e. on information included in SDM-Site Laxemar (Rhén et al. 2008, 2009, SKB 2009). The hydrogeological conditions are modelled using two model setups. One focusses on the facility scale, using a discrete fracture approach around the repository, and the other focusses on the catchment scale. Of the former, five models have been set up, using five stochastic discrete fracture network (DFN) realisations. Particles are then released and the performance measures Darcy flux, equivalent flow rates at particle starting positions, advective travel times, and F-factors are calculated for the pathlines determined for these particles. In addition, particle exit locations at the interface between the bedrock and the regolith are obtained. The second model setup, the catchment-focussed model, uses a continuous porous medium approach based on an up-scaling of the discrete fracture network (Joyce et al. 2019). Simulations there are carried out both with and without chemical reactions, respectively.

The radionuclide transport calculations in SE-SFL for the near-field are based on repository-scale hydrogeological modelling using a continuous porous medium approach (Abarca et al. 2019). The modelling is carried out using initial and boundary conditions for water pressure and chloride mass fraction that are taken from the regional groundwater flow model of Joyce et al. (2019) for 2000 AD. The regional model also provides the hydraulic properties of the bedrock such as the anisotropic permeability tensor and the porosity. The near-field hydrogeological modelling of Abarca et al. (2019) considers three situations with intact, partly degraded, and fully degraded concrete backfill in BHK. In the radionuclide transport calculations for the near-field, the effects of concrete degradation on properties of the concrete (hydraulic conductivity, porosity, effective diffusivity) and the chemical environment (pH) in the waste vault are furthermore included. The input for this is taken from the reactive transport modelling of the development of the cement and concrete materials in BHK (Idiart and Shafei 2019, Idiart et al. 2019a, b, Idiart and Laviña 2019).

The near-field model is built in the compartment simulation tool Ecolego[1]. Two models have been set up to account for the different designs and type of waste in the vaults BHA (legacy waste, bentonite backfill) and BHK (mainly metallic waste, concrete backfill). The near-field models account for the groundwater flow in the waste vault, with significantly lower flow rates in BHA than in BHK due to the difference in hydraulic conductivity of the backfill materials. Diffusive transport is also taken into account, with the effective diffusivity D_e varying with material in the vaults and depending on the charge of the species assumed for each radionuclide. Further, radioactive decay (half-life) and sorption onto cement and bentonite in the vaults (expressed as sorption coefficients K_d and sorption reduction factors) affect retardation and retention in the near-field model. In addition, in the BHK model, inclusion of a representation of corrosion contributes to retardation and retention for a fraction of the radionuclide inventory induced in metal. Although part of the activity in BHA is likely contained in solid materials such as metals and recycled nuclear fuel, the uncertainty in the initial inventory is significant, so all radionuclides in the BHA near-field model are assumed to be dissolved instantaneously upon closure.

The main assessment code for the geosphere is a new implementation of the same conceptual model that underlies FARF31 (Lindgren et al. 2002) built in Matlab; see Appendix B for a detailed description. The code uses a compartment concept and is therefore denoted FARFCOMP. It uses particle pathline data from the hydrogeological model in terms of advective travel times and F-factors. Then radionuclide-specific data (effective matrix diffusivity D_e, sorption properties, half-life) are used to apply retardation to the advective travel time and calculate radionuclide decay and, when relevant, ingrowth. FARFCOMP uses the release of radionuclides from the Ecolego near-field models as source term.

The calculation tool for the biosphere is also built in Ecolego and uses radionuclide-specific data applicable to the biosphere (**Biosphere synthesis**). The releases from the geosphere calculated with FARFCOMP are used as the radionuclide source terms for the biosphere calculations.

[1] http://ecolego.facilia.se/ecolego/show/Ecolego+Wiki

2.4 Modelling approach

The radionuclide transport calculations are carried out as dynamic calculations over the whole assessment period of 1 000 000 years, during which transport conditions may change due to barrier degradation, climate change, and shoreline displacement (depending on the calculation case). The dynamic radionuclide transport calculations are dependent on the hydrological and hydrogeological calculations. The latter are carried out as steady-state calculations for a limited number of time-points representative of the respective environmental conditions including different stages of landscape development. Water-flow-related data for use in the transport modelling are obtained from these hydrogeological calculations.

Radionuclide transport and dose calculations have been performed for each of the evaluation cases as defined in step 8 of the safety evaluation methodology and briefly presented in Section 2.4.1. To ensure that all the entities are coupled correctly together and that the transport of radionuclides from the waste to the recipients in the biosphere is modelled in a correct manner, a stepwise approach has been used in SE-SFL. A set of preliminary modelling attempts was made for verification and identification of possible technical problems e.g. in the links between entities. Typically, each entity (near-field, geosphere or biosphere) has been tested in stand-alone mode before it has been coupled to another entity. The modelling tools are coupled indirectly, i.e. the modelling chain has not been executed in continuous mode, but rather for one entity at a time followed by a manual or semi-automatic transfer of files to the subsequent calculation tool.

2.4.1 Evaluation cases

The overall approach to the selection and definition of evaluation cases is described in Section 2.5.8 in the **Main report**. An evaluation case and, if applicable, its variants, are defined by a set of parameter values corresponding to properties of the various parts of the system.

The evaluation cases include a base case assuming present-day conditions in the repository environs, as well as cases performed to explore the influence of various features, and the effects of uncertainties in the intrinsic properties of the system. For each evaluation case, one or several variants are defined and subjected to transport calculations. Figure 2-3 shows the SE-SFL evaluation cases grouped by the type of condition they consider, and Table 2-1 gives a brief overview of what conditions are altered compared with the *present-day evaluation case* in the three respective domains (near-field, geosphere, biosphere).

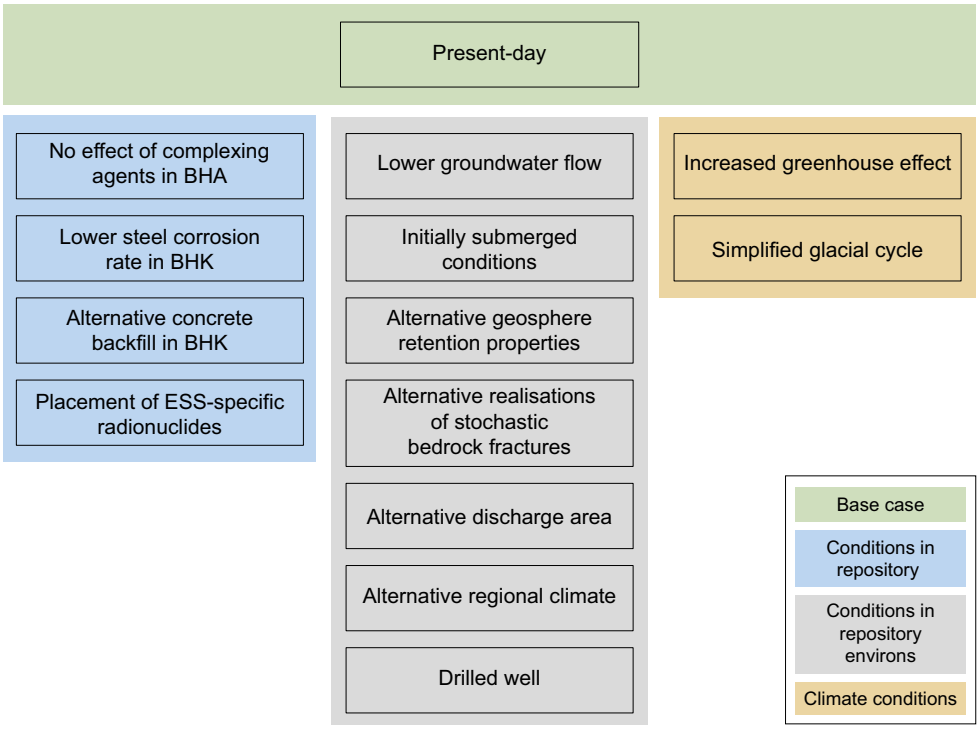

Figure 2-3. *Evaluation cases included in SE-SFL. For a description of how these cases were selected, see Section 2.5.8 in the Main report.*

Table 2-1. Summary of evaluation-case implementations in the three transport models.

Evaluation case	Near-field	Geosphere	Biosphere	Remarks
No effect of complexing agents in BHA	Sorption reduction factors not applied	As in base case	As in base case	No effect on non-sorbing radionuclides
Lower steel corrosion rate in BHK	Factor 10 lower steel corrosion rate	As in base case	As in base case	
Alternative concrete backfill in BHK	Concrete porosity and diffusivity halved. Permeability decrease by scaling advective flow by factor 0.1	As in base case	As in base case	Similar concrete properties as in Lagerblad et al. (2017), Mårtensson and Vogt (2019) and Idiart et al. (2019b)
Placement of ESS-specific radionuclides	ESS radionuclides considered in BHA and BHK, respectively	As in base case	As in base case	
Lower groundwater flow	Flow rates in waste and backfill scaled by factor 0.1, 0.01 and 0.001, respectively	Advective travel time and F-factor scaled by factor 10, 100 and 1 000, respectively	As in base case	Three variants
Initially submerged conditions	Initial period of 100-fold lower groundwater flow rates	Initial period of 100-fold lower groundwater flow rates	Biosphere object starts as sea basin, becomes a lake due to shoreline displacement	Three variants with initial periods of different length
Alternative geosphere retention properties	As in base case	Alternative bedrock sorption coefficients and diffusivities	As in base case	Bedrock data from Forsmark and Olkiluoto, respectively
Alternative realisations of stochastic bedrock fractures	BHA in its base-case eastern position or in the western, normally BHK's, position. Affects connectivity to geosphere: R_{plug} and Q_{eq}	5 realisations of stochastic DFN with different t_w and a_w	As in base case	10 variants: 2 BHA positions × 5 DFN realisations. Performance of BHK not assessed
Alternative discharge area	As in base case	As in base case	Discharge into biosphere objects with different properties, 9 in Laxemar and 6 in Forsmark	
Alternative regional climate	As in base case	As in base case	Increased groundwater flow in biosphere object, corresponding to three other regions of Sweden, respectively	Correspond to increased precipitation and/or lower temperature
Drilled well	As in base case	Release to the well = base-case geosphere release × fraction of particles that reach the well in the hydrogeological particle tracking	Garden plot household exposed through drinking water, and ingestion of vegetables and potatoes from a well-irrigated kitchen garden	Sufficiently small group (5 individuals) for use of more lenient risk criterion of 10^{-5}. Dose dominated by U-238+ from BHA
Increased greenhouse effect	As in base case	As in base case	Increased atmospheric CO_2 and decreased discharge rate of ground and surface water. Increased plant water deficit	Water deficit of plants covered by increased groundwater uptake or by irrigation, respectively
Simplified glacial cycle	Groundwater flow rates scaled by scaling factor that varies in time, following the progression of the glacial cycle	Groundwater flow rates scaled by the same scaling factor as in the near-field	Periglacial: discharge to lake via a through talik. Glacial: discharge to sea basin beyond the ice margin. Glacial retreat: flushing of radionuclides from regolith and erosion of upper regolith layers	No account of: mechanical effects, groundwater flushing to depth

2.4.2 Simplifying assumptions

Radionuclide transport and dose models used as assessment models in post-closure safety analyses represent features, events and processes (FEPs) judged to be relevant and to a level of detail deemed sufficient for the purpose. Thus, these models include a multitude of simplifying assumptions. In general, important aspects of the variants of the reference evolution are extracted to the *present-day*, *increased greenhouse effect* and *simplified glacial cycle* evaluation cases, and aspects that are judged to have minor importance are simplified in the calculations (see Chapter 5). There are other aspects of the variants of the reference evolution that have been neglected in the evaluation cases, although they might influence the evolution of the barriers and repository performance. These simplifications are discussed in Section 8.3.

Most of the assumptions made in the radionuclide transport and dose modelling in SE-SFL are based on corresponding assumptions made in SR-PSU and/or SR-Site. This includes several cautious simplifying assumptions made as a means of managing uncertainties. It is assumed that these assumptions lead to overestimation of calculated dose, in comparison to alternative, more realistic assumptions. These include that all radionuclides are unaffected by solubility limitations, that no radionuclide is affected by the presence of others (except ingrowth from parent radionuclides), that waste containers provide no transport resistance, that dissolved radionuclides do not reprecipitate, and that all radionuclides that reach the biosphere are discharged into a geographically limited area. Some of the cautious simplifying assumptions made in the radionuclide transport and dose modelling in SE-SFL are discussed Section 8.4.

2.4.3 Mean annual effective dose

In the evaluation, the annual dose corresponds to the mean annual effective dose over a lifetime for an individual living in the area with the highest concentration of radionuclides. Furthermore, adults were considered to provide a sufficiently good approximation of the average exposure during a lifetime. This is in line with the ICRP recommendations for long-lived solid waste (ICRP 1998, 2006). To estimate annual exposure during the lifetime of an individual, projected doses have been averaged over a period of 50 years, which is the integration period used by ICRP in the derivation of dose coefficients for adults. The dose coefficients used in the dose calculations consider retention of radionuclides in the human body and exposure from decay products, as well as the different radiation sensitivities of various tissues and organs. Doses calculated using these coefficients are committed effective doses, which are appropriate for calculating the probability of harmful effects of ionizing radiation using the dose to risk factor given in the Swedish regulation (SSM 2008a).

2.4.4 Management of uncertainties

The evaluation of uncertainties in assessments is an important part of the safety evaluation. The objective has been to identify the most important uncertainties in a systematic way and address them in the analysis. Uncertainties are addressed at different levels of the analysis. The sensitivity analysis with a multitude of evaluation cases (Chapters 6–7) addresses aspects of scenario uncertainty, system uncertainty, model uncertainty, parameter uncertainty and spatial variation in parameters as defined in the general advice to the SSM regulation (SSM 2008b). Some of these uncertainties are handled in the analysis underlying the evaluation cases, e.g. through multiple realisations of the hydrogeological discrete fracture network or different assumptions regarding the hydrochemical model set-up. Even though considerable efforts have been made in SE-SFL to identify and address uncertainties in a systematic way, in some parts of the analysis simplifications have been introduced, given the objective of SE-SFL. Uncertainties associated with, for instance, the simplifications that are introduced in the FEP processing by neglecting processes (**FEP report**), are not always fully addressed and are left for analysis in forthcoming safety assessments.

3 Radionuclide inventory and selection of radionuclides for transport modelling

3.1 Introduction

The prioritisation and selection of radionuclides to consider in the safety evaluation of SFL described here is mainly based on the half-lives of the radionuclides together with a criterion on radiotoxicity from ingestion of the waste at the time of repository closure (Crawford 2018). In addition, the radiotoxicity from external radiation from each radionuclide in the initial inventory has been calculated to aid the selection process.

3.2 Screening based on ingestion doses

The radionuclides with the highest radionuclide inventory are not necessarily those that contribute most to the radiotoxicity of the waste. For example, radiation from I-129 has much higher bioavailability and energy than that from Ni-59 and thereby a higher radiotoxicity. One way to estimate the radiotoxicity is by calculating the committed effective dose from ingestion of the radionuclide inventory. Hence, the radiotoxicity of the total radionuclide inventory has been calculated as a function of time starting from 2075-12-31. This is the reference date used in the compilation of data for BHA[2] and BHK (Herschend 2014). The data for radiotoxicity at the reference date are plotted versus the half-life for the waste to be deposited in BHA BHK in Figure 3-1. The vertical red line corresponds to a half-life of 10 years which delineates the cut-off for relevant radionuclides defined in SR-Site and SR-PSU (SKB 2010b and Chapter 3 in SKB 2015b). Any non-chain radionuclides to the left of this dividing line can be immediately excluded from calculations according to the previously adopted methodology. It can be noted that the inventory of any nuclide with a half-life of 10 years or less will decrease by at least 3 orders of magnitude within the first 100 years after closure. Care must be taken for radionuclides belonging to decay chains, however, since some decay products (e.g. Po-210, Ra-228) will be produced by ingrowth both in the repository and along migration paths and may contribute to the geosphere release rate in a non-negligible fashion. Co-60 is a key nuclide from which the inventory of other radionuclides sometimes is calculated through the use of correlation factors. In addition, Co-60 represents the second largest radionuclide inventory in BHK at repository closure, which is why this radionuclide is included in the analysis despite having a half-life of less than 10 years.

Nuclides with a total radiotoxicity of less than 0.1 Sv (horizontal green line) are excluded on the basis that they will contribute negligibly to annual doses relative to the sum of nuclides above this line. The value of 0.1 Sv is arbitrary but is loosely based on the lowest level at which cancer induction due to chronic exposure (on a yearly basis) is thought to be statistically verifiable in population cohort studies (e.g. Brenner et al. 2003). It should be noted that many nuclides that might be considered significant dose contributors at closure are not present in significant quantities after a few hundred years due to rapid decay (e.g. Sr-90, Cs-137 and Co-60). Some decay products, on the other hand, have significantly increased radiotoxicity owing to ingrowth (e.g. Pb-210 and Ac-227).

The main systematic difference between the two waste streams is that the legacy waste for BHA has a significantly larger inventory of U-234, U-235, U-238, and transuranic elements (with some exceptions for individual decay products). The waste to be deposited in BHK, on the other hand, generally contains a much larger inventory of fission and activation products (with the exceptions of Cs-134, Cs-135, Cs-137, Cl-36, Tc-99, and Be-10). The waste to be deposited in BHA is also characterised by much larger proportions of long-lived radionuclides relative to the waste to be deposited in BHK.

The resulting list of radionuclides that are included in the transport calculations for the waste to be deposited in BHK and the waste to be deposited in BHA is summarised in Table 3-1.

[2] Herschend B, 2015. Long-lived waste from AB SVAFO and Studsvik Nuclear AB. SKBdoc 1431282 ver 1.0, Svensk Kärnbränslehantering AB.

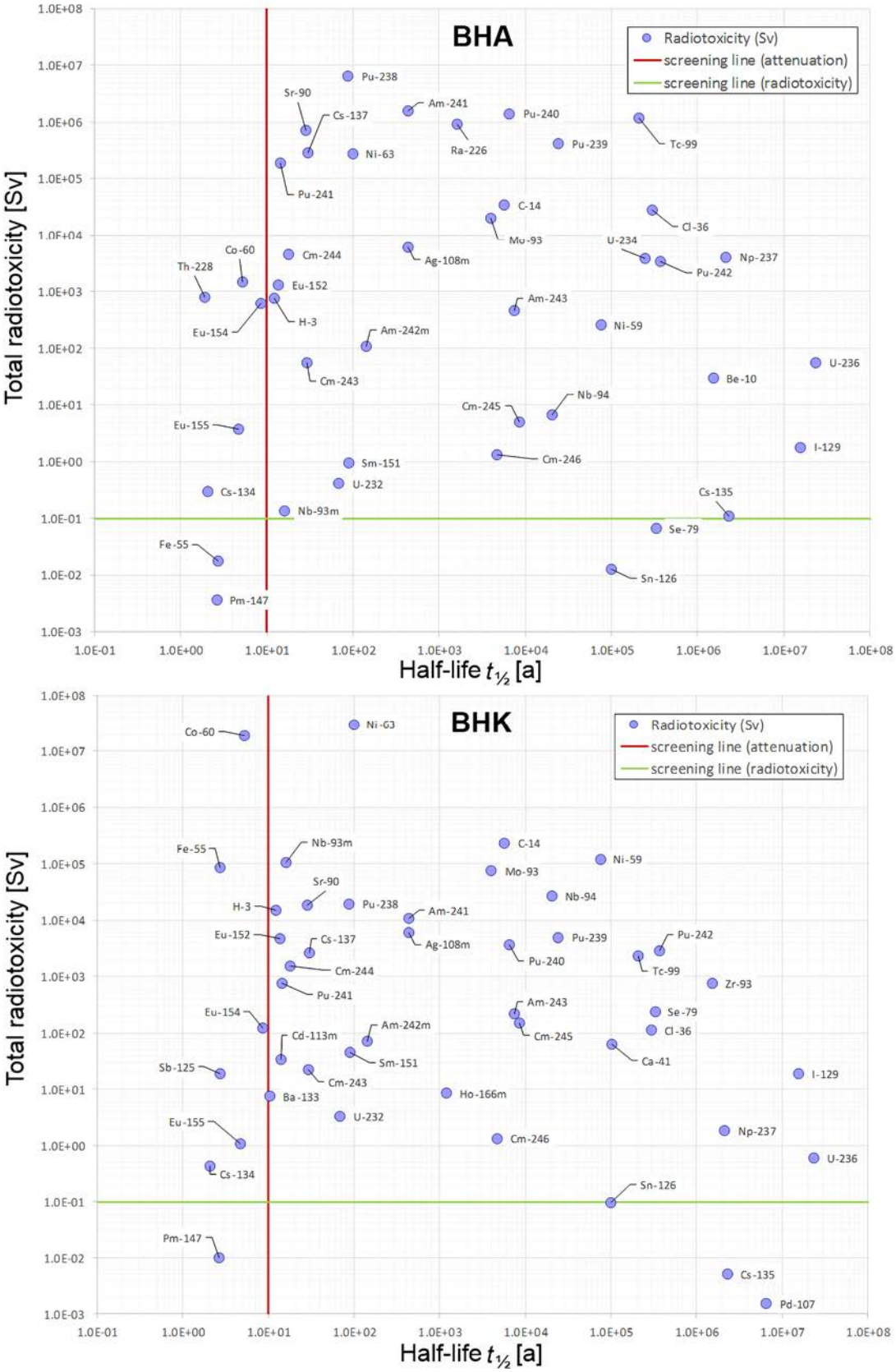

Figure 3-1. *Total radiotoxicity at 2075 AD versus half-life for all nuclides present in the waste to be deposited in BHA (top) and BHK (bottom). The red and green lines represent the screening cut-offs which are the same as those used previously in SR-Site and SR-PSU. Figure adapted from Crawford (2018).*

Table 3-1. Radionuclides included in the transport calculations for the waste to be deposited in BHA and BHK.

Radionuclide					
H-3	Sr-90	Ba-133	Ra-228	U-236	Pu-242
Be-10	Mo-93	Cs-135	Th-228	Np-237	Am-243
C-14	Nb-93m	Cs-137	Th-229	Pu-238	Cm-243
Cl-36	Zr-93	Sm-151	Th-230	U-238	Cm-244
K-40	Nb-94	Eu-152	Pa-231	Pu-239	Cm-245
Ca-41	Tc-99	Ho-166m	Th-232	Pu-240	Cm-246
Ni-59	Pd-107	Pb-210	U-232	Am-241	
Co-60	Ag-108m	Po-210	U-233	Pu-241	
Ni-63	Cd-113m	Ra-226	U-234	Am-242m	
Se-79	I-129	Ac-227	U-235	Cm-242	

3.3 External doses

In the calculation of external doses, the radionuclides present at repository closure are assumed to be located on the surface of an area of 1 m^2 and exposure from external radiation for 1 year is calculated. Using the same criterion for minimum radiotoxicity at the reference date for external dose as for dose from ingestion, i.e. 0.1 Sv, results in a list of radionuclides of concern. Most of these radionuclides are already included in the analysis based on radiotoxicity from ingestion.

Only two radionuclides, Co-60 and Eu-154, would have been excluded from the analysis based on the criterion of a half-life of less than 10 years but included based on their external dose. However, the total amount of Eu-154 at repository closure is modest, so this radionuclide is excluded from further analysis. Co-60 on the other hand is included in the analysis since it, as mentioned in Section 3.2, is a key nuclide from which the inventory of other radionuclides sometimes is calculated. In addition, Co-60 represents the second largest radionuclide inventory in BHK at repository closure both in terms of radiotoxicity (Figure 3-2) and activity (Figure 5-9).

3.4 Radionuclides to be included from ESS

Since the plans for the construction and operation of the European Spallation Source, ESS, are not yet finalised, only limited information is available concerning the likely amount and composition of its waste[3]. Due to these uncertainties, the waste volume and amount of material from ESS are not considered in the safety evaluation of SFL. Instead, the list of radionuclides from ESS has been screened for radionuclides that are specific to this waste when compared with the list of radionuclides in the BHK and BHA inventories (Crawford 2018). Chain nuclides have also been considered in the screening. The resulting list of radionuclides (Table 3-2) is included in a dedicated evaluation case, which assesses if there is a preferred placement for these radionuclides in SFL (see Section 6.5).

The ESS waste is expected to contain Ar-39.[3] As a noble gas, argon has a limited solubility in water of ~0.1 g/L at ambient conditions. Ar-39 is thus expected to be transported out mostly in gaseous form rather than dissolved. Since gas transport is not included in the radionuclide transport model, Ar-39 is not included in the calculations in SE-SFL. The gaseous Ar-39 has low radiotoxicity and is not taken up by plants in the biosphere, and thus noticeable doses from Ar-39 would require a high inventory. The exclusion of Ar-39 from the transport calculations will be re-assessed in future safety analyses, based on an updated inventory from ESS.

[3] Persson P, 2018. Characteristics of radioactive waste from ESS to be disposed in SKB facilities. Technical Report, Document number ESS-0036701, Revision 2(3), SKBdoc 1701742 ver 1.0, Svensk Kärnbränslehantering AB.

Table 3-2. Radionuclides included in the transport calculations for the ESS waste.

Radionuclide			
Si-32	La-137	Eu-150	Tb-158
Ti-44	Gd-148	Tb-157	Re-186m

4 Modelling concepts and tools

4.1 Introduction

This chapter provides a description of the modelling concepts and tools for radionuclide transport calculations performed for SE-SFL. In this safety evaluation, the radionuclide transport calculations are performed using a chain of modelling tools developed for the following three domains:

1. Waste domain and near-field barriers.
2. Geosphere; here also referred to as the host rock.
3. The surface environment.

One main modelling tool has been used for each domain. Alternative tools, analytical solutions, and scoping calculations have also been used to support the modelling methodologies. The Ecolego software has been used for modelling radionuclide transport in near-field and the surface environment; the radionuclide transport in the geosphere has been modelled using a newly developed tool FARFCOMP. In the calculations, it is essential to ensure that the models can adequately describe the transport mechanisms within the respective domains, and that the models of the different domains are properly linked to each other. In other words, the three domains in the modelling chain should:

1. Implement compatible process descriptions, at least at a general level.
2. Use numerically compatible codes where the output from one code can be used as input in another code.
3. Use compatible definitions of the parameters, so that the inputs and outputs are not only numerically compatible but also represent the same features, events, and processes (FEPs).

4.2 Coupling of the radionuclide transport models to hydrogeological and geochemical models

In support of SE-SFL, Joyce et al. (2019) carried out groundwater flow, solute transport and geochemical calculations from around 8000 BC to 60 000 AD for Laxemar assuming constant temperate climate conditions. In the calculations, the groundwater flow evolves due to shoreline displacement. Beyond 2000 AD, the simulated flow field in the repository surroundings, and the simulated flow paths from the waste vaults to the surface, do not change significantly (Joyce et al. 2019). The simulated flow field for 2000 AD is therefore chosen to represent the post-closure groundwater flow in Laxemar. This flow field served as boundary and initial conditions for the more detailed model of groundwater flow in the repository (Abarca et al. 2019). In that model, the BHA and BHK vaults are divided into a set of sections along their longitudinal axes, Figure 4-1. The sections are thereafter divided into smaller control volumes to give an appropriate representation of groundwater flow through and around the waste packages, as schematically shown in Figure 4-2.

In the near-field transport model (Wessely and Shahkarami 2019), the required groundwater flow information in the waste domain and near-field barriers is adopted from the results of the repository scale simulation (Abarca et al. 2019), whereas the equivalent flow rates, Q_{eq}, and groundwater flow information at the vault-bedrock interface are directly adopted from the hydrogeological model (Joyce et al. 2019). The only exception is the total equivalent flow rate Q_{eq}^{T} in the degraded-zone case, which is estimated as the difference between the flow entering the vault and the flow passing through the waste domain (Abarca et al. 2019). The procedure is described in detail in Sections 2.9.5 and 2.9.6 in Shahkarami (2019).

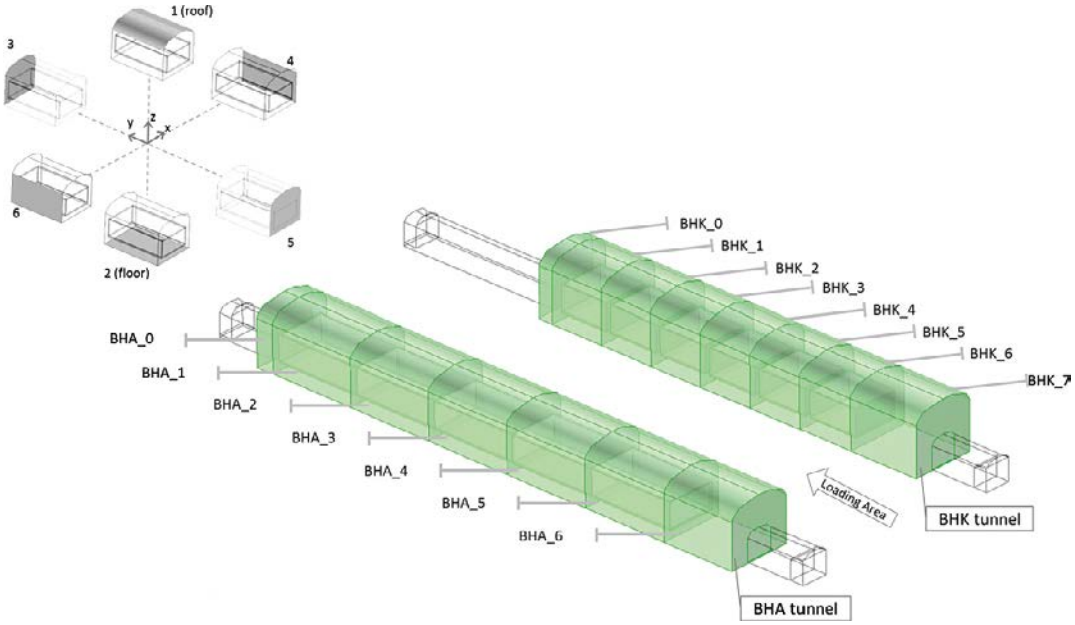

Figure 4-1. *The sections along the BHA and BHK vaults and their surfaces (Abarca et al. 2019).*

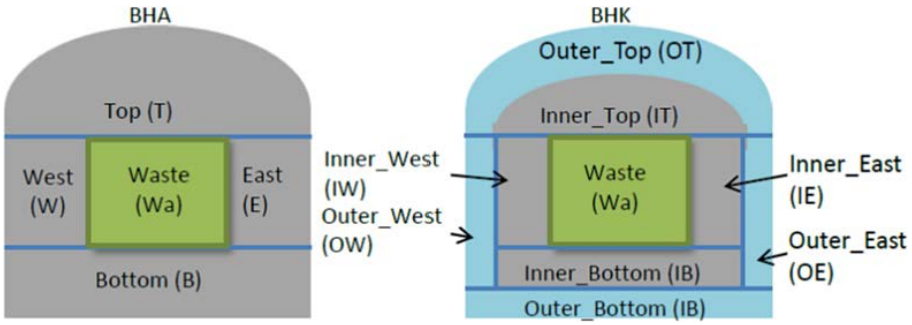

Figure 4-2. *The control volumes in the BHA and BHK vaults and their labels (Abarca et al. 2019).*

Release of radionuclides from the near-field to the fractures in the surrounding host rock serves as a source term to the geosphere transport model. At the vault-host-rock interface, the groundwater carrying radionuclides flows in a multitude of trajectories. Therefore, in the near-field model, distribution of the total radionuclide release over the host rock trajectories is done by assigning a source-term distribution factor to each such trajectory. The capacity of water within each trajectory to transport the radionuclides is calculated by multiplying this distribution factor by the vault's total release rate (Shahkarami 2019).

In the geosphere transport calculations, trajectory information is directly adopted from the hydrogeological modelling (Joyce et al. 2019). For each trajectory, the advective travel time, F-factor, and initial Darcy flux are provided. Given these data, the radionuclide transport rates in the geosphere can be calculated in the geosphere model. In the SE-SFL radionuclide transport modelling chain, the release from the geosphere serves as a source term to the biosphere model. It should be noted that the geosphere model results in an activity release per each trajectory and that those trajectories terminate at different locations. However, the results of the hydrogeological modelling (Joyce et al. 2019), indicate that most of the total potential release from the SFL repository would typically end up close to one of three biosphere objects, namely 204, 206 or 210 (see Figure 4-13). Furthermore, in three of five fracture network realisations, object 206 receives most of the discharge from the repository. Therefore, in the biosphere model, the total radionuclide release from SFL is pessimistically assumed to be discharged homogenously into biosphere object 206. The effect of this assumption is evaluated in the *discharge area evaluation case* (Section 6.3).

4.3 Near-field model

The near-field radionuclide transport model in SE-SFL includes two separate models for the BHA and BHK vaults (Wessely and Shahkarami 2019). The models rely on a compartmental conceptualization of the waste packages and engineered barriers in the backfill and address the diffusive and advective transport of radionuclides in the repository near-field. Thus, the near-field components are divided into compartments with homogenous properties, where the radionuclides and other materials in each compartment are assumed to be well mixed.

Groundwater flow rates in the near-field and geosphere are estimated in separate modelling activities (Abarca et al. 2019, Joyce et al. 2019), which serve as input to the BHA and BHK models.

4.3.1 Processes handled in the near-field model

The full set of physical and chemical processes acting in the near-field are detailed in the **FEP report**. An overview of the important transport mechanisms in the near-field model is provided below. The corresponding mathematical equations are found in Section 4.3.2.

Diffusion

The backfill materials in the waste vaults are porous. Radionuclides released from the waste are transported by molecular diffusion in the pore water and eventually reach water-bearing fractures in the surrounding rock. Diffusion is explicitly expressed in the activity transport equations of the near-field models, and values of effective diffusivities, porosities, diffusion length and cross-section areas of the backfill compartments are required inputs (Shahkarami 2019).

Advection

Advection is explicitly included in the activity transport equations of the near-field models. The groundwater flow through the vaults and waste is supplied by the repository scale model (Abarca et al. 2019). The flow, together with volumes and sorption data for the waste vaults, serve to calculate the retardation and advective transport of radionuclides. The radionuclide transport modelling implicitly takes the time-dependent degradation of the concrete barriers into account in terms of altered flow rates and transport properties, i.e., sorption and effective diffusion coefficients (Shahkarami 2019). No account is taken of degradation of the bentonite barrier.

Dispersion

Mechanical dispersion is mixing due to local variation in the water flow within the pore-structure of a porous medium. The term hydrodynamic dispersion is used to describe the combined effect of molecular diffusion and mechanical dispersion. In contrast to molecular diffusion, dispersion is not represented explicitly in the near-field models. However, the spatial discretisation of the compartment models introduces numerical dispersion in the radionuclide transport. See Wessely and Shahkarami (2019) for further details. In the radionuclide transport models for BHA and BHK, numerical dispersion is comparable to the expected influence of mechanical dispersion (Shahkarami 2019).

Sorption

Many of the dissolved radionuclides can be immobilised by sorption on cementitious and clay materials in the waste and backfill domains. A sorption reaction is often characterized by a sorption coefficient that expresses the ratio between the adsorbed mass onto the solid phase and the mass in the fluid (e.g. Bodin et al. 2003). Given linear equilibrium, the sorption coefficient can be expressed as:

$$K_d^n = \left.\frac{c_s^n}{c_{\mathrm{aq}}^n}\right|_{\mathrm{eq}} \qquad 4\text{-}1$$

where c_s^n [kg/kg] is the mass concentration of the species n in the solid phase, expressed as the mass of species n per unit mass of solid for sorption onto the porous medium; and c_{aq}^n is the concentration in the fluid phase, expressed as a mass of the species n per unit volume of the fluid [kg/m^3].

In the near-field radionuclide transport models, linear equilibrium sorption is explicitly included, parametrized by the linear volumetric sorption coefficient, K_d [m^3/kg] (Shahkarami 2019).

Radioactive decay and ingrowth

Radionuclides may decay in the waste and during transport in the backfill, but they may also be formed by ingrowth. The half-life, rate of ingrowth, and travel times affect the release to the surface ecosystem. Many nuclides have more than one decay mode. The fraction of particles which decay by a specific decay mode relative to the total number of decaying particles is expressed by the branching ratio *Br*.

Corrosion

Part of the metallic waste in BHK contains radionuclides that have been formed by neutron activation of steel during the operation of nuclear reactors. After repository closure, these radionuclides are assumed to be released as the steel corrodes. Anoxic conditions prevail in the repository and steel will be corroded by water. The rate of corrosion is also influenced by the high pH of the concrete porewater. The anoxic corrosion rate determined for SR-PSU is used also in SE-SFL (Shahkarami 2019).

Solubility

Solubility limits are not considered in the modelling. All radionuclide species in the waste packages are assumed to be dissolved instantly in the water-saturated system and pore- and groundwater, except for radionuclides released slowly through the corrosion of metals.

4.3.2 Conceptual model (compartment approach)

The radionuclide transport models in the near-field rely on the compartmental conceptualization of the near-field barriers and waste packages. In this approach, the waste packages and the barriers are divided into compartments with homogenous properties. This simplification reflects the uncertainty in the description of the system and its future evolution. However, it should be noted that the level of discretisation must be chosen appropriately to avoid overestimation of dilution (by mixing) and underestimation of possible peak radiological impacts (Wessely and Shahkarami 2019).

In the near-field model, the BHA and BHK backfills are represented with five compartments (Figures 4-3 and 4-4 respectively). Each compartment is assumed to be a homogeneous entity of the modelled system with its own averaged properties, where the radionuclide inventory depends on local processes (e.g. radioactive decay) and exchange processes with connected compartments (e.g. advective and diffusive transport).

BHA model

The waste in BHA is deposited in metal containers and stabilized with grout. The containers are emplaced in a concrete structure and the vault is backfilled with bentonite, as shown schematically in Figure 4-1. A detailed description of BHA is given in the **Initial state report** and Shahkarami (2019).

In the compartmental representation of BHA, the vault is assumed to be a cuboid with one waste compartment and three groups of bentonite backfill compartments, namely, inflow, outflow and side (including top and bottom) compartments (Figure 4-3). The geometry adopted in the radionuclide transport model is more symmetric compared to the geometry in the **Initial state report**. The simplified geometry is less sensitive to flow direction. The waste compartment includes the concrete structure, the waste, the waste packages, and the grout. The waste compartment is modelled as homogeneous in terms of materials and radionuclide inventory. The backfill compartments include an inflow compartment at one short end of the vault; an outflow compartment at the opposite short end; and compartments representing the backfill above, below and on two sides of the waste compartment. Each of the backfill compartments consist of five equally sized sub-compartments, where the outermost boundary sub-compartments connect to the geosphere model at the rock-vault interface.

The near-field model assumes one-dimensional diffusive transport within each sub-compartment, with net mass flow towards or away from the waste compartment depending on the concentration gradients. Furthermore, simulations of the near-field hydrology (Abarca et al. 2019) have shown that the groundwater flow is mainly directed along the length of the vault whereas the vertical flow component is small. Thus, in the near-field model, it is assumed that all the water that goes through the waste enters and leaves the vault through its short ends, i.e., inflow and outflow compartments. Even though the model is quite symmetric, there is still some dependence on the flow direction, where e.g. a vertical flow would give different results, albeit only slightly since diffusion is the dominating transport mechanism in BHA.

The parameterisation of the BHA compartment model is detailed in Shahkarami (2019).

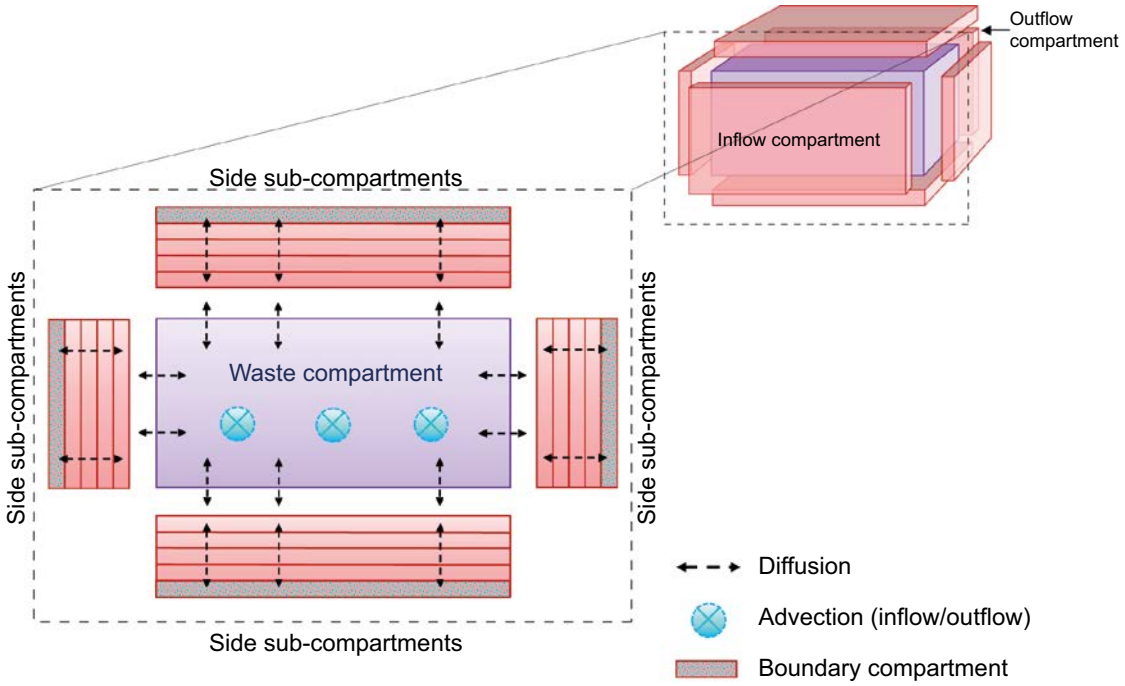

Figure 4-3. *Schematic diagram of the compartment model of BHA, seen from the short end into the length of the vault. The bentonite backfill, shown in pink, is discretised into six compartments, each in turn consisting of five sub-compartments. The outflow backfill compartment is on the far end, behind the waste compartment, and the inflow compartment is in front of the waste compartment.*

BHK model

The waste in BHK mostly consists of metallic parts with induced activity. The metallic parts are stored in steel tanks and stabilized with grout. The steel tanks are emplaced in concrete structures and the vault is backfilled with concrete, as shown schematically in Figure 1-1. A detailed description of the BHK geometry is given in the **Initial state report** and Shahkarami (2019).

In the compartmental representation of BHK, the vault is assumed to be a cuboid with one waste compartment and three groups of concrete backfill compartments (Figure 4-4). The geometry adopted in the radionuclide transport model is more symmetric compared to the geometry in the **Initial state report**. The simplified geometry is less sensitive to flow direction. The waste compartment represents the six concrete caissons, the waste, the waste packages, and the grout. The waste compartment is modelled as homogeneous in terms of materials and radionuclide inventory.

The backfill compartments include an inflow compartment at the top; an outflow compartment at the bottom; and a side compartment representing the backfill on the sides. Each of the backfill compartments consist of five equally sized sub-compartments. The outermost boundary sub-compartments connect to the geosphere model at the bedrock-vault interface.

The model assumes one-dimensional diffusive transport within each sub-compartment, which may be directed towards or from the waste compartment depending on the concentration gradients. Furthermore, simulations of the near-field hydrology (Abarca et al. 2019) have shown that the groundwater flow is directed vertically down through the BHK vault. Therefore, the main advective outflow of radionuclides to the bedrock occurs across the bottom backfill-bedrock interface, whereas no advective flow of radionuclides occurs across the top backfill-bedrock interface. The model also assumes a small groundwater flow component in the horizontal plane, allowing for an advective outflow through the side interface compartment as well, illustrated with smaller blue arrows in Figure 4-4. The parameterisation of the BHK compartment model is detailed in Shahkarami (2019**)**. Even though the model is fairly symmetric, there is still some dependence on the flow direction where e.g. a horizontal flow along the vault would give a different result since the advection directionality is different between the six backfill compartments.

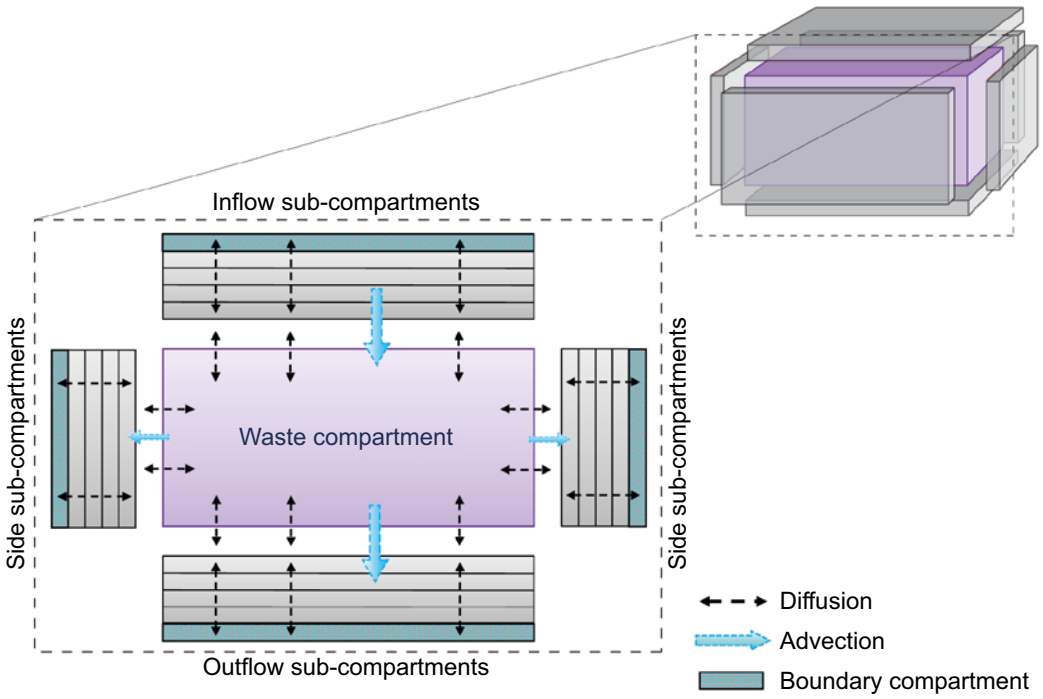

Figure 4-4. *Schematic illustration of the BHK model including the discretised backfill (grey), consisting of compartments and sub-compartments.*

Activity transport equation

Assuming that the near-field components, i.e., waste package and backfill, can be represented by continuous porous media, a transport equation for radioactivity is set up. A spatially continuous transport equation that accounts for radioactive decay, sorption, ingrowth from parent radionuclides, diffusion, advection, and release from an internal source term can generally be expressed as (Fetter 1999).

$$\left(\frac{\partial}{\partial t}+\lambda^n\right)\left((\varepsilon^n+K_d^n\rho_{\text{bulk}})c^n\right)-\sum_p\left(\varepsilon^m+K_d^p\rho_{\text{bulk}}\right)Br_p^n\lambda^n c^p = +\nabla\cdot(D_e^n\nabla c^n)-u_D\cdot\nabla c^n+r_c^n \qquad 4\text{-}2$$

where:

c^n = Activity concentration of species n in the pore water, which is a function of time and position [Bq/m^3].

ε^n = Diffusion-available porosity for species n [-].

λ^n = Decay constant of species n [s^{-1}].

ρ_{bulk} = Bulk density of the sorbing material i.e. concrete or bentonite [kg/m^3].

K_d^n = Sorption coefficient for species n [m^3/kg].

Br_p^n = Branching ratio from parent radionuclide p to radionuclide n [-].

D_e^n = Effective diffusivity of species n [m^2/s].

u_D = Darcy flux of the water [m/s].

r_c^n = Rate of release of species n per unit volume by corrosion of metallic waste [Bq s^{-1} m^{-3}].

$(\varepsilon^p + K_d^p \rho_{\text{bulk}}) Br_p^n \lambda^n c^p$ = Rate of activity ingrowth of decay product n per unit volume from parent radionuclide p [Bq s^{-1} m^{-3}].

The terms on the left-hand side of Equation 4-2 represent the accumulation of the species in the water and solid by sorption, as well as radioactive decay and ingrowth. ε is the diffusion-available porosity defined as the fraction of the total porosity available for diffusive transport of anions, cations and neutral species. The branching ratio for a decay, Br_p^n, is the fraction of a certain parent radionuclide p decaying by a specific decay mode, relative to the total amount decaying. In other words, the branching ratio is equal to the ratio of the partial decay constant to the overall decay constant of that radionuclide. Radioactive decay and ingrowth are modelled as first-order reaction terms parameterised with decay constants (Shahkarami 2019). In mathematical terms:

$$\frac{\partial A^n}{\partial t}=-\lambda^n A^n+\sum_p Br_p^n\lambda^n A^p \qquad 4\text{-}3$$

where:

A^n = Induced activity of radionuclide n [Bq].

Br_p^n = Branching ratio from parent radionuclide p to radionuclide n [-].

$\lambda^n A^p$ = Ingrowth by parent radionuclide p [Bq/s].

On the right-hand side of Equation 4-2, the first two terms describe diffusion and advection, respectively, and the third term represents the release from the waste by corrosion (Equation 4-16). Dispersion is not explicitly represented in the compartmental approach but the spatial discretization of the system in the near-field model introduces a numerical dispersive effect with respect to radionuclide transport, which corresponds to a Péclet number, Pe = 10 (Wessely and Shahkarami 2019).

In the compartmental approach, the radionuclide inventory in an individual compartment can change due to (a) local processes such as radioactive decay, (b) exchange processes with neighbouring compartments such as advection and diffusion, and (c) exchange processes with sources and sinks, i.e., boundary conditions. As a result, the change in a compartment's inventory can be described by the following continuity equation:

$$\left(\frac{\partial}{\partial t}+\lambda^n\right)\left(V_j\left(\varepsilon_j^n+K_d^n\rho_{\text{bulk}}\right)c_j^n\right)-\sum_p V_j\left(\varepsilon_j^p+K_d^p\rho_{\text{bulk}}\right)Br_p^n\lambda^n c_j^p=\sum_k\left(N_{kj}^n-N_{jk}^n\right)+r_{cj}^n \qquad 4\text{-}4$$

with

V_j = Volume of compartment j [m^3].
ε_j^n = Diffusion-available porosity for species n in compartment j [-].
N_{kj}^n = Activity release rate of species n from compartment k to j [Bq/s].
r_{cj}^n = Rate of release of species n by corrosion of metallic waste in compartment j [Bq/s].

All other variables are defined following Equation 4-2. Note that r_c^n in Equation 4-2 is in units of [Bq s^{-1} m^{-3}] and r_{cj}^n in Equation 4-4 is summed over an entire compartment j, in units of [Bq/s]. In order to account for the retardation by sorption of the migration of a sorbing species in comparison with the migration of a non-sorbing one, a retardation coefficient is defined as follows:

$$R_j^n=1+\frac{K_d^n\rho_{\text{bulk}}}{\varepsilon_j^n} \qquad 4\text{-}5$$

This allows Equation 4-4 to be rewritten as follows:

$$\left(\frac{\partial}{\partial t}+\lambda^n\right)\left(R_j^nV_j\varepsilon_j^nc_j^n\right)-\sum_p\left(R_j^pV_j\varepsilon_j^pc_j^p\right)Br_p^n\lambda^n=\sum_k\left(N_{kj}^n-N_{jk}^n\right)+r_{cj}^n \qquad 4\text{-}6$$

The default initial condition is zero for all the sub-compartments, except for the BHA waste compartment, where the initial condition is determined by the inventory of the species. In what follows, the implementation of the compartment approach in the SFL near-field model is discussed followed by the mathematical descriptions of the important transport mechanisms. A more detailed account of the transport equation and radionuclide transport processes can be found in Chapters 3 and 4 in Wessely and Shahkarami (2019).

Diffusive transport in bentonite and intact concrete

Consider two neighbouring compartments, namely j and k, as depicted in Figure 4-5. When the neighbouring compartments have comparable cross-section surface areas, the diffusive transfer rate between the compartments can be expressed as a combination of a forward and a backward diffusive transfer as follows:

$$N_{jk}^n-N_{kj}^n=\frac{c_j^n-c_k^n}{R_{kj}^n+R_{jk}^n} \qquad 4\text{-}7$$

Where R_{jk}^n [s/m^3] is the diffusive resistance against the transport of species n, from compartment j toward compartment k, given by:

$$R_{jk}^n=\frac{l_{jk}/2}{A^{jk}\times D_{e,j}^n} \qquad 4\text{-}8$$

A^{jk} [m^2] is the contact area between the compartments j and k; l_{jk} [m] is the diffusion length of compartment j in the direction of compartment k; $D_{e,j}^n$ [m^2/s] is the effective diffusivity of species n in compartment j.

When diffusion occurs from a larger compartment to a small hole or narrow fracture (See Figure 4-6), most of the transport resistance is located in the close proximity of the smaller feature (Neretnieks 1986). The transport resistance can, therefore, be approximated by a plug through which the nuclides are transported. The plug has the same thickness and cross-sectional area as the fracture and extends a distance l_{plug} into the donating compartment, as schematically shown in Figure 4-6. Neretnieks (1986) showed that the diffusion resistance of the plug can be expressed as:

$$R_{\text{plug}}^n=\frac{l_{\text{plug}}}{D_{e,k}^iA_f} \qquad 4\text{-}9$$

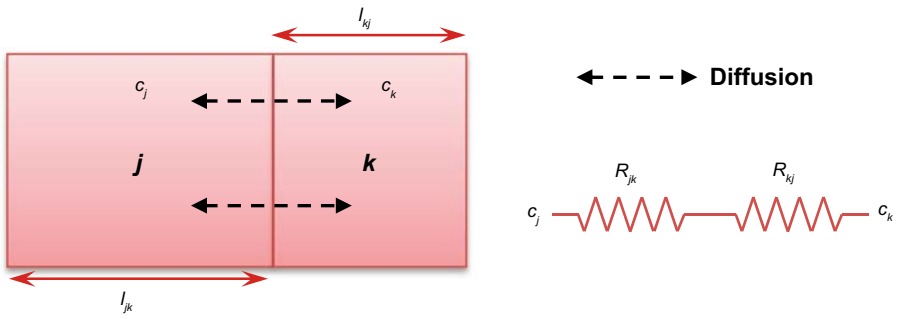

Figure 4-5. *Diffusion between compartments of comparable sizes.*

Hence, the transport rate from the large compartment k to the small compartment m can be determined by:

$$N_{km}^n - N_{mk}^n = \frac{c_k^n - c_m^n}{R_{km}^n + R_{\text{plug}}^n + R_{mk}^n} \qquad 4\text{-}10$$

where A_f [m^2] is the contact area between the compartments. The R_{km}^n can often be neglected compared with the plug resistance R_{plug}^n. The general approach to estimate the plug resistance is provided by Neretnieks (1986). The formulation is also detailed in Shahkarami (2019).

A similar situation occurs at the vault-bedrock interface, where radionuclides in the boundary compartment can diffuse to the water in a fracture in the surrounding bedrock (see Figure 4-7).

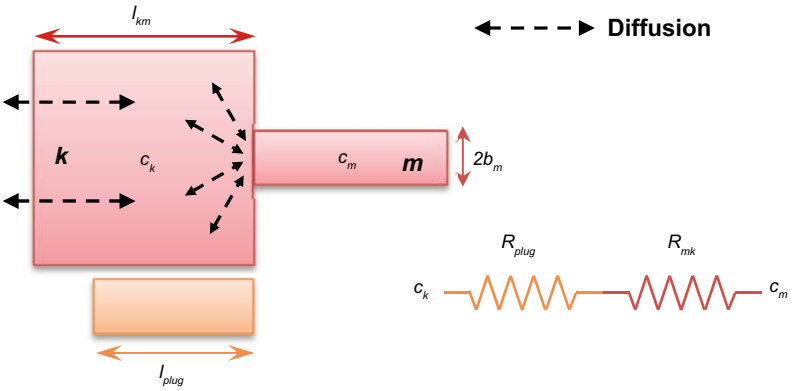

Figure 4-6. *Diffusion between large and narrow compartments (R_{km}^n is neglected).*

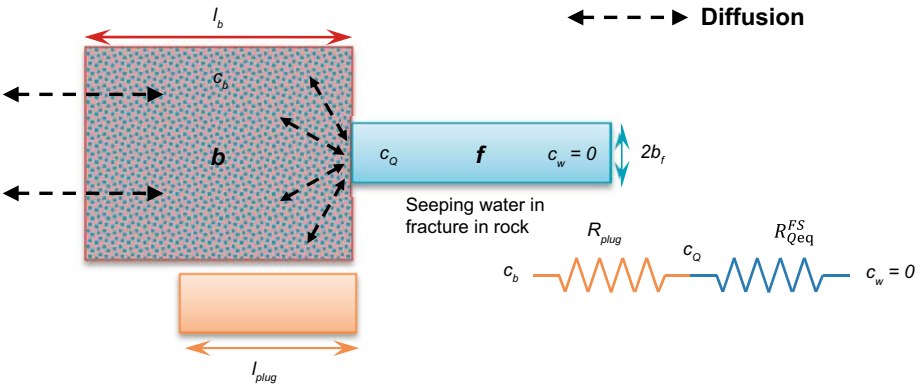

Figure 4-7. *Diffusive transport from the boundary compartment to the groundwater in the fracture in the rock (R_b^n is neglected).*

During the time the flowing groundwater with concentration $c_w = 0$ is in contact with the backfill, the water is exposed to the concentration at the water-backfill interface, c_Q. The amount of radionuclide that can be transported by the flowing water in the fracture can be estimated by introducing the concept of equivalent flow rate, Q_{eq} (Wessely and Shahkarami 2019). Hence, the total diffusive transport rate to the fracture in the host rock can be determined by:

$$N_{bf}^n = \frac{(c_b^n - c_w^n)}{R_b^n + R_{\text{plug}}^n + R_{\text{eq}}^n} \quad 4\text{-}11$$

Where c_b is the activity concentration in the boundary compartment and $R_{eq} = 1/Q_{eq}$. It should be emphasized that the diffusion transport resistance in the boundary compartment, R_b^n, can often be neglected compared with the plug resistance. It should also be noted that in the near-field model, the concentration in the flowing water in the fracture is assumed zero, $c_w = 0$.

Advective transport between compartments

Provided that the full-mixing assumption is attained in a compartment j, the advective release to the neighbouring compartment k can be expressed as:

$$N_{jk} = \begin{cases} 0, & Q_{jk} < 0 \\ c_j Q_{jk}, & Q_{jk} \geq 0 \end{cases} \quad 4\text{-}12$$

where Q_{jk} [m^3/s] is the water flow rate from compartment j to compartment k and its value is obtained from the water flow calculations made by the repository scale flow model (Abarca et al. 2019). For a boundary compartment at the vault-bedrock interface, the advective release to the host rock can be obtained from:

$$N_b = Q_b c_b \quad 4\text{-}13$$

where Q_b [m^3/s] is the water flow rate from the boundary compartment to the fracture in the rock and c_b [Bq/m^3] is the activity concentration in the boundary compartment.

Boundary condition formulation at the vault-bedrock interface

At the vault-rock interface, radionuclides can migrate from the boundary compartment by both diffusion and advection. Therefore, the total release rate from one boundary compartment N_T [Bq/a] is corresponds to adding Equations 4-11 and 4-13:

$$N_T = \frac{(c_b - c_w)}{R_b + R_{\text{plug}} + R_{\text{eq}}} + Q_b c_b \quad 4\text{-}14$$

where the radionuclide index, i.e. the superscript *n*, has been dropped for the sake of clarity. An estimate of the release from the entire vault N_{vault} [Bq/a] can be made using the water flow rate through the whole vault and the total diffusive resistance of the whole buffer.

$$N_{\text{vault}} = \frac{c_{\text{vault}}}{R_{\text{buffer}} + R_{\text{plugtot}} + R_{\text{eqtot}}} + Q_{\text{vault}} c_{\text{vault}} \quad 4\text{-}15$$

where

c_{vault} [Bq/m^3]: the average concentration in the pore water.

R_{buffer} and R_{plugtot} [a/m^3]: the diffusive resistance against transport in the backfill and the plug resistance, respectively.

$R_{\text{eqtot}} = 1/Q_{\text{eqtot}}$ [a/m^3]: the resistance associated with diffusion from the backfill to the flowing water in the bedrock fracture, where Q_{eq} is the sum of the equivalent flow rates in all fractures.

Q_{vault} [m^3/a]: the water flow rate through the whole vault.

Release of radionuclides due to the corrosion of metallic waste components

The waste in BHK contains metallic components with neutron-induced activity. Therefore, the radionuclides within the metallic components are assumed to be released from the components by corrosion. The corrosion rate is assumed to be 10 nm/a, based on the parameterisation of corrosion rate for stain-

less steel under alkaline, anoxic conditions in SR-PSU (Table 5-4 in SKB 2014d, Shahkarami 2019). In the near-field model, the metallic components are categorized with respect to their corrosion times, in the following groups with increasing thickness:

- Surface contamination and very thin metallic components (thickness < 1 mm), instant release upon repository closure.
- Component thickness of 1−10 mm with corrosion time of 50 000 years.
- Component thickness of 10−20 mm with corrosion time of 500 000 years.
- Component thickness of more than 20 mm with corrosion time of 1 000 000 years.

Radionuclides associated with surface contamination and very thin metallic components are assumed to be instantly released. However, radionuclides in the other categories are assumed to be released gradually by corrosion. Once released, the radionuclides are assumed to be available for transport from the waste domain.

It should be noted that the thickness of each component included in a category is conservatively assumed to be equal to the lower limit of the thickness interval for that category, i.e., 1 mm, 10 mm and 20 mm. Furthermore, the corrosion time, i.e. the time at which the metal components are assumed to be fully corroded, is calculated as half of the component thickness (since the corrosion is assumed to act from both sides) divided by the corrosion rate.

Each of the above metallic waste categories is represented by a well-mixed compartment. The induced activity in the compartment can change through decay, ingrowth and the activity release due to corrosion, as expressed by:

The expression below describes the release of radionuclides from the BHK metal parts with different thicknesses:

$$\left(\frac{\partial}{\partial t}+\lambda^n\right)A_l^n-\sum_p Br_p^n\lambda^n A_l^p=-r_{c,l}^n=-\sum_l H(T_l-t)\frac{A_l^n}{T_l-t} \qquad 4\text{-}16$$

where

A_l^n = Induced activity of radionuclides n in waste fraction l [Bq].

Br_p^n = Branching ratio from parent radionuclide p to radionuclide n.

$\lambda^i A_l^p$ = Ingrowth by parent radionuclide p [Bq/s].

$R_{c,l}^n$ = Release rate of radionuclides n due to corrosion of waste fraction l [Bq/s].

T_l = The time it takes to corrode the metal components in waste fraction l [s].

$H(t)$ = The Heaviside step function.

Figure 4-8 shows the rate at which radionuclides become available for mass transport as a result of corrosion. The curves are calculated from the radionuclide inventory in the metallic components, the corrosion rate, the component thicknesses, and the half-lives of the radionuclides.

The distribution of metallic parts in the BHK waste and the assumed corrosion rate are detailed in the **Initial state report** and Shahkarami (2019**)**.

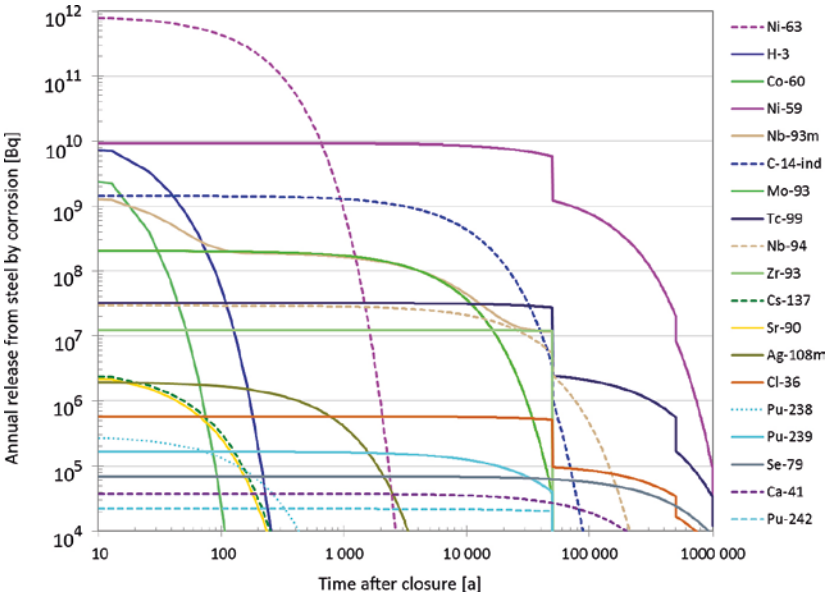

Figure 4-8. *Radionuclide release from corroding waste in BHK.*

4.4 Geosphere model

The radionuclide transport in the geosphere is modelled using a newly developed tool in Matlab, called FARFCOMP. The implementation of the radionuclide transport model in FARFCOMP is based on the corresponding model used in the SR-PSU safety assessment (SKB 2015b). A detailed description of FARFCOMP is provided in Appendix B and an overview of the main features of the tool is presented here.

In the regional hydrogeology model for SE-SFL, groundwater carrying radionuclides flows through discrete fractures (Joyce et al. 2019). The paths of radionuclides are determined by particle tracking, where a multitude of particles are injected in fractures that intersect the near-field vaults. Each individual particle is then followed, tracing out its transport path, i.e. trajectory, which is built up from a series of fracture segments. Figure 4-9 illustrates a subset of the trajectories obtained from the hydrogeological model, tracing 100 water particles from the BHA waste vault to the surface in the *present-day evaluation case*. The particle travel time t_w [a] and the flow-related transport resistance, the F-factor F [a m^{-1}], are recorded in each segment of the trajectory that the water particle follows, and the sums of the recorded values for each trajectory are used as input parameters to the geosphere radionuclide transport model, FARFCOMP.

In general, the geosphere model relies on the dual-porosity concept and describes transport of radionuclides in discrete parallel fractures situated in a porous rock matrix. Figure 4-10 illustrates the conceptual parallel fracture-matrix system, where a constant groundwater velocity v [m a^{-1}], fracture aperture $2b$ [m], and distance between fractures, i.e., maximum penetration depth $2d_{max}$ [m] is applied.

The geosphere model incorporates a compartmental representation of the fracture-matrix system to approximate the solution to the same dual-porosity problem previously obtained by the semi-analytical Fortran code FARF31 (Norman and Kjellbert 1990). The model then solves the radionuclide transport in one single discrete fracture with constant properties. The required flow-related input data are the total advective travel time t_w [a] of a water particle passing through the fracture network and the sum of the flow-related transport resistances, the F-factors F [a m^{-1}] over all fracture segments. These parameters are calculated using a particle-tracking algorithm within ConnectFlow (Joyce et al. 2019).

Eventually, by calculating a weighted sum over all trajectories, the radionuclide release into the biosphere is determined. In this way, release from all possible pathways within the geosphere and macrodispersion, arising from the multiple flow-paths, are considered. The weighted sum is calculated by using the radionuclide release from the waste vault weighted by the probability of entering the specific trajectory as a source term (Shahkarami 2019).

The geosphere assessment tool FARFCOMP has been verified in a series of comparisons with other codes (see Appendix B).

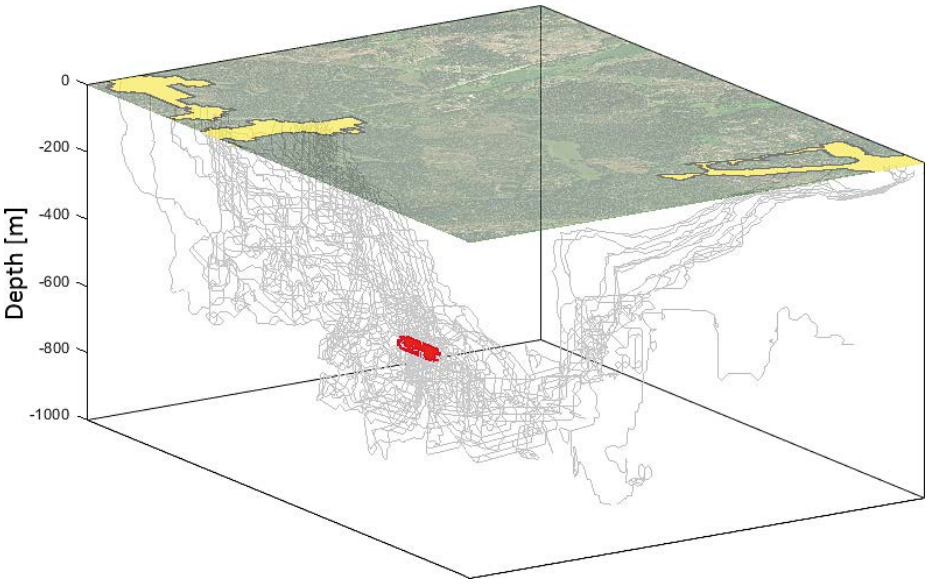

Figure 4-9. *Subset of trajectories (grey) from the BHA waste vault (red) to biosphere objects (yellow).*

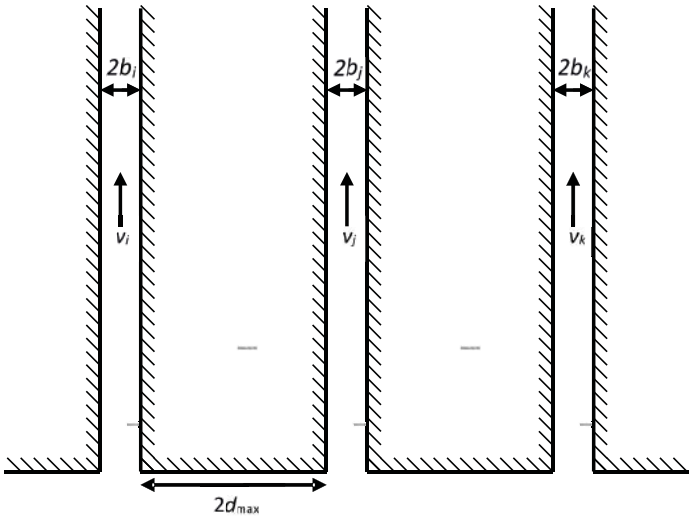

Figure 4-10. *Conceptual parallel-fracture-matrix system used in the geosphere model. After Tang et al. (1981).*

4.4.1 Processes handled in the geosphere model

All the physical and chemical processes identified in the geosphere are discussed in the **FEP report**. However, only a few of them are relevant for radionuclide transport modelling in the geosphere and these are:

1. Radioactive decay and ingrowth.
2. Advection along the fractures.
3. Longitudinal hydrodynamic dispersion along the fractures.
4. Molecular diffusion from the fracture to the porous matrix.
5. Sorption in the rock matrix.

Radioactive decay and ingrowth are included in the modelling and described by radionuclide-specific decay constants and branching ratios (see Equations 4-17 and 4-18). Sorption in the rock matrix is included in the model. However, sorption on the fracture surfaces (on e.g. fracture minerals), and fracture fill are pessimistically disregarded in the geosphere model. Advection, dispersion, rock matrix diffusion and sorption in the geosphere are discussed below.

Advection

Advection is explicitly included in the geosphere model. The hydrogeological simulations in the geosphere were performed as described in Joyce et al. (2019). The groundwater flow information used in the radionuclide transport calculations is directly obtained from the results of these simulations.

Dispersion

In the geosphere model, dispersion along the individual trajectories is explicitly modelled by means of the constant Péclet number, Pe = 10, that quantifies the ratio between advective and dispersive transport (see Equations 4-17 and 4-18).

Rock-matrix diffusion

The rock matrix is porous, and radionuclides can enter the stagnant water in the pores of the rock matrix by molecular diffusion and be withdrawn from the groundwater. The exchange between the flowing water in the fracture compartment and the adjacent rock matrix is included in the geosphere model. Fickian diffusion is assumed in the rock matrix, where a finite penetration depth is considered (Shahkarami 2019).

Sorption

Sorbing nuclides can, in addition, be retarded by sorption onto the matrix internal surface, and thereby be given more time to decay and for ingrowth. The sorption model in the geosphere comprises equilibrium sorption in the rock matrix, which is parametrized by the linear sorption coefficient, K_d. However, sorption on the fracture surface, or possible fracture fill, is conservatively disregarded in the geosphere model.

4.4.2 Conceptual model and mathematical formulation

The idealized physical fracture-matrix system that is modelled is illustrated in Figure 4-10. A constant groundwater velocity in each fracture is applied. The transport processes in such system can be described by the following two coupled, one-dimensional equations, one for the fracture and one for the porous matrix. The coupling is provided by the continuity concentrations along the interface.

$$\frac{\partial C_f^n}{\partial t} = -v\frac{\partial C_f^n}{\partial z} + D_L\frac{\partial^2 C_f^n}{\partial z^2} - \lambda^n C_f^n + \sum_{p\in P_n}\lambda^n C_f^p Br_p^n + \frac{D_e^n}{b}\frac{\partial C_m^n}{\partial x}\bigg|_{x=0} \qquad 4\text{-}17$$

$$R_m^n\frac{\partial C_m^n}{\partial t} = \frac{D_e^n}{\varepsilon_m}\frac{\partial^2 C_m^n}{\partial x^2} - R_m^n\lambda^n C_m^n + \sum_{p\in P_n} R_m^p\lambda^n C_m^p Br_p^n \qquad 4\text{-}18$$

In the above equation:

C_f^n = Activity concentration of radionuclide n in the flowing water of the fracture [Bq m^{-3}].

C_m^n = Pore-water activity concentration of radionuclide n in the matrix adjacent to the fracture [Bq m^{-3}].

t = Time [a].

v = Mean water velocity in water-bearing fracture [m a^{-1}].

z = Distance in the flow direction [m].

D_L = Longitudinal dispersion coefficient [m^2 a^{-1}].

b = Half-aperture of the fracture [m].

D_e^n = Effective diffusivity of radionuclide n in the rock matrix [m^2 a^{-1}].

x = Distance into the rock matrix [m].

λ^n = Decay rate for radionuclide n [a^{-1}].

P_n = Set of indices of parents of radionuclide n [-].

Br_p^n = Branching ratio from parent radionuclide p to radionuclide n [-].

R_m^n = Capacity factor for radionuclide n in rock matrix [-], defined as:

$$R_m^n = \frac{\varepsilon_m + K_{d,m}^n \rho_m}{\varepsilon_m} \quad 4\text{-}19$$

with

ε_m = Porosity of the rock matrix [-].

$K_{d,m}^n$ = Sorption coefficient in rock matrix for radionuclide n [m^3 kg^{-1}].

ρ_m = Bulk density of the rock matrix [kg m^{-3}].

The initial conditions are:

$$C_f^n\big|_{t=0} = 0 \quad 4\text{-}20$$

$$C_m^n|_{t=0} = 0 \quad 4\text{-}21$$

The boundary conditions are given by:

$$C_f^n\big|_{z\to\infty} = 0 \quad 4\text{-}22$$

$$Q_{\text{tube}}\left(C_f^n - \frac{D_L}{v}\frac{\partial C_f^n}{\partial z}\right)\bigg|_{z=0} = F_{\text{in}}^n \quad 4\text{-}23$$

$$C_m^n|_{x=0} = C_f^n \quad 4\text{-}24$$

$$\frac{\partial C_m^n}{\partial x}\bigg|_{x=d_{\max}} = 0 \quad 4\text{-}25$$

Q_{tube} = Volume flow of water in the fracture [m^3 a^{-1}].

F_{in}^n = Inlet activity flow of radionuclide n to fracture [Bq a^{-1}].

$d_{\max}$ = Maximum penetration depth into the rock matrix [m].

The desired quantity is the output release F_{out}^n [Bq a^{-1}] for radionuclide n at the end of the fracture z_{tot} [m]:

$$F_{\text{out}}^n = Q_{\text{tube}}\left(C_f^n - \frac{D_L}{v}\frac{\partial C_f^n}{\partial z}\right)\bigg|_{z=z_{\text{tot}}} \quad 4\text{-}26$$

F_{out}^n = Output release of radionuclide n from the fracture [Bq a^{-1}].

z_{tot} = Total length of the fracture [m].

In the geosphere model, the rock matrix and transport paths, i.e., trajectories, are divided into one-dimensional smaller compartments to approximate the solution to the dual-porosity problem. Figure 4-11 shows a schematic view of the fracture-matrix system implemented in the geosphere model. Each box represents a compartment and the arrows represent the flow of radionuclides between these compartments. Solid blue arrows represent advective transport, dashed blue arrows represent transport by dispersion, and orange arrows represent transport by diffusion.

The advective path through fractures in the rock is divided into fracture compartments of equal length that have constant properties. For the rock-matrix compartments on the other hand, the thicknesses increase exponentially from the fracture-matrix interface into the matrix (Figure 4-12) because a higher numerical resolution is required near the rock-matrix-fracture interface, due to the high concentration gradient there.

This is done by using a constant factor adjusted so that the total thickness of the rock matrix equals the maximum penetration depth $d_{\max}$ [m]. The level of discretisation along the trajectories, thickness of the first matrix compartment, maximum penetration depth and the level of discretisation in the porous matrix are then input parameters to the geosphere model.

In the geosphere model, transport of radionuclides within and between compartments is described by defining transfer rates [a^{-1}]. The annual release of a radionuclide from a compartment [Bq] can then be described by the total activity of the radionuclide in the given compartment [Bq] times the sum of the transfer rates out from the compartment. Details on the derivation of the transfer rates incorporated in the geosphere model are presented in Appendix B.

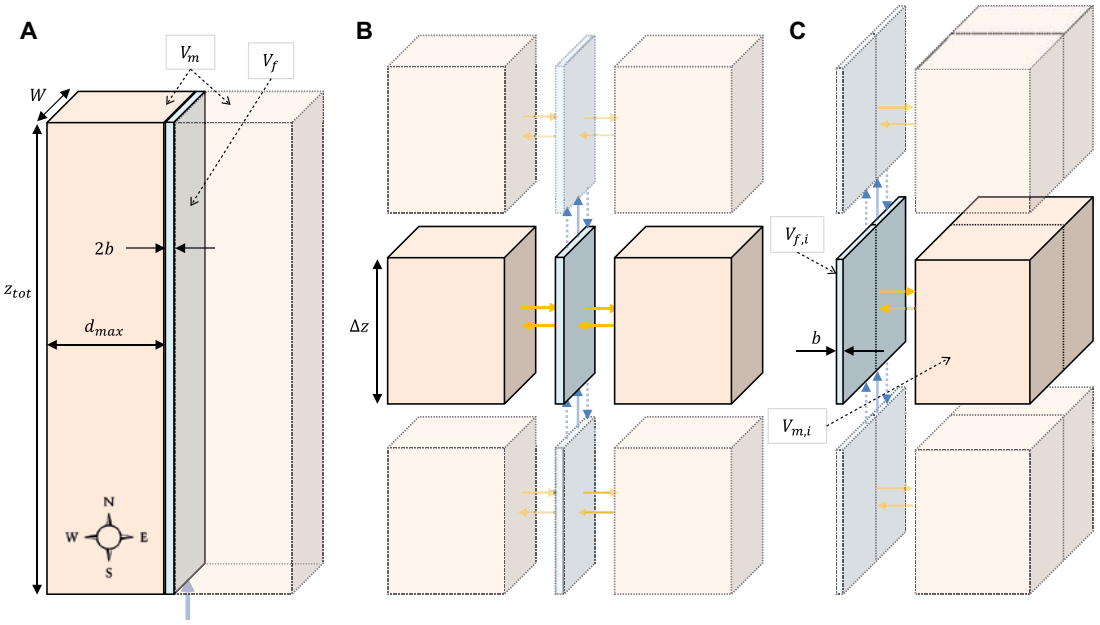

Figure 4-11. *Schematic view of the fracture-matrix system implemented in the geosphere model (A). Discretising the simple volumes in (A) in sections along the fracture (B). Rearranging the volumes so that only one rock matrix volume needs to be considered per discretised fracture volume (C). V_f and V_m are the volumes of the modelled fracture and porous rock matrix, respectively. z_{tot} is the total length of the fracture and Δz is the length of fracture compartment i. Blue arrows represent advective (solid) and dispersive (dashed) transport along the fracture and yellow arrows represent diffusive transport with the rock matrix.*

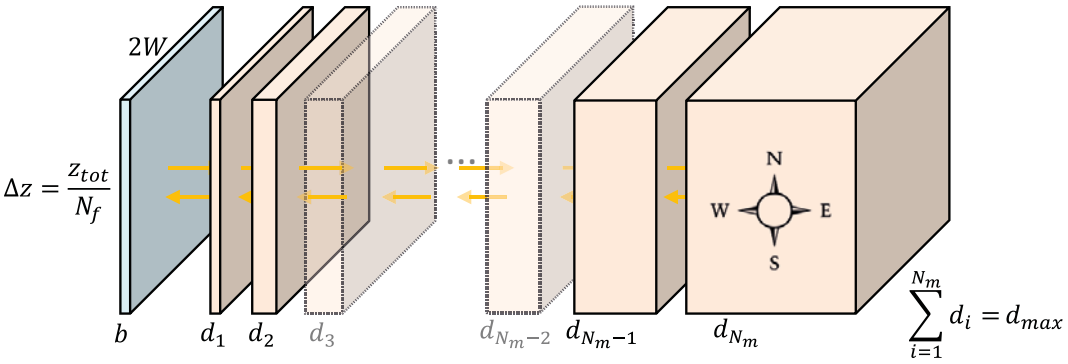

Figure 4-12. *Schematic view of the rock matrix discretisation. d_1 [m] is the depth of the first matrix compartment adjacent to the fracture compartment and N_m is the number of rock-matrix compartments [-].*

4.5 Biosphere model

The radionuclide transport in the biosphere is described by the biosphere model. This consists of sub-models for radionuclide transport in the biosphere, i.e., natural and cultivated ecosystems, and modules for the calculation of doses to humans.

The radionuclide transport model for the biosphere is based on the corresponding model used in the SR-PSU assessment (Saetre et al. 2013). As the waste vaults are postulated to be located in a coastal landscape, and the assessment period covers hundreds of thousands of years, the model must have the capabilities to handle both terrestrial and aquatic ecosystems and temporal development driven by changes in the relative sea level, ecosystem succession and/or climate change. Moreover, the model needs to handle transport, accumulation and decay of radionuclides (including ingrowth of decay products) with different geochemical behaviour.

In the SR-PSU assessment, the biosphere model was primarily applied to one discharge area and the down-stream area in the landscape. The model simulated transport and accumulation of radionuclides in two linked ecosystems (i.e. an aquatic and a mire ecosystem), and the transitions between ecosys-

tems (i.e. lake isolation and lake ingrowth) were handled in a continuous manner. In SE-SFL, SKB applies this model to multiple potential discharge areas but does not evaluate the potential dose consequences in down-stream areas due to dispersion of radionuclides in the landscape. This simplification is judged reasonable because exposure in biosphere objects receiving the release through groundwater discharge typically results in higher doses than exposure in downstream objects (SKB 2010c, 2014e).

4.5.1 Biosphere objects

Discharge areas for deep groundwater in Laxemar were identified from hydrological modelling (Werner et al. 2006, Sassner et al. 2011). The two studies produced similar patterns, with discharge areas located in lakes and mires, along streams and at the coastline as well as in coastal bays. These areas are parts of the landscape where released radionuclides from the repository can potentially reach the biosphere and are referred to hereafter as biosphere objects.

In total, nine biosphere objects in Laxemar, representing four different ecosystem types, are described in SE-SFL (Figure 4-13). These areas include two semi-enclosed sea bays (201 and 208), lake Frisksjön (207) and the Gäster mire (203). Moreover, since deep groundwater tended to be discharged in streams running in valleys where the land is presently cultivated, five agricultural biosphere objects are included. These are chosen to represent different sized areas of arable land and different locations in the landscape, ranging from small objects in the uppermost catchment of a stream network (204 and 206) to relatively large areas along the banks of the stream Laxemarån (212 and 213).

The biosphere objects are bounded such that they represent clearly defined ecosystems, reflecting reasonably homogenous biotic properties, e.g., type of vegetation and rates of primary production and decomposition, and abiotic characteristics, e.g., regolith stratification and groundwater hydrology (SKB 2014e, Lindborg 2010).

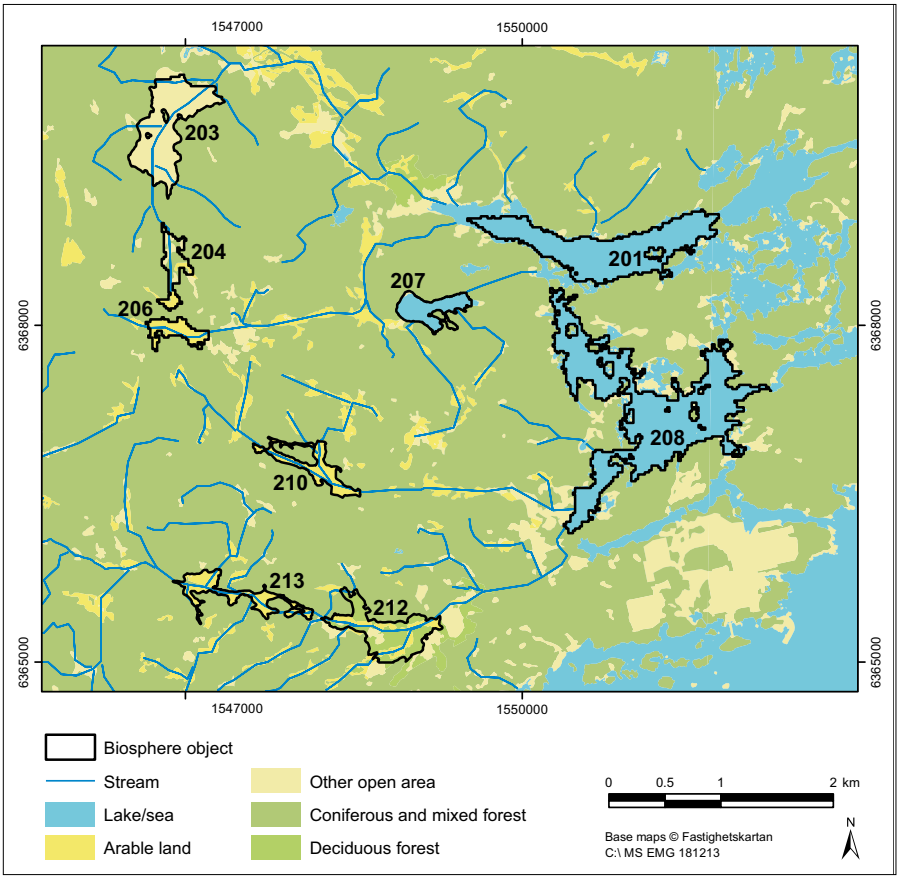

Figure 4-13. *The nine biosphere objects projected onto the present land-use map in the Laxemar area. The objects represent different ecosystems and locations in the landscape, and deep groundwater is expected to be discharged in all of them. The outlined area of biosphere objects 201 and 208 corresponds to the future lake basins that are somewhat smaller than the sea basins present today. Figure from Biosphere synthesis.*

Due to isostatic uplift, sea-level change and ecosystem succession, the sizes and properties of aquatic discharge areas are expected to change over time. Thus, when the landscape is covered by water, the sea basins set the boundary for the aquatic part of the biosphere object. Accumulation of sediments primarily occurs in the central deeper parts of the sea basin. Therefore, this part of the object is used to assess accumulation of radionuclides in the regolith throughout the succession, and the size of the central sea basin is approximated by the size of the future uplift-caused lake, i.e. the lake basin. As the biosphere object emerges from the sea, the area, depth and volume of open water is continuously reduced, and the sea bay finally becomes isolated. At this point, the biosphere object turns into a lake-mire complex, and the total areal extension of the object does not change. However, the lake/wetland ratio within the object will change continuously due to the ingrowth of wetland vegetation. The modelling of the natural succession of biosphere objects is described in detail in the **Biosphere synthesis**.

4.5.2 Radionuclide transport model

A compartmental model is used to simulate the transport of radionuclides in the biosphere objects (Saetre et al. 2013). The model assumes that the distribution of radionuclides in the biosphere can be represented by a limited number of homogenous and interconnected compartments.

This is a highly simplified representation of radionuclide transport in the biosphere. However, because the period of interest and spatial scale for SE-SFL are in the order of hundreds of thousands of years and hundreds of hectares, respectively, it is considered reasonable to represent the ecosystem using temporally and spatially averaged conditions.

Two types of natural ecosystems are simulated: aquatic, i.e., sea, lakes and streams, and terrestrial, including mires (Figure 4-14). The distribution of radionuclides in aquatic ecosystems is represented by six compartments associated with regolith layers, two compartments associated with the water, and one compartment associated with aquatic primary producers (Figure 4-14, Table 4-1). Correspondingly, the distribution of radionuclides in mire ecosystems is represented by eight compartments associated with regolith layers and one compartment associated with the mire vegetation (Figure 4-14, Table 4-1).

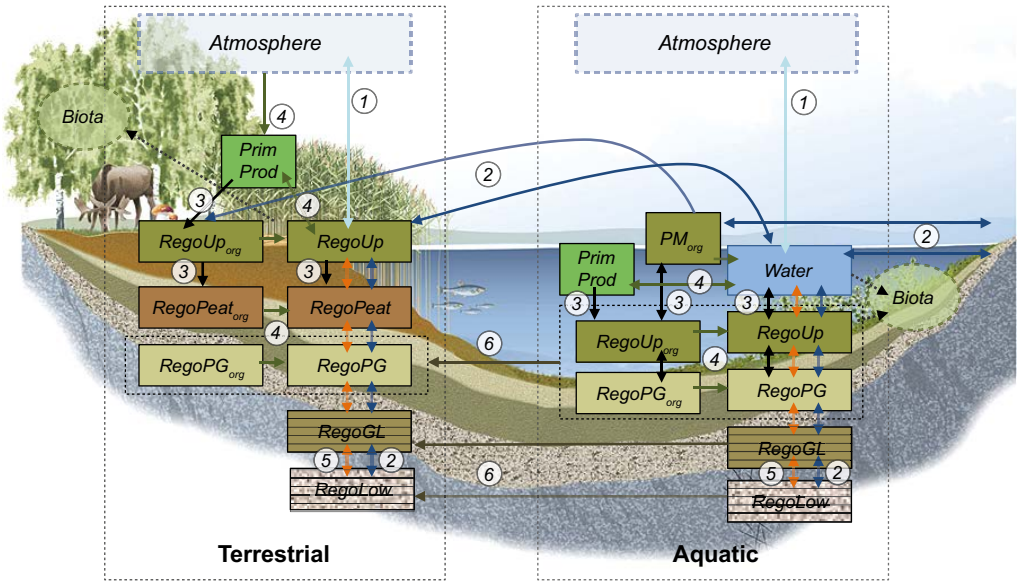

Figure 4-14. *Schematic representation of the biosphere radionuclide transport model for simulating transport and accumulation in a discharge area with two natural ecosystems delimited by thin dotted black lines. Each box within the ecosystems corresponds to a radionuclide inventory associated with a physical compartment. Note that in SE-SFL, the lower regolith layers are represented by five sub-compartments each. Arrows represent radionuclide fluxes between compartments and fluxes into and out of the system. Radionuclide fluxes are linked to mass fluxes of solutes (orange), gas (1, light blue), water (2, dark blue) and solid matter (3, black), to transitions between inorganic and organic forms of radionuclides (4, green), to diffusion in soil pore water (5, red), and to ingrowth of wetland vegetation (6). The atmosphere also serves as a source and sink of radionuclides. The activity concentrations in atmosphere and crop are calculated assuming equilibrium. Figure adapted from the Biosphere synthesis.*

The *present-day evaluation case* in SE-SFL reflects the existing conditions in Laxemar. Because many of the biosphere objects are presently cultivated (Figure 4-13), the agricultural model has been updated in SE-SFL compared to SKB's earlier safety analyses for the Forsmark area. The updated model, schematically presented in Figure 4-15, enables evaluation of continuous cultivation in a discharge area. Since long-term accumulation of organic matter is expected to be limited in agricultural ecosystems, the model does not have separate compartments for radionuclides stored in organic matter. Following standard radioecological practice (e.g. IAEA 2007), the upper soil layer is set to a relatively shallow depth, and below this layer a compartment representing unsaturated soil below ploughing depth is added.

Table 4-1. Brief description of compartments representing radionuclide inventories in the radionuclide transport model for the biosphere. Note that the PM_{org} compartment is also referred to as $Water_{org}$ in the technical model description (Saetre et al. 2013).

Names	Description
Aquatic	
Water	Radionuclides in open water of sea basins, lakes and streams, including radionuclides dissolved in water and adsorbed to particulate matter.
PM_{org}	Radionuclides stored in organic particulate matter suspended in the water column.
Prim Prod	Radionuclides stored in aquatic primary producers, including radionuclides in pelagic, microbenthic and macrobenthic primary producers.
RegoUp	Radionuclides in the upper oxic and biologically active layer of aquatic sediments, including radionuclides in pore water and adsorbed on sediment particles.
$RegoUp_{org}$	Radionuclides incorporated into organic particulate matter in the upper aerobic and biological active layer of aquatic sediments.
RegoPG	Radionuclides in post-glacial aquatic sediments (clay gyttja) below the biologically active layer, including radionuclides in pore water and adsorbed on sediment particles.
$RegoPG_{org}$	Radionuclides incorporated into organic particulate matter in post-glacial aquatic sediments (clay gyttja) below the biologically active layer.
RegoGL	Radionuclides in glacial clay (typically overlaid by post-glacial deposits), including radionuclides in pore water and adsorbed on sediment particles.
RegoLow	Radionuclides in till (typically overlaid by glacial clay), including radionuclides in pore water and adsorbed on sediment particles.
Mire	
PrimProd	Radionuclides stored in mire vegetation biomass, including both above- and below-ground biomass of bryophytes, vascular plants, dwarf shrubs and trees.
RegoUp	Radionuclides in the upper oxic and biologically active layer of wetland peat (acrotelm peat), including radionuclides in pore water and adsorbed on peat.
$RegoUp_{org}$	Radionuclides incorporated into organic matter in the upper aerobic and biologically active layer of peat (acrotelm peat).
RegoPeat	Radionuclides in deep, permanently anoxic, wetland peat (catotelm peat), including radionuclides in pore water and adsorbed on peat.
$RegoPeat_{org}$	Radionuclides incorporated into organic matter in the deep, permanently anoxic wetland peat (catotelm peat).
RegoPG	Radionuclides in post-glacial sediments (clay gyttja) overlaid by wetland peat, including radionuclides in pore water and adsorbed on sediment particles.
$RegoPG_{org}$	Radionuclides incorporated into particulate organic matter in post-glacial sediments (clay gyttja) overlaid by wetland peat.
RegoGL	Radionuclides in glacial clay buried under wetland peat and typically overlaid by post-glacial deposits. Inventory includes radionuclides in pore water and adsorbed on sediment particles.
RegoLow	Radionuclides in till, buried under wetland peat and typically overlaid by glacial clay. Inventory includes radionuclides in pore water and adsorbed on sediment particles.
Agricultural	
RegoUp	Radionuclides in the upper (ploughed) unsaturated soil layer of cultivated land, including radionuclides in pore water and adsorbed on peat.
RegoSub	Radionuclides in the unsaturated sub-soil layer of cultivated land, including radionuclides in pore water and adsorbed on peat.
RegoPG	Radionuclides in post-glacial sediments (clay gyttja) overlaid by cultivated soil, including radionuclides in pore water and adsorbed on sediment particles.
RegoGL	Radionuclides in glacial clay buried under cultivated soil and typically overlaid by post-glacial deposits. Inventory includes radionuclides in pore water and adsorbed on sediment particles.
RegoLow	Radionuclides in till, buried under cultivated soil and typically overlaid by glacial clay. Inventory includes radionuclides in pore water and adsorbed on sediment particles.

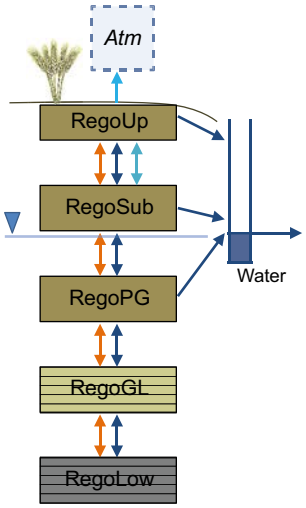

Figure 4-15. *Schematic representation of the radionuclide transport model used for permanent agricultural ecosystems. Each box corresponds to a radionuclide inventory associated with a regolith layer as explained in Table 4-1. Note that the lower regolith layers are represented by five sub-compartments each. Solid arrows represent radionuclide fluxes between compartments and fluxes out of the system. Radionuclide fluxes are linked to diffusion of gas (light blue) and solutes (orange), and to mass fluxes of water (dark blue). The water from the three uppermost compartments is drained to a ditch. The activity concentrations in atmosphere and crop are calculated assuming equilibrium. Figure from the report.*

Finally, to broaden the ensemble of examined conditions in potential discharge areas, non-coupled versions of the biosphere sub-models for mire and aquatic ecosystems are used to calculate environmental concentrations in these ecosystems under stationary conditions.

In response to the review of the SR-Site assessment (Egan et al. 2012), the discretization of the two deepest regolith layers was increased in the SE-SFL biosphere model. The till layer (RegoLow), typically represents the major part of the regolith stack, and the groundwater flux rates are relatively low in this layer. Given these conditions, the numerical dispersion within one compartment will typically overestimate the degree of physical dispersion, and thus underestimate the solute transport time through the layer. For transport in one dimension, five compartments result in a numerical dispersion that equals a physical dispersivity corresponding to a tenth of the transport length. Moreover, since the sorption coefficient in the glacial clay (RegoGL) is typically an order of magnitude larger than that in the till layer (Tröjbohm et al. 2013), the numerical dispersion in one compartment would lead to a similar underestimation of the breakthrough time for many radionuclides also in this layer. Consequently, both the RegoLow and RegoGL layers are represented by five stacked sub-compartments. The performance of the more fully discretized model is evaluated in the **Biosphere synthesis**.

The updated biosphere models are implemented in the Ecolego 6 software. In the models, radionuclides are released to the deepest regolith layer (RegoLow) of a biosphere object. The dynamic change in the radionuclide content of each compartment is related to the flow of water, solid matter or gas, as well as diffusion, photosynthesis, mineralisation and radioactive decay and in-growth (Table 4-2). All the processes that are incorporated in the model are discussed in the **Biosphere synthesis**. The endpoints of the transport modelling are radionuclide concentrations in environmental media, i.e., ground- and surface waters, the various layers of the regolith, mire vegetation and the atmosphere. Humans, plants and animals are then assumed to be in contact with the radionuclides through these media.

Table 4-2. Overview of radionuclide flows (processes) included in the radionuclide transport model (see Figure 4-14). The processes have been categorised with respect to the driving force of the flux, namely mass-flux of solid (MS), water (MW) or gas (MG), diffusion in water (DW) or in gas (DG), or incorporation into or release from organic matter due to photosynthesis (PP) or mineralisation (Min). "Y" indicates that the process is included as a dynamic flow between compartments in the aquatic, mire or agricultural sub-model. * indicates that only the steady-state outcome of the process is accounted for. Indices indicate that flows occur between ecosystems (BTW), that the initial inventory in agricultural soil is conditioned on environmental concentrations in natural ecosystems (INIT), or if the flow is only represented in one (or two) systems of cultivation; drained mire (DM), infield–outland agriculture (IO) or a garden plot (GP).

Process	Related FEP	Type	Radionuclide flux		
			Aqua	Mire	Agri
Biological					
Bioturbation	Bioturbation	MS	Y		Y^{DM}
Plant uptake	Uptake, Primary production	PP	Y	Y	*
Leaf retention/translocation	Uptake, Primary production				$*^{GP}$
Litter respiration/release	Primary production, Decomposition	Min	Y	Y	Y^{IO}
Litter production	Excretion, Particle release/ trapping	PP	Y	Y	
Regolith Mineralisation	Decomposition	Min	Y	Y	Y
Vegetation ingrowth^{BTW}	Primary production, Covering, Terrestrialisation	MS	Y	Y	
Water bound					
Advective horizontal^{BTW}	Convection	MW	Y	Y	
Advective vertical	Convection	MW	Y	Y	Y
Diffusion (vertical)	Convection		Y	Y	
Ground water uptake	Convection	MW			Y^{DM}
Solid liquid phase dissociation	Reactions, Sorption/desorption		*	*	*
Sediment dynamics					
Sedimentation	Deposition	MS	Y		
Resuspension	Resuspension	MS	Y		
Burial	Deposition, Resuspension, Decomposition	MS	Y	Y	
Gas transport / transition					
Degassing	Phase transition, Convection	MG	Y	Y	Y
Gas uptake	Phase transition	MG	Y	Y	
Gas exchange within unsaturated soil	Convection				Y
Leaf degassing	Convection				Y^{GP}
Human behaviour					
Drain/cultivate$^{BTW, INIT}$	Stage of succession				Y^{DM}
Fertilise^{BTW}	Anthropogenic release	MS			$Y^{IO,GP}$
Irrigate	Anthropogenic release	MW			Y^{GP}
Radiological					
Radionuclide decay/ingrowth	Decay		Y	Y	Y

4.5.3 Exposure of humans

Radionuclide concentrations in soil, water, air and organisms are used when calculating the dose to humans. Doses arise from external exposure (radiation from the ground, air and water), inhalation of radionuclides, and ingestion of radionuclides through food and water. This is schematically shown in Figure 4-16. The selection of exposure pathways is based on the SR-PSU analysis of potential pathways relevant to assess the long-term safety of a geological disposal facility (SKB 2014e). Potentially important pathways were identified and mapped to one (or more) exposed groups (see below). The exclusion of pathways that contributed insignificantly to dose in SR-PSU (e.g. adventitious ingestion of sediments) was confirmed to also be justified for the dose-contributing radionuclides in SE-SFL (**Biosphere synthesis**).

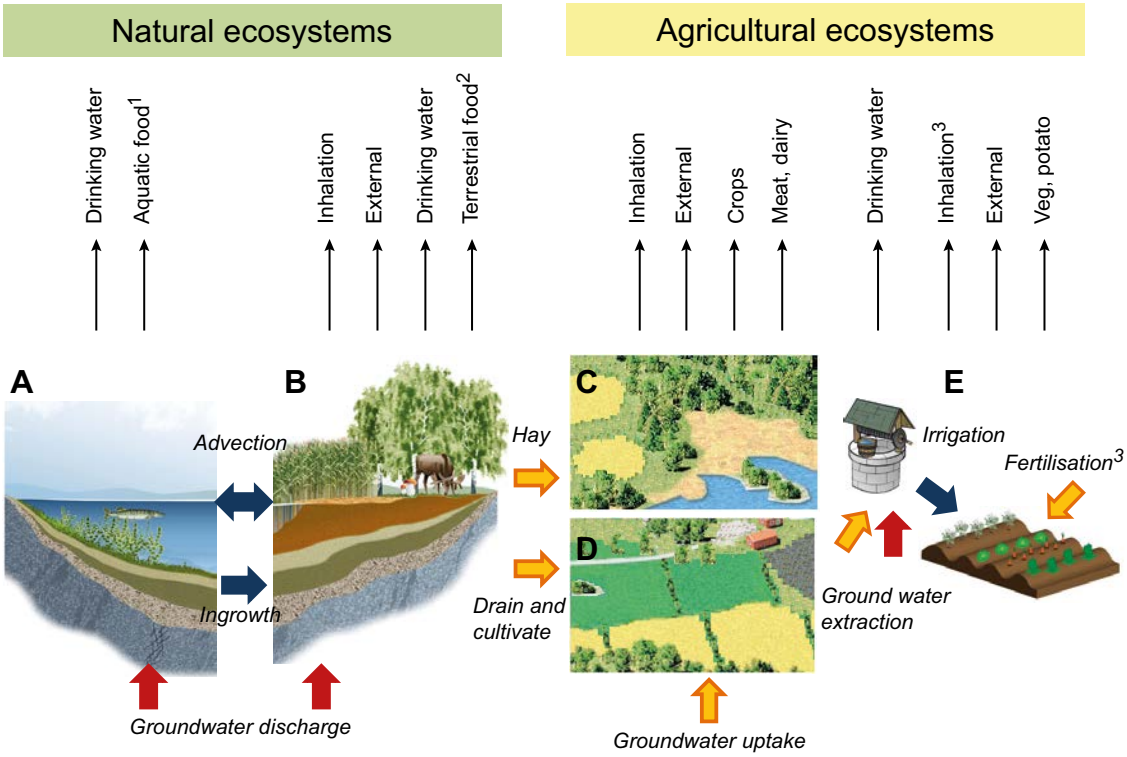

Figure 4-16. *Exposure pathways included in the dose calculations for exposed populations using natural resources and/or living in biosphere objects. Hunter-gatherers use natural aquatic (A) and mire (B) ecosystems. The other three exposed populations represented different uses of arable land, namely infield–outland agriculture (C), draining and cultivating the mire (D) and small-scale horticulture on a garden plot (E). Bold arrows represent input of radionuclides from the bedrock (red), from natural ecosystems or deep regolith deposits (orange), or water-bound transfer of radionuclides within the biosphere (blue). The thin arrows (top) represent exposure routes. Superscripts 1 = fish and crayfish, 2 = game, berries and mushrooms, and 3 includes exposure to radionuclides from combustion of biofuel. Figure from Biosphere synthesis.*

Four potential most-exposed populations were included in the analysis. These groups were considered credible to use as bounding cases for the most exposed groups with respect to exposure through all major exposure pathways in SR-PSU (SKB 2014e). When characterising the most exposed groups, physical and biological characteristics of the biosphere objects, human requirements for energy and nutrients, and habits from historical and present societies were considered (Saetre et al. 2013, SKB 2014e). The four exposed populations identified were the following.

Hunter-gatherers (HG) – A hunter and gatherer community using the undisturbed biosphere for living space and food. The major exposure pathways are from foraging discharge areas in the landscape (fishing, hunting, and collecting berries and mushrooms), and from drinking water from surface water (streams or lakes). Land use and habits of a typical hunter-gatherer community were extracted from historical records and the community is assumed to be made up of 30 individuals that utilise a forage area of approximately 200 km^2.

Infield–outland farmers (IO) – Self-sustained agriculture in which infield farming of crops is dependent on nutrients from wetland (outland). Radionuclides in wetland hay reach the cultivated soil through fertilization with manure. The major exposure pathways are from growing food and raising livestock, and from drinking water from a dug well (or from surface water). A self-sufficient community of infield–outland farmers is assumed to be made up of 10 persons. A wetland area of 0.1 km^2 (10 ha) is needed to supply winter fodder to the herd of livestock corresponding to the need of manure for infield cultivation of this group.

Family farmers (DM/Agr) – Self-sustained industrial agriculture on a former lake or wetland, where both crops and fodder are cultivated on organic soils. Radionuclides reach the cultivated soil through plant uptake of groundwater (DM/Agr) and may have accumulated for an extended time prior to

drainage (DM). The major exposure pathways are from growing food and raising livestock and from drinking water from a dug well (or from surface water). A self-sufficient community of drained-mire farmers is assumed to be made up of 10 persons. A wetland area of 6 ha is needed for food production.

Garden-plot households (GP) – A household that is self-sustained with respect to vegetables and root crops produced through small-scale horticulture. Radionuclides reach the cultivated soil through fertilization (with algae or biomass ash) and irrigation. The major exposure pathways are from growing food, and from drinking water from a dug well (or from surface water). A garden-plot household is assumed to be made up of 5 persons and a 270 m^2 area garden plot is enough to support the family with vegetables and root crops. The productivity and diet for this group has been determined from present habits.

The HG community uses undisturbed ecosystems, whereas the other three groups actively cultivate the land. For HG and DM/Agr, exposure occurs within the boundaries of the biosphere object. However, for the IO and GP group exposure occurs from utilizing resources from the biosphere object (e.g. organic fertilizers, biofuel or irrigation water), and the location of the exposed area is not constrained by the boundaries of the biosphere object.

During marine conditions, natural ecosystems can be used for food and as a source for organic fertilizers, but no cultivation of the biosphere object is possible. The possibility to use the biosphere object for agriculture and water supply increases when the shoreline has passed. Hay and surface waters can be used when the objects have become isolated from the sea. Wells can be dug and mires can be drained when the risk of salt water intrusion has decreased, which is assumed to occur when the land is at least 1 m above sea level.

4.6 Development of transport tools within SE-SFL

In the SE-SFL project, several developments and improvements have been made in terms of modelling radionuclide transport.

New near-field models have been developed to describe radionuclide transport in the SFL repository (Wessely and Shahkarami 2019), which rely on a compartmental conceptualization of the near-field components and incorporate many of the important transport-related processes. The models are accompanied by supporting calculations, which aim to confirm the correct implementation of the compartmental approach and the validity of the assumptions underlying the models. The developed models have been implemented in the Ecolego software. Three different degradation states are defined in the model to study the effect of the future hydrological evolution of the concrete backfill on the extent of radionuclide release. These are included in the near-field transport model for BHK to represent three degradation states (see Section 5.2.3).

A new geosphere assessment tool, FARFCOMP, has been developed (Appendix B). FARFCOMP also relies on the compartmental approach and is implemented in Matlab for calculations of radionuclide transport in the geosphere. The tool has been verified in a series of comparisons with other codes, e.g., MARFA (Painter and Mancillas 2009, 2013), as described in Appendix B. Furthermore, some developments that have not been explicitly taken into account in SE-SFL have been performed. These include implementation and demonstration of the concept of using spatially and time-varying K_d values in transport simulations in MARFA (Trinchero et al. 2018), as well as further development and demonstration of modelling of gas migration for the near-field and the geosphere (Silva et al. 2019a, b).

As a result of SSM's reviews of SR-Site and SR-PSU (e.g. SSM 2018, 2019, Walke et al. 2017), the biosphere models have been somewhat modified in SE-SFL. In addition to the developments mentioned above (e.g. increased discretization, a new agricultural model, and time-independent versions of individual ecosystem models) the model realism, consistency and transparency has been improved. For example, several of the model parameters have been replaced by functions in the model code, and the specific activity approach is consistently used to model transport and uptake of C-14. Large-scale irrigation is considered relevant for warmer climates, and translocation of intercepted radionuclides is included in plant uptake under irrigation regimes. A new method for the derivation of hydrological parameters has also been developed, and it has been implemented as a sub-routine in the time-independent models for terrestrial ecosystems. Description of the updates and their effects on the model output, i.e. transport and accumulation of radionuclides, is given in the **Biosphere synthesis**.

5 Radionuclide transport and dose calculations for the reference evolution

5.1 Introduction

In this chapter, the post-closure safety of the SFL repository is analysed using evaluation cases that are related to the three variants of the reference evolution of the repository and its environs (**Main report**, Chapter 6). The reference evolution describes the future evolution of the repository and its environs under the assumption that the repository is located at the example location in Laxemar, and that the repository is designed in accordance with the proposed repository concept. Further, material properties for the repository components are taken from previous safety assessments, e.g. a bentonite similar to that planned for the buffer in the Spent Fuel Repository is assumed for BHA backfill, and a concrete similar to the construction concrete employed in the existing SFR repository is assumed for BHK backfill.

The three evaluation cases address the effect of different climate assumptions:

- The *present-day evaluation case* (Section 5.2) constitutes the base case for the radionuclide transport and dose calculations in SE-SFL and assumes a constant present-day climate.
- The *increased greenhouse effect evaluation case* (Section 5.3) analyses the effect of a future climate affected by anthropogenic action, including the effect of differences in crop irrigation.
- The *simplified glacial cycle evaluation case* (Section 5.4) is based on a simplified glacial cycle that includes cold climate conditions, manifested through lower air temperatures, permafrost growth and an ice sheet overriding the site. In addition, the glacial period is followed by sea-submerged conditions.

As described in Section 2.2, the objective for the *present-day evaluation case* is not to establish a main scenario as defined by the regulations, but to have a simplified base case that in a straightforward way can be compared with cases with alternative assumptions and different temporal evolutions. Thus, the base case is intentionally simplified and is not intended to represent the most probable development of the repository and its environs. Chapter 2 in the **Main report** elaborates on the selection and purpose of evaluation cases in SE-SFL.

To allow a first evaluation of how the properties of the proposed repository concept evolve over time under relevant future climate developments, the base case is complemented by the *increased greenhouse effect* and *simplified glacial cycle* evaluation cases. These evaluation cases are based on information given in the description of the reference evolution (**Main report**, Chapter 6). In general, important aspects of the variants of the reference evolution are extracted to the evaluation case and aspects that are judged to have minor importance have been simplified. This includes, for instance, the temporal evolution of the groundwater flow due to shoreline displacement that was found not to yield large differences in the *present-day* and *increased greenhouse effect* variants of the reference evolution and that is not represented in the corresponding evaluation cases. However, there are also aspects that might influence the repository performance that have been neglected, most notably the temporal evolution of the bentonite backfill that has been described in the reference evolution (**Main report**, Section 6.2.9). In consequence, the set of evaluation cases presented in this chapter will need to be further developed to reflect all aspects that have to be included in a main scenario as required for a full safety analysis and as described in the general guidance to SSM's regulations.

In addition to the climate-variant cases analysed in this chapter, several alternative evaluation cases are described in Chapters 6 and 7, analysing the sensitivity of the calculated releases and doses in the base case to repository-internal and -external conditions, respectively.

The general structure of the evaluation cases presented in this chapter includes a description of the external conditions as well as the handling of the case regarding the near-field, geosphere, and biosphere models. Furthermore, the resulting near-field and geosphere releases are presented and analysed. Finally, the dose consequences are analysed, where the term "dose" as used in SE-SFL is described in Section 2.4.2. The aim is to gather **insight** into the roles of features and processes in the different parts of the system for activity releases and resulting doses.

5.2 Present-day evaluation case

5.2.1 General description

The *present-day evaluation case* constitutes the base case for the radionuclide transport and dose calculations in SE-SFL. It assumes that present-day conditions prevail in the bedrock and biosphere throughout the entire analysis period of 1 million years after repository closure. For consistency with this assumption, present-day external conditions are also assumed to prevail during the entire analysis period. The repository near-field is taken to evolve from its assumed initial state by the effect of features, events and processes (FEP) that are considered in SE-SFL and that are relevant under the assumption of constant present-day conditions in the repository environs (see the **FEP report**). Important FEPs are, for instance, metallic waste corrosion and concrete degradation in BHK, and sorption onto cement and bentonite.

5.2.2 External conditions

Present-day climate conditions are assumed to prevail throughout the entire analysis period of 1 million years after repository closure. Thus, temperate climate conditions are assumed, without the presence of permafrost or ice-sheets. Further, the present-day relative sea level is assumed for the entire analysis period, thus the ongoing shoreline displacement is not considered.

5.2.3 Handling in the near-field model

For the radionuclide transport calculations in the near-field, information on the development of flow-related, and non-flow-related, migration properties is needed. Specifically, degradation of the concrete backfill in BHK is considered. The near-field development, and the migration properties, assumed in the *present-day evaluation case* are described in the following subsections. For a complete description of the data used, see Chapter 2 of Shahkarami (2019).

In the *present-day evaluation case*, the repository is assumed to become instantly saturated with groundwater upon closure. It then remains saturated for the full assessment period. Diffusion and advection will move the dissolved radionuclides away from the waste, through the engineered barriers, to the surrounding rock.

Release of radionuclides from the waste

The radionuclide inventories, half-lives and branching ratios are provided in Sections 2.3 and 2.4 of Shahkarami (2019). There is limited knowledge about the BHA radionuclide inventory due to its legacy nature. Thus, it is conservatively assumed that all BHA radionuclides are dissolved into the porewater of the waste compartment and are available for transport immediately after repository closure, despite the fact that some of the radionuclides are likely to be in non-soluble form (Section 2.3.1 in Shahkarami 2019).

The waste in BHK mainly contains metallic components with neutron-induced activity. The release of this activity is controlled by corrosion, as described in Section 4.3.2 and further detailed in Sections 2.5.3 and 2.5.4 of Shahkarami (2019). This release is calculated considering the distribution of different types of metallic parts in the BHK waste and their associated radionuclide inventory as well as the corrosion rate, the component thickness, and the radionuclide half-lives (Equation 4-16). The activity is assumed to be evenly distributed within the metallic waste, since the neutrons that induce the activity have a penetration depth, depending on temperature and neutron energy, of several centimetres in steel, which is larger than the metal thickness. In addition to the corrosion-released activity, a remaining fraction of the initial activity in BHK that represents surface contamination and the thinnest metallic components is assumed to be released into the water phase immediately upon saturation of the repository.

Near-field development

A fraction of the radionuclides can sorb onto cement and bentonite in the waste vaults, allowing time for radioactive decay and ingrowth before the radionuclide is transported out of the waste vault. The presence of complexing agents may however reduce sorption. The composition of the waste in BHA

is uncertain but an inventory of cellulose has been estimated (see Section 6.2.8 in the **Main report**). Cellulose, found for example in wood, paper and cotton tissues, is a precursor to the complexing agent isosaccharinate (ISA) that is formed by hydrolysis of cellulose in a Ca^{2+}-rich alkaline environment.

The bentonite backfill in BHA and the concrete backfill in BHK are designed to retard the release of radionuclides from the near-field. The bentonite is assumed to have constant transport properties over the whole simulation period, as discussed in detail in Section 6.2.9 of the **Main report**. The transport properties of the concrete backfill, however, change because of chemical leaching by incoming groundwater. Thus, the porosity and hydraulic conductivity, and the effective diffusivity, in the concrete backfill increase with time, as discussed in detail in Section 6.2.10 of the **Main report**. Furthermore, the degradation affects the chemical environment in the waste vault, which affects sorption of radionuclides to the cement grout in the waste domain and in the concrete backfill. Concrete leaching in the BHK vault starts at the interface between the concrete backfill and the rock. The leaching front then moves slowly through the backfill, towards the concrete structures holding the BHK waste packages and grouting. Dedicated modelling studies of concrete degradation (Idiart and Laviña 2019, Idiart and Shafei 2019, Idiart et al. 2019a, b), and of the near-field hydrogeology (Abarca et al. 2019), have been performed for SE-SFL. These studies have taken input from dedicated calculations with a site-specific hydrogeological and geochemical model (Joyce et al. 2019), also used to determine the assumptions on flow-related migration properties in the geosphere model (Section 5.2.5). The development of migration properties in BHK in the *present-day evaluation case* is based on these studies, as described in the following subsections. The resulting transport, and retardation, in the SE-SFL near-field model is also described.

It is worth noting that the concrete considered in the *present-day evaluation case* is cautiously assumed to have an effective hydraulic conductivity of 8.3×10^{-10} m/s, adhering to the assumptions for concrete structures in SR-PSU (SKB 2014d). Concrete with significantly lower hydraulic conductivity, as well as lower effective diffusivity, is achievable (Mårtensson and Vogt 2019, Idiart et al. 2019b). The effect of using such a concrete is evaluated in the alternative concrete backfill in BHK case (Section 6.4).

Flow-related migration properties

Since the hydrogeological system in the bedrock surrounding the repository is assumed to be constant during the complete analysis period of 1 million years, the future evolution of the near-field hydrogeology is determined by the hydraulic properties of the repository components. Thus, for BHA, the near-field flows are constant during the complete analysis period. In BHK, the concrete backfill is assumed to degrade from intact to fully degraded concrete. The degradation affects the hydraulic conductivity, and thus groundwater flow in the waste vault. In the near-field transport model for BHK, the time evolution of the groundwater flow due to concrete degradation is simplified by representing three consecutive states from intact concrete to fully degraded concrete. A transition period of 100 years between the different states, with the water flow changing linearly, is applied for numerical reasons. The transition time points from one state to the other are chosen based on Idiart and Laviña (2019); see also Idiart and Shafei (2019) and Idiart et al. (2019a). The three degradation states, and the periods over which these are assumed to prevail in the near-field transport model for BHK, are:

- *Intact concrete* – The concrete backfill is intact and essentially unaffected by leaching. This state holds for 85 ka after repository closure, until the portlandite has leached out of the outer quarter of the backfill.
- *Degraded zone* – Leaching of cement minerals has resulted in degraded, significantly more permeable concrete in the outer half than in the inner intact half of the concrete backfill. This is assumed to prevail during the subsequent ~700 ka until the calcium-silicate-hydrate gel (C-S-H) in the outer half of the backfill has leached out.
- *Degraded concrete* – The full backfill volume has now degraded resulting in substantially higher hydraulic conductivity compared with the intact concrete state, assumed to last for the remainder of the total analysis period of one million years.

The water flows used in modelling advection (and implicitly dispersion) in the near-field transport models are based on dedicated modelling of the near-field hydrogeology through the SFL vaults and waste (Section 6.2.6 in the **Main report**, Abarca et al. 2019). This includes a simulation with constant hydraulic conditions representing intact concrete in BHK and conforming to the results of

the hydrogeological modelling of Joyce et al. (2019), described in the **Main report** (Section 6.2.5), as well as additional simulations representing the degraded-zone and degraded-concrete states. During the intact concrete period, the total flow through the BHK waste vault is two orders of magnitude higher than the flow through BHA (Section 2.6.3–2.6.4 in Shahkarami 2019) This difference correlates with the hydraulic conductivities assumed for the backfill materials, with a hydraulic conductivity of 1×10^{-13} m/s for bentonite backfill in BHA and of 8.3×10^{-10} m/s for the intact concrete backfill in BHK. In the modelling of groundwater flow for the degraded-zone state, a higher hydraulic conductivity of 1×10^{-7} m/s for the symmetrically defined outer half of the concrete backfill leads to a hydraulic cage effect. It acts as a bypass, redirecting water around the waste (Abarca et al. 2019), resulting in decreased water flow through the waste, but increased total water flow through the BHK vault as compared with the intact concrete state. For the degraded concrete state, the water flow in the entire waste vault, i.e. including the waste domain, is increased as compared with the intact concrete period.

The near-field transport model for BHA has a simplified representation of the flow through the waste and backfill, where the water is assumed to flow only in the direction along the vault (Section 2.6.3 in Shahkarami 2019). The water flow from the waste towards the backfill outflow compartment used in the model is 1.55×10^{-3} m^3/a. Since the hydraulic properties of the bentonite backfill are assumed to not change with time, this flow rate is applied for the entire analysis period of one million years.

The near-field transport model for BHK assumes that water flow enters the vault from above and leaves through the sides and floor of the vault (Section 2.6.4 in Shahkarami 2019). For the initial period of intact concrete, the water flow from the waste compartment to the outflow (i.e. floor) compartment is 0.696 m^3/a, and 0.020 m^3/a to the side compartment (Figure 5-1). During the period of degraded zone concrete, the hydraulic cage effect is assumed to lead to a reduction to ~50 % in the flow as compared to the intact concrete period. Finally, during the period of completely degraded concrete, the water flow from the waste to the outflow and side compartments is approximately doubled as compared with the period of intact concrete.

The groundwater flow rates through the BHK backfill outflow and side compartments are approximated by the magnitudes of groundwater flow rates leaving the BHK waste control volumes towards the backfill (Section 2.8.4 in Shahkarami 2019). This is a fair approximation for intact and degraded concrete, since the magnitudes of groundwater flow rates through the BHK waste control volumes are comparable to those in the backfill compartments (Figure 6-4 in Abarca et al. 2019). During the degraded zone period, this is a reasonable approximation for the groundwater flow transporting radionuclides from the waste to the backfill and out of the repository. During this period, the transport

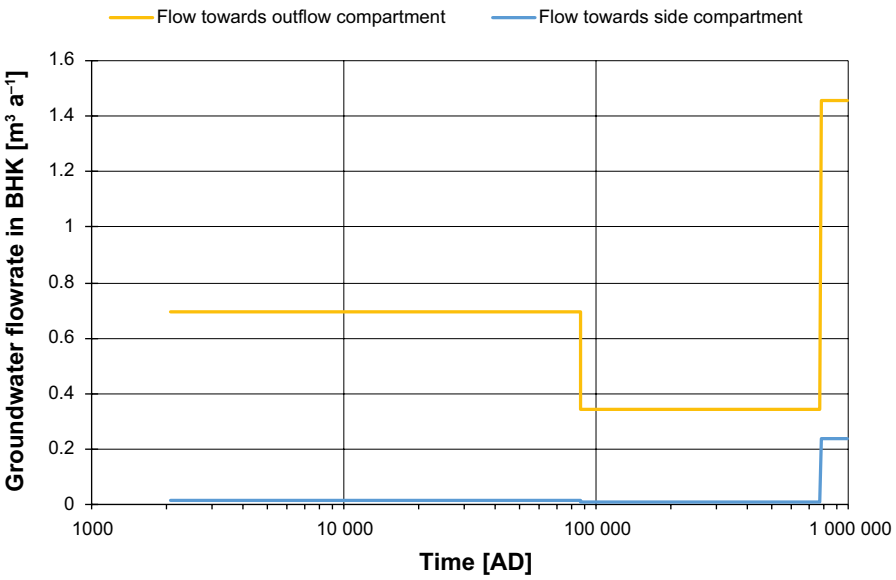

Figure 5-1. *Development of groundwater flow rates from the BHK waste compartment towards the backfill outflow compartment and backfill side compartment, respectively. The data are described in Sections 2.6 and 2.8 of Shahkarami (2019).*

is expected to be mostly driven by diffusion to the groundwater seeping tangentially past the low-permeable backfill interface. In the near-field model, this is reflected in the high value selected for the total equivalent flow in the degraded zone period (Section 2.9.6 in Shahkarami 2019).

The advective transport rate for a non-sorbing radionuclide in the near-field transport model, resulting from the water flows described here, is described in the section below on *Transport by advection and diffusion*.

Non-flow related migration properties

Porosity and effective diffusivity

A simplified development of the porosity and effective diffusivity of the inner and outer parts of the BHK concrete backfill, due to concrete degradation (Table B-2 in Idiart and Laviña 2019), is used in the near-field model (Sections 2.7.1 and 2.8 in Shahkarami 2019). In addition to the spatially symmetric degradation assumed for the flow-related properties in the previous subsection, the increase of the porosity and effective diffusivity due to concrete degradation is assumed be faster where incoming groundwater meets the backfill than where water leaves the backfill. This is because the outgoing water has undergone chemical equilibration with the backfill porewater, reducing its leaching aggressiveness (Idiart et al. 2019a). Therefore, during the degraded-zone and degraded-concrete periods, the concrete properties representing the outer backfill in Idiart and Laviña (2019) are used for the inflow compartments in the near-field radionuclide transport model for BHK, and the inner-backfill properties are used for the outflow compartments (Figure 5-2).

Unlike the concrete in BHK, the porosity and effective diffusivity of the bentonite backfill in BHA are assumed to be constant over the full assessment period (Sections 2.7.1 and 2.8.1 in Shahkarami 2019). The physical porosity of the bentonite backfill exceeds that of the concrete backfill. However, only cations can make use of the full physical porosity of the bentonite backfill of 0.43. For anions, the diffusion-available porosity, 0.17, is lower. The effective diffusivity in the bentonite backfill in BHA for both anions (1.0×10^{-11} m^2/s) and cations and neutral species (1.2×10^{-10} m^2/s) exceeds that of the intact concrete backfill in BHK (Figure 5-2).

In the waste compartments of both BHA and BHK, a constant effective diffusivity equal to the diffusivity of radionuclides in water, i.e. 2.0×10^{-9} m^2/s, is conservatively assumed (Sections 2.6.1 and 2.6.2 in Shahkarami 2019). For the concrete structure surrounding the waste in BHA and BHK, the porosity is assumed to increase with time in a similar manner as the development assumed for the concrete backfill outflow compartments, shown in Figure 5-2 (Section 2.5.1 in Shahkarami 2019).

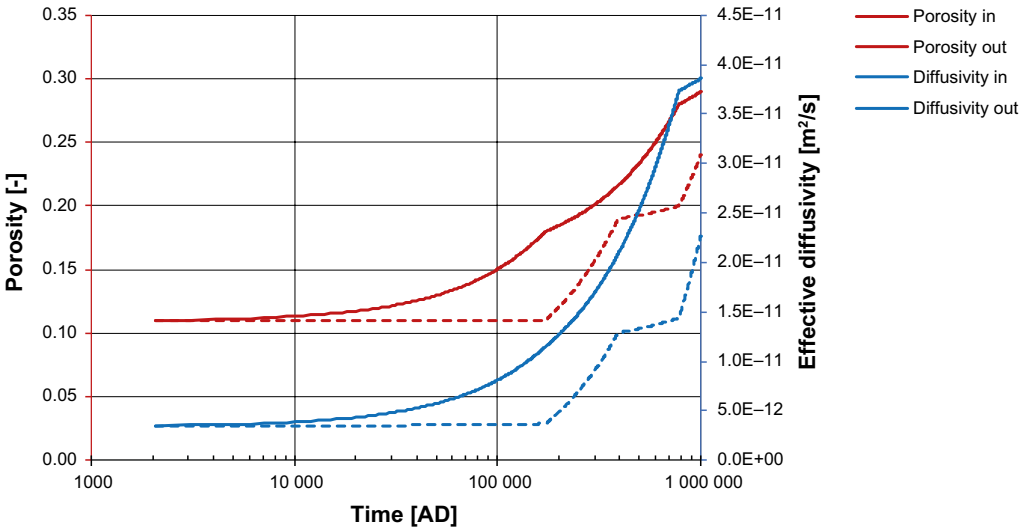

Figure 5-2. *Development of porosity and effective diffusivity in the BHK backfill due to concrete degradation. The values for the inflow compartment are shown with solid lines and for the outflow compartments with dashed lines. The data are linearly interpolated between the time points given in Table B-2 in Idiart and Laviña (2019), i.e. at repository closure (2075 AD) and 170 ka, 390 ka, 780 ka, and 1 000 ka after closure. The data are described in Sections 2.7 and 2.8 of Shahkarami (2019).*

Sorption coefficients and sorption reduction factors

Sorption onto cement and bentonite is characterised by a sorption coefficient K_d [m^3 kg^{-1}] that expresses the ratio between the adsorbed mass concentration onto the solid phase and the mass concentration in the fluid (Section 4.3.1 and Tables 2-18 and 2-31 in Shahkarami 2019). Selected sorption coefficients and half-lives of the radionuclides that give the largest contributions to near-field releases in the *present-day evaluation case* are given in Table 5-1.

To account for the effect of complexing agents on sorption in BHA, sorption of specific radionuclides is reduced in the near-field model for BHA by dividing the K_d values by a sorption reduction factor ranging from 1 to 10 000 (Table 2-20 in Shahkarami 2019). The sorption reduction factors are taken from SR-PSU, for solubility-limited concentrations of ISA in portlandite-buffered water (SKB 2014d). In the *present-day evaluation case*, the sorption reduction factors are applied during the complete analysis period of one million years. Thereby, it is conservatively assumed that complexation is not affected by the evolution in the waste vault, and that the complexing agents neither degrade nor are transported away.

In BHK, the waste exclusively consists of metallic parts. Therefore, no organic material that might form metal-organic complexes will be present in this waste vault. However, the sorption coefficients in BHK are affected by the changes in the chemical conditions in the waste vault, where concrete chemical degradation is associated with a pH evolution (Section 6.2.10 in the **Main report**). Thus, K_d values are assumed to vary, based on the simplified pH development of Table B-1 in Idiart and Laviña (2019). As described in the previous section, the concrete chemical degradation is assumed to occur faster where incoming groundwater meets the backfill, as compared with degradation where water leaves the backfill. Therefore, the pH decreases faster in the inflow compartments than in the waste, outflow, and side compartments of BHK (Table 2-19 in Shahkarami 2019). Four different K_d values are used, applied at points in time which correspond to pH > 12.5 (state I), pH ≈ 12.5 (state II), pH ≈ 12 (state IIIa), and pH ≈ 10.5 (state IIIb), respectively (Table 2-18 in Shahkarami 2019). Between these time points, K_d is obtained by linear interpolation between neighbouring points.

Table 5-1. Properties of the radionuclides that are among the top-three contributors to either the near-field releases, geosphere releases, or dose, from BHA or BHK. Sorption coefficients K_d for bentonite, cement (states I and IIIb), and the geosphere, and the effective diffusivity D_e in bentonite. The information for all radionuclides and cement degradation states is given in Sections 2.5.5, 2.5.6, 2.7.4, 2.7.5, 2.7.6, 2.8.1 and 3.3.5 in Shahkarami (2019).

Radionuclide	Half-life [a]	K_d bentonite [m^3/kg]	K_d cement state I [m^3/kg]/ state IIIb [m^3/kg]	K_d geosphere [m^3/kg]	Effective diffusivity in bentonite [m^2/s]
Ag-108m	438	0	0/0	0.00065	1.2×10^{-10}
C-14-org	5 730	0	0/0	0	1.2×10^{-10}
C-14-ind	5 730	0	0/0	0	N/A
Ca-41	103 000	0.005	0.035/0.047	0	1.2×10^{-10}
Cl-36	301 000	0	0.001/0.001	0	1.0×10^{-11}
Mo-93	4 000	0	0.003/0	0	1.0×10^{-11}
Ni-59	76 000	0.3	0.03/0.2	0.0021	1.2×10^{-10}
Tc-99	211 000	63[a]	3.0[a]/3.0[a]	0.099	1.2×10^{-10}

[a] Sorption coefficients for bentonite and cement for Tc-99 are reduced by a factor of 10 000 in BHA, to represent the effect of complexing agents.

Transport by advection and diffusion

The rate of advective transport from the repository to the bedrock, resulting from the assumptions on water flow (Figure 5-1) and porosity (Figure 5-2), are illustrated for a non-sorbing tracer in Figure 5-3. The hydraulic-cage effect during the degraded-zone period, described with the flow-related properties above, is clearly seen in the figure. Multiplying the rate of transport by the inventory in the boundary compartment, and summing over the inlet, outlet and side compartments, gives the release of the radionuclide from the waste vault.

As described in Section 4.3.2, diffusive transport from the boundary compartment to the seeping water in the fractured rock is determined by the diffusive resistance against the transport between neighbouring compartments (R_b), the plug resistance (R_{plug}) and the equivalent flow rate (Q_{eq}). During the intact concrete period for BHK, the total equivalent flow rate (i.e. summed over all fractures

that intersect the vault) is 0.251 m^3/a, as compared with 0.187 m^3/a for BHA (Joyce et al. 2019 and Sections 2.9.2 and 2.9.6 in Shahkarami 2019). To account for the simulated increased flow in the outer degraded concrete (Abarca et al. 2019) during the degraded zone period in BHK, Q_{eq} is increased to be the difference between the water flow in the degraded concrete and the intact concrete. The resulting total equivalent flow rate is 4.52 m^3/a (Section 2.9.6 in Shahkarami 2019). Further, the diffusion length is divided by two to account for the reduced amount of intact concrete during this period. These two changes result in an increased rate of diffusive transport from BHK to the bedrock as compared with the intact concrete period (Figure 5-3, dashed lines). During the degraded concrete period, a decrease of the transport rate is seen; this is an effect of the underlying assumptions where a conservative choice of an almost immediate switch of water flow (Figure 5-1) is combined with a more realistic interpolation of the porosity (Figure 5-2). The rate of diffusive transport from BHA to the bedrock is significantly lower than from BHK, both for anions and cations (Figure 5-3); due to the high plug resistance at the bentonite–fracture interface in BHA compared with the internal resistance in the border concrete compartment in BHK. When comparing the rate of advective and diffusive transport in BHA one must bear in mind that the volume of the side compartment is roughly 30 times larger than that of the outlet compartment. Since transport within the waste vault is dominated by diffusion in BHA, this leads to significantly higher inventory in the side compartment than in the outlet compartment. Thus, transport out of BHA is dominated by diffusion for both cations/neutral species and anions even though the diffusive rate is lower than the advective rate for anions.

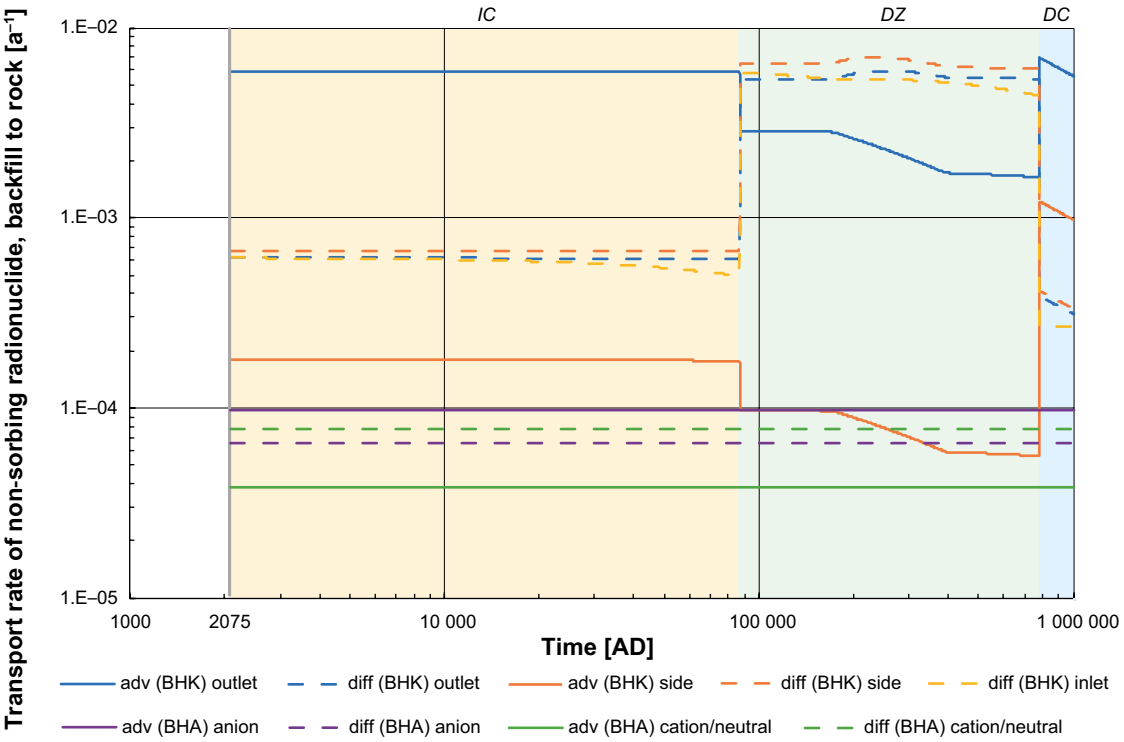

Figure 5-3. *Rate of transport [a^{-1}] for a non-sorbing tracer from the backfill to the bedrock, illustrating the effects of constant flow rates and porosity in BHA and varying flow rates and porosity due to concrete degradation in BHK. For a non-sorbing radionuclide, the annual release from the waste vault is determined as the rate of transport, multiplied by the inventory in the outer-most compartments, summed over the inlet, outlet and side compartments. The advective transport (adv, solid lines), is shown for the direction of the outlet compartments of the backfill in BHA (see Figure 4-1). Since the advective transport in BHA is assumed to occur along the vault, there is no advective transport through the side compartments. For BHK, the advective transport is also shown for the direction of the side compartments of the backfill (see Figure 4-2). The net effective transport due to diffusion over the backfill-bedrock interface (diff; dashed lines), is also shown for both waste vaults. For BHA, separate lines are shown for cations/neutral species and anions. The flow data for the waste compartment and the backfill are detailed in Sections 2.6 and 2.8 in Shahkarami (2019). The porosity and effective diffusivity data are detailed in Section 2.7 in Shahkarami (2019). The pale background colours indicate the degradation periods: yellow for intact concrete (IC), green for degraded zone concrete (DZ) and blue for fully degraded concrete (DC).*

Retardation coefficient

The unitless retardation coefficient R is a measure of the barrier capability to retard the transport of radionuclides by means of sorption. As described in Section 4.3 (Equation 4-5):

$$R = 1 + K_d \times \frac{m}{V\varepsilon}$$

where K_d is the sorption coefficient [$m^3\ kg^{-1}$], m is the mass [kg] of the sorbing material, V is the total volume [m^{-3}], and ε is the unitless porosity.

The coefficient describes how many times slower the transport of a radionuclide subjected to adsorption is as compared with the velocity of the flowing water in the pore spaces, i.e. the transport velocity of a non-sorbing radionuclide. The inverse of the retardation coefficient can be interpreted as the fraction of radionuclides in the barrier that is dissolved within the pore volume of the barrier material. The minimum value of R is one and occurs when sorption is absent ($K_d = 0$) and, when radionuclides sorb onto surfaces within the barriers ($K_d > 0$), the value of R is greater than one.

As concrete degrades in BHK, the porosity and density of the backfill change over time, as do the sorption properties of the concrete. The degradation is mainly driven by dissolution and leaching of cement hydrates (Idiart and Laviña 2019). In the near-field model, the effects of these processes are described as temporal development of the parameter values, e.g. as changes in the porosity (Figure 5-2). Similarly, temporal changes in the chemical environment and leaching of minerals, affect sorption onto concrete. Consequently, when the retardation coefficient for the cement in the concrete barrier in BHK is calculated, sorption is adjusted to account for changes in pH of the concrete (see Table 2-19 in Shahkarami 2019) and the loss of hydrated cement (see Section 2.7.3 in Shahkarami 2019).

The evolution of the retardation coefficients in the BHK concrete is faster in the lid than in the walls and floors of the waste vault because of faster degradation, as discussed in previous subsections and in Idiart and Shafei (2019). In the model, this is represented by assuming that the properties of the lid develop in accordance with the outer concrete in Idiart and Laviña (2019), whereas the properties of the walls and floor develop in accordance with the inner concrete in Idiart and Laviña (2019); see Section 2.7.1 in Shahkarami (2019). Carbon and silver are assumed not to sorb onto cement (i.e. they are non-sorbing) and therefore the advective transport of these radionuclides has the same velocity as the water throughout the assessment period (Figure 5-4). Chloride sorbs weakly onto cement throughout the assessment period ($K_d = 10^{-3}\ m^3\ kg^{-1}$). However, the retardation coefficient as described above decreases with time as cement (which provides the surface for sorption) is depleted by leaching and the pore volume in the concrete increases (Figure 5-4).

The retardation of all sorbing elements (e.g. Mo, Ca and Ni) is affected in a similar way by the loss of cement and the increased porosity. However, as the sorption for Mo, Ca and Ni also responds to the changes in the chemical environment, the effects of degradation on the sorption coefficients (Table 2-17 in Shahkarami 2019) are superimposed on the changes caused by the mass loss of cement. For example, Mo becomes mobile ($K_d = 0$) when the mineral C-S-H_{jen} has been depleted by leaching. Thus, the retardation coefficient in the outer concrete for Mo decreases to unity at 360 ka after closure (and 40 ka later for the inner concrete). The sorption of Ca is also affected by the leaching of C-S-H_{jen}, but in the opposite direction. Consequently, the sorption, and the retardation coefficient for Ca increase by almost an order of magnitude when the mineral has been depleted in the outer concrete at 360 ka after closure (Figure 5-4).

In addition, the sorption coefficients of Ca and Ni are sensitive to changes in the pH in the waste vault. The initial pH in the concrete backfill is highly alkaline. However, as Na and K alkalis are leached out, the pH in the outer concrete declines by half a unit over the initial 5 000 years of the assessment. The pH decline is similar in the inner concrete, but the change takes an additional 5 000 years to complete; see Idiart and Laviña (2019) and Table 2-19 in Shahkarami (2019). The sorption coefficients and thus the retardation coefficient for Ca decrease by an order of magnitude in response to this drop in pH. The response in sorption of Ni is similar in magnitude but opposite in direction; the sorption (and the retardation) coefficient for Ni increases by almost an order of magnitude in the initial period of the assessment (Figure 5-4).

In SE-SFL, it is assumed that the bentonite barrier stays intact. Potential effects of bentonite erosion, degradation, and chemical evolution are evaluated briefly (Section 6.2.9 in the **Main report**) but deemed small enough to neglect in the modelling. Further, the sorption reduction factors, applied to account for the effect of complexing agents on sorption in BHA, are applied during the complete analysis period of one million years. Therefore, for each radionuclide, the retardation coefficient is constant throughout the assessment period. However, it can be noted that the retardation coefficient varies over four orders of magnitude between the assessed radionuclides (Figure 5-5). Moreover, for several radionuclides, the sorption and retardation coefficients are significantly reduced due to the postulated abundance of complexing agents in the BHA waste. The sensitivity of the results to this assumption is examined in *the no complexing agents in BHA evaluation case* (Section 6.2).

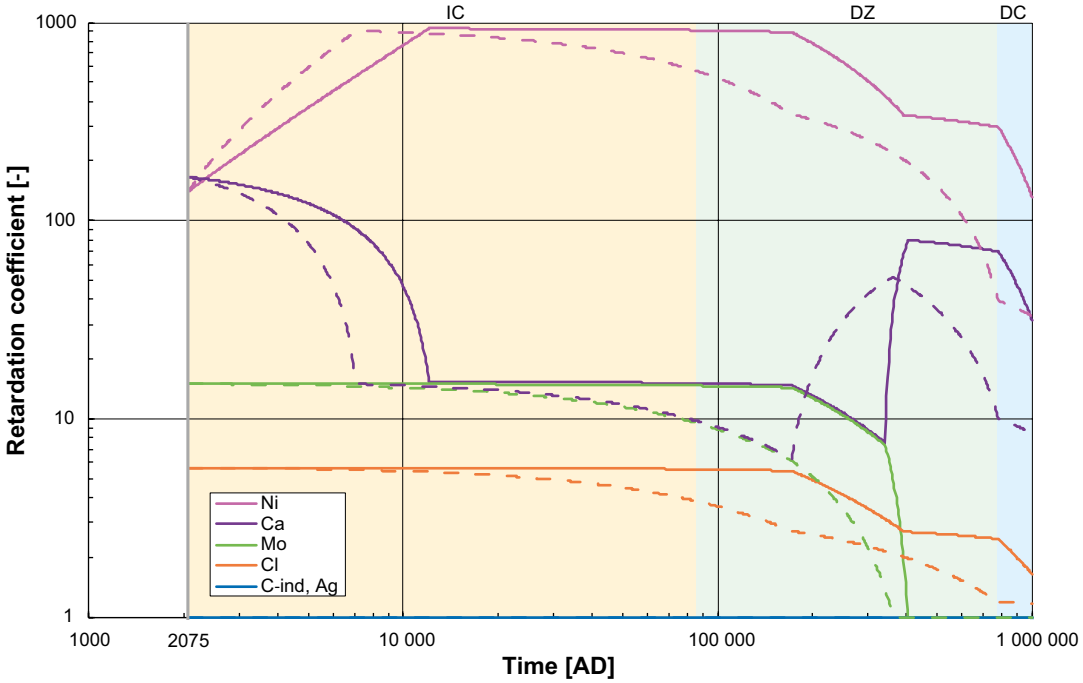

Figure 5-4. *Temporal development of the retardation coefficient (R) in the concrete barrier for five elements that contribute to the dose from BHK. Dashed lines represent the concrete lid (i.e. where groundwater enters the waste vault) and solid lines represent the concrete floor and walls (i.e. where groundwater leaves the waste vault). The pale background colours indicate the degradation periods: yellow for intact concrete (IC), green for degraded zone concrete (DZ) and blue for fully degraded concrete (DC).*

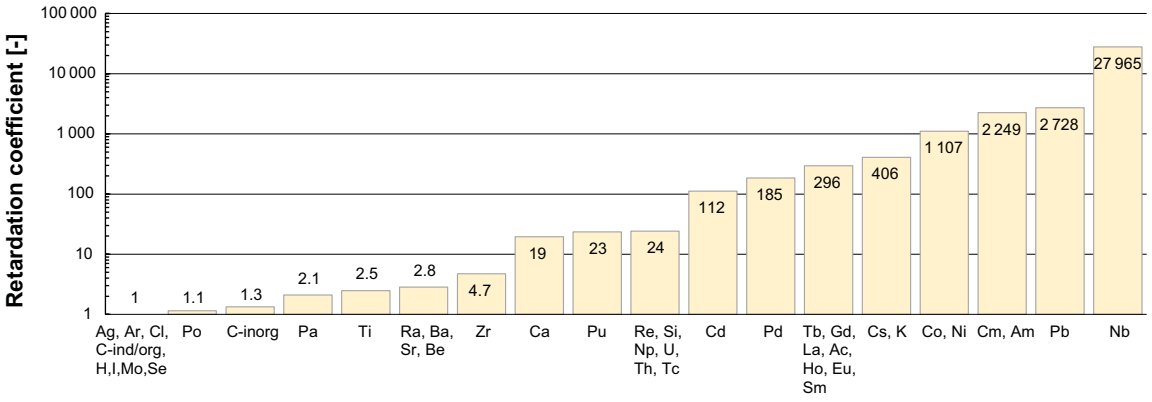

Figure 5-5. *Retardation coefficient R in the bentonite barrier of BHA for all assessed radionuclides.*

5.2.4 The interface between the near-field and geosphere

For each of the repository vaults, BHK and BHA, a radionuclide source term is delivered from the near-field radionuclide transport model to the geosphere model. The source terms provide the amount of activity [Bq] to the host rock for each radionuclide and time step.

Each vault intersects several fractures that connect the near-field to the biosphere through the fracture network. Therefore, the release from the near-field is distributed among the intersecting fractures that are the first segments of the trajectories through the geosphere to the biosphere. Trajectories that do not connect to the biosphere are neglected. This is a pessimistic assumption since it results in a larger part of the near-field release entering the biosphere.

In BHK, the source-term distribution factor for trajectory j is calculated as

$$DF^{j}_{BHK} = \frac{U_j \times L_{f,j}}{\sum_j U_j \times L_{f,j}}$$

Where U_j is the groundwater flow per meter in the intersecting fracture and $L_{f,j}$ is the length of the intersection of the fracture and the vault. The values of U_j and $L_{f,j}$ are calculated in the hydrogeological modelling of Joyce et al. (2019). A distribution factor for a trajectory is equal for all radionuclides and can take a value between 0 and 1 and the sum over all trajectory distribution factors is equal to 1. Since advective transport dominates in BHK, the distribution factors in BHK depend solely on the advective groundwater flow, while the effect of diffusive transport is neglected.

In BHA, the source term distribution factor for trajectory j is calculated as

$$DF^{j}_{\mathrm{BHA}} = \frac{\dfrac{1}{R^{j}_{\mathrm{plug}} + 1/Q^{j}_{\mathrm{eq}}}}{\sum_j \dfrac{1}{R^{j}_{\mathrm{plug}} + 1/Q^{j}_{\mathrm{eq}}}}$$

Where $R^{j}_{\mathrm{plug}} + 1/Q^{j}_{\mathrm{eq}}$ is the total effective diffusive transport resistance at the fracture opening where trajectory j originates (for details see Section 2.9.2 in Shahkarami 2019) and includes the constriction at the fracture opening (R^{j}_{plug}, which is also referred to as plug resistance in the bentonite; see Section 4.3.2) and the resistance corresponding to the capacity of the groundwater to transport radionuclides into the fractures ($1/Q^{j}_{\mathrm{eq}}$). The value of R^{j}_{plug} is derived from the effective diffusivity in bentonite, the aperture of the fracture, and the length of the intersection between the fracture and the vault (Section 2.9.2 in Shahkarami 2019). The values of the two fracture properties and of Q_{eq} are calculated in the hydrogeological modelling of Joyce et al. (2019). Because R^{j}_{plug} depends on the effective diffusivity in bentonite, which differs for anions, cesium, and cations/non-charged solutes, different distribution factors are implemented for these three categories. Since transport in the bentonite backfill is dominated by diffusion, advective flow through the bentonite into the fractures is not considered in the calculation of the distribution factors.

To obtain the release into the trajectory j for a given radionuclide and time step, the source term distribution factor is multiplied by the source term for the given radionuclide and time step. The distribution factors are assumed to be constant, whereas the source terms may vary over time.

It should be noted that the groundwater flows calculated at the interface between the repository vault and the rock are not identical in the hydrogeological near-field model (Abarca et al. 2019) and geosphere model (Joyce et al. 2019). The boundaries between the near-field and geosphere in the hydrogeological and radionuclide transport models do not coincide. In order to provide continuity in the radionuclide transport model, the value of the radionuclide release [Bq a^{-1}] is transferred between the near-field and geosphere models.

5.2.5 Handling in the geosphere model

Flow-related and non-flow-related migration properties are needed for the SE-SFL radionuclide transport geosphere calculations. The flow-related migration properties are calculated using a site-specific hydrogeological discrete fracture network model (Joyce et al. 2019). The non-flow-related migration

properties are taken from the safety analysis work for the Laxemar site, as presented in SKB (2010d) that compares the safety related site characteristics of Laxemar and Forsmark with respect to a Spent Fuel repository. For a few radionuclides that were not included in SR-Site, data were taken from SR-PSU, and for a handful of radionuclides non-flow-related migration properties were approximated from element analogues (Section 3.3 in Shahkarami 2019).

Flow-related migration properties

In the *present-day evaluation case,* the groundwater flow is assumed constant and simulated for 2000 AD using the first of five available realisations of the stochastic DFN model (Joyce et al. 2019), which is the only realisation which includes deterministic properties of the hydraulic conductor domain. The flows are obtained from the variant by Joyce et al. (2019) that did not include the effect of chemical reactions, which were shown to have a limited effect on water composition (**Main report**, Section 6.2.7). In this fracture network realisation, the repository is comparatively well connected to the geosphere (Section 4.4.1 in Joyce et al. 2019), which implies that the flow paths are more numerous and/or have higher flows that can transport radionuclides in comparison with the realisations with a less well-connected repository. The choice of fracture network can thus be seen as cautious. The sensitivity of the performance of BHA (including the bedrock as a natural barrier) to variation in the discrete fracture network is examined in *the alternative realisations of stochastic bedrock fractures evaluation case* (see Section 7.5).

In the particle-tracking calculations, ten particles were released from each of the rock fractures intersecting the BHA and BHK vaults and tracked through the fracture network to the surface (Joyce et al. 2019). Of the 9 590 particles released, 4 459 were successfully tracked to the surface. For every particle track that reaches the surface, flow-related properties were summed along the sections of the trajectory (e.g. t_w and F-factor). A representative volume-specific flow-wetted area a_w [m^2/m^3] was also calculated for each pathway by dividing the F-factor for the pathway by the total travel time t_w. This relative area represents the travel time weighted average along the flow pathway. Summary statistics of the flow-related properties along the pathways are given in Table 5-2. Statistics for flow and corresponding distributions are found in Joyce et al. (2019). Those particles that flowed into the repository rather than to the surface were disregarded.

Table 5-2. Statistics for flow-related migration properties for the DFN realisation used in the base case. Note that 2 424 particle pathways reached the surface from BHA, whereas the corresponding number from BHK is 2 035. Data from Joyce at al. (2019).

Waste Vault Statistic	Travel time t_w [a]	Flow-related transport resistance F-factor [a m^{-1}]	Relative flow-wetted area a_w [m^2 m^{-3}]	Trajectory length L [m]
BHA				
Average	8.98×10^2	2.13×10^5	6.25×10^2	2.43×10^3
Median	2.43×10^2	7.88×10^4	3.20×10^2	2.18×10^3
Min	3.28×10^1	9.46×10^3	2.20×10^1	1.38×10^3
Max	5.12×10^4	4.78×10^6	4.19×10^3	1.32×10^4
BHK				
Average	2.09×10^2	6.59×10^4	3.93×10^2	2.28×10^3
Median	1.45×10^2	4.75×10^4	3.24×10^2	2.09×10^3
Min	3.55×10^1	7.86×10^3	2.50×10^1	1.45×10^3
Max	3.93×10^3	2.47×10^6	2.09×10^3	1.37×10^4

Non-flow-related migration properties

The non-flow-related migration properties used in the radionuclide transport modelling are summarised in Table 5-3. The sorption coefficients and half-lives of the radionuclides that give the largest contributions to geosphere releases in the *present-day evaluation case* are given in Table 5-1. In the modelling, radionuclides are allowed to penetrate up to 4.5 m into the rock matrix, corresponding to half the average spacing between conductive fractures at the Laxemar site.

Table 5-3. Non-flow-related migration properties. Data described in Sections 2.4 and 3.3 in Shahkarami (2019).

Parameter	Value
Rock matrix porosity [-]	0.19
Effective diffusivity cations and non-charged species [m^2/s] [a]	2.7×10^{-14}
Effective diffusivity anions [m^2/s] [b]	8.5×10^{-15}
Maximum penetration depth in the rock matrix [m]	4.5
Rock matrix density [kg/m^3]	2700
Geosphere sorption coefficient [$m^3\ kg^{-1}$],	Radionuclide-specific
Radionuclide half-life [a^{-1}]	Radionuclide-specific
Decay chain and branching ratio	Radionuclide-specific

[a] Ac, Am, Ar, Ba, Be, Ca, Cd, Cm, C-org, Cs, Eu, Gd, Ho, K, Ni, Np, Pa, Pb, Pd, Pu, Ra, Sm, Sr.
[b] Ag, C-inorg, Cl, Co, H, I, La, Mo, Nb, Po, Re, Se, Si, Tb, Tc, Th, Ti, U, Zr.

Note that some radionuclides are assumed to belong to different species categories (anion vs. cation/neutral) for different purposes, e.g. in the geosphere vs. in the near-field, depending on assumptions regarding conditions such as redox potential, pH, and water composition. For several radionuclides, highly conservative assumptions regarding their speciation have been warranted due to large uncertainties (Section 3.3.1 in Shahkarami 2019).

5.2.6 The interface between the geosphere and the biosphere

The results of the set of model realisations of groundwater flow in the bedrock surrounding the repository in Laxemar (Joyce et al. 2019) indicate that most of the total potential release from SFL would typically end up underneath, or close to, one of three biosphere objects 204, 206 or 210. In three of the five fracture network realisations, object 206 received most discharge from the repository. Therefore, the total radionuclide release from SFL is assumed to be discharged homogenously into biosphere object 206. The effect of this assumption is evaluated in the *discharge area evaluation case* (Section 6.3).

5.2.7 Handling in the biosphere model

The development of the landscape is an important aspect for the biosphere model. Moreover, the surface hydrology needs to be quantified for the relevant ecosystems in order to calculate radionuclide transport. In the model, several ecosystem parameters are used that must be known. More importantly, to finally calculate the exposure, the exposed groups must be defined. The handling of these aspects of the biosphere model is described in the following subsections.

Landscape development

The *present-day evaluation case* assumes that present-day conditions persist for the repository environs and external conditions. As the release is directed to an agricultural ecosystem in biosphere object 206, the ongoing shoreline displacement and landscape development can be neglected. The physical and biological properties of the ecosystem receiving the discharge are assumed to be constant during the entire analysis period of 1 million years after repository closure. Consequently, the present regolith layer thicknesses are used for the agricultural ecosystem throughout the simulations (Nyman et al. 2008). An alternative state of the discharge area is also assessed in this evaluation case, namely a mire ecosystem that could have developed in the lake basin of 206 in the absence of human intervention. The regolith stratigraphy of this mire ecosystem is set to reflect the mature mire state, given the development of the lake that historically occupied object 206. For details on the simulations of landscape development, see Chapter 3 in Grolander and Jaeschke (2019).

Surface hydrology

Hydrological flow rates for the two ecosystem states are derived from a water balance representing the present conditions in object 206. Separate conceptual water-balance models and descriptions of the regolith profile are used for the two ecosystems. The upper soil layers in the agricultural field are assumed to be unsaturated and drained by ditches surrounding the cultivated land. In the mire ecosys-

tem, all regolith layers are assumed to be saturated and excess ground and surface water is discharged into a central stream. There are differences in the discharge from the local catchment, and from the bedrock, depending on the ecosystem state. In particular, the vertical discharge profile is affected by regolith depth and the percolation rate is dependent on the ecosystem state (Chapter 5 in Grolander and Jaeschke 2019). However, the differences in discharge are generally small and only affect radionuclide transport to a small degree. Following the SR-PSU methodology, the surface hydrology for a drained and cultivated mire (DM), a garden plot (GP) and a field cultivated according to the infield–outland system (IO) are simplified (Grolander 2013).

Ecosystem parameters

In the recent safety assessment of the SFR repository and its extension (SR-PSU), parameter values reflected the present and future conditions of Forsmark. The difference in regional climate between Laxemar and Forsmark is modest (+1.4 °C in average annual temperature and + 53 mm in average annual precipitation, Chapter 3 in the **Climate report**), and consequently most parameter values derived for terrestrial ecosystems in Forsmark (Grolander 2013) are relevant also for the SFL safety evaluation (Chapter 8 in Grolander and Jaeschke 2019). However, the values of a few terrestrial ecosystem parameters have been updated in SE-SFL to reflect the conditions in Laxemar. For terrestrial ecosystems these include: the length of the irrigation season for a garden plot and the wind velocity at 10 m height. Due to a model update, a handful of new parameters are introduced in SE-SFL. These include soil respiration, the fraction of inorganic chlorine in primary producers, and the concentrations of three essential elements (Ca, Cl and K) in plants, fungi and soil pore water. Moreover, not all element distribution and transfer factors, i.e. K_d and concentration ratio (CR) values, derived for Forsmark are considered to be applicable for the Laxemar site, as the geochemical properties of the two sites differ (Chapter 6 in Grolander and Jaeschke 2019). In SE-SFL, values for element-specific parameters are based on data from Laxemar when available. Thus, for terrestrial ecosystems, CR-values for herbivores and mire vegetation are given site-specific values. In addition, parameters for eight new elements (Be, Gd, K, La, Re, Si, Tb, and Ti) are included in SE-SFL, and values for these parameters are approximated from element analogues.

Exposed populations

Exposure routes include ingestion of food and drinking water, inhalation from respiration, and direct external radiation. Ingestion of food is expected to be the most important exposure pathway, and consequently the exposed population of primary interest in this evaluation case is self-sustaining farmers. Thus, the land-use and productivity of a family farm (Agr) from the turn of the nineteenth century is assumed for permanent cultivation of the object (Saetre et al. 2013, Grolander 2013). For potential exposure from a mire ecosystem, all the land-use variants from SR-PSU are utilized, including hunter-gatherers (HG), infield–outland farmers (IO), and a household with a garden-plot (GP). Potential exposure from draining the mire and cultivating it for 50 years is also assessed (DM), using the same assumptions for land-use and productivity as for permanent cultivation. Historical data have been used to generate parameter values that reflect typical land-use, habits and agrarian productivity for all exposed populations, except for the household with the garden plot, for which present-day habits have been assumed (Section 7.2 in the **Biosphere synthesis**).

5.2.8 Annual releases from the near-field

Radioactivity in the waste available for transport – BHA

Illustrating the activity content unaffected by transport, Figure 5-6 shows the temporal development of the activity in the BHA waste for the 15 radionuclides contributing most to the inventory at closure, assuming all radionuclides remain in the waste vault. The activity is dominated by Tc-99 and Ni-63, followed by C-14, H-3, Pu-241, Cl-36, Pu-238, Sr-90 and Cs-137 with two orders of magnitude lower initial inventories. A number of these radionuclides have half-lives between 10 and 500 years and thus, the activity is significantly decreased within a few thousand years. Out of the ten radionuclides contributing most to the inventory at closure, only Tc-99, C-14 and Cl-36 have half-lives longer than one thousand years.

With time, the rate of ingrowth exceeds that of decay for some radionuclides, e.g. Ra-226, resulting in increasing activity.

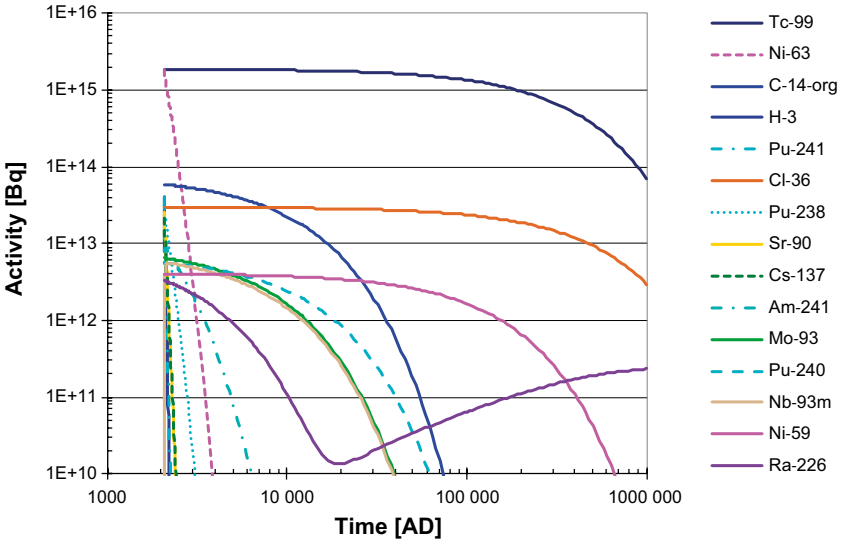

Figure 5-6. *Activity in the waste in BHA as function of time, assuming no release to the waste surroundings.*

Transport through the near-field – BHA

At the vault-bedrock interface, radionuclides can migrate from the boundary compartment by both diffusion and advection (Section 4.3.2). The total release rate N_{vault} of a radionuclide from the entire vault to the bedrock are estimated with Equation 4-15, which is repeated here for convenience:

$$N_{\text{vault}} = \frac{c_{\text{vault}}}{R_{\text{buffer}} + R_{\text{plugtot}} + R_{\text{eqtot}}} + Q_{\text{vault}} c_{\text{vault}} \qquad 5\text{-}1$$

In BHA, the water flow rate Q_{vault} [m^3/a] from the vault to the bedrock fractures is an order of magnitude lower than the term representing diffusive transport $1/(R_{buffer} + R_{plugtot} + R_{eqtot})$ for anions (Table 5-4), and two orders of magnitude lower than for cations/neutral species. For anions such as Cl^-, the plug resistance dominates the total transport resistance for diffusion, i.e. the sum (R_{buffer} + $R_{plugtot}$ + R_{eqtot}), whereas for cations/neutral species such as organic C-14, the resistance associated with diffusion from the backfill to the flowing water in the bedrock fracture, R_{eqtot}, dominates.

The residence time T_{res} [a] for radionuclides inside the vault is a quantification of the time dilution by sustained release that ensures that the annual releases are only a small fraction of the total inventory. The residence time indicates how long time it takes to release the majority of the activity of a specific radionuclide. It is commonly estimated as the total inventory I_{vault} [Bq] in the vault divided by the annual release N_{vault} [Bq/a], assuming no decay, using a steady-state solution of the radionuclide transport model for the vault:

$$T_{\text{res}}^{\text{transp}} = \frac{I_{\text{vault}}}{N_{\text{vault}}} \qquad 5\text{-}2$$

An alternative estimate of the residence time which does not rely on explicit transport modelling (but still on hydrological modelling) can be made, in terms of water flow rates and diffusive resistance:

$$T_{\text{res}}^{Cap} = \frac{Cap_{\text{vault}}}{Q_{\text{tot}}} \qquad 5\text{-}3$$

where Q_{tot} [m^3/a] corresponds to the flow rate out from the vault by both diffusion and advection:

$$Q_{\text{tot}} = \frac{1}{R_{\text{buffer}} + R_{\text{plugtot}} + R_{\text{eqtot}}} + Q_{\text{vault}} \qquad 5\text{-}4$$

and Cap_{vault} [m^3] is the total capacity of the vault, discussed in Section 4.1 in Wessely and Shahkarami (2019). The capacity is a measure of volume available to a potentially sorbing particle, i.e. the volume adjusted for porosity and sorption. It is generally given by:

$$Cap = V(\varepsilon + K_d \rho_{\text{bulk}}) \qquad 5\text{-}5$$

This expression enters into the left hand side of Equation 4-4 and the parameter definitions are given after Equation 4-2.

Table 5-4 shows the residence time estimated both as the steady-state transport solution (Equation 5-3) and via the capacity (Equation 5-4). For BHA, residence times are in the order of hundred thousand years and longer, even for non sorbing radionuclides.

Table 5-4. Terms contributing to the near-field activity release from BHA in the *present-day evaluation case* for a few important radionuclides.

Term from Equation 5-1	Cl-36[1]	C-14-org[2]	Tc-99[2]	Mo-93[1]	Ni-59[2]
Q_{vault} [m³/a]	0.00155	0.00155	0.00155	0.00155	0.00155
$1/(R_{buffer} + R_{plugtot} + R_{eqtot})$ [m³/a]	0.040	0.124	0.124	0.040	0.124
R_{buffer} [a/m³]	0.856	0.071	0.071	0.856	0.071
$R_{plugtot}$ [a/m³]	18.5	2.7	2.7	18.5	2.7
R_{eqtot} [a/m³]	5.3	5.3	5.3	5.3	5.3
Q_{tot} [m³/a]	0.042	0.125	0.125	0.042	0.125
Cap_{tot} [m³]	13300	13700	214000	22800	10400000
T_{res}^{Cap} [ka]	317	109	1710	543	83100
T_{res}^{transp} [ka]	315	109	1700	541	82800

[1] Anion
[2] Cation/neutral

Annual near-field release from BHA

The total annual activity release from the BHA near-field is dominated by the radionuclides that dominate the initial inventory and have half-lives longer than a few thousand years, i.e. Tc-99, C-14 and Cl-36 (Figure 5-7). Ni-63, with an initial inventory similar to that of Tc-99, does not contribute significantly to the release from BHA, due to its short half-life (100 years) and strong sorption onto bentonite (K_d = 0.3 m³/kg).

Initially, C-14 dominates the total annual activity release, but from about 4000 AD and for the remaining analysis period of one million years Tc-99 dominates (Figure 5-7). These two radionuclides together give a release that is at least one order of magnitude higher than any of the other radionuclides at all points in time. Both Tc-99 and Cl-36 are very long-lived (half-lives of 211 ka and 301 ka, respectively), and contribute to the release from BHA for most of the one-million-year analysis period. The combination of sorption onto bentonite, and a somewhat shorter half-life however, leads to an accumulated activity release of Tc-99 of about ten times that of Cl-36, although the initial inventory of Tc-99 is about sixty times that of Cl-36 (Figure 5-6).

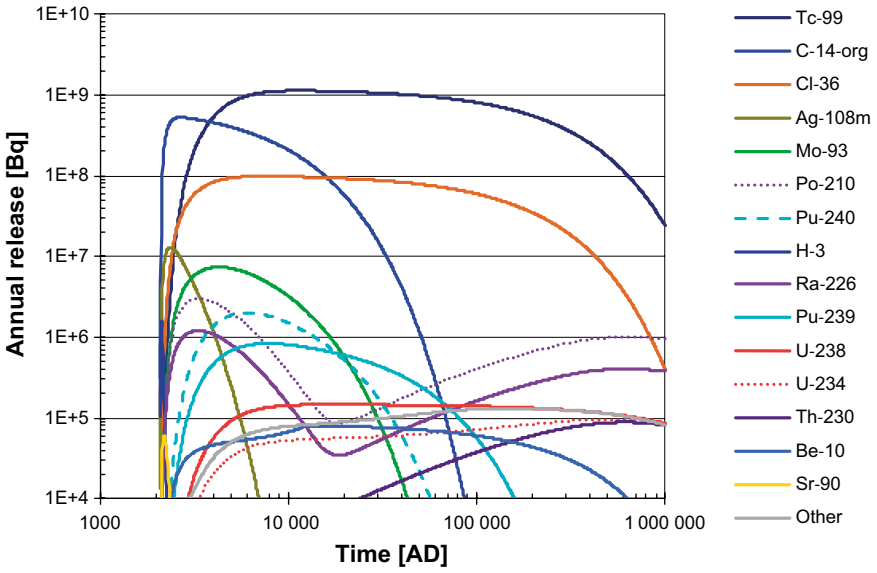

Figure 5-7. *Annual near-field activity release from BHA in the present-day evaluation case. Radionuclides with maximum annual release larger than 1×10^4 Bq are shown individually, whereas remaining radionuclides are grouped in the "Other" series.*

Due to retention in the near-field, the total accumulated activity release from BHA during the one-million-year analysis period is less than a tenth of the total initial activity in BHA. Retention is least efficient for Cl-36, for which BHA releases almost 60 % of its initial inventory until one million years after closure. For Tc-99, which sorbs onto bentonite, the corresponding accumulated release is 15 % of the initial inventory. Although C-14 does not sorb neither onto cement nor bentonite (Table 5-1), the major part (93 %) is retained and decays in the near-field due to the combination of a slow rate of transport (Figure 5-3) and a shorter half-life than that of Cl-36 and Tc-99.

Retention is even more efficient for Mo-93, with a half-life somewhat shorter than that of C-14 (Table 5-1), and a low but non-zero K_d for cement, resulting in that about 99 % of the initial inventory is retained and decays in the near-field. Also, for radionuclides with long half-lives, significant retention can be achieved with strong sorption in the bentonite. For instance, for Ni-59, with a half-life of 76 ka and a relatively high K_d for bentonite (0.3 m^3/kg), about 99.95 % of the initial inventory is retained and decays in the BHA near-field.

As described for Ni-63, the initial inventory is well retained in BHA for several radionuclides with shorter half-lives than a thousand years and sorption coefficients greater than zero in cement and bentonite. Examples among the 15 radionuclides contributing most to the initial activity inventory are Pu-241, Pu-238, Sr-90, Cs-137 and Am-241, despite the fact that sorption of Pu, Sr and Am is assumed to be significantly reduced due to the presence of ISA (Section 2.5.6 in Shahkarami 2019). Non-sorbing radionuclides with shorter half-lives than a thousand years may, however, contribute to the total annual activity release during the first few thousands of years after closure given a sufficient initial inventory (e.g. the anionic Ag-108m).

Beyond 10 ka after closure, the ingrowth of decay products leads to increasing near-field activity releases from specific radionuclides with time. For example, Ra-226 shows two release maxima, the first from Ra-226 present in the BHA waste at closure, which reaches a release maximum at approximately 3000 AD, and the second due to ingrowth at approximately 600 ka after closure. Ra-226 sorbs to a lesser extent than U and Th-isotopes in the near-field and thus is more mobile than its parent radionuclides.

The development with time of the activity inventory in the grouted waste and bentonite backfill is illustrated for the three radionuclides that contribute most to the total activity release from BHA, C-14, Tc-99 and Cl-36, in Figure 5-8. The relative releases are shown, i.e. normalised to an initial release from waste to backfill of unity. These figures also show the cumulative decay in different parts of the system, as well as the net releases from the grouted waste compartment and from the near-field to the geosphere. For the non-sorbing C-14, it takes only a few centuries to reduce the inventory in the grouted waste, mainly by diffusion into the bentonite backfill, to half its initial value (orange stack in Figure 5-8 left panel). The high transport resistance from the backfill to the water conducting rock fractures (as indicated by relatively high values of $R_{plugtot}$ and R_{eq} in Table 5-4) limits the rate of C-14 release.

For Tc-99, which does not sorb onto concrete but sorbs onto bentonite, most of the inventory in waste diffuses into the bentonite within a couple of centuries and is then dispersed within the bentonite backfill (Figure 5-8 middle panel). The Tc-99 activity in the bentonite backfill then only decreases slowly due to the long half-life, sorption onto bentonite, and the high transport resistance from the backfill to the water-conducting rock fractures. In contrast to Tc-99, Cl-36 sorbs to cement in the waste domain but not to bentonite. Cl-36 is retained in the grouted waste and construction concrete much more effectively (Figure 5-8 right panel), whereas the release from the bentonite to the geosphere is retarded by the slow diffusion of anions and limited by the slow transfer from the bentonite to the fractures. Thus, for long-lived radionuclides, even relatively weak sorption in cement and bentonite is an important retention mechanism together with the slow transfer from the bentonite backfill to the fractures. Illustrating this, the annual relative release to the geosphere of all three radionuclides in Figure 5-8 is smaller than 0.003 at all times, i.e. less than 0.3 % of the initial annual release from the waste to the backfill.

Radioactivity in the waste available for transport – BHK

Figure 5-9 shows the temporal development of the activity in the BHK waste for the 15 radionuclides contributing most to the inventory at closure, assuming all radionuclides remain in the waste vault. It can be noted that the BHK waste has a markedly different initial inventory from BHA (compare

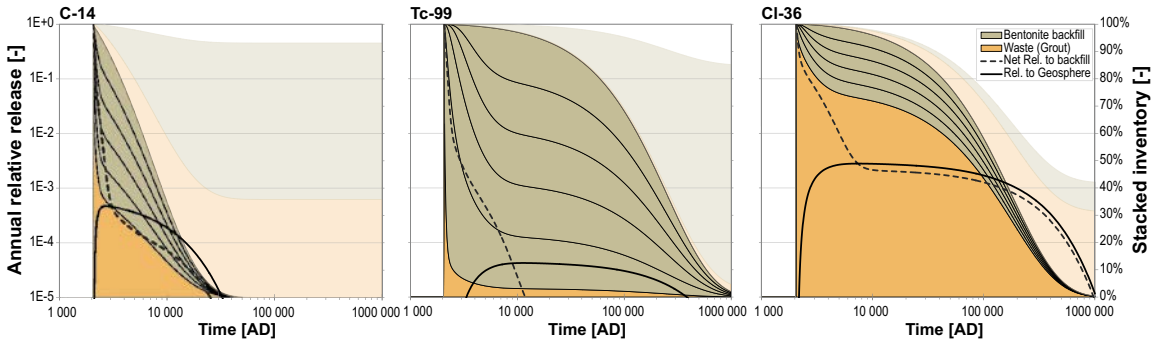

Figure 5-8. *Activity of organic C-14 (left panel), Tc-99 (middle panel) and Cl-36 (right panel) in BHA as a function of time. The left y-axis (log-scale) describes the annual relative net releases from the waste to the bentonite (dashed black lines) and from the bentonite backfill to the geosphere (solid black lines); these are normalised to an initial waste release of unity, and the release to backfill is the net release, i.e. subtracting the smaller backwards transport from backfill to the waste compartment. The right axis (arithmetic scale, normalised to 100 %) is related to the fate of the initial activity inventory. The plot shows (from bottom to top) stacked relative activity content in the waste and grout (orange) and the bentonite backfill (dark khaki), and cumulative decay in the waste and grout (pale orange) and in the bentonite (pale khaki).*

Figure 5-6 and the left panel in Figure 5-9). The initial activity is about two orders of magnitude greater in BHK than in BHA, due to high activity from Ni-63 and Co-60. These radionuclides have relatively short half-lives though (5.3 and 100 years, respectively) and about 1 000 years after closure the activity in BHA slightly exceeds that of BHK.

As described in Section 5.2.3, the waste in BHK mainly contains metallic components with neutron-induced activity which is assumed to become available for transport due to corrosion (illustrated in Figure 4-6). In addition to the corrosion-released activity, a remaining fraction of the initial activity in BHK that represents surface contamination and the thinnest metallic components is assumed to be released into the water phase immediately upon saturation of the repository. Taking the delayed release by the slow corrosion into account, leads to reductions in the activity available for transport in BHK (Figure 5-9 right panel). Since the main contributors to the high initial activity in BHK, Ni-63 and Co-60, mainly occur in metallic parts and have relatively short half-lives, the activity from these radionuclides available for transport in BHK is significantly reduced by accounting for the sustained release by corrosion. A similar effect is noted for C-14 and Mo-93, although slightly less pronounced. For more long-lived radionuclides, e.g. Ni-59 and Tc-99, the activity available for transport increases until 50 ka after closure, when metallic components of thickness less than 20 mm have completely corroded (Section 4.3.2).

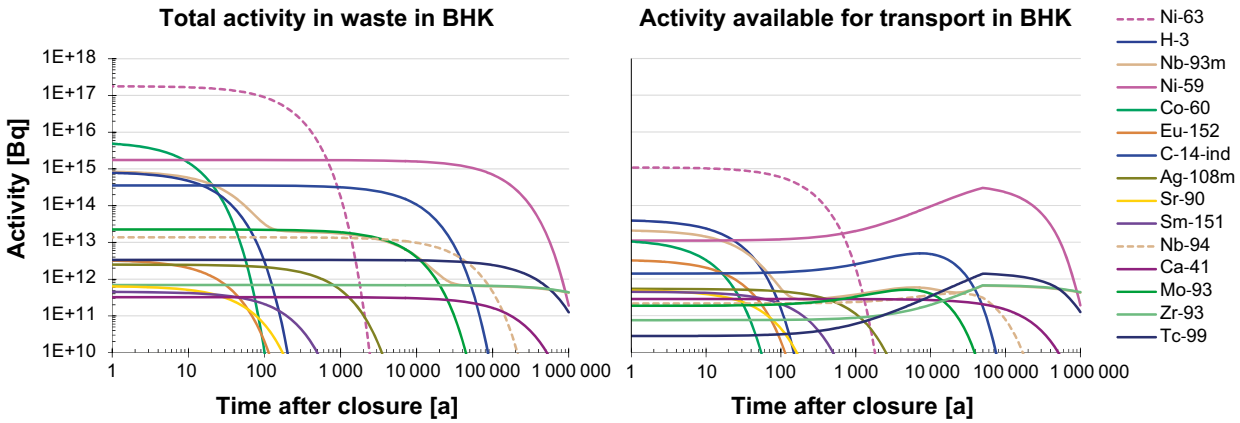

Figure 5-9. *Activity in the waste in BHK as a function of time after closure (after 2075 AD), assuming no transport to the waste surroundings (left panel). Activity in the waste in BHK available for transport, i.e. taking the delayed release by slow corrosion into account while still assuming no transport to the surroundings (right panel).*

Transport through the near-field – BHK

In contrast to BHA, the water flow rate from the boundary compartment to the bedrock fracture (Q_{vault}) changes over time due to degradation of the concrete backfill which is described as three distinct periods in the modelling (Section 5.2.3). During the intact-concrete (IC) and degraded-concrete (DC) periods, advection contributes more than diffusion to the release from BHK, as illustrated by a larger value for Q_{vault} compared to $1/(R_{buffer} + R_{eqtot})$ in Table 5-5. In the degraded-zone (DZ) period, the diffusive and advective contributions to the near-field release are comparable. This is due to the hydraulic cage effect, i.e. that water preferentially flows through the degraded parts of the system and thus decreases the hydraulic gradients that drive the flow through the intact parts of the backfill. During this period, the diffusive resistance in the non-degraded parts of the backfill still limits diffusive transport.

Table 5-5 also shows the residence time estimated in the same way as for BHA, i.e. via the vault capacity (Equation 5-3) and via the steady-state transport solution (Equation 5-2), respectively. Note that the capacity Cap_{tot} and residence time T_{res} may vary substantially during the DC period due to material changes affecting e.g. K_d, and the values for this period given in Table 5-5 should thus be interpreted with caution. Non-sorbing radionuclides have also mostly been transported out of the vault by this time.

Table 5-5. Terms contributing to the near-field activity release from BHK in the *present-day evaluation case* for the three concrete degradation states for a few important radionuclides.

	Term from Equation 5-1				
Period	Q_{vault} [m³/a]	$1/(R_{buffer} + R_{eqtot})$ [m³/a]	R_{buffer} [a/m³]	R_{eqtot} [a/m³]	Q_{tot} [m³/a]
IC (2075 AD)	0.715	0.112	4.91	3.98	0.828
DZ (87 600 AD)	0.353	0.502	1.77	0.221	0.854
DC (782 000 AD)	1.69	0.209	0.790	3.98	1.90

Term from Equation 5-1	**Period**	**Cl-36**	**C-14-ind**	**Tc-99**	**Mo-93**	**Ni-59[a]**
Cap_{tot} [m³]	IC	15 900	4 600	34 000 000	38 600	2 270 000
	DZ	15 500	4 830	32 100 000	36 900	2 140 000
	DC	12 500	6 660	17 700 000	6 660	1 180 000
T_{res}^{Cap} [ka]	IC	19.2	5.56	41 000	46.6	2 740
	DZ	18.2	5.65	37 600	43.2	2 510
	DC	6.59	3.50	9 280	3.50	622
T_{res}^{transp} [ka]		16.2	5.25	32 700	38.0	2 190

[a] The residence time and vault capacity of Ni-59 are calculated assuming a cement K_d = 0.2 corresponding to degradation state II (Table 2-18 in Shahkarami 2019 and Section 5.2.3) since state I starting at 2075 AD has a much lower K_d of 0.03, only lasts for a few thousand years, and thus is less representative for the longer IC period. The K_d values of the other four radionuclides in the Table are unchanged between degradation states I and II.

Annual near-field release from BHK

The total annual activity release from the BHK near-field is dominated by radionuclides with the largest inventory available for transport and half-lives longer than a few thousand years, i.e. C-14 and Ni-59 (Figure 5-10). Although Ni-63 has an initial available inventory two orders of magnitude larger than that of C-14 and Ni-59 (Figure 5-9), it does not contribute significantly to the release from BHK, due to its short half-life and sorption of Ni onto cement (see K_d for Ni-59 in Table 5-1).

C-14 dominates the annual release from BHK during the first ~25 ka after closure, resulting in a maximum total release about 6000 AD. During this period, the significantly lower releases of Ag-108m, Mo-93 and Ca-41 also reach their maxima. From about 100 ka after closure, Ni-59 dominates the release from the BHK near-field with a maximum at about 400 ka after closure.

The release of activity due to corrosion results in increasing activity available for transport until about 10 ka after closure for e.g. C-14 in BHK (Figure 5-9). Therefore, the maximum activity release for C-14 in BHK occurs later than that from BHA, and the decrease in the activity release following the maximum is less rapid in BHK than in BHA due to sustained release by corrosion (compare Figure 5-7 and Figure 5-10). Compared with the activity release for a non-sorbing radionuclide such as C-14, even a low K_d leads to retention and a later maximum annual release for Mo-93 than C-14. For radionuclides with long half-lives that sorb more strongly onto cementitious materials, such as Ni-59, the annual-release maximum is reached significantly later.

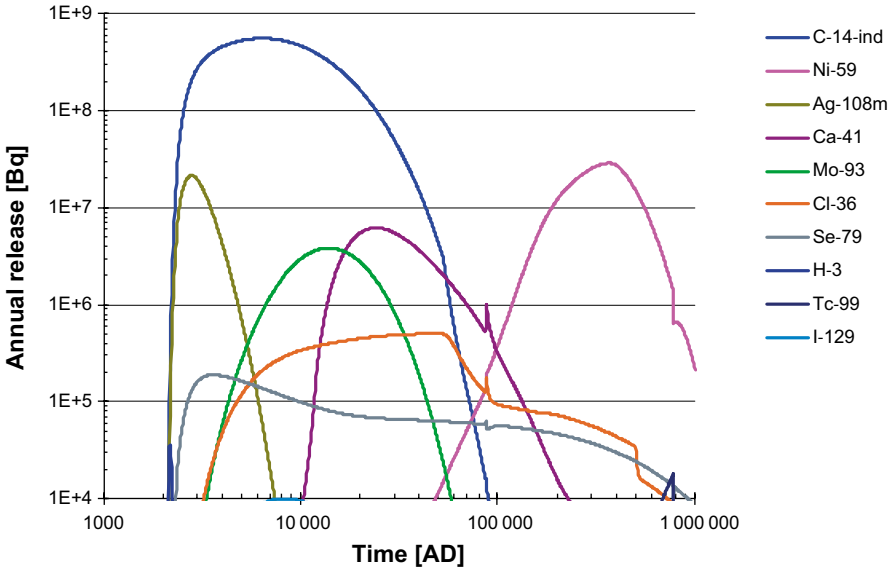

Figure 5-10. *Annual near-field activity release from BHK in the present-day evaluation case. Radionuclides with a maximum annual release larger than 1×10^4 Bq are shown, remaining radionuclides do not reach this threshold even when summed together. An artefact from the simplified representation of the development in groundwater flow and sorption due to concrete degradation (see Section 5.2.3) is seen around 87 000 AD and 800 000 AD when the groundwater flow is abruptly changed to simulate the transition from intact to degraded zone concrete.*

The accumulated activity release from BHK varies depending on radionuclide half-life, the distribution between metallic components of different thickness and the fraction assumed available for transport at repository closure, and, sorption on cement in the waste and the backfill. For the non-sorbing C-14, 98 % of the initial inventory is retained and decays in the BHK near-field, i.e. 2 % is released to the geosphere. Retention is even more efficient for Mo-93, with a half-life somewhat shorter than that of C-14 (Table 5-1), and a low but non-zero K_d for cement, resulting in about only 0.3 % of the initial inventory released. For Ni-59, with a half-life of 76 ka and a relatively high K_d for cement (Table 5-1), about 0.5 % of the initial inventory is released.

Retention for the long-lived non-sorbing Cl-36 in BHK is similar to that in BHA, with 56 % of the initial inventory retained until one million years after closure. Cl-36 contributes significantly less to BHK than BHA near-field release, with about two orders of magnitude lower maximum release rate of Cl-36 from BHK than from BHA (compare Figure 5-7 and Figure 5-10). This is mainly attributed to the initial inventory of Cl-36, which differs by about two orders of magnitude.

The development with time of the activity inventory in the metal, the grouted waste and the concrete backfill is illustrated for the two radionuclides that contribute most to the total activity release from BHK, C-14 and Ni-59, in Figure 5-11. This figure also shows the cumulative decay in different parts of the system, as well as the net releases from the grouted waste compartment and from the near-field to the geosphere. In comparison to organic C-14 in BHA (Figure 5-8 left panel), induced C-14 in BHK (Figure 11 left panel) is retained longer in the waste due to the slow release by corrosion. Thus, in BHK, most (> 97 %) of the C-14 activity decays before it is released from the metal by corrosion. Once released to the concrete barrier, the advective transport through the concrete barrier is relatively fast.

Similarly for Ni-59, a large proportion (91 %) of the activity decays before it is released from the metal by corrosion (Figure 5-11 right panel). In contrast to C-14, Ni-59 sorbs to cement in the waste and backfill and therefore is much more effectively retarded in the grout and concrete barrier.

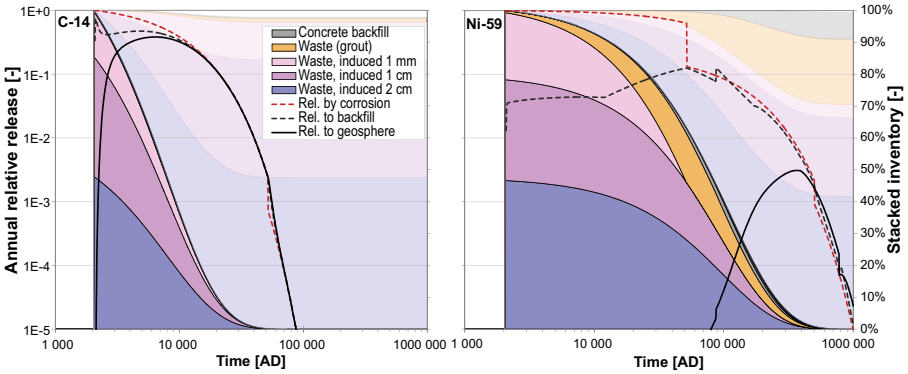

Figure 5-11. *Activity of induced C-14 (left panel) and Ni-59 (right panel) in BHK as a function of time. The left y-axis (log-scale) describes the annual relative releases from the metallic waste by corrosion, from waste to the concrete backfill (dashed black lines), and to the geosphere from the concrete backfill (solid black lines); these are normalised to a maximum corrosion release of unity, and the release to backfill is the net release, i.e. subtracting the smaller transport from backfill back into the waste compartment. The right y-axis (arithmetic scale, normalised to 100 %) is related to the fate of the activity. The plot shows (from bottom to top) stacked relative activity content available for transport in the waste or grout (orange), in the metal waste (purple, violet, pink), and in the concrete backfill (dark grey), and cumulative decay in the metal waste for the three component thicknesses (pale violet shades), in the grout (pale beige), and concrete barrier (pale grey). Activity contents available for transport in the concrete and the waste grout are too small to be visible in the left panel.*

5.2.9 Annual release from the geosphere

Mobile radionuclides are released at relatively higher rates from both BHA and BHK (Figure 5-12). The accumulation of mobile radionuclides in the geosphere is limited and the activity contained in the geosphere never exceeds 10 % of the cumulative release of C-14 and Mo-93 from BHA (Figure 5-13). Nevertheless, radioactive decay during geosphere transport reduces release of C-14 and Mo-93 from BHA by approximately 15 % (Figure 5-14), as compared with the near-field release. In addition, longitudinal dispersion along the flow pathways and variation in transport times between pathways (macro-dispersion) results in a distribution of the maximum release over time, which results in annual geosphere releases that are 20 % (Mo-93) and 30 % (C-14) below the corresponding maximum near-field releases (Figure 5-12). The difference in reduction due to dispersion between the two radionuclides (5 % and 15 %) is caused by differences in the temporal dynamics of the near-field release. That is, the distinct initial release maximum of C-14 is more affected by the temporal smoothing (due to dispersion) than the wider release pulse of Mo-93.

Many radionuclides in BHK are mostly contained within metallic parts and have an annual near-field release that is limited by the corrosion rate (see Section 5.2.8). Thus, the maximum releases of mobile radionuclides occur later from BHK than from BHA, and elevated release levels are sustained for a longer period. Moreover, due to faster groundwater flow from BHK, the median travel time is reduced by 40 % as compared with the flow paths from BHA (Table 5-2). The combination of more prolonged releases from the near-field and shorter travel times explains why the maximum accumulation of C-14 and Mo-93 in the bedrock is more than halved compared with the release from BHA (≤ 2 % of the cumulative release, Figure 5-13). The reduction of the maximum BHK annual release by geosphere transport is similar for C-14 and Mo-93, amounting to 4–5 % (Figure 5-12), and it is almost exclusively caused by radioactive decay. As the maximum release is maintained over an extended period, dispersion in the geosphere has almost no reducing effect on the maximum annual release. Cl-36, which has a long half-life, is almost unaffected (< 1 % reduction) by radioactive decay during the geosphere transport from both vaults (Figure 5-14). The maximum annual release from BHA is reduced by ~6 % due to dispersion, but the maximum release of Cl-36 from BHK is only marginally affected by geosphere transport (Figure 5-12). Finally, ingrowth of Nb-93m, a decay product of Mo-93, influences the release from the geosphere. This explains why the annual release of ‘Other’ radionuclides from BHK is considerably higher from the geosphere than from the near-field (Figure 5-12).

Sorbing radionuclides contribute quantitatively to the geosphere release from BHA (Tc-99) and BHK (Ni-59) after approximately 10 000 and 100 000 years respectively. In contrast to mobile radionuclides, considerable amounts of the strongly sorbing and long-lived radionuclide Tc-99

(K_d ~ 0.1 m^3 kg^{-1}) accumulate in the bedrock (up to 30 % of the cumulative release from BHA, data not shown). Sorption in the bedrock reduces the maximum annual geosphere release from BHA by almost 80 % in comparison with the near-field release (Figure 5-12). Most of this reduction is due to radioactive decay in the rock matrix. The retention also slows down the transport of Tc-99, and the maximum annual geosphere release occurs more than 100 000 years later than the maximum near-field release (Figure 5-12). Thus, the activity (and geosphere release) of Tc-99 is still building up long after the near-field release starts to decline, and the geosphere release never reaches the steady-state level corresponding to the maximum near-field release, i.e. the maximum geosphere release is below 40 % of the maximum near-field release (Figures 5-12 and 5-14). Ni-59 sorbs less strongly to the rock matrix than Tc-99 (K_d ~0.002 m^3 kg^{-1}), and the median travel time from BHK to the surface is shorter than for BHA. Consequently, retention in the geosphere has a smaller effect on the geosphere release of Ni-59. Still, the maximum annual release is 25 % lower from the geosphere than from the near-field. The reduction is primarily due to radioactive decay of Ni-59 that has sorbed in the rock matrix, whereas dispersion has little effect on the release maximum (data not shown in the figures).

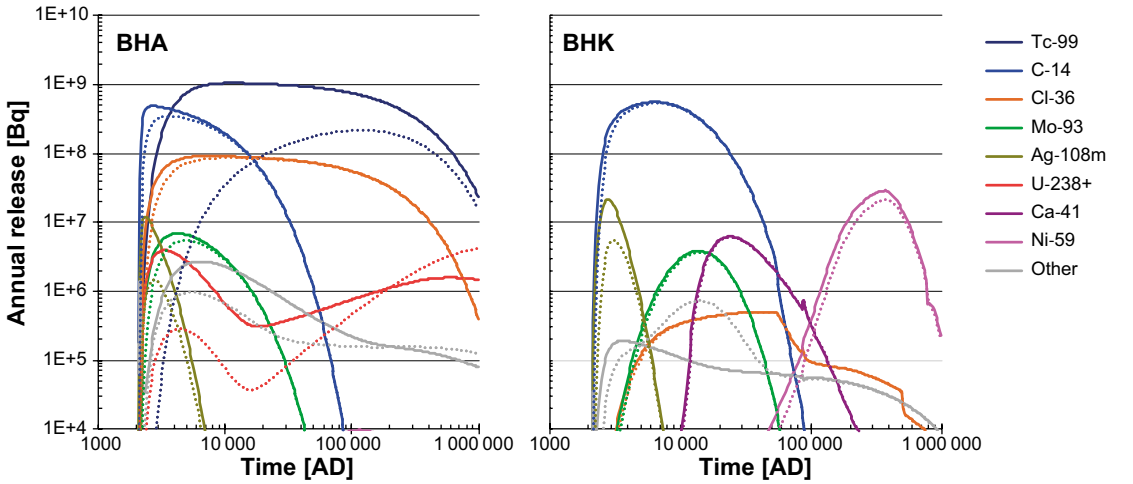

Figure 5-12. *Annual releases from the near-field (solid lines) and the geosphere (dotted lines) from BHK and BHA in the present-day evaluation case. Note that the difference between the near-field and the geosphere release from BHK is barely visible for Cl-36, Ca-41 and Mo-93. The top three radionuclides for maximum near-field activity release and the top three radionuclides for maximum annual dose from BHA and BHK are included in the figure. The sum of the release from radionuclides in the U-238 decay chain (U-238, U-234, Th-230, Ra-226, Pb-210, Po-210) is also included, labelled U-238+.*

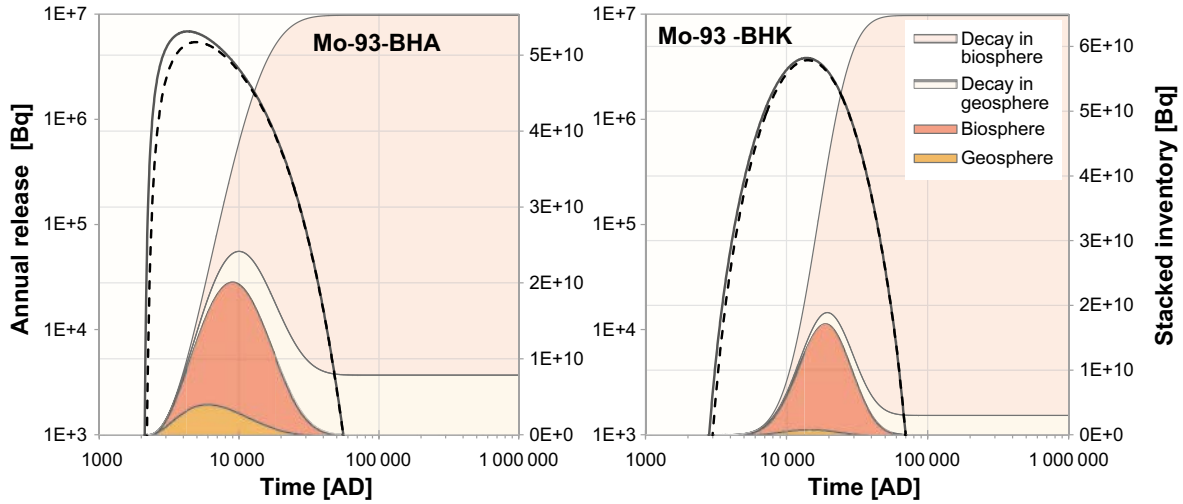

Figure 5-13. *The fate of Mo-93 released to the geosphere as function of time. The plot shows (from bottom to top) stacked activity content in the geosphere (brown) and in the surface system (red), and cumulative decay in the geosphere (pale beige) and in the biosphere (pale pink) (linear scale on right axis). The near-field and geosphere annual releases are shown for reference (black solid and dashed lines, logarithmic scale on left axis).*

The fraction of the near-field release that is also released from the geosphere (i.e. the relative geosphere release) decreases with increased degree of sorption and increases as the radioactive half-life increases. This relationship can be illustrated for a wide array of radionuclide property combinations under steady-state, as is done for BHA in Figure 5-14[4], where relative geosphere release increases from the top left towards the bottom right corner. Such a map shows that releases of short-lived radionuclides with $T_{½} < 30$ years such as Sr-90, H-3 and various decay products, are effectively reduced by the geosphere transport, irrespective of their sorption in the rock matrix. However, for longer-lived ($T_{½} > 30$ years) radionuclides that are released in any quantities from the near-field, the potential reduction from decay in the geosphere is limited. This is primarily because the activity of sorbing radionuclides with a half-life similar to that of the geosphere transport time has already been strongly reduced by radioactive decay in the waste vault before reaching the fractures in the geosphere (e.g. Cs-137 and Am-241), and their cumulative near-field release is thus smaller than 1 000 Bq, the threshold for inclusion in this analysis. However, there are two exceptions to this rule, as for BHA the decay in the geosphere reduces the release of Ag-108m and of Pu-238, -239 and -240 by a factor of five or more (Figure 5-14). The reason why these radionuclides have not been strongly reduced already in the near field is that Ag is assumed to be mobile in the near-field, and that the strong sorption properties of Pu are assumed to be greatly reduced by complexing agents in the near-field.

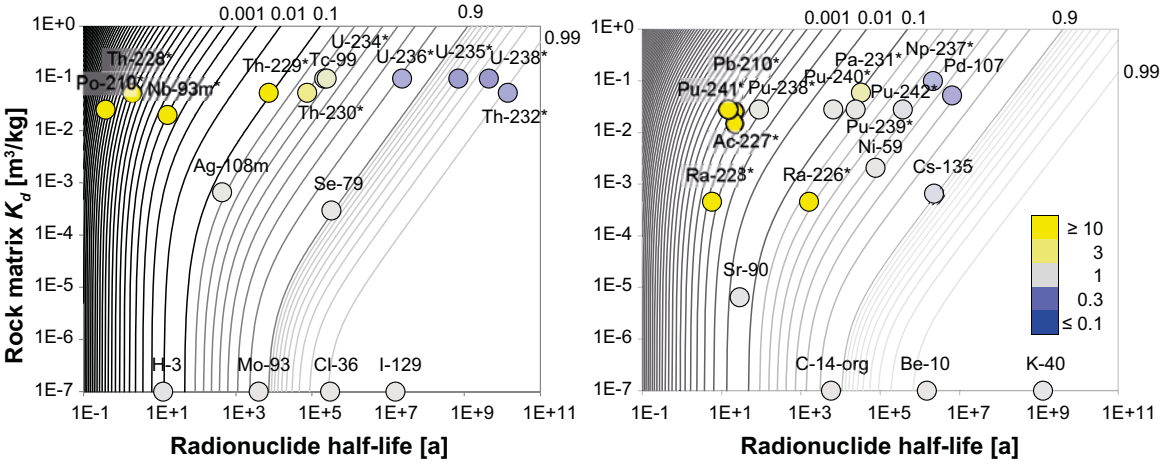

Figure 5-14. *Release from the geosphere of activity from BHA, expressed relative to the release from the near-field, as a function of sorption coefficient K_d and half-life, calculated for steady-state conditions[4] excluding ingrowth of decay products. Results are presented in the form of a contour map, where each light-grey isoline from 0.99 to 0.9 corresponds to a 0.01 decrement in relative release, grey isolines from 0.9 to 0.1 correspond to decrements of 0.1, and black isolines below 0.1 correspond to steps of a factor 10. Circle colours represent the million-year-cumulative geosphere release from BHA relative to the cumulative near-field release, divided by the corresponding value from steady-state calculations; hence, grey indicates a good match between cumulative and steady-state results. Note that mobile radionuclides (with $K_d = 0$) have been placed on the x-axis, i.e. with an arbitrarily low y value. Radionuclides which have a cumulative near-field and geosphere release below 1 000 Bq during the full assessment period are considered to have been reduced to insignificant levels and have been excluded for clarity of presentation. The left panel shows anions ($D_e = 2.7 \times 10^{-7}$ m² a⁻¹) and the right panel shows cations/neutral species ($D_e = 8.5 \times 10^{-7}$ m² a⁻¹). * indicates radionuclides that are decay products.*

[4] The illustration is based on the steady state solution to transport with longitudinal dispersion but with no limits on diffusion depth in the rock matrix (Equation B-57 in Appendix B).

By comparing the fraction of the cumulative near-field release that reaches the geosphere during the full assessment period in *the present-day evaluation case* with the steady-state solution (see also next section), it is evident that retardation in the rock matrix has reduced the release of long-lived and sorbing radionuclides. That is, the activity of these radionuclides has not reached the steady-state levels, corresponding to the near-field release without accounting for decay products. For example, not all the activity of U-238 released from the near-field has decayed or left the geosphere, but instead the geosphere activity is still building up at the end of the assessment (as indicated by blue colour in the upper right corner of Figure 5-14). The comparison also highlights that most (and sometimes all) of the geosphere release of short-lived decay products (e.g. Po-210, Pb-210 and Nb-93m) is due to ingrowth from parent radionuclides (bright yellow symbols in Figure 5-14). It is interesting to note that transport through the geosphere initially reduces the release from the uranium series significantly (primarily by radioactive decay of Ra-226 and its decay products) but, by the end of the simulation, the geosphere release is clearly higher than the near-field release (Figure 5-12). The increase in activity towards the end of the assessment period is primarily due to ingrowth of Ra-226 and its decay products from Th-230 that has accumulated in the bedrock matrix.

Effects of flow-related properties

The near-field release is distributed over more than two thousand flow-pathways for each of the waste vaults. Each flow pathway is characterised by a travel time t_w [a^{-1}] and a flow-wetted surface area per unit volume of the fracture a_w [m^2/m^3]. A short travel time is either the result of a high advective flux or a short pathway, and it favours fast transport towards the surface. Narrow fractures have a large flow-wetted surface area per unit volume that enhances diffusion transport into the rock matrix. In the geosphere model, the rate of diffusion into the rock matrix is typically much higher than the rate of advective flux. Thus, the release from most pathways will be retarded, and/or reduced by radioactive decay, in the rock matrix. The degree of retardation and reduction strongly depend on the sorption in the rock matrix and the half-life of the radionuclides of interest.

The factors affecting the reduction of the release from the geosphere can be illustrated by the steady-state solution to the geosphere release N_{geo} [Bq/a], for a given near-field release N_{NF} [Bq/a]. Ignoring the ingrowth of decay products, the longitudinal dispersion effects and limitations of the rock matrix diffusion depth, the steady-state solution for the relative geosphere release N_{geo}/N_{NF} [Bq a^{-1}/(Bq a^{-1})] becomes (Equation 58 in Appendix B):

$$\frac{N^n_{\text{geo}}}{N^n_{NF}} = e^{-\lambda^n_{pathway}\, t_w} \qquad 5\text{-}6$$

where

t_w = Total advective travel time [a].

$\lambda^n_{pathway}$ = The effective decay rate for the flow pathway for radionuclide n [a^{-1}] defined as:

$$\lambda^n_{pathway} = \lambda^n + a_w\sqrt{\lambda^n D^n_e R^n_m} \qquad 5\text{-}7$$

where

λ^n : Decay constant for radionuclide n [a^{-1}].

a_w : Area of the flow-wetted surface per volume of water [$m^2\ m^{-3}$].

D^n_e : Effective diffusivity of radionuclide n in the rock matrix [$m^2\ a^{-1}$].

R^n_m : Retardation coefficient for radionuclide n in rock matrix [-] defined as:

$$R^n_m = \varepsilon_m + K^n_{d,m}\rho_m \qquad 5\text{-}8$$

where

ε_m : Effective porosity of the rock matrix [-].

$K^n_{d,m}$: Sorption coefficient in rock matrix for radionuclide n [$m^3\,kg^{-1}$].

ρ_m : Bulk density of the rock matrix [kg m^{-3}].

The first term λ^n in Equation 5-8 represents the effect of radioactive decay in the fracture, whereas the second term ($a_w\sqrt{\lambda^n D^n_e R^n_m}$) represents decay in the rock matrix. The relative geosphere release of sorbing radionuclides ($Kd^n_m\rho_m \gg \varepsilon_m$) will typically be determined by the rate of diffusion into

the rock matrix ($a_w\sqrt{\lambda^n D_e^n R_m^n} \gg \lambda^n$). Thus, the relative geosphere release for sorbing radionuclides (e.g. Ni-59, Tc-99 and Ag-108m) decreases exponentially with the product of the travel time t_w and the volume-specific flow-wetted area a_w (Tc-99 in Figure 5-14). This is typically also true for radionuclides with a long half-life ($\lambda^n \ll a_w^2 D_e^n R_m^n$) as a low decay rate decreases decay in the fracture more than decay in the rock matrix. This applies even if sorption is low (e.g. Cl-36), but the quantitative reduction due to radioactive decay is typically marginal (or even negligible) in this case. On the other hand, radionuclides that exhibit little sorption ($\varepsilon_m \gg K_{d,m}^n \rho_m$) and a short half-life (e.g. Sr-90) primarily decay in the fracture ($\lambda^n \gg a_w^2 D_e^n R_m^n$), and the relative geosphere release thus decreases exponentially with the travel time t_w. For mobile radionuclides ($K_d = 0$) with a half-life of a few thousand years (e.g. C-14 and Mo-93) the relative importance of diffusion strongly depends on the aperture of the fracture. Thus, in relatively thin fractures with a large area to volume ratio, diffusion into the rock matrix determines the geosphere release (i.e. $t_w \times a_w$ or F-factor, see Section 4.4), whereas the release from relatively open fractures (with small values of a_w) is primarily determined by the travel time (see arrows for Mo-93 in Figure 5-15). Given the distribution of travel times and flow-wetted areas of pathways from BHA, significant reduction of fluxes of radionuclides with half-lives like those of Mo-93 and C-14 is primarily associated with large advective travel times (dark blue circles for Mo-93 in Figure 5-15).

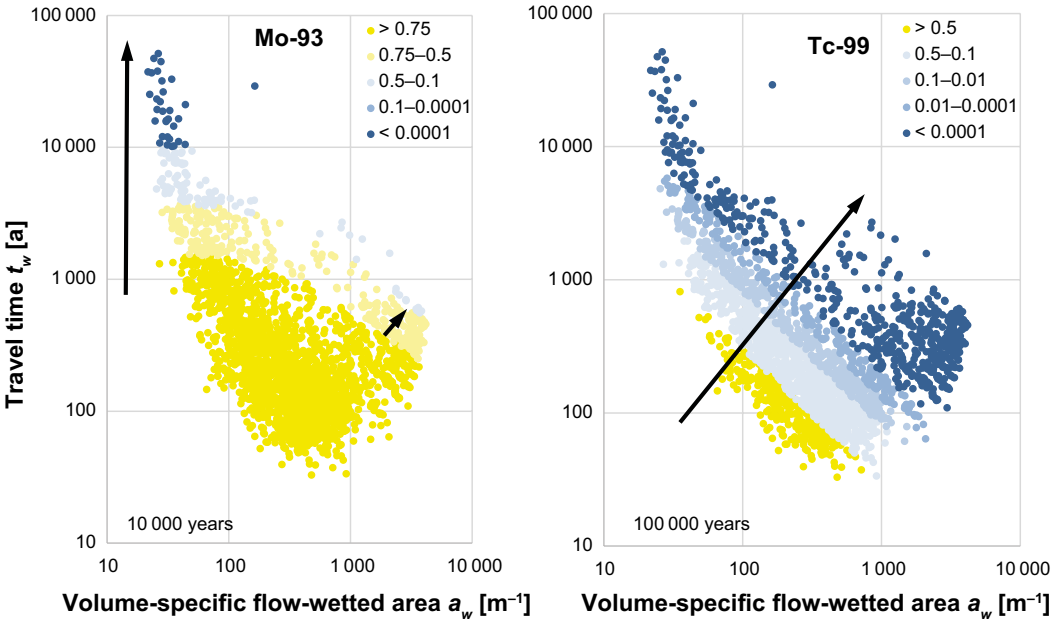

Figure 5-15. *Effects of travel time (t_w) and volume-specific flow-wetted area (a_w) on the release of Mo-93 and Tc-99 from BHA. Each point in the graph corresponds to an individual flow pathway, and the colour indicates the proportion of the near-field release that reaches the biosphere (geosphere release relative to near-field release). The arrows indicate the main factors determining the retention: the vertical arrow corresponds to decay in relatively open fractures (determined by variation in t_w), whereas the diagonal arrows correspond to decay in the rock matrix (determined by variation in the product $t_w \times a_w$, i.e. the F-factor). The length of the arrows gives a rough indication of the relative importance of variation in t_w versus $t_w \times a_w$ for variation of the geosphere release. Note that the colour scaling has a finer resolution in the region between 1 and 0.1 for Mo-93. The results are based on a constant annual near-field release that has prevailed for 10 000 (Mo-93) and 100 000 years (Tc-99), which roughly corresponds to the length of the maximum annual release from BHA.*

The release to the biosphere is the sum of the release over all the flow pathways from a waste vault to the surface. Differences in the properties between the pathways will result in dispersion of the release. Moreover, the reduction due to radioactive decay may vary substantially between the flow pathways. A comparison of the fraction of the near-field release that reaches the biosphere from the two vaults gives an indication of how sensitive the results in *the present-day evaluation case* are to variations in transport pathways in the geosphere that are associated with the positions of the two waste vaults. (A more detailed analysis of the sensitivity to flow pathways is carried out in *the alternative bedrock fracture network evaluation case*). However, to not confound the effect of the geosphere transport with the dynamics of the release (Figure 5-12) and/or the principles used to distribute the release between flow pathways for different repository types (Section 5.2.4), the comparisons are made for steady-state conditions given a constant near-field release.

The comparison shows that the sensitivity of the geosphere release to the properties of the geosphere transport pathways varies between radionuclides. As previously shown, the releases of mobile radionuclides with a half-life above a few thousand years (i.e. Cl-36, C-14 and Mo-93) are typically only reduced marginally in the geosphere (Figure 5-14). However, a few slow flow pathways from BHA do not conform to this pattern, as transport along these pathways may reduce the activity of C-14 and Mo-93 by 50 % or more (right panel in Figure 5-16). However, the frequency of these pathways is very low, and consequently the difference in release between the two positions is small (i.e. less than 10 %, left panel in Figure 5-16).

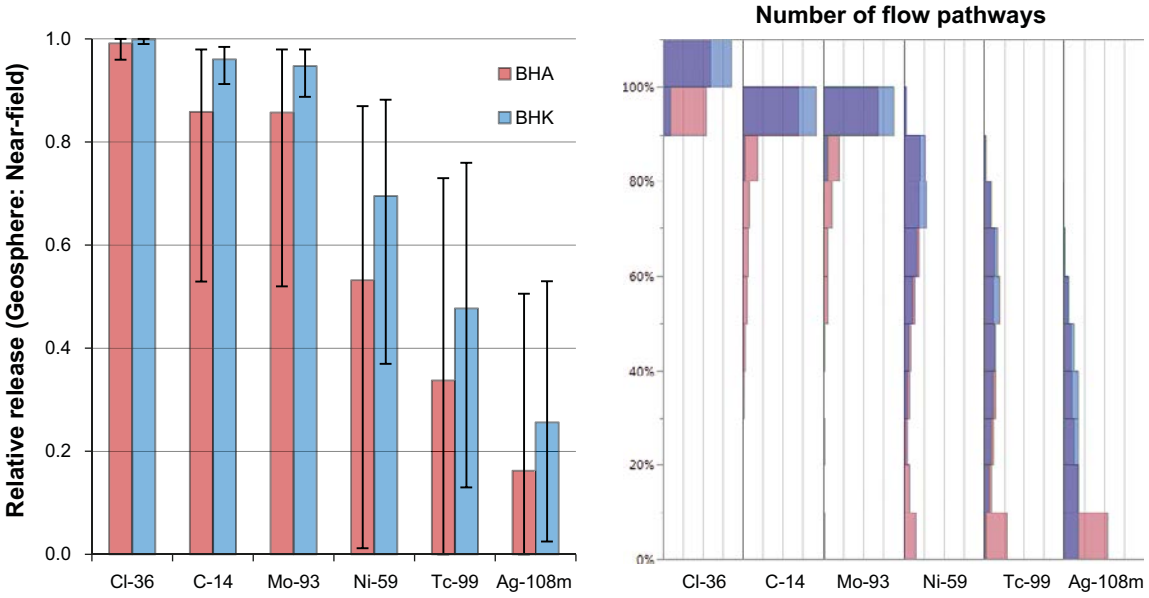

Figure 5-16. *Steady-state activity release from the geosphere relative to the near-field release, as affected by radioactive decay and as a function of the flow pathways from two waste vault positions: BHA (red) and BHK (blue). Left: Statistics (mean, 5th and 95th percentiles) of relative release from more than 2 000 flow pathways. Right: Frequency distributions of the relative releases. Flow pathways for which the geosphere release is unaffected by radioactive decay are grouped into the uppermost bin (≥ 100 %). Note that the number of successful pathways from the simulations, and thus the total area summed over all bins in the right panel, is larger for BHA than for BHK.*

For radionuclides that sorb in the rock matrix, the picture is somewhat different. For example, the release of Ni-59 is reduced by all pathways. The frequency of pathways from BHK is relatively evenly distributed in the range between 40 % and 90 % relative release or, equivalently, 10 % and 60 % reduction (5th and 95th percentiles), whereas the span covering 90 % of the BHA pathways is wider (10–99 % reduction). The variation in release between pathways is high also for Tc-99 and Ag-108m, and the frequency of pathways that reduce the geosphere release significantly (i.e. by 90 % or more) clearly increases from Ni-59 (~10 % from BHA) to Ag-108m (~50 % from BHA) as expected from the relationship between the K_d and the half-life (Figures 5-14 and 5-16). The pathways that result in a large reduction are characterised by a high diffusive rate in relation to the rate of advective transport, i.e. a large value of $t_w \times a_w$ (see Tc-99 in Figure 5-15). The pathways from the two waste vault positions largely overlap with respect to their characteristics. However, BHA clearly has a higher frequency of pathways associated with a higher rate of diffusive transport, i.e. thin fractures with $t_w \times a_w$ larger than about 2.5×10^5 a m^{-1}. This translates into a noticeable reduction of the release of sorbing radionuclides from the BHA position, as compared with a release from the BHK position. That is, given an equal, constant near-field release, the summed geosphere release of Ni-59 from all BHA pathways is 25 % smaller than that from the BHK pathways. Similarly, the release of Tc-99 and Ag-108m is 30 and 40 % lower from the BHA pathways than from the BHK pathways (Figure 5-16).

5.2.10 Annual doses

As noted in Section 5.2.7, all release from the geosphere is pessimistically assumed to be discharged into the till of biosphere object 206. Annual doses are calculated accounting for radionuclide transport through the regolith layers in an agricultural ecosystem (similar to present-day conditions) or through the regolith in an undisturbed mire ecosystem. Self-sufficient agriculture on a drained and cultivated mire (DM) yields higher doses than other uses of natural resources in the object, including hay-making in an infield–outland farming system (IO), small-scale fertilisation and irrigation of a garden plot (GP), or hunting and gathering (HG) (Figure 5-17, data for BHK not shown). Moreover, cultivation after drainage results in a considerable higher dose than continuous farming of the object (Agr). The reason for this is primarily that in the DM case, radionuclides can accumulate in peat for a long time prior to human exposure. The following interpretation of the results is therefore focussed on the DM land-use variant of the mire ecosystem. In this variant, radionuclides accumulate continuously in the mire ecosystem up to the point of drainage. The dose from early cultivation (50 years following drainage) is evaluated for each point in time, cautiously assuming that the mire has not been disturbed prior to the time of drainage.

At the time point for maximum total dose, ~10 000 AD for BHA and 18 000 AD for BHK, ingestion of crops is the most important exposure pathway in the drained mire. However, for release from BHA the importance of exposure from well water increases with time, as the activity of Tc-99 and decay products from the uranium series reach the biosphere. After 40 000 AD, the dose contribution from a dug well makes up between 10 and 30 percent of the total dose from DM (Figure 5-17). Drinking water also contributes substantially to the dose for other land-use variants (Agr, GP, IO), but the contribution never exceeds that from ingestion of crops at the times when the annual dose reaches maximum levels. The contribution of well water to the dose from BHK is small for all land use variants and times (data not shown). This is because the primary dose-contributing radionuclides (C-14 and Mo-93) are poorly retained in the lower regolith layers and are easily taken up by plants.

The releases of several radionuclides from both vaults yield DM doses that are of the same order of magnitude as the regulatory risk limit for a final repository for radioactive waste (Figure 5-18). C-14 dominates the early doses and Mo-93 is the main contributing radionuclide to maximum total doses from both vaults. Cl-36 contributes significantly to the dose from BHA for the first 200 000 years, and Tc-99 contributes significantly to the dose for the latter 900 000 years of the simulation period. U-238 and its decay products (e.g. U-234, Th-230, Ra-226, Pb-210 and Po-210) contribute to the dose from BHA at the end of the assessment period, where U-238 itself is the main contributor due to its long half-life. Ni-59 dominates the dose from BHK in the latter part of the assessment period. The total contribution of all other radionuclides is small in comparison with the above-listed radionuclides (Ni-59 excluded) and the total dose contribution from these is an order of magnitude (or more for BHK) below the regulatory limit.

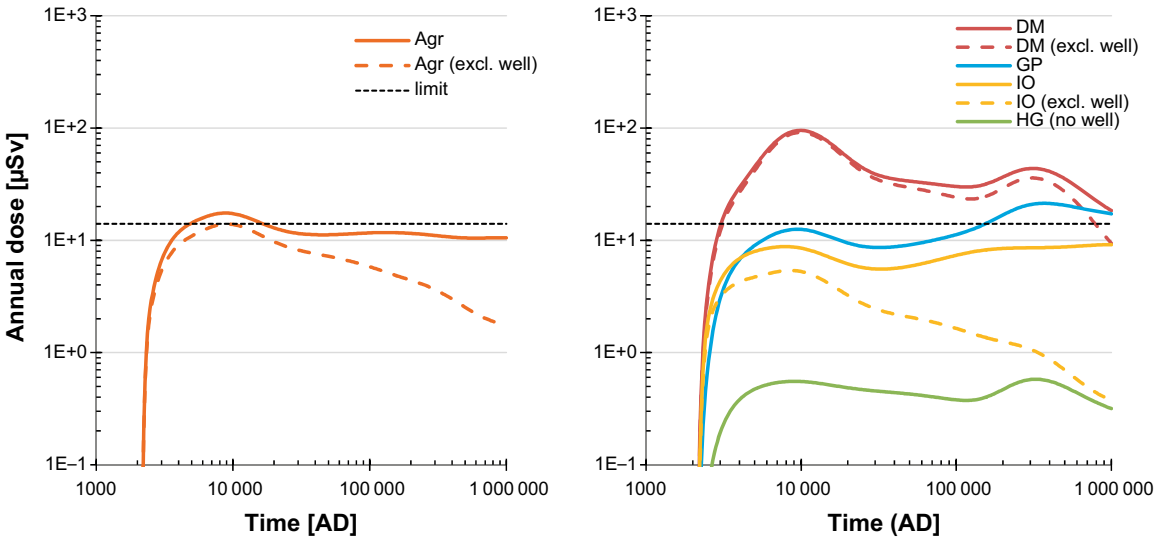

Figure 5-17. *Annual dose due to releases from BHA for permanently cultivated agricultural soil (left) and different land use variants of a mire ecosystem (right) in biosphere object 206. A description of the different land use variants can be found in Section 4.5.2. The dose contribution from well water is illustrated by replacing exposure from well water with exposure from stream water (dashed coloured lines). Dashed black lines show the dose corresponding to the regulatory risk limit (14 µSv). Agr = self-sufficient farming, DM = self-sufficient farming of a drained mire, GP = small scale cultivation of a garden plot, IO = infield–outland farming, HG = hunting and gathering.*

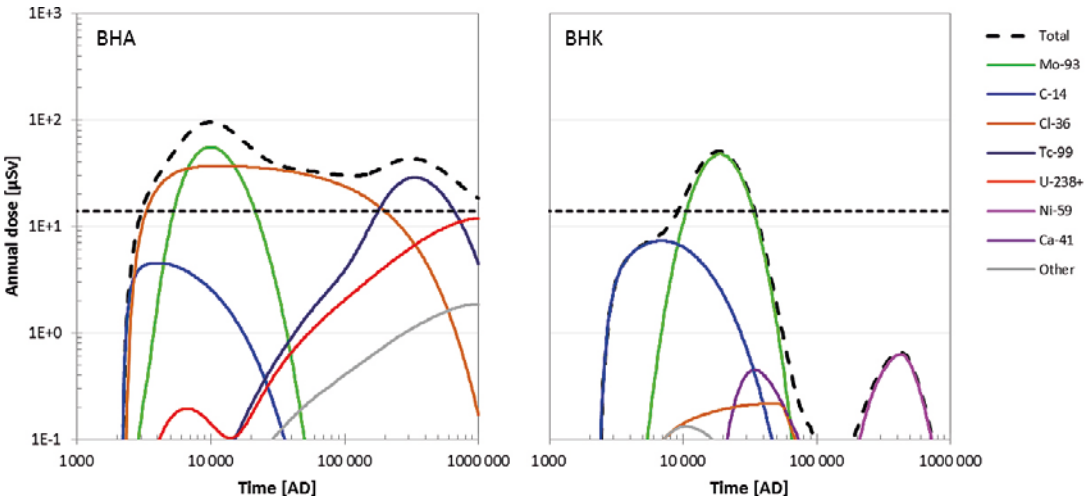

Figure 5-18. *Annual dose from BHA and BHK from draining and cultivating the mire ecosystem in biosphere object 206. The total dose (long-dashed black line) is shown together with the contributions from individual radionuclides (coloured lines), compared to the dose corresponding to the regulatory risk limit (short-dashed black lines at 14 µSv).*

The relative importance of individual radionuclides varies over time, primarily as a function of the geosphere release (Figure 5-19, data from BHK not shown). Thus, the dynamics of the dose from non- and weakly sorbing radionuclides (C-14 and Cl-36) closely follows that of the geosphere release. However, the transport from the bedrock to the surface delays the maximum annual dose from Mo-93 by approximately 5 000 years and of Tc-99 (BHA only) by more than 200 000 years. These delays are caused by retention and decay in the regolith as discussed in more detail in the next few paragraphs.

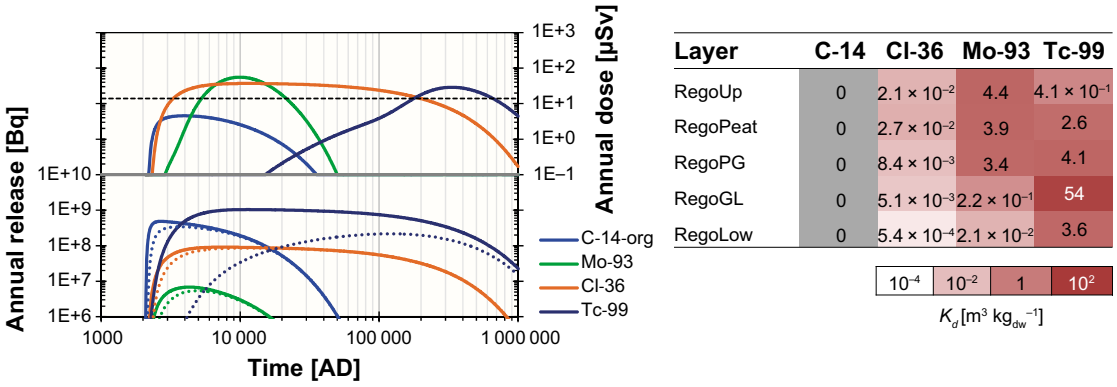

Figure 5-19. *Annual release and dose from BHA (left) and sorption coefficients for different regolith layers (right). The contributions from individual radionuclides are shown with coloured lines. In the lower left panel solid lines represents release from the near-field, whereas dotted lines represent release from the geosphere. In the upper left panel, the dashed black line corresponds to the dose corresponding to the regulatory risk limit (14 µSv).*

To illustrate the transport and accumulation of dose-contributing radionuclides in the biosphere, the spatial (vertical) and temporal patterns of activity and the groundwater concentrations in the regolith are examined below. The geosphere release from BHA is used for the illustration. The pore-water concentration of all radionuclides decreases towards the surface, as the deep groundwater is diluted with groundwater from the local catchment (and to a lesser extent also with meteoric water) (left y-axes in Figure 5-20). The retention in regolith layers is proportional to the groundwater concentration. For highly mobile radionuclides (e.g. C-14 and Cl-36), the accumulation of activity is limited, and a high proportion of the activity is in form of dissolved radionuclides. Consequently, variation in the activity between regolith layers primarily reflects differences in pore water concentration and in pore volume. As the transport through the regolith profile is relatively fast, the dynamics of activity in the regolith column closely follows that of the geosphere release (Figure 5-19). The residence times of inorganic carbon and chloride in the regolith are only 10 and 50 years, and consequently the proportions of C-14 and Cl-36 that decay in the regolith are insignificant. However, both C-14 and Cl-36 are stored in organic matter in the peat (including surface peat, RegoUp). The dynamics of these pools are slower (Figure 5-20), because they follow the rate of organic matter accumulation.

The transport of sorbing radionuclides is considerably retarded as the activity in solids successively accumulates along the flow path. The retention primarily reflects the strength of sorption (K_d value) in regolith layers and, to a lesser extent, also the pore water concentration and the mass of the layer, i.e. the thickness and density. Mo-93 sorbs relatively strongly to the organic-matter-rich upper regolith layers (right panel in Figure 5-19), which results in a considerable accumulation, particularly in post-glacial deposits (RegoPG in Figure 5-20). The residence time for molybdenum in the regolith stack is 6 600 years. As Mo-93 has a relatively short half-life of 4 000 years, more than 50 % of the activity reaching the biosphere is lost through radioactive decay, and most of this decay occurs in post-glacial deposits which is the first of the organic layers with high sorption. Tc-99 is also a sorbing radionuclide, but it primarily accumulates in the deeper inorganic regolith layers (RegoLow and RegoGL in Figure 5-20), and the activity in these layers makes up 98 % (or more) of the total activity in the regolith. As the potential for accumulation is large, and the groundwater flow rate is relatively slow in the lower part of the regolith, the residence time for technetium is 200 000 years. This time is in same order of magnitude as the half-life for radioactive decay (210 000 years) and consequently the geosphere release is approximately halved before it reaches the upper parts of the regolith horizon. The retardation in the lower regolith profile initially restricts the exposure pathways to extraction of well water. However, after approximately 100 000 years, Tc-99 breaks through the glacial clay layer and shortly thereafter reaches the peat (Figure 5-20) where it can lead to exposure, e.g. after drainage and cultivation. Consequently, the dose from Tc-99 increases substantially when this happens (Figure 5-18).

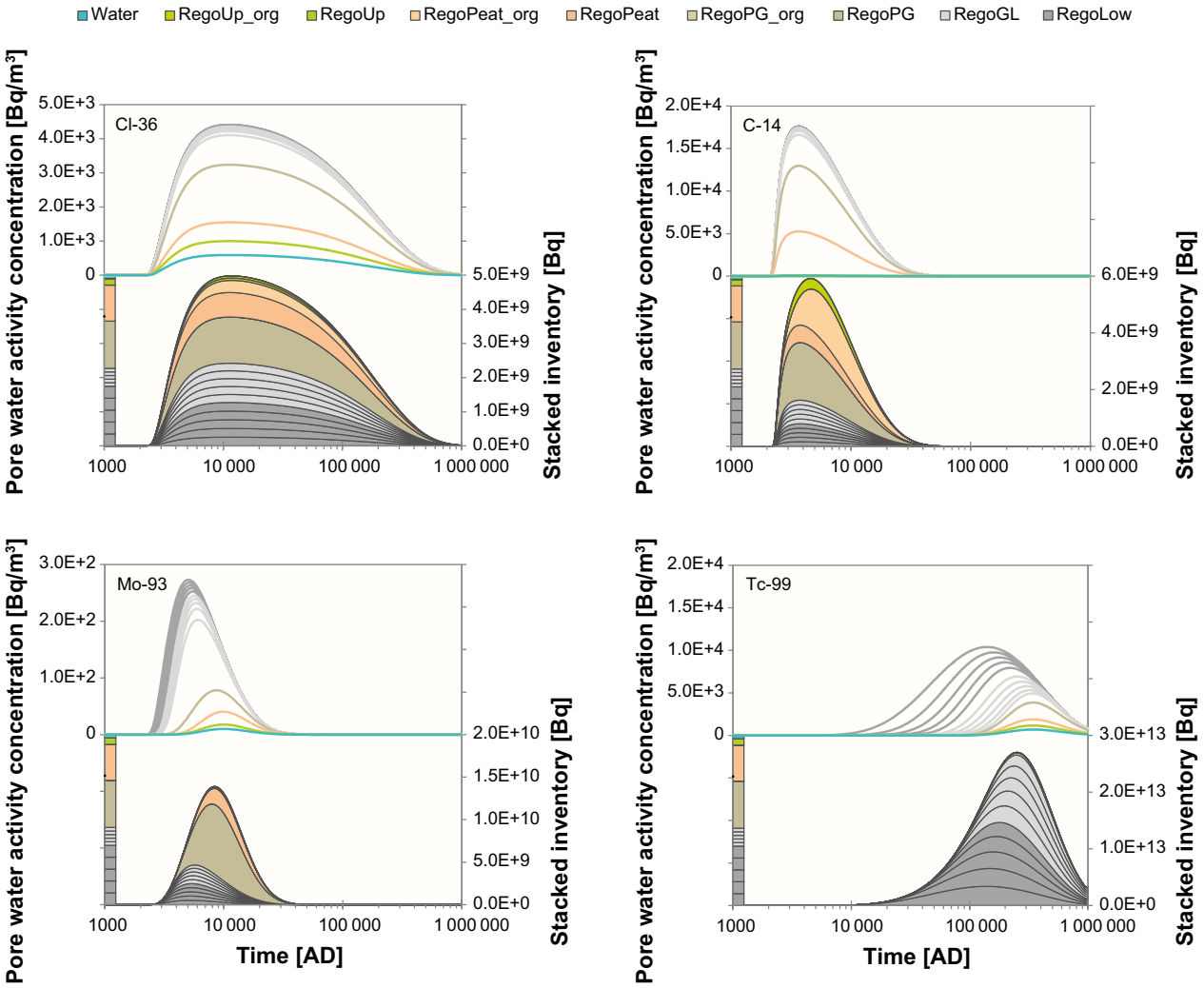

Figure 5-20. *The activity concentration in pore water (lines, left y-axis) and the stacked total activity (bottom of each panel, right y-axis) in regolith layers of a mature mire ecosystem in object 206 for release from BHA. The stacked bar in the column on the left shows the relative regolith layer thickness. Note that the two lowest regolith layers (RegoLow and RegoGL) have been divided into five separate sub-layers. Figure from Biosphere synthesis.*

Some radionuclides contribute marginally (Ca-41 and Ni-59) or practically not at all (Ag-108m) to the total dose despite their relatively high annual release from the geosphere (Figure 5-21). Moreover, among the radionuclides that contribute most to dose (e.g. C-14, Mo-93, Cl-36 and Tc-99), the dose consequences for a given activity release vary by almost three orders of magnitude. The main biosphere processes that influence the relationship between geosphere release and dose from ingestion of crops are: retention and decay, accumulation in peat, leaching from cultivated soil, plant uptake, and the radiotoxicity.

In Figure 5-22, the relative influence of these processes is shown for radionuclides with an annual geosphere release exceeding 10 000 Bq. For example, while the proportion of the release that decays during the transport through the regolith layers is similar for Ca-41 and Mo-93, molybdenum accumulates much more effectively in peat. The leaching rate from the cultivated soil is similar for the two radionuclides, as is the availability for uptake by plants. However, the radiotoxicity of Mo-93 is significantly higher. Together these factors result in the dose being about two orders of magnitude larger for Mo-93 than Ca-41, given an identical geosphere release (Figure 5-21).

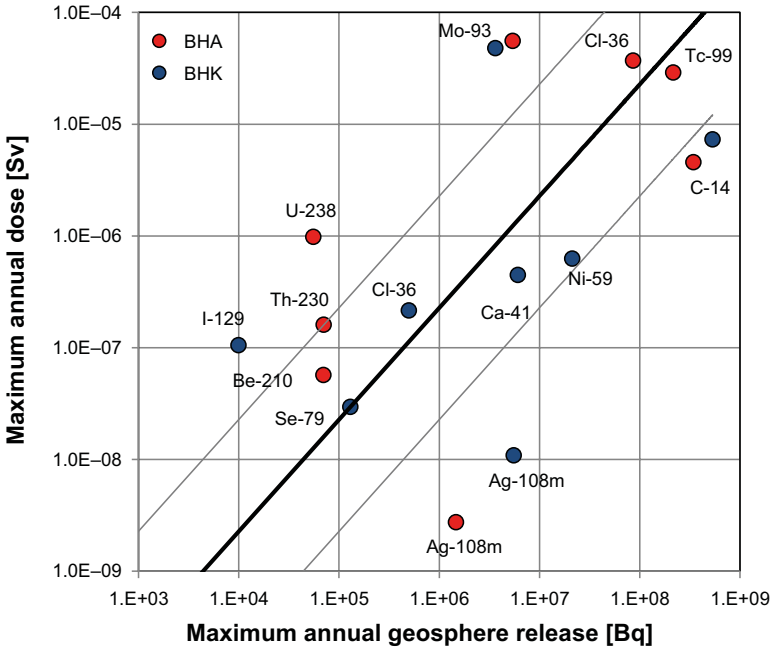

Figure 5-21. *Maximum annual dose as a function of maximum annual release from the geosphere. All displayed radionuclides have a maximum annual release of at least 10^4 Bq from either BHA (red) or BHK (blue). Decay-product radionuclides with a dose which primarily reflects the release or accumulation of the parent radionuclide (rather than the release of the decay product itself) have been excluded from the graph for clarity (Ra-226, Po-210, Pb-210, Pu-239 and Nb-93m). The line represents the median relationship between the maximum dose and the maximum release (2×10^{-13} Sv/Bq) and the grey lines show 10:1 and 1:10 ratios of this relationship.*

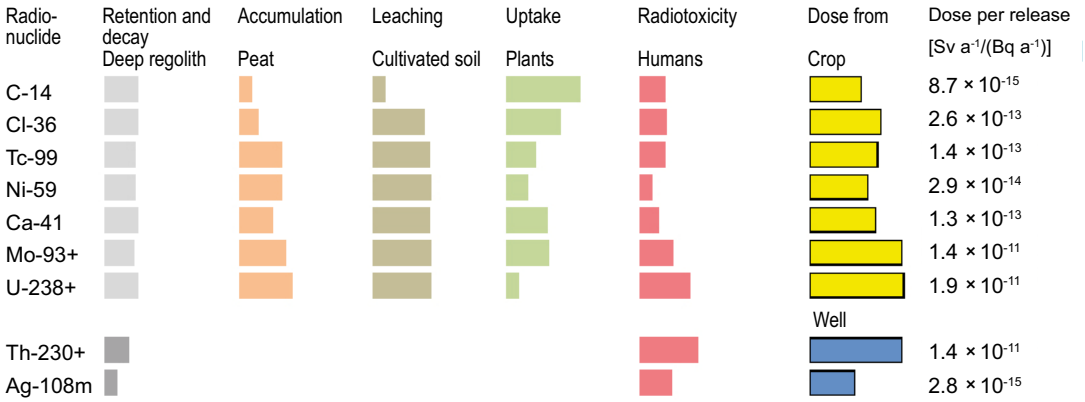

Figure 5-22. *The influence of radionuclide properties on the dose for the dominating exposure pathway from a unit release. Coloured bars without contours represent the relative importance on dose of various processes: retention and decay in deep regolith (a longer bar means less decay), accumulation in peat, leaching in cultivated soil (a longer bar means less leaching), plant uptake, and radiotoxicity in humans. Properties are scaled so that the length of the bars corresponds to an additive positive dose response (on a logarithmic scale). Radionuclides are organised according to the major pathway of exposure; ingestion of crops (yellow, upper) and ingestion of drinking water from a dug well (blue, lower). Note that the effects of the first two processes: retention and decay and accumulation, result from the interaction between radionuclide-specific properties and object-specific properties, whereas the three remaining properties are primarily driven by radionuclide-specific properties. Plus sign (+) indicates that the dose includes the contribution of decay products.*

Retention and decay have a strong effect on the dose-release relationship and radionuclides that are strongly sorbing relative to their half-life may never reach the surface of the biosphere. Thus, less than a few percent of the geosphere release of Th-230 and Ag-108m escapes the lowest regolith layer, and consequently exposure from well water is the only significant exposure pathway. However, the combined effect of smaller losses due to radioactive decay, higher toxicity, and the contribution of toxic decay products (Ra-226, Pb-210 and Po-210), makes the dose from Th-230 almost four orders of magnitude higher than that from Ag-108m given an equivalent geosphere release.

Although all five processes contribute to the dose-release response to some extent, accumulation in peat (K_d), plant uptake (CR or equivalent) and radiotoxicity (including ingrowth of radioactive decay products during 50 years of cultivation) are the three factors that explain most of the variation of the relation between release and dose between the radionuclides that reach the peat layer in biosphere object 206. Excluding C-14, which differs from the other radionuclides both in transport properties and uptake mechanisms, the effects of peat accumulation, plant uptake and toxicity all vary by approximately three orders of magnitude. However, plant uptake tends to be negatively correlated to the strength of sorption, and the total variation in the dose-release response (again excluding C-14) in the examined radionuclides is below three orders of magnitude.

Retention and decay depend on the properties of the object, and in objects with a thin peat layer accumulation in post-glacial sediments (and occasionally even in glacial clay) may be relevant for the initial activity in the cultivated soil. Thus, the differences between radionuclides with respect to these two properties are specific to biosphere object 206. The sensitivity of retention, decay and accumulation in layers exposed by drainage to object properties are examined in the *discharge area evaluation case*.

5.2.11 Conclusions

The *present-day evaluation case* constitutes the intentionally simplified base case for the radionuclide transport and dose calculations in SE-SFL. It assumes that present-day conditions prevail in the bedrock and biosphere throughout the entire analysis period of 1 million years after repository closure. This evaluation case is based on the base variant of the reference evolution, which describes the future evolution of the repository and its environs under the assumption that the repository is located at the example location in Laxemar, and that the repository is designed in accordance with the proposed repository concept. Further, material properties for the repository components are taken from previous safety assessments, e.g. bentonite similar to that planned for the buffer in the Spent Fuel Repository is assumed for BHA backfill and concrete similar to the construction concrete employed in the existing SFR repository is assumed for BHK backfill.

Retention in the near-field model

The total annual near-field activity release from BHA and BHK is dominated by the radionuclides that dominate the initial (available) inventory and have half-lives longer than a few thousand years, i.e. Tc-99, C-14 and Cl-36 from BHA (Figure 5-7) and C-14 and Ni-59 from BHK (Figure 5-10). Several radionuclides that contribute significantly to the initial inventories of BHA (Figure 5-6) and BHK (Figure 5-9), e.g. Ni-63, do not contribute significantly to the release, due to their short half-lives and strong sorption onto cement and bentonite in the near-field.

The activity release from the near-field for a specific radionuclide is determined by the radionuclide half-life, sorption onto cement in the grouted waste and onto bentonite (BHA) or concrete (BHK) in the backfill. The near-field release from BHA is further influenced by the weakened sorption onto cement and bentonite due to complexing agents, and the charge-dependent effective diffusivity in bentonite. In BHK, two additional factors that significantly affect the near-field release are the slow release by corrosion and the fraction of radionuclides that is instantly available for transport.

The importance of radioactive decay, release by corrosion (BHK) and transport from the waste vaults for the fraction of the initial inventory released from the waste vault can be illustrated using a steady-state solution of the radionuclide transport model for the waste vaults (Figure 5-23). A hypothetical residence time (T_{res}) is estimated, assuming no radioactive decay, as the total inventory in the vault divided by the annual release. In order to evaluate the advective and diffusive transport separately, the advective and diffusive residence times are calculated by setting the diffusivity or flow of water to zero when calculating the steady-state solution.

For BHA the release of a non-decaying species is determined by the residence time T_{res} and $T_{res} \times \ln(2)$ is an estimate for the time it would take to transport half of the initial inventory out of the vault.

For BHK the release of a non-decaying species is determined by the corrosion rate if the time it takes to corrode a metallic waste component T_{corr} is larger than the residence time. In this case half of the inventory will be transported out of the vault after half of the corrosion time has passed. If the corrosion time is smaller than the residence time $T_{res} \times \ln(2)$ is an estimate for the time it would take to transport half of the initial inventory out of the vault. Note that the metallic waste components have been separated into three fractions with three different corrosion times.

Similar estimates can be made of the fraction of radionuclides that will decay within a vault and how much activity that will be transferred to the geosphere.

In order to estimate the relative activity that will be transferred from BHA to the geosphere one can consider two limiting cases, the residence time is much larger than the half-life $T_{½}$ and the residence time is much smaller than the half-life. The relative activity transferred is approximately $T_{½}/(T_{res} \times \ln(2))$ and $1 - T_{res} \times \ln(2)/T_{½}$ respectively.

In order to estimate the relative activity that will be transferred from BHK to the geosphere one can consider three limiting cases:

- The corrosion time is much larger than the residence time and the half-life is much larger than the corrosion time, the relative activity transferred is approximately $1 - T_{corr} \times \ln(2)/T_{½}$. In this case most of the activity is released, this would be the case for Cl-36.
- The corrosion time is much larger than the residence time and the half-life is much smaller than the corrosion time, the relative activity transferred is approximately $T_{½}/(T_{corr} \times \ln(2))$. In this case most of the nuclides decay within the metallic waste, this would be the case for C-14.
- The corrosion time is much smaller than the residence time and the half-life is much smaller than the residence time, the relative activity transferred is approximately $T_{½}/(T_{res} \times \ln(2))$. In this case most of the activity decays within the buffer, this would be the case for Tc-99 and Ni-59.

For BHK a possible fourth case applicable for Mo-93 is when the half-life is smaller than both the residence time and the corrosion time. In this case the nuclides will decay both within the metallic waste and the buffer.

Figure 5-24 shows the accumulated relative activity for five important radionuclides in each repository system component from waste to biosphere. For the non-sorbing C-14, the total effect of retention in the near-field is similar in BHA and BHK, with about 98 % of the initial inventory retained in the BHK near-field as compared to about 93 % in BHA (Figure 5-24). However, retention is achieved

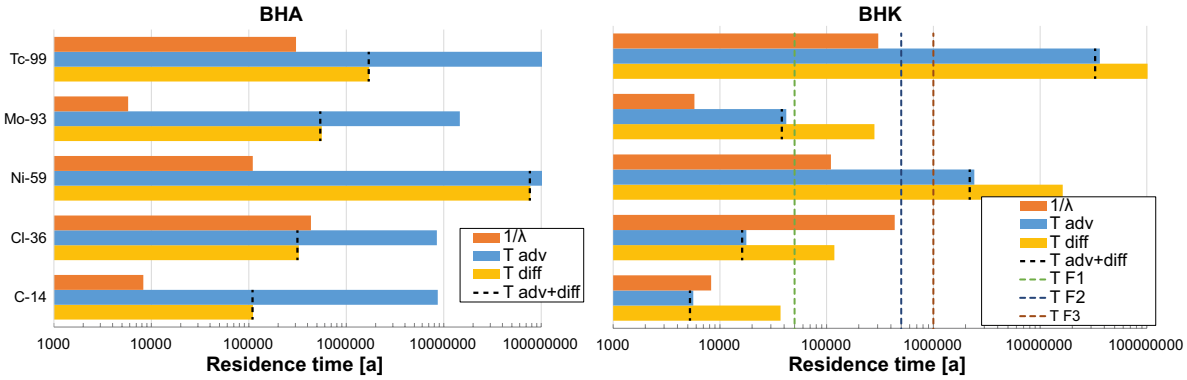

Figure 5-23. *Timescales associated with the processes that together determine the fraction of the initial inventory of a radionuclide that is released from the waste vault. Radioactive decay is represented by the half-life (orange bars). Advective (blue bars) and diffusive (yellow bars) transport is represented by the time it would take to transport half of the initial inventory out of the vault, assuming no radioactive decay. The release by corrosion in BHK is represented by the corrosion time, i.e. the time it takes to completely corrode the components in the fractions F1 (dashed green line), F2 (dashed blue line) and F3 (dashed red line). Note that 1/λ is shown, whereas the half-life* $T_{1/2} = \ln(2)/\lambda$.

from different mechanisms. In BHA, the advective transport is effectively hindered by the bentonite barrier, leading to slow diffusive transport that significantly reduces the activity through radioactive decay; the residence time for C-14 in the vault is more than one order of magnitude larger than its half-life (Figure 5-23 left panel). In BHK, the near-field retention is mainly due to radioactive decay before the activity is released from the metal by corrosion; only 4 % of the total initial C-14 inventory ever becomes available for release from the near-field since even the thinnest fraction F1 of the metallic waste in BHK has a corrosion time approximately one order of magnitude longer than the half-life of C-14 (Figure 5-23 right panel). The fraction of a radionuclide released from a metallic component in BHK can be estimated from the ratio between the half-life and the corrosion time, i.e. it will differ between waste fractions with different corrosion times. Retention in the grout is similar in BHK and BHA, where the activity is nearly halved when released from the grouted waste. In BHK, retention in the concrete backfill is limited since the advective transport is relatively fast; the residence time for C-14 in the concrete is shorter than its half-life.

Compared with C-14, retention is more efficient for Mo-93 because of its low but non-zero K_d in cement and its somewhat shorter half-life (Table 5-1). In BHA, Mo-93 decays significantly in the bentonite backfill due to the slow diffusive transport (Figure 5-24). The residence time of Mo-93 BHA is approximately two orders of magnitude larger than its half-life. In BHK, radioactive decay before release from the metal by corrosion and decay in the concrete grout and backfill reduces the Mo-93 activity to a similar extent (Figure 5-24). Both the corrosion time and the residence time are substantially larger than its half-life.

Ni-59 has a significantly longer half-life than C-14 and Mo-93 and relatively high K_d for cement and bentonite. This, in combination with to the slow diffusive near-field transport, yields very strong retention in BHA and activity decay by three orders of magnitude in the bentonite backfill (Figure 5-23 left panel). The residence time for Ni-59 in BHA is approximately three orders of magnitude larger than its half-life (Figure 5-24 left panel). Retardation of Ni-59 by sorption is effective also in BHK, which results in a near-field activity release that is significantly reduced (Figure 5-23 right panel) and occurs later compared with Mo-93 and C-14 (Figure 5-10). That is, decay in the metal and decay during sorption onto cement in the grout, reduces the accumulated activity release by about two thirds in each step. Further, decay due to sorption in the concrete backfill reduces the activity released from the grouted waste by more than an order of magnitude, illustrated by a residence time for Ni-59 in BHK that is more than one order of magnitude larger than its half-life (Figure 5-24).

Of the radionuclides that contribute substantially to the near-field release and dose, retention is least efficient for the long-lived and non-sorbing Cl-36 (Figure 5-23 left panel). Only about 40 % of the initial inventory is retained in the near-field, and the retention is similarly poor in the two waste vaults (Figure 5-23 right panel). However, the absolute release of Cl-36 is relatively low due to a smaller initial inventory compared with several other radionuclides. The maximum annual release from BHK is about two orders of magnitude lower than from BHA (compare Figure 5-7 and Figure 5-10), a direct reflection of the differences in initial inventory size.

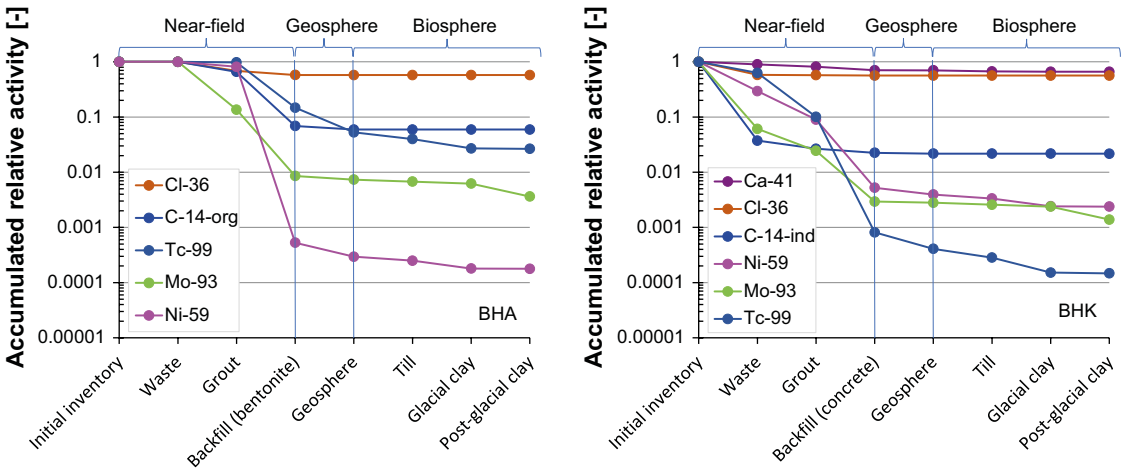

Figure 5-24. *Relative activity transferred along the way from the initial inventory in BHA (left panel) and BHK (right panel) to the biosphere, accumulated over the entire analysis period of one million years.*

For Tc-99, with a similar half-life as Cl-36 (Table 5-1), retention in the BHA and BHK near-fields are stronger than for Cl-36 due to sorption. Tc-99 sorbs strongly also onto bentonite, however sorption in BHA is assumed to be severely weakened (by a factor of 10 000) due to complexing agents. Therefore, Tc-99 retention in the backfill is significantly stronger in BHK than in BHA (Figure 5-23). As a result, the residence time for Tc-99 is 8 000 ka for BHA and 160 000 ka for BHK (Figure 5-24).

The slow release by corrosion that is represented in the BHK near-field model significantly reduces the annual near-field activity releases compared with an instantly available source. If the total initial inventory in BHK were to be available for transport at closure, a two orders of magnitude higher maximum annual release for the non-sorbing C-14 would be observed (data not shown). For strongly sorbing radionuclides, the effect of slow release due to corrosion is less important since the residence time becomes larger than the corrosion time. Thus, assuming that all Ni-59 is available for instant release would only elevate the maximum annual release by a factor of three as compared with the base case (data not shown).

Retention in the geosphere model

The release from the geosphere is modified compared to the near-field release due to dispersion, sorption, and decay during the transport through the geosphere. Radioactive decay significantly reduces the geosphere releases of radionuclides with a short half-life in comparison with the travel time through the geosphere (e.g. H-3 and Sr-90), and those with the potential for sorption in the rock matrix (e.g. Ag-108m and several Pu isotopes). The geosphere release of Tc-99, which has a relatively long half-life, is reduced by a factor of between two and three (Figure 5-23) due to the combined effect of retardation and radioactive decay in the rock matrix. On the other hand, the effect of geosphere transport on the release of mobile radionuclides with a half-life of a few thousand years (C-14 and Mo-93) is limited, and for Cl-36 the reduction in the releases as a consequence of geosphere transport and decay is even less important (Figure 5-23).

The release to the surface is the result of transport along more than two thousand flow pathways, and retention and decay may differ significantly between pathways. The characteristics of the flow pathways from BHA and BHK largely overlap. However, all five DFN realisations performed for SE-SFL by Joyce et al. (2019) consistently show an elevated frequency of pathways with longer travel times for BHA than for BHK, as well as an elevated frequency of pathways in thinner fractures. Consequently, there is a noticeable difference in the potential for release of sorbing radionuclides (Ni-59, Tc-99 and Ag-108m) from the two positions, where the reduction of activity through decay in the geosphere is greater for BHA (Figure 5-23). The release of non-sorbing radionuclides (C-14, Mo-93 and Cl-36) is, however, relatively insensitive to variation in flow pathways, and the difference in release between the two positions is consequently marginal.

Taken together, retention and decay in the geosphere in the base case have a marginal effect on the release of non-sorbing radionuclides, and the effect on long-lived sorbing radionuclides is higher but still limited. The relatively large contribution of C-14, Cl-36 and Mo-93 to the geosphere release (and dose) from the repository highlights the importance of retardation in the near-field also of non-sorbing radionuclides for the overall performance of the repository (Figure 5-23).

Annual doses and retention in the biosphere model

The total annual dose from each waste vault is within an order of magnitude of the dose corresponding to the regulatory risk criterion of 14 μSv in *the present-day evaluation case*. The annual doses from several individual radionuclides are within an order of magnitude of this limit: C-14 and Mo-93 for both vaults and Tc-99, Cl-36 and the uranium series for BHA (Figure 5-18). Draining and cultivation of a mire in the discharge area is the land use that causes the highest dose. This is primarily because radionuclides can accumulate in peat over a long period of time prior to exposure, and because the dose-contributing radionuclides predominantly yield dose through ingestion of food.

The temporal dynamics of nuclide-specific doses is primarily driven by the release from the geosphere, as reflected by similarly shaped curves in Figures 5-12 and 5-18. However, the variation in annual dose for a given release spans more than three orders of magnitude for nuclides that are released in substantial amounts to the surface, where e.g. Mo-93 gives large doses relative to its activity release compared

with e.g. Ni-59 (Figure 5-21 and 5-22). The mechanisms behind the nuclide-specific behaviour in the biosphere system and the dose response can be divided into five factors; retention and decay, accumulation, leaching from cultivated soil, plant uptake, and radiotoxicity.

Radionuclide retardation (sorption) and decay in the regolith influence the timing and the fraction of the geosphere release that reaches the upper part of the regolith profile. Several environmental factors affect retardation. However, sorption in the lower part of the regolith profile is a key property, and radionuclides that display strong sorption relative to their rate of radioactive decay, will not reach the surface in noticeable amounts. Sorption properties in the upper section of the regolith profile determine the potential for accumulation in regolith that may be exposed by drainage. Moreover, sorption in the drained soil determines the rate of leaching, which decreases the soil activity during cultivation. Plant uptake is assumed to be proportional to soil concentrations, but the proportionality constant varies between radionuclides. Finally, the dose that is caused by a given intake of activity is determined by how a radionuclide is metabolised and by the type and energy of its ionising radiation, both contributing to its radiotoxicity.

All these factors vary by several orders of magnitude among radionuclides that have a substantial geosphere release, as reflected by a large spread in the relationship between the geosphere releases and the annual doses in Figure 5-21 and 5-22. In the biosphere modelling, leaching from cultivated soil, plant uptake, and toxicity are properties that are assumed to be marginally affected by conditions in the discharge area, and patterns from present-day calculations can in this sense be viewed as valid for a broad range of environmental conditions. Conversely, decay due to retention and accumulation depends on the properties of the discharge area, e.g. size of object, soil depth and groundwater discharge. Thus, the reported trends between radionuclides cannot easily be generalised to other discharge areas. The sensitivity of retardation, decay and accumulation in layers exposed by drainage to variations in object properties are examined in the *discharge area evaluation case*.

5.3 Increased greenhouse effect evaluation case

The *increased greenhouse effect evaluation case* is designed to analyse post-closure safety for the *increased greenhouse effect variant* of the SE-SFL reference evolution (Section 6.3 in the **Main report**). The increased greenhouse effect evaluation case illustrates the effects of this specific change in external conditions on post-closure safety. External conditions due to an increased greenhouse effect are derived from temperature and precipitation changes expected according to IPCC's intermediate emissions scenario RCP4.5. During the growing season, discharge and runoff may be reduced in a warmer climate (**Main report**, Section 6.3.5) and the water deficit for crops is expected to increase. On an annual basis, the geosphere and near-field conditions are, however, not expected to be affected by the increased greenhouse effect in a way that significantly affects repository performance. Dose consequences of a warmer climate are thus evaluated in biosphere object 206, by adjusting the atmospheric concentration of CO_2 and by modifying the discharge rate of ground- and surface-water. Two variants of this case are evaluated; in the first, crop water deficit is covered by an increased uptake of groundwater through capillary rise, whereas in the second variant it is covered by irrigation with surface water.

5.3.1 External conditions

The climate is assumed to be temperate throughout the assessment period, but during the first 23 000 years, climate conditions are warmer than at present. After this initial period, the climate returns instantaneously to present-day conditions, which then prevail for the remaining part of the assessment period of 10^6 years. The warmer climate case corresponds to an intermediate emission scenario in which the atmospheric CO_2 concentration stabilises at 543 ppm. The elevated CO_2 level is expected to cause an increase in mean annual temperature and annual precipitation, resulting in values that are 2.6 °C and 12 % higher than present conditions. Taking the projected change in near-surface temperature and precipitation during the vegetation season (June−August), the present conditions in western Poland are identified as a reasonable regional analogue to the climate conditions projected to Laxemar in this evaluation case (**Climate report**).

5.3.2 Handling in the near-field and geosphere models

The properties of the engineered barriers are assumed to develop as described in *the present-day evaluation case*. The warmer climate is not expected to cause any additional chemical, thermal, or mechanical effects on the structural integrity of the waste vaults or significantly affect the transport times in the near-field and the geosphere. Thus, the pattern and magnitude of groundwater flow in the bedrock and repository from the present-day calculations are used also in this evaluation case. However, the response to changes in climate of the groundwater circulation near the surface and associated recharge and discharge are considered in the calculations (see below).

5.3.3 Handling in the biosphere model

Radionuclides from the repository are discharged to the same biosphere object as in the *present-day evaluation case*, namely biosphere object 206. Although the annual precipitation is assumed to increase, the discharge of groundwater is expected to decrease in a warmer climate (see Surface Hydrology below).

Landscape development

As in *the present-day case*, landscape development is not considered. That is, the geometry and stratigraphy of the discharge area does not change, and no biological succession is accounted for during the entire assessment period of 1 million years. Dose consequences are examined in two variants of the biosphere object, namely a continuously cultivated field and a mire ecosystem, both located in the original lake basin.

Surface Hydrology

An increased greenhouse effect is expected to result in a decrease of groundwater discharge from the bedrock (−8.3 %), and in a lower runoff (−20 %) (Losjö et al. 1999, Grolander and Jaeschke 2019). These changes are projected to propagate through the regolith profile. Thus, the discharge through the lower regolith profile (RegoLow, RegoGL and RegoPG) is expected to decrease by approximately 10 %, whereas the reduction of discharge in the upper peat of the mire is expected to be similar to that of the net precipitation and runoff, i.e. −18 % (Figure 5-25, details in Grolander and Jaeschke 2019).

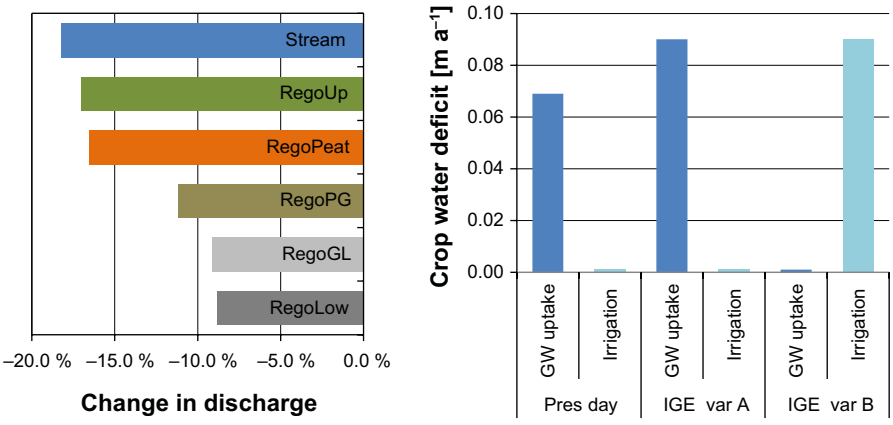

Figure 5-25. *Parameters describing hydrology and water uptake in the increased greenhouse effect evaluation case. Left: Change in groundwater discharge in the undisturbed mire ecosystem relative to present-day conditions. Right: Water deficit of crops (cereal, potato and fodder) and type of water sources covering the deficit in present-day conditions, and in the two variants of warmer climate. Short bars represent a value of zero.*

Exposed population

The land-use variants from the *present-day evaluation case* are used also in this evaluation case. That is, a family farm is used to evaluate exposure from the permanently cultivated land (Agr), and the potential exposures from a mire ecosystem are evaluated for the exposed groups: hunter-gatherers (HG), infield–outland farmers (IO), a household with a garden-plot (GP), and a family farm cultivating the drained mire (DM).

Ecosystem

In a warmer climate (where increased precipitation does not compensate for higher evapotranspiration), the plant water deficit during the vegetation period will increase. The increased demand for water can either fully or partly be supplied by an increased groundwater uptake through capillary rise, and/or it can be covered by irrigation. Using western Poland and a dry year in southern Sweden as reasonable climate analogues, the water deficit is projected to increase by 30 % (Grolander and Jaeschke 2019). Moreover, it is conservatively assumed that the deficit is fully compensated by radionuclide-containing water, either from groundwater (variant A) or from irrigation with surface water (variant B) (Figure 5-25).

Large-scale irrigation of cereal and fodder production is not practiced in Laxemar under present climatic conditions. Adding large-scale irrigation as an exposure pathway to family farming (DM and Agr) thus has required definition of new parameters describing the practice (Grolander and Jaeschke 2019). Moreover, the processes for accumulation on leaves and edible parts of crop, element translocation (cereals and potatoes) and leaf weathering (fodder) have been added to the models describing agriculture in warmer conditions (Chapter 8 in the **Biosphere synthesis**). Finally, the concentration of stable CO_2 in the atmosphere is elevated (543 ppm) in both variants, and the amounts and frequency of irrigation of a garden plot (GP) are adjusted to reflect warmer conditions.

5.3.4 Annual doses

Increased greenhouse conditions result in an increase of the maximum dose both from BHA (24 %) and from BHK (11 %), when the crop-water deficit is covered by groundwater uptake. In this case just like in the present-day case, the dose resulting from draining and cultivating the mire (DM) is considerably higher than that which results from continuous cultivation of the biosphere object (Agr) (Figure 5-26) and, than that from all other land-use variants (data not shown). In the DM variant, cultivation is preceded by a mire stage with lower groundwater flows. If the crop water deficit during the vegetation season is covered by irrigation water rather than groundwater uptake, the resulting dose is generally lower, and the lowest doses result from continuous irrigation on the permanently cultivated land (Agr). The annual dose returns to the level of the *present-day evaluation case* when the external conditions returns to present day levels in all examined calculation variants.

The elevated maximum dose in the *increased greenhouse effect case* is primarily due to an increased accumulation of Cl-36 in peat (prior to cultivation) in combination with an increased groundwater uptake of Cl-36 during cultivation of the drained mire. For both mechanisms, it is the lower discharge in the warmer climate that leads to less groundwater dilution of Cl-36, which in turn leads to increased radionuclide concentrations in groundwater. The accumulation of Mo-93 is marginally affected by changes in groundwater flows, < 10 % increase of the annual dose. The primary source for Mo-93 in the cultivated soil is the activity accumulated in mire peat. However, the groundwater activity of Mo-93 is reduced by radioactive decay, and the reduction becomes greater with decreasing groundwater flow due to an extended transit time. Thus, the effect of a decreased dilution is partly counteracted by a decrease in the amount of the activity that reaches the peat. Consequently, the effects of a warmer climate decreases when Mo-93 contributes to the annual dose, and when Mo-93 is the dominating species, the maximum dose from increased greenhouse conditions differs little from that in present-day conditions (the DM variant for BHK in Figure 5-26).

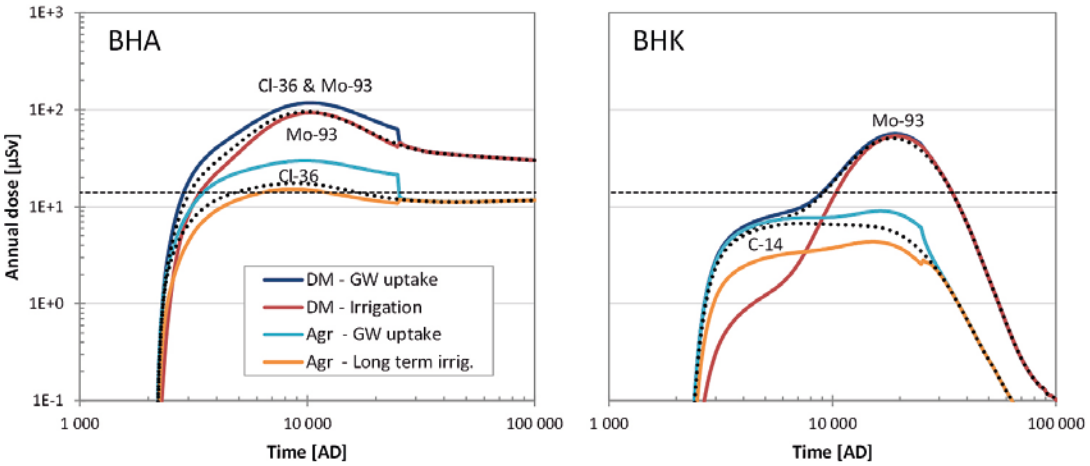

Figure 5-26. *Annual dose for release from BHA (left) and BHK (right) in the increased greenhouse effect evaluation case. Two land-use variants are examined: draining and cultivating a mire (DM) and continuous cultivation (Agr). The crop water deficit is either covered by groundwater (GW, variant A) or by irrigation (variant B). Dose in the present-day evaluation case is shown for reference (black dotted lines). Note that external conditions return to present day characteristics at 26 000 years after repository closure, and that the time axis has been truncated at 100 000 AD.*

The effect of irrigation is evaluated using stream water to cover the crop water deficit. This is reasonable because stream water is generated locally and readily available in the discharge area. As stream water is diluted with the runoff generated in the catchment, the dilution is more than a factor three larger than in groundwater available for plant uptake, i.e. pore-water in the saturated regolith layer below the drained soil. The effect of surface water dilution can clearly be seen when calculation variants of continuous cultivation are compared (light blue and orange lines for Agr in Figure 5-26), as accumulation in peat does not influence the results. Thus, when the plant water deficit is covered by irrigation water the annual dose is consistently clearly lower than when the deficit is covered by groundwater uptake, irrespective of which radionuclides are contributing to the dose. However, the observed dose difference is smaller than the concentration difference between surface- and groundwater because irrigation water reaches the biologically active layer directly whereas a fraction of radionuclides taken up through capillary rise will be lost through percolation and drainage before reaching the uppermost soil layer.

In SFL, leaf interception also contributes to the radionuclide concentration of the irrigated crop. Approximately 6 % of radionuclides intercepted on cereal and potato leaves are translocated to edible parts, and most of the intercepted radionuclides on fodder remain at harvest. However, the storage capacity of leaves is limited to 1−2 mm of 45 mm irrigation water per event, and the contribution of intercepted radionuclides is negligible (< 1 %) or marginal (< 5 %) for plant concentrations of Cl-36 and Mo-93, as compared with the contribution of root uptake. For C-14 the contribution from interception is also negligible, as CO_2 in a thin water film will equilibrate with the atmosphere within minutes and the intercepted C-14 will be lost to the atmosphere (Saetre et al. 2013).

5.3.5 Conclusions

The *increased greenhouse effect evaluation case* shows that the combination of a decrease in groundwater discharge and an increase in plant water demand may increase the annual dose from some radionuclides. However, the changes in external conditions are unlikely to result in an annual dose that is substantially higher than that calculated for present-day conditions. The largest effects may be expected for weakly sorbing radionuclides; for example, the dose from Cl-36 may be increased by 50 %. However, this is not true for C-14, since dilution caused by increased atmospheric concentrations of stable CO_2 will counteract the effect from an increased groundwater concentration. The effects of a warmer climate on radionuclides for which transport and accumulation are quantitatively affected by radioactive decay, such as Mo-93 is also expected to be less pronounced. This is because a decrease in groundwater flow will decrease the release of radionuclides discharged to upper regolith

layers. The effects of a warmer climate on radionuclide accumulation may be reversed if irrigation is assumed to cover the crop water deficit since irrigation causes smaller crop activities compared with those resulting from plant root uptake, at least for the dose-contributing radionuclides examined.

5.4 Simplified glacial cycle evaluation case

The *simplified glacial cycle evaluation case* is designed to analyse post-closure safety for the *simplified glacial cycle variant* of the SE-SFL reference evolution (Section 6.4 in the **Main report**). This variant is included in the analysis with the aim of covering the colder end of the range within which future climate may vary. Moreover, it facilitates evaluation of the importance for post-closure safety of periglacial, glacial, and submerged conditions, and the transitions between these states.

5.4.1 External conditions

The development of external conditions in the *simplified glacial cycle variant* of the SE-SFL reference evolution is based on the *simplified glacial cycle climate case* of the **Climate report**. The *simplified glacial cycle climate case* describes the overall climate development in the reconstruction of the last glacial-interglacial cycle, analysed in previous safety assessments, e.g. in SR-Site (SKB 2010e, 2011a), for more details see Sections 4.1 and 4.3 of the **Climate report.** An early periglacial period at around 19 000 AD, in agreement with the *early periglacial climate case* in SR-PSU (SKB 2014f), is combined with a simplified glacial cycle similar to that evaluated in the *glaciation and post-glacial conditions scenario* in SR-PSU (SKB 2015a). The sequence of events from 2000 AD to 102 000 AD is illustrated in Figure 5-27. In the *simplified glacial cycle evaluation case*, the sequence of climate domains from 2000 AD to 102 000 AD is repeated every 100 000 years until one million years after repository closure to represent the effects of repeated Late Quaternary glacial-interglacial cycles.

Periods of periglacial climate conditions

In the *simplified glacial cycle evaluation case,* permafrost is assumed to appear and then develop to a continuous cover at the repository site over the first 100 years of the periglacial periods. In accordance with the main assumptions of SE-SFL (**Climate report**, Section 1.1), the repository is located below the maximum permafrost depth. During this transition, a talik is assumed to have formed under a lake downstream of the repository, such that the release of radionuclides from the repository can occur in the talik. The transition from the periglacial to the temperate climate domain at 20 500 AD is assumed to occur over the last 100 years of the periglacial period. For the second periglacial period that ends at 57 000 AD, the permafrost is assumed to decay over the initial 100 years of the period of glacial climate domain. This is in line with the notion that permafrost may melt under insulating warm-based ice-sheet conditions (see e.g. Section in 4.5.3 in SKB 2010e). Thus, sub-glacial permafrost is assumed to prevail for 100 years until the conditions at the ice-sheet bed turn from cold-based to warm-based (**Climate report**, Sections 4.3 and 4.4).

The durations of the transitions between the temperate, periglacial and glacial climate domains in this climate case are based on previous studies (**Climate report**, Chapter 2).

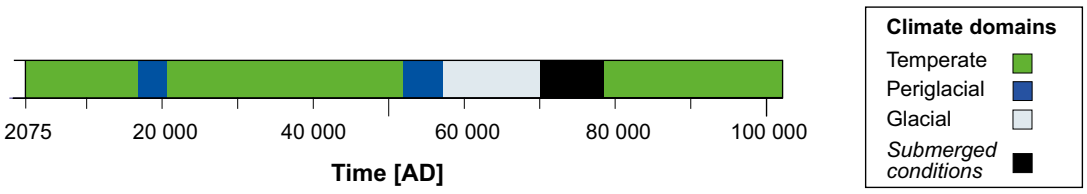

Figure 5-27. *The climate development at Laxemar in the first 100 000 years of the simplified glacial cycle climate case, shown as a succession of climate domains and submerged periods. Adapted from Figure 4-3 in the Climate report.*

Post-glacial transition from submerged to terrestrial conditions

For the post-glacial period, the shoreline displacement is assumed to be identical to the one reconstructed for Laxemar from around 10 000 BC, when the surface above the repository location was submerged, until the ongoing post-glacial shoreline regression will be complete in around 30 000 years (**Climate report**, Section 3.2 and Appendix B). The surface above the repository is presently located at an average elevation of 21.5 m above mean sea level and became terrestrial, according to the reconstruction, around 8800 BC. In the *simplified glacial cycle evaluation case*, this occurs at 74 000 AD in the first cycle. Biosphere object 206 is at present located at an altitude of 12.3 m above mean sea level and it became isolated as a lake at 4100 BC. In the *simplified glacial cycle evaluation case*, this occurs at 78 700 AD in the first cycle.

5.4.2 Handling in the near-field and geosphere model

The properties of the engineered barriers in SFL are assumed to develop in the same way as in the *present-day evaluation case*. In the *simplified glacial cycle variant* of the reference evolution, described in Section 5.4 of the **Main report**, potential effects of the colder climate on chemical, thermal and mechanical effects are discussed. However, for simplicity, the same chemical, thermal, and mechanical effects on the structural integrity of the waste vaults are assumed as in the *present-day evaluation case*. The changes in the external conditions in this evaluation case are assumed to influence the rate of groundwater flow in the repository and the geosphere, but to have no effect on the pattern of the flow field and thus the length of the flow pathways.

The groundwater flow rate is expressed relative to the groundwater flow rate in the *present-day evaluation case*. Previous studies performed for the reconstructed glacial period for the Spent Fuel Repository in Laxemar (Vidstrand et al. 2010a) and Forsmark (Vidstrand et al. 2013, 2014a) and for the extended SFR in Forsmark (Odén et al. 2014) were used to estimate the groundwater flow for various parts of the glacial period. The relative effects of shoreline displacement, and ice-sheet advance and retreat, on groundwater flow rate were summarised in a scaling factor (Figure 5-28, and Section 6.4.5 in the **Main report**).

Thus, in the near-field model, the total flow of water through the waste $Q_{\text{advective}}$ is multiplied by the scaling factor. The capacity of groundwater to carry away radionuclides at the outer backfill boundary, Q_{eq}, is less affected by changes in hydrogeology than $Q_{\text{advective}}$ and is thus scaled by the square-root of the same factor for BHA and during the intact-concrete period for BHK. However, during the interval when the BHK barrier is partially degraded, the total equivalent flow rate represents the groundwater flow in the degraded part of the backfill rather than the total groundwater flow in the bedrock fractures. Therefore, Q_{eq} is scaled by the original (non-square-rooted) scaling factor. Similarly, the total advective travel time t_w [a] for a water particle, and the sum of the flow-related transport resistances F [a m^{-1}], were scaled by division by this factor when used in the geosphere model. The derivation of the scaling factors for the different climate periods is discussed in Appendix C. For discussion on the effects of scaling groundwater flow rates on radionuclide transport see the *lower groundwater flow evaluation case* (Section 7.2).

Periods of periglacial climate domain

In the simulations performed for periglacial conditions in Forsmark and Laxemar, the magnitude of the median groundwater flow in the unfrozen parts of the bedrock varies between 0.4 to 3 times the magnitudes simulated for present-day conditions (Appendix C). However, a simplified flow development is used in SE-SFL, where the groundwater flow during the periods of periglacial conditions is assumed to be the same as during present-day conditions.

Ice-sheet advance and retreat

During periods of glacial conditions, the gradient of the ice-sheet surface determines the groundwater flow. In the simulations (Vidstrand et al. 2010a, 2013, 2014a), a steep ice-sheet profile, resulting in an associated large increase in groundwater flow, was assumed during ice-sheet advance over a region with permafrost. A flatter profile, resulting in a smaller increase in groundwater flow, was assumed during the ice-sheet retreat (Figure 7 in Vidstrand et al. 2013). These assumptions are in accordance with the Weichselian ice-sheet reconstruction (Sections 2.2 and 4.3 in the **Climate report**, Appendix 2 in SKB 2010e).

The evolution assumed in the *simplified glacial cycle evaluation case* is based on the general evolution simulated for Forsmark (Figure 7 in Vidstrand et al. 2013) and for Laxemar (Figure 6-6 in Vidstrand et al. 2010a). As a relevant example, the maximum groundwater flow increase during ice-sheet advance is taken to be 35 (Appendix C). The maximum occurs 50 years after the ice-sheet margin has passed the repository location, in agreement with the simulations.

The evolution assumed for ice-sheet retreat is based on the general evolution simulated for Forsmark (Figure 7 in Vidstrand et al. 2013), since no such simulations have been performed for Laxemar. In the simulations, the maximum groundwater flow increase during ice-sheet retreat varies in the range 3 to 20 times the magnitude simulated for present-day conditions. To not overestimate the amounts of radionuclides that are flushed out in the submerged period (when dose consequences are expected to be marginal) the maximum scaling factor during ice-sheet retreat is set to 3. The maximum occurs just as the ice-sheet margin passes the repository location, in agreement with the simulations.

During peak glaciation, the ice-sheet surface gradients are low and similar to the regional topographical gradients in the Laxemar area during temperate terrestrial conditions. During the period between ice-sheet advance and retreat the groundwater flow rate is therefore assumed to be the same as during present-day conditions. The evolution of the groundwater flow assumed in the *simplified glacial cycle evaluation case* is summarised in Table C-1 in Appendix C. The detailed evolution for the period with varying flow is shown in Figure 5-28.

Transition from submerged to terrestrial temperate conditions

The scaling of the groundwater flow during the transition from submerged to terrestrial temperate conditions was determined based on previous modelling studies of groundwater flow in Laxemar and Forsmark. Simulations of bedrock hydrology in Laxemar suggest that the groundwater flow rate at repository depth was approximately 100 times lower than today during the submerged period prior to the emergence of land in Laxemar (Vidstrand et al. 2010a). In accordance with these results the groundwater flow rate is assumed to be 100 times lower than in the *present-day evaluation case* until the coastal influence starts, i.e. at 74 400 AD (in the first cycle).

Simulations of bedrock hydrology in Forsmark suggest that the groundwater flow at repository depth increases approximately linearly from sea-covered conditions until times when the landscape has emerged out of the sea (Odén et al. 2014). In accordance with the pattern in Forsmark, it is assumed that the groundwater flows increase linearly until biosphere object 206 has reached the stage of an isolated lake, i.e. at 78 700 AD in the first cycle.

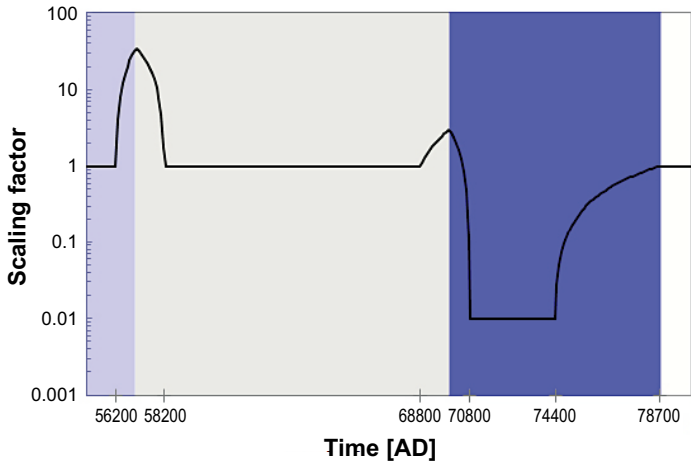

Figure 5-28. *Scaling factor representing groundwater flow in bedrock and repository in the simplified glacial cycle evaluation case relative to present-day temperate terrestrial conditions, see further Table C-1. The evolution is shown for the period 52 000–82 000 AD, during which the scaling factor deviates from 1. Background colour represents climate domains, i.e. surface condition where lavender = periglacial, grey = glacial, blue = submerged, and white = temperate.*

5.4.3 Handling in the biosphere model

Overview over climate conditions

In periods of temperate climate, radionuclides from the repository are discharged to the same biosphere object as in the *present-day evaluation case*, namely biosphere object 206. During periods of periglacial climate, the mire in object 206 is assumed to be frozen, and consequently not connected to flowing bedrock groundwater. During this period, release is instead assumed to reach a lake via a through talik, as represented by Lake Frisksjön (object 207). Given the size of this lake (190 m radius and 4 m average water depth) it is plausible that a through talik may form under the waterbody when permafrost reaches a depth down to 300 m (Hartikainen et al. 2010, Claesson Liljedahl et al. 2016).

When Laxemar is in the glacial climate domain, radionuclides from the geosphere are assumed to be discharged to a sea basin beyond the ice margin. The location of the ice margin is expected to vary, and it will be located at distance from the repository for much of this period. Instead of a detailed description of the fate of radionuclides during this period, a simplifying assumption is used in the biosphere calculations. The turnover time of an off-shore basin is expected to be short. However, it cannot be excluded that radionuclides may, at times, discharge to a coastal location. Therefore, the recipient is cautiously assumed to be a semi-enclosed coastal basin with a relatively shallow water depth and low turnover, represented by the present state of object 208.

In this evaluation case, the glacial cycle is repeated ten times. When the ice sheet retreats most unconsolidated regolith layers on top of the till are expected to be removed by glacial erosion. Moreover, the remaining regolith is assumed to be flushed out by large quantities of surface water when the ice sheet melts. Thus, the radionuclide inventory in all regolith layers is assumed to be negligible at the start of the submerged period in each interglacial-glacial cycle.

Landscape development

Object 206 starts as mire in this evaluation case. After glaciation, the area will be submerged, and it is assumed that the groundwater flows will reach the central parts of the basin (which will later become the lake basin) during this period. As the land rises, the sea basin will develop into a bay, which finally gets isolated from the sea. The development of the object, i.e. the change in bathymetry and the accumulation of post-glacial sediments during the submerged period is described with the coupled regolith-lake development model (RLDM) (Brydsten and Strömgren 2010). The original size of the lake is estimated from present conditions (area and regolith stratigraphy) and the development of the lake is described as a function of mire vegetation ingrowth and net sediment accumulation. According to the projected development, the mire ingrowth is completed 4 400 years after isolation. For details on the landscape development see Chapter 3 in Grolander and Jaeschke (2019). The biosphere objects used to assess consequences of a release during permafrost and glacial conditions do not change during the simulations of these periods.

Surface hydrology

This evaluation case includes several discharge areas that are in states that cannot be observed in Laxemar today. Thus, a conceptual water-balance model in combination with empirically derived rules for percolation and discharge from the surrounding local catchment is used to calculate groundwater flows which are object and state specific. The procedure used is described in detail in Section 5.9 in Grolander and Jaeschke (2019) and is briefly outlined below.

For temperate conditions, groundwater flows for the submerged stage of object 206 are calculated from the projected regolith stratigraphy (at 10 000 BC) and a reduced rate of deep groundwater discharge (by a factor of 0.1[5]). This period is assumed to prevail for as long as the average water depth exceeds 6 m. Water flows for the lake and mire parts of the object are calculated using boundary conditions from the available water balance for terrestrial conditions. Groundwater flows for coastal conditions are calculated by linear interpolation in the period between the sea stage (water depth > 6 m) and the start

[5] This value corresponds to the change in groundwater discharge for an object between fully submerged conditions (covered by 5.7 m of water, and with 98 % of the catchment below water) and emerged conditions (Section 5.5 in Grolander and Jaeschke 2019).

of the land stage (i.e. at lake isolation). The surface hydrology for a drained and cultivated mire and other cultivated land (GP and IO) are strongly simplified (Saetre et al. 2013).

For periglacial conditions, net precipitation and runoff is assumed to increase by approximately 20 %, whereas the discharge from bedrock is assumed to be unaffected by permafrost. All groundwater flows and solute diffusion are halted by permafrost in the mire that fully covers the lake basin in object 206, except for the active layer which is represented by the upper regolith. Groundwater from the bedrock is instead assumed to reach the unfrozen lake part of object 207. In the transition periods between temperate and periglacial domains, the runoff and bedrock discharge into object 206 is calculated by linear interpolation.

When glacial conditions persist, the discharge is assumed to reach the semi-enclosed bay that is object 208, and constant vertical and lateral water flows from permanent aquatic conditions are used in the calculations (as described in the *discharge area evaluation case)*. The location of biosphere objects 206, 207 and 208 are shown in Figure 4-11.

Ecosystem

Parameter values for the properties of terrestrial and aquatic ecosystems are the same as the ones used for temperate conditions in *the present-day evaluation case* and the *discharge area evaluation case*, except for a few parameters in periods of permafrost. These include biological parameters like biomass, net primary production and mineralisation in the mire, and the production of fish and crayfish in the lake. A few additional chemical and physical parameters e.g. CO_2 concentration in the atmosphere, the solubility of CO_2 in water and the coefficient for gas exchange, are also altered in the periglacial periods (Section 10.5 in Grolander and Jaeschke 2019). For periods between temperate and periglacial domains, parameter values are calculated by linear interpolation.

Exposed population

For temperate conditions all exposed groups for natural ecosystems (sea, lake and mire) are included in this evaluation case. Hunter-gatherers (HG) can forage the area in all conditions. A garden plot household (GP) can also be exposed in both submerged and terrestrial conditions (through fertilisation by algae and later by irrigation), whereas the infield–outland farming (IO) depends on hay from the terrestrial part of the object. When the biosphere object is sufficiently elevated above the sea level, consequences of converting the lake-mire complex into an agricultural ecosystem (by draining, DM) are also evaluated in parallel with the potential exposure from the natural ecosystem.

During periglacial climate conditions, cultivation is not possible due to permafrost, and water cannot be extracted from a dug or drilled well. Thus, during these periods only HG is evaluated as the most exposed group. Similarly, during glacial conditions when consumption of fish obtained from a submerged environment is the main *exposure* pathway, only the HG group is evaluated.

5.4.4 Annual release from the near-field and geosphere models

As the chemical, thermal, and mechanical conditions associated with periglacial, glacial, and submerged conditions are assumed to have negligible additional effects on the structural integrity of the engineered barriers and the corrosion rate in the waste vaults (BHK), the annual near-field (and geosphere) releases are similar to those in *the present-day evaluation case* for large parts of the simulation period. This is especially true in periods of emerged conditions prior to the passage of the ice front, and for the first 50 000 years of the simulations, the release rates are identical to those in the present-day calculations. However, as the groundwater flow-rate through the bedrock and repository is assumed to respond to inland-ice advances and retreats, and to the relative sea level, the near-field and geosphere transport is accelerated when the ice front is advancing over the repository (and to a lesser extent also during its retreat), whereas transport is retarded when the landscape above the repository is submerged.

The mass release from BHA is primarily driven by diffusion. Nevertheless, the release in BHA is still somewhat affected by groundwater flow, since at low flow rates, the release to the bedrock will be limited by the groundwater capacity to export radionuclides at the outer backfill boundary. The response is relatively weak, the releases of dose-contributing radionuclides increase by a factor of up to two (Figure 5-29).

The near-field release from BHK is more responsive to an increase in groundwater flow than the release from BHA, and the releases of dose-contributing radionuclides from BHK increase between one (C-14) and two (Ni-59) orders of magnitude when the ice front passes above the waste vault (Figure 5-29). This relatively significant response is expected, as advection is the dominating mass transport process in BHK when the concrete is intact, and radionuclides that have accumulated in the barriers may be transiently flushed out upon changed advective conditions (e.g. Ni-59).

Radionuclide properties affect the response to increased groundwater flow rates, and the near-field release of weakly sorbing species tends to respond to a lesser degree than the release of sorbing species for both vaults. This is because the initial increase in advective transport associated with the approaching ice will effectively reduce the total activity of solute radionuclides, and when the adsorbed activity is small or non-existent, significantly less activity will be available for transport at maximum flow rates. Thus, the relative increase in release of C-14 ($K_d = 0$) from BHK during the first flow maximum is significantly smaller than for Ni-59 ($K_d = 3 \times 10^{-2}$ m^3/kg) (Figure 5-29).

The relationship between the release rate during the passage of the ice front and the maximum near-field release rate given constant present-day conditions depends on the half-life, which affects the long-term release pattern of individual radionuclides. The maximum release rate of the relatively short-lived radionuclides (C-14 and Mo-93) occurs within the first 20 000 years, and thereafter the release rate declines due to radioactive decay. Thus, the elevated annual release associated with the passage of the ice front (at 50 000 AD) will not exceed the maximum release during the initial temperate period. On the other hand, the release rates of radionuclides with a long half-life (Cl-36, Tc-99 and Ni-59) will reach their overall maximum levels when the ice front is passing above the repository (Figure 5-30).

The transport of radionuclides through the bedrock is primarily driven by advection and thus, it is not surprising that the response to increased advection is similar for near-field and geosphere release rates from BHK (Figure 5-30). However, the geosphere release from BHA shows a much stronger response to the passage of the ice front than the near-field release. This apparent amplification is caused by long-term accumulation in the rock matrix prior to the approach of the ice front. The pattern is clearly seen in the release of Tc-99 during the first ice-front approach when the annual geosphere release increases by a factor of 30, as compared with a factor of 2.5 for the corresponding near-field release (Figure 5-30). As with the annual near-field release, the response of the overall maximum release from the geosphere depends on the long-term release pattern of the individual radionuclides. Thus, the maximum annual geosphere release of relatively short-lived radionuclides (C-14 and Mo-93 from both waste vaults) is unaffected by glacial conditions, whereas the release of more long-lived radionuclides is increased by a factor of 10 for Ni-59 to 30 for Tc-99 (Figure 5-30).

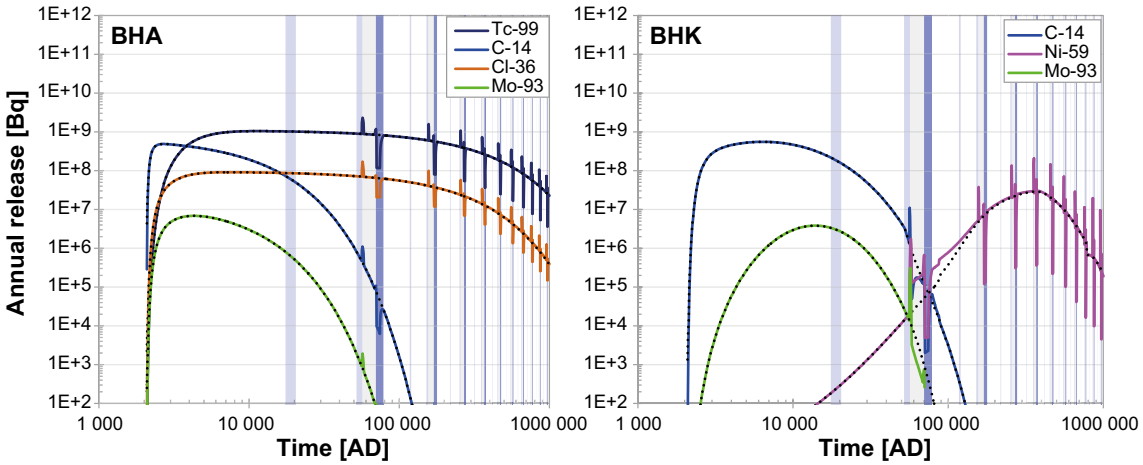

Figure 5-29. *Annual near-field release from BHA (left) and BHK (right) in the simplified glacial cycle evaluation case. Coloured lines represent radionuclides (C-14, Cl-36, Mo-93, Tc-99 and Ni-59). The annual near-field releases in the present-day evaluation case are shown for reference (black dotted lines). Background colour represents climate domains (surface conditions); white = temperate, lavender = periglacial, light grey = glacial, and blue = submerged. Note that the simulations start at 2075 AD and that ten glacial cycles occur during the simulation time.*

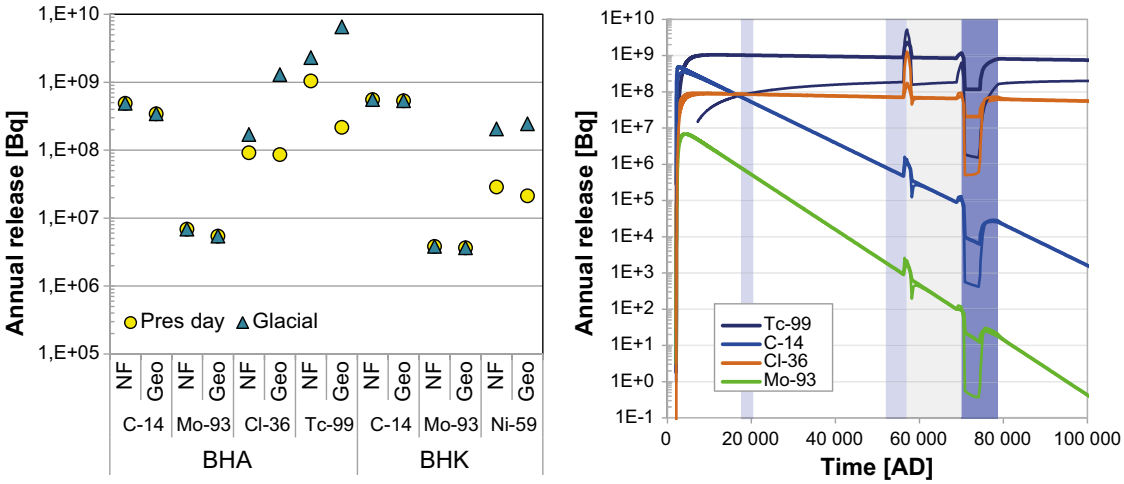

Figure 5-30. *Annual near-field and geosphere releases in the simplified glacial cycle evaluation case. Left: Maximum annual release from the near-field and geosphere (teal triangles) from BHA and BHK, as compared with the corresponding rates in the present-day evaluation case (yellow circles). Right: Release from BHA during the first 100 000 years. Bold lines represent release from the near-field and thin lines represent release from the geosphere. Background colour represents climate domains (surface conditions) as in Figure 5-29. Note that the time scale is linear.*

When the landscape is submerged, the groundwater flows are significantly reduced. The reduced rate of advection decreases the release rate from the near-field, and the release rate from the geosphere is reduced by approximately two orders of magnitude (all radionuclides in Figure 5-30, data from BHK not shown). Thus, radionuclides released from the near-field during submerged conditions tend to accumulate and decay in the rock matrix instead of reaching the geosphere–biosphere interface. The effects of submerged conditions are discussed in detail in *the initially submerged conditions evaluation case* (Section 7.3).

5.4.5 Annual dose

The annual dose in the *simplified glacial cycle evaluation case* varies as a function of the release from the geosphere, the conditions at the surface and the properties of the biosphere objects receiving the release. During temperate periods, the geosphere release and surface conditions are similar to those postulated in *the present-day evaluation case*, and conditions and doses are thus identical in the initial temperate period. Thus, during subsequent temperate periods, the annual doses to the most exposed group are similar in the two evaluation cases. For mobile radionuclides, the annual dose to the most exposed group in the simplified glacial cycle case never exceeds that resulting from constant present-day conditions (Figure 5-31). Meanwhile, the doses from sorbing and long-lived radionuclides, whose dose maxima tend to occur later in time (e.g. Tc-99 from BHA), are effectively reduced at later times in the *simplified glacial cycle evaluation case*. This is due to the re-initiation of the radionuclide inventories in the regolith layers at the end of each interglacial–glacial cycle driven by glacial erosion and flushing from glacial melt-water.

In the periglacial period, permafrost prevents discharge of deep groundwater and thus release of radionuclides to the mire in object 206. The annual dose resulting from foraging the mire in cold conditions is significantly lower than in temperate conditions when the mire can be drained and cultivated, and the annual dose from the mire decreases with time, as radionuclides in the active layer are leached out (Figure 5-32). In the permafrost landscape, the release from the geosphere is instead discharged to the lake in object 207 through a talik. When permafrost conditions coincide with substantial annual releases of C-14, such as from BHK in in the first periglacial period, the dose from the lake talik may be significantly higher than the dose from foraging the mire. However, the annual dose under periglacial conditions is still an order of magnitude below that from the drained mire during temperate conditions in the first interglacial–glacial cycle, and several orders of magnitude lower in subsequent cycles.

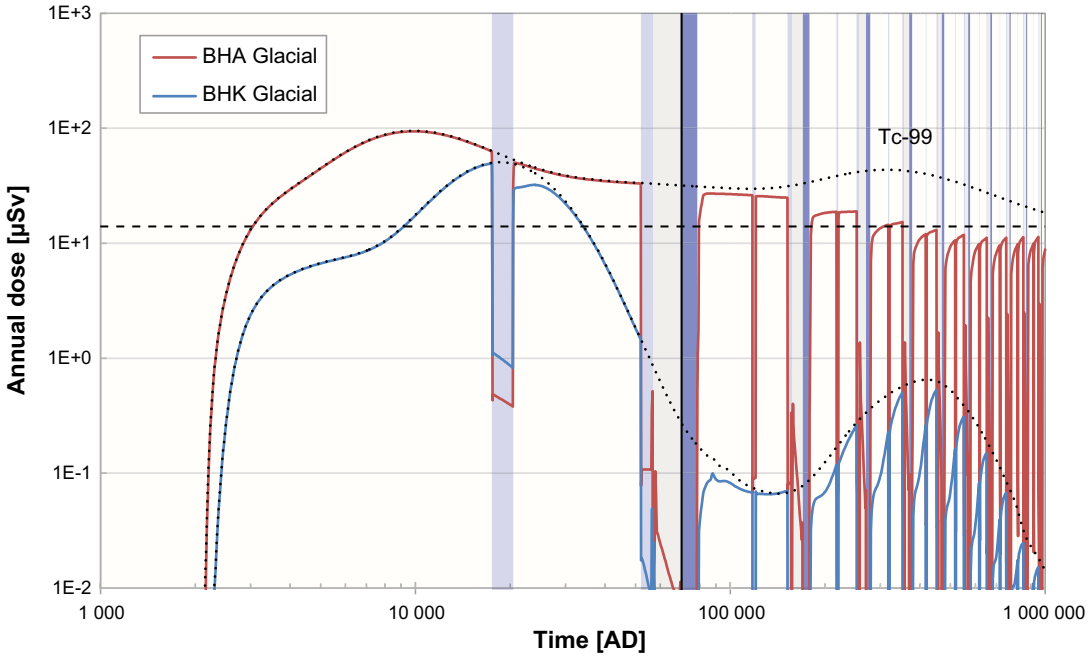

Figure 5-31. *Annual dose for release from BHA (red line) and BHK (blue line) in the simplified glacial cycle evaluation case. Doses in the present-day evaluation case are shown for reference (black dotted lines), where exposure from Tc-99 dominates the dose from BHA during the second half of the simulation time (Figure 5-18). Background colour represents climate domains (surface conditions) as in Figure 5-29. The vertical black line indicates the start of the second interglacial–glacial cycle.*

In the glacial period, there is no exposure in the biosphere objects above the repository, as the area is covered by an inland ice sheet. Instead, consequences of a release in this period are evaluated in a semi-enclosed sea bay located somewhere in front of the ice sheet (with properties from object 208). The releases of Cl-36, Tc-99 (BHA) and Ni-59 (BHK) from the geosphere reach their maxima when the ice front is approaching and passing the repository (see above and Figure 5-29). Moreover, radionuclides with a residence time in the regolith of the same order as their half-life (e.g. Mo-93) will be transported faster when groundwater flows are enhanced. This will have a dose-increasing effect to the most exposed group at the end of the second periglacial period, i.e. at the beginning of the glacial period. However, this effect is by far overshadowed by the dose-decreasing effects from elimination of exposure pathways at the surface caused by permafrost and submerged conditions, i.e. inhibition of cultivation and extraction of well water (Figure 5-31).

After the ice retreat, the landscape above the repository is submerged, and the regolith above the repository is assumed to have been depleted of radionuclides by glacial erosion and flushing with large volumes of glacial meltwater. In the submerged period, as in the temperate period, radionuclides are assumed to be discharged to object 206 which develops from an open sea bay towards a semi-enclosed bay. The annual dose from this period increases over time as radionuclides successively build up in the regolith layers and the exchange of water with the Baltic Sea decreases because of shoreline regression. However, even at the end of this period when the bay is isolated from the sea, the annual dose from consumption of aquatic food (HG in Figure 5-31) is at least an order of magnitude below that resulting from draining and cultivating a mire ecosystem.

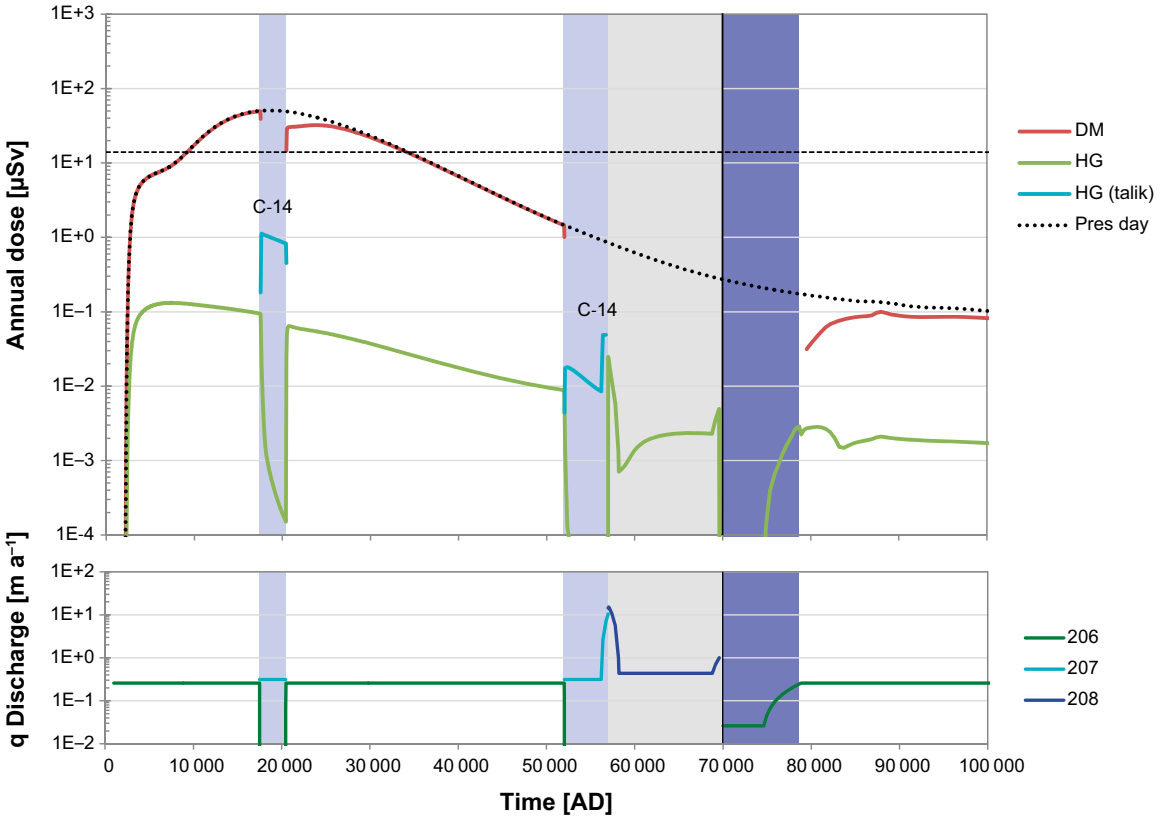

Figure 5-32. *Annual dose for release from BHK in the first interglacial-glacial cycle as a function of exposed group and biosphere object. Lines in upper panel represent the annual dose to different exposed groups; red = drained mire farmers, olive green = hunter-gatherers, cyan = hunter-gatherers at the lake talik. The black dashed line represents the annual dose in the present-day evaluation case (drained mire farmers). Lines in the lower panel represents the groundwater flow from the bedrock to different biosphere objects; green = 206, cyan = 207 and dark blue = 208. Background colour represents climate domains/surface conditions (as in Figure 5-28). The black vertical line indicates the start of the second interglacial-glacial cycle. Note that the time scale is not logarithmic.*

5.4.6 Conclusions

In the *simplified glacial cycle evaluation case*, a detailed and cyclically repeated chain of events is adopted to illustrate the release of radionuclides and dose consequences due to the passage of an inland ice sheet and to shoreline displacement. Groundwater flow is changed in synchrony along the model chain and the conditions and properties of the surface system are modified according to climatic conditions and the succession of discharge areas. Although the maximum annual release of several dose-contributing radionuclides increases when the ice front passes the repository, the annual dose never exceeds the maximum levels recorded in the initial temperate period. This is because dose-contributing radionuclides like Mo-93 and C-14 have decayed significantly by the time that the ice approaches, and because the surface conditions associated with the maximum release, i.e. permafrost or submerged conditions, prevent both exposure through cultivation of mire peat, with a continuous history of radionuclide accumulation, and extraction of well water.

The results from the more detailed, and to some extent more realistic, calculations in the *simplified glacial cycle evaluation case* suggest that doses estimated with the simplifying assumptions of constant external conditions (as applied in the *present-day evaluation case*) may overestimate doses in periods with a cold climate or a submerged landscape. This is also the case for the doses from radionuclides that requires several hundreds of thousands of years to reach maximum dose rates, as repeated glaciations are expected to interrupt their accumulation in the regolith layers.

6 Sensitivity of the safety evaluation to conditions in the repository

6.1 Introduction

The sensitivity of the calculated near-field releases and doses to different properties and conditions in the repository is analysed in this chapter. Moreover, the performance of the barrier system with regards to radionuclides that are expected to be present in the ESS waste is analysed. The following four evaluation cases are presented in the following subsections of this chapter.

- *No effect of complexing agents in BHA,* illustrating the effect of assuming that no complexing agents are active in the waste domain in BHA (Section 6.2).
- *Lower steel corrosion rate in BHK*, illustrating the sensitivity of the results to the steel corrosion rate (Section 6.3).
- *Alternative concrete backfill in BHK*, illustrating the effect of using concrete with a lower hydraulic conductivity, porosity, and diffusivity (Section 6.4).
- *Placement of ESS-specific radionuclides*, evaluating which vault is most suitable for the ESS-specific radionuclides and illustrating the effect of assuming that complexing agents are present in the BHA waste domain for these radionuclides (Section 6.5).

Differences as compared with the base case, i.e. the *present-day evaluation case*, are described. For the evaluation cases described in this chapter, there are no differences as compared with the base case for the geosphere and biosphere models. The sensitivity of the calculated releases and doses to site-specific conditions is evaluated in Chapter 7.

6.2 No effect of complexing agents in BHA

In the base case it is assumed that complexing agents are formed from cellulose in the BHA inventory. The complexing agents are assumed to form complexes with the radionuclides, making them more soluble and reducing their sorption onto cement and bentonite.

This case evaluates the effect of assuming that no complexing agents are present, or that they have no effect, in the waste domain in BHA. The case can be used as a basis to discuss the effects of different types of uncertainties related to complexing agents.

6.2.1 Handling in the near-field model

In the base case, the effect of complexing agents is accounted for by applying sorption reduction factors for sorption onto cement and bentonite in BHA, which are specific for each element (see Table 5-1 and Shahkarami 2019, Table 2-20). The sorption coefficients (K_d values) are divided by the sorption reduction factors and thus radionuclide sorption to cement and bentonite is reduced. Important species that are affected by the sorption reduction factors are Tc(IV) and tetravalent actinides such as U(IV) and Pu(IV). In this evaluation case, where no effect of complexing agents is accounted for, the sorption reduction factors are not applied in the near-field model.

Figure 6-1 shows the retardation coefficient R in bentonite, as defined in Section 5.2.3, illustrating the effect of neglecting the effect of complexing agents for all assessed radionuclide species, as compared with the base case where complexing agents are taken into account. The results show that the sorption reduction due to complexing agents significantly decreases the retardation of several radionuclides, such as Tc-99 and U-238.

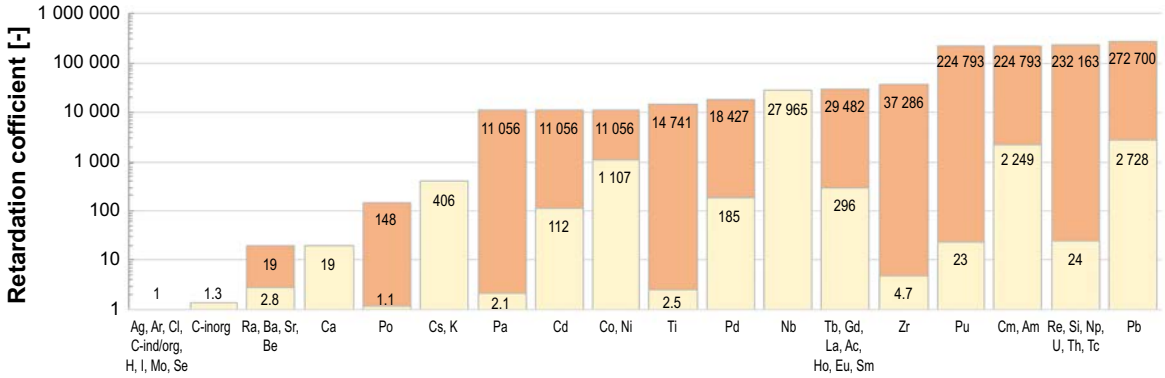

Figure 6-1. *Retardation coefficient R in the BHA bentonite barrier for all assessed radionuclides grouped and sorted by size of the coefficient. Beige fields represent retardation coefficients of the base case and the full stacks represent retardation coefficients without the assumed effect of complexing agents.*

6.2.2 Annual release from the near-field model and annual doses

Excluding the effect of complexing agents on near-field sorption has a strong effect on the retardation of those radionuclides with high sorption reduction factors and high K_d values for sorption to cement and/or bentonite. The increase in retardation coefficient as compared with the base case (Figure 6-1), leads to a more than ten orders of magnitude decrease in the maximum near-field releases of Tc-99 and the tetravalent actinides Pu-239 and Pu-240 that dominate the near-field release in the base case (Figure 6-2 left panel). Similarly, the increased retardation of uranium results in near-field releases of U-238 and U-234 that are several orders of magnitude lower than in the base case. However, retardation of, for example, Ra-226 is less affected by assuming no effect of complexing agents and consequently the near-field release of the entire U-238 decay chain (U-238+) is only about two orders of magnitude lower than in the base case (Figure 6-2 left panel). Assuming no effect of complexing agents results in significantly lower doses from Tc-99, the U-238 decay chain and all other long-lived and sorbing radionuclides that dominate annual doses at the end of the simulation period in the base case (Figure 6-2 right panel).

The near-field release does not differ from the base case for the weakly or non-sorbing radionuclides Mo-93, C-14, and Cl-36, as no sorption reduction is assigned to these in the base case (Figure 6-2 left panel). As these radionuclides are the dominating dose contributors during the first 50 000 years of the assessment, the maximum annual doses in the *no effect of complexing agents in BHA evaluation case* do not differ from the base case (Figure 6-2 right panel).

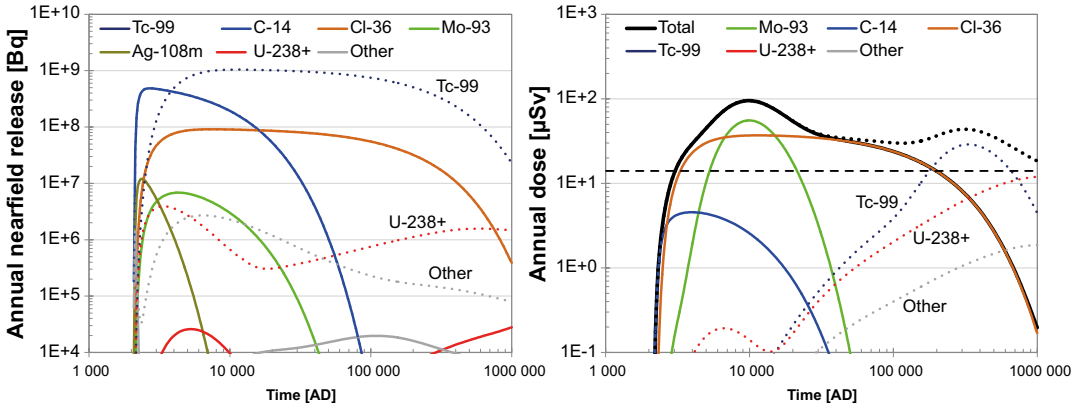

Figure 6-2. *Annual near-field activity release (left panel) and annual doses including total of all radionuclides (right panel) from BHA for the no effect of complexing agents evaluation case (solid lines). The corresponding near-field releases and annual dose for the base case are shown as dotted lines of the same respective colour. The top three radionuclides for maximum near-field activity release and the top three radionuclides for maximum annual dose from BHA are included in the figure. The sum of the release/dose from radionuclides in the U-238 decay chain (U-238, U-234, Th-230, Ra-226, Pb-210, Po-210) is also shown. The dose (14 µSv) corresponding to the risk criterion is indicated with a dotted black line.*

6.2.3 Conclusions

- The occurrence or absence of complexing agents has no effect on the radionuclides (Mo-93, C-14 and Cl-36) dominating the dose resulting from BHA for about 50 000 years after closure.
- The assumption that there is no effect of complexing agents in BHA leads to a substantial decrease in near-field release for highly sorbing radionuclides affected by the sorption reduction factors applied in the base case. Most notable are the reductions in the releases of Tc-99 and tetravalent actinides, such as U-234, U-238, Pu-239 and Pu-240.
- For the period after about 50 000 years after closure, doses decrease in comparison with the base case due to the increased near-field sorption of Tc-99 and the tetravalent actinides, making Cl-36 the dose dominating radionuclide.

6.3 Lower steel corrosion rate in BHK

The waste in BHK comprises reactor internals from different nuclear power facilities. These are metallic parts that will release radioactivity at rates depending on their corrosion rate. This evaluation case illustrates the effect of a significantly lower corrosion rate than that assumed in the base case. As in the base case, alkaline anoxic conditions are assumed to prevail in the BHK during the complete analysis period.

6.3.1 Handling in the near-field model

Since most of the metallic waste planned for disposal in BHK is stainless steel, the corrosion rate of 0.01 μm/a used for stainless steel under alkaline anoxic conditions in SR-PSU (Table 5-3 in SKB 2014d) is applied also in the *present-day evaluation case* of SFL. This value is higher than recently reported long-term corrosion rates, such as 0.0004 μm/a for simulated repository conditions (Sakuragi et al. 2016), or 0.001 μm/a (lower end of the range for stainless steel corrosion under alkaline anoxic conditions recommended for use in PSAR for SR-PSU data to be published in Data report for PSAR SR-PSU; Sidborn 2018). This lower end is used here to represent a significantly lower (by a factor 10) corrosion rate than in the base case.

As in the base case, the corrosion rate is assumed to be constant throughout the assessment period until the metal has corroded completely and all induced activity has been released. There are, however, fractions of the radionuclide inventory that are not contained within metal or are present in very thin metallic parts (< 1 mm). Those fractions are assumed to be available for instant release and consequently not influenced by changes in the corrosion rate. This is a pessimistic assumption, in particular with the lower corrosion rate than in the base case, as even very thin metal may give retention on timescales of more than 100 000 years. The rest of the radionuclides are categorized into three thickness intervals of metal (1−10 mm, 10−20 mm, and > 20 mm), and in the model the thickness of each category is conservatively set to the lower limit of interval, i.e., 1 mm, 10 mm and 20 mm. Assuming that the activity is evenly distributed in the metal, all activity in these fractions will be completely released within 50 000, 500 000, and 1 000 000 years in the base case (for more details, see Section 4.3.3 in this report, **Initial state report** and Shahkarami (2019)).

6.3.2 Annual release from the near-field model and annual doses

Applying a lower corrosion rate for the metallic waste in BHK, results in lower releases of activity from the near-field and lower doses. However, the changes in near-field release and doses are not proportional to the change in corrosion rate, mainly due to the contribution from the instant-release fraction (Figure 6-3 left panel). With reduction of the corrosion rate by a factor ten, the maximum total dose decreases by a factor four (right panel in Figure 6-3). This reduction is fully explained by the response of Mo-93, which dominates the dose in the base case, but the response to changes in corrosion rate varies among radionuclides.

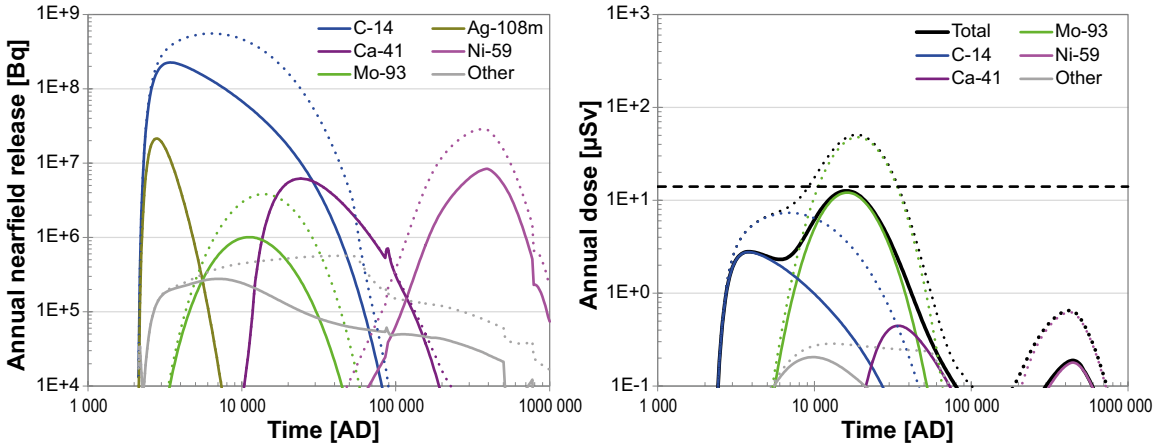

Figure 6-3. *Radionuclide release from the near-field (left panel) and annual doses including the total of all radionuclides, with the corrosion rate decreased to one tenth of the base-case rate. Near-field releases and doses in the base case are shown as dotted lines for comparison. The dose (14 µSv) corresponding to the risk criterion is indicated with a dotted black line.*

If the instant-release fraction in the initial state is so large that it dominates the actual near-field release, a decreased corrosion rate will have no significant effect on the total near-field release. An example of this is Ca-41 with an 88 % instant-release fraction in the initial state, and this is particularly evident for mobile radionuclides with short half-life (e.g. Ag-108m with 22 % instant-release fraction in the initial state). For the most dose-contributing radionuclides, Mo-93 and C-14, the instant-release fraction is less than 1 % of the initial inventory. Nevertheless, due to the relatively slow release term due to corrosion even in the base case, the instant-release fraction contributes significantly to the near-field release, at least during the early period before the maximum annual near-field release occurs (Figure 6-4). When the corrosion rate (and consequently the release from the metal fraction) decreases, the instant-release fraction becomes more important. Reducing the corrosion rate by a factor ten decreases the maximum annual near-field release of Mo-93 and C-14 from the metal fractions proportionally. The total radionuclide-specific near-field releases only decrease to 25 % and 41 % of the original, respectively. This is due to the contribution from the corrosion-unaffected instant-release fractions that dominate the near-field release at the lower corrosion rate (Figure 6-4).

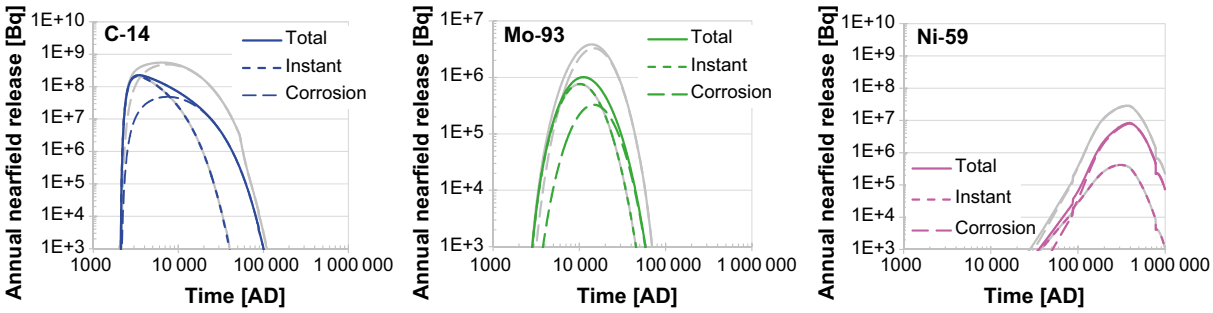

Figure 6-4. *The annual near-field release of C-14 (left panel), Mo-93 (middle) and Ni-59 (right) by waste fraction. The coloured lines show the near-field release (solid line) with reduced corrosion rate and the contribution from the instant-release fraction (dotted) and the metal fraction that become available through corrosion (dashed), respectively. The grey lines are the corresponding releases in the base case (the instant-release fraction is not affected by the corrosion rate and the two curves fully overlap).*

The fraction of Ni-59 available for instant release is similar to that of C-14 and Mo-93 (Table 6-1), but the relatively strong sorption of Ni-59 in the repository decreases the importance of the instant-release fraction. Due to retention of Ni-59 in the repository, the maximum near-field release rate in the base case occurs later than for the two mobile radionuclides (around year 400 000 AD). At the time of the maximum release rate, a large proportion of the metal-bound fraction has become available through corrosion and therefore this fraction dominates the near-field release in the base case. With the lower corrosion rate, the maximum near-field release rate decreases to 28 % of the base-case release rate but is still greatly dominated by the corroded metal fraction. The reason why it does not decrease more (to 10 %) is that a large proportion (21 %) of Ni-59 is initially contained within the thinnest metal fraction that is completely corroded long before (by 50 000 AD) the near-field release maximum occurs in the base case. With the lower corrosion rate, still most of this fraction (80 %) corrodes before the near-field release rate maximum occurs and the effect of the slower corrosion is therefore less than expected from the corrosion rate reduction.

Table 6-1. The fraction of the inventory in BHK that is available for instant release, half-life and the sorption coefficient (K_d) in intact (State I) and chemically degraded (State II–IIIB) of BHK cement (See Table 2-17 in Shahkarami 2019) for radionuclides that contribute significantly to the total dose or have a relatively large activity release from the near-field.

			K_d in cement [m^3 kg^{-1}]			
Radionuclide	**Instant-release fraction**	**Half-life [a]**	**State I**	**State II**	**State IIIA**	**State IIIB**
Ag-108m	21.6 %	438	0	0	0	0
C-14-ind	0.4 %	5730	0	0	0	0
Ca-41	88.3 %	103 000	0.035	0.003	0.003	0.047
Mo-93	0.8 %	4000	0.003	0.003	0.003	0
Ni-59	0.6 %	76 000	0.030	0.200	0.200	0.200

6.3.3 Conclusions

- The decreases in near-field releases and doses are not proportional to the decrease in corrosion rate, mainly because the instant-release fraction also contributes to the release. When the corrosion rate decreases, the activity in the instant-release fraction of the inventory becomes increasingly important in the release from the near-field.
- Reducing the corrosion rate by a factor ten from the base case rate only reduces the maximum activity release rate from the near-field (and maximum annual doses) by a factor of four. This reduction is fully controlled by the response of Mo-93, which dominates the dose in the base case. However, other nuclides (e.g. C-14) might be more important in different conditions (see e.g. aquatic objects in the *discharge area evaluation case*), resulting in somewhat different responses to changes in corrosion rates.
- The effects of the corrosion rate on near-field releases and doses varies among radionuclides depending on the inventory in the instant-release fraction and in the thicker metal fractions that are influenced by corrosion, but retention and decay rates also influence the response. Consequently, the uncertainty in corrosion rate needs to be evaluated in relation to the assumptions about, and uncertainty in, the initial distribution of the radionuclide inventory between the instant-release and thicker metal fractions. Other factors influencing the retention of radionuclides within BHK, such as sorption properties (K_d) and groundwater flow through the repository (e.g. concrete permeability) might also moderate the effects of varying corrosion rates.

6.4 Alternative concrete backfill in BHK

The quality of the concrete used as the backfill material in BHK is a design consideration. Idiart et al. (2019b) modelled the long-term evolution of transport parameters that are affected by degradation for five potential concrete compositions. The results show that it should be possible to achieve a concrete that has more favourable properties than the properties assumed for the concrete composition in the base case, which represents the construction concrete employed in the existing SFR repository. The effect of improved concrete transport properties for the BHK backfill is illustrated in this evaluation case.

6.4.1 Handling in the near-field model

The concrete backfill is assigned an initial porosity and effective diffusivity that are half of the values used in the base case. A lower hydraulic conductivity is accounted for by reducing the advective flow through intact concrete within and out of the near-field by a factor of 10. These parameter values are comparable with the properties of a concrete containing limestone and dolomite additions which has been developed by Lagerblad et al. (2017) and used in the construction of large components representative of the caissons in 2BMA in large scale experiments in the Äspö Hard Rock Laboratory (Mårtensson and Vogt 2019) and analysed by Idiart et al. (2019b).

In the *alternative concrete backfill in BHK case,* the timing of leaching events and cement degradation is assumed to be the same as in the base case (Section 5.2.3), as are sorption coefficients (K_d) in cement. However, the values of the water flow through the waste domain and the backfill are scaled by a factor of 0.1 and the porosity and diffusivity are scaled by a factor of 0.5 while the concrete is intact or partly degraded. When the concrete is assumed to be completely degraded at about 780 000 AD, the water flow, porosity, and diffusivity are cautiously assumed to be the same as in the base case.

In Figure 6-5, the temporal development of advective and diffusive transport rate for non-sorbing radionuclides in all relevant directions over the backfill-rock interface is shown. During the intact concrete phase (IC) the advective transport rate decreases five times compared with the base case and the diffusive rate is slightly increased due to the lower porosity and resulting higher concentrations of non-sorbing radionuclides. This makes total diffusive transport out of the near-field slightly more important than the advective transport during the intact concrete phase, and, as in the *base case*, the diffusive transport becomes increasingly important in relation to the advective transport during the degraded zone phase (Figure 6-5).

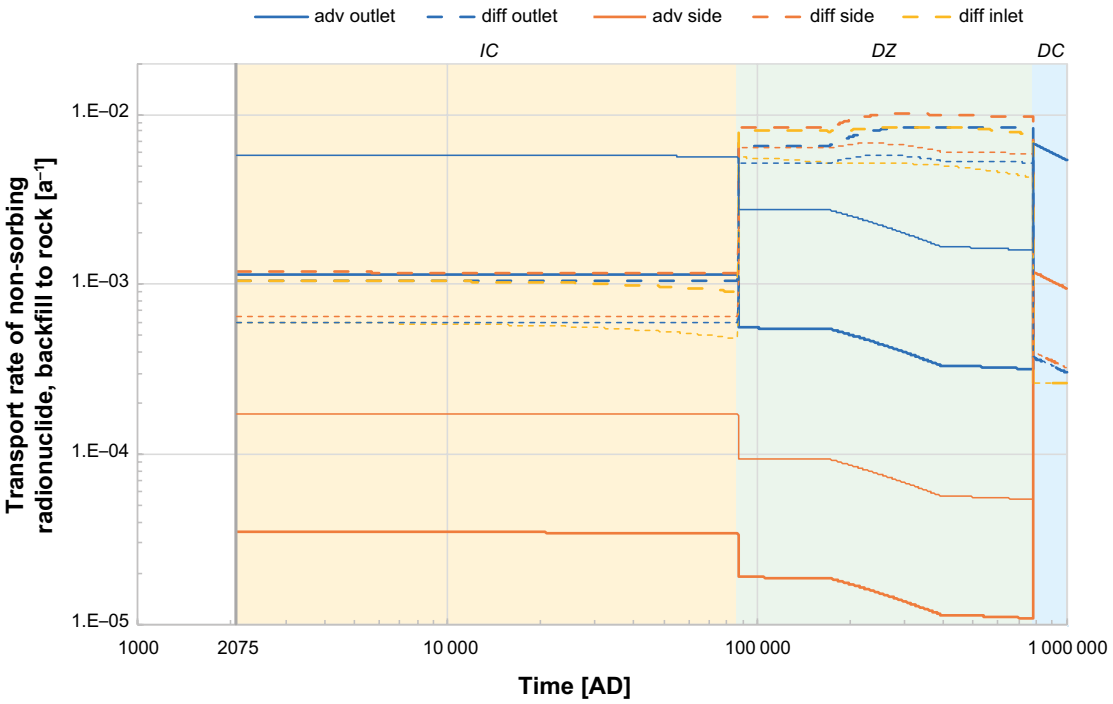

Figure 6-5. *The rate of transport for a non-sorbing radionuclide from the backfill to the rock [a^{-1}], illustrating the effects of varying flow rates and porosity over time due to concrete degradation (Intact Concrete, IC; Degraded Zone, DZ; Degraded Concrete, DC) in the alternative concrete backfill in BHK evaluation case (thick lines) compared with the base case (thin lines). The release from the waste vault is estimated from the rate of transport multiplied by the inventory (for non-sorbing radionuclides) in the outer-most compartments, summed over the inlet, outlet and side compartments. The advective transport rate (adv, solid lines) for the direction of the outlet and side compartments of the backfill (see Figure 4-2) and the transport rate due to diffusion in all directions over the backfill-rock interface (diff, dashed lines) are shown.*

The total release of radionuclides from the waste vault is estimated from the rate of transport multiplied by the inventory in the pore water of the outer-most compartments, summed over the inlet, outlet and side compartments. For non-sorbing radionuclides, the inventory in the pore water equals the total inventory of a compartment, but for sorbing radionuclides the inventory in pore water is estimated by dividing the total inventory by the retardation coefficient $R = (1 + K_d \times m/(V\varepsilon))$, see section 5.2.3). The lower porosity (ε) in the alternative concrete thus decreases the near-field release further by increasing the retardation factor for sorbing nuclides. For non-sorbing radionuclides, however, the decreased transport is counteracted by the increased pore water concentration because of the lower porosity.

6.4.2 Annual release from the near-field model and annual doses

For almost all radionuclides, the maximum near-field activity release rates decrease in comparison with the base case due to the combined effect of decreased hydraulic conductivity, porosity and diffusivity (Figure 6-6 left panel). As in the base case, the highest activity release rates come from induced C-14, but the maximum release rate is delayed by 3 700 years and is about four times lower than in the base case. The differences in near-field release rates between the alternative concrete and the base case are related to the half-life, cement sorption (K_d), and instant-release fraction of the radionuclides. The response is stronger for radionuclides with a high proportion of decay within the near-field (strong sorption and/or short half-life) but weaker for radionuclides where the corrosion rate rather than the transport out of the repository is limiting the near-field release.

Thus, the decrease in the near-field release of the sorbing (and somewhat faster decaying) Mo-93 by two orders of magnitude is larger than the decrease in near-field release of C-14. In the *base case,* Mo-93 is the dominating radionuclide, but in the *alternative concrete backfill in BHK case*, C-14 is the dose-dominating radionuclide and the *resulting total maximum annual dose* occurs about 8 000 years earlier and is 3 % of the maximum dose in the base case (Figure 6-6).

For Ca-41, the onset of the degraded zone period at about 87 000 AD entails a more distinct release peak than in the *base case*. This is, however, a model artefact caused by the assumption of very sudden increase in advective transport rate after a period of Ca-41 accumulation during the IC and DZ phases with slow release (Figure 6-6). In reality, the transport rate will increase more gradually between the concrete degradation stages.

The near-field release and dose curves in the *alternative concrete backfill evaluation case* are similar to the results for the *lower groundwater flow evaluation case*, in which the water flow in the geosphere is reduced by a factor of ten. The similarities and differences between these two evaluation cases are discussed in Section 7.2.

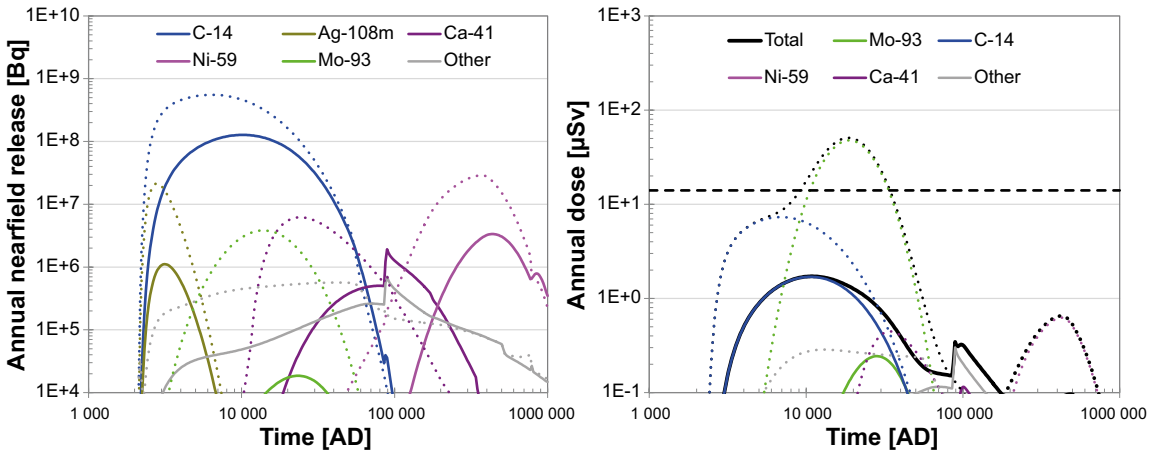

Figure 6-6. *Activity release from the near-field (left panel) and annual dose (right panel) for the evaluation case with alternative concrete backfill in BHK. For comparison, the respective curves for the base case are also shown (dotted lines). The dose (14 µSv) corresponding to the risk criterion is indicated with a dotted black line.*

6.4.3 Conclusions

- A more favourable concrete composition with lower hydraulic conductivity, porosity and diffusivity can significantly improve the repository performance. In the *alternative concrete backfill in BHK case* the maximum dose becomes 3 % of the value for the base case.
- The decrease in the near-field release of the sorbing Mo-93 is larger than for the non-sorbing C-14, and the dose-dominating radionuclide switches from Mo-93 in the base case to C-14 in the alternative concrete case. In general, radionuclides with a high proportion of decay in the near-field (in the base case), i.e. due to high sorption and/or high decay rate, are more affected by a lower advective flow due to more favourable concrete composition.
- The values of the transport parameters in the alternative concrete backfill in BHK are comparable with the properties of the concrete developed for 2BMA (Lagerblad et al. 2017, Mårtensson and Vogt 2019, Idiart et al. 2019b). In addition to the improved transport properties which are applied in the modelling, the concrete developed for 2BMA also has lower porosity and diffusivity, so cement leaching should be suppressed (Idiart et al. 2019b) compared to what is assumed here (and in the base case). This implies that the degraded-zone period would occur later, if at all, within the time frame of the analysis. Consequently, the late time releases of Ca-41 and Ni-59 would decrease even further, resulting in an overall improved long-term performance of BHK.

6.5 Placement of ESS-specific radionuclides

As described in Section 3.4, radioactive waste from the ESS facility is included in SE-SFL. Owing to uncertainties in the inventory data for this waste, it is evaluated in a separate evaluation case. This evaluation case is intended to investigate whether a clear advantage exists for using either the BHA or the BHK barrier concept for radionuclides specific to the ESS inventory.

As it is assumed that the released radionuclides have no effect on their environment or on any other radionuclide, a radionuclide's activity release, and thus its dose contribution, both scale proportionally to its inventory. Since the actual ESS inventory is still largely unknown, a unit initial activity inventory of 1 Bq is here assumed for each of the radionuclides. The transport modelling thus provides information on annual releases of the radionuclides relative to this assumed inventory, but not on the absolute releases. For comparison, all radionuclides included in the base case are also included in the calculations with a unit initial activity inventory of 1 Bq.

6.5.1 Handling in the near-field model

The ESS-specific radionuclides are assumed to be available for transport at repository closure, in the same way as the legacy waste in BHA in the base case. In order to illustrate if one of the two barrier concepts, BHA or BHK, is more suitable for these radionuclides, five variants of this evaluation case (A−E) have been modelled (Table 6-2).

Table 6-2. Variants of the placement of ESS-specific radionuclides evaluation case.

Variant	Waste vault	Charge	Sorption reduction factors
A	BHK	N/A	N/A
B	BHA	Anion	Yes
C	BHA	Cation	Yes
D	BHA	Anion	No
E	BHA	Cation	No

The speciation of the ESS-specific radionuclides in the repository environment is not well characterised. Since the effective diffusivity in bentonite is different for anions compared with cations and neutral species, the evaluation for the ESS-specific radionuclides is performed twice, assuming that they are anions or cations, respectively. The radionuclide charge state does not affect transport through concrete. Further, sorption coefficients, and sorption reduction factors due to the presence of complexing agents, are not well known for the ESS-specific radionuclides. Therefore, element analogues have

been used to select values. For all the ESS-specific radionuclides, the sorption capacity in cement and bentonite is assumed to be influenced by the presence of complexing agents formed from cellulose in the legacy waste (Table 6-3). As described in the *no effect of complexing agents in BHA evaluation case* (Section 6.2), the amount of cellulose in the legacy waste is not well-known and, therefore, the evaluation for the ESS-specific radionuclides is also performed assuming no effect of complexing agents. Since no complexing agents are assumed to be present in the waste in BHK, sorption reduction factors are not applied in variant A (Table 6-2).

Table 6-3. Selected properties of the ESS-specific radionuclides included in the placement of ESS-specific radionuclides evaluation case. Data for two of the main contributors to near-field activity release in the base case (C-14 and Tc-99) are also included for reference. The information for all radionuclides and cement degradation states is found in Shahkarami (2019).

Radionuclide	Half-life [a]	K_d cement (state II) [$m^3\ kg^{-1}$]	K_d bentonite [$m^3\ kg^{-1}$]	Sorption reduction factor
Si-32	132	30	63	10 000
Ti-44	60	10	4	10 000
La-137	60 000	10	8	100
Gd-148	75	10	8	100
Eu-150	37	10	8	100
Tb-157	71	10	8	100
Tb-158	180	10	8	100
Re-186m	200 000	3	63	10 000
C-14	5 730	0	0	1
Tc-99	211 000	3	63	10 000

6.5.2 Annual release from the near-field model

For all ESS-specific radionuclides, the maximum activity is released in variant C (Table 6-4 and Figure 6-7), where ESS-specific radionuclides are placed in BHA and are assumed to have diffusion coefficients characteristic of cations. Since anions are transported less efficiently than cations and neutral species through bentonite, the maximum activity release is lower in variant B than in variant C. Variants B and C show generally higher annual releases, explained by the application of sorption reduction factors due to the presence of complexing agents. In variant D, where ESS radionuclides are placed in BHA with diffusion characteristics of anions and no effect of complexing agents, a considerable decrease in the activity release is observed, compared to variant B, where the sorption reduction factors are applied. This decrease is notable especially for the radionuclides Si-32, Ti-44 and Re-186m, which have very high sorption reduction factors in variant B. The same can be noted comparing the variants C and E.

Table 6-4. Maximum annual near-field activity release for the *placement of ESS-specific radionuclides evaluation case* given as $\log_{10}$(release [Bq]), i.e. −33 means 10^{-33} Bq. Cell backgrounds coloured from low to high values on a scale from white to dark red.

Radionuclide	Variant A	Variant B	Variant C	Variant D	Variant E
Si-32	−33	−15	−9	−39	−32
Ti-44	−31	−11	−7	−34	−27
La-137	−12	−10	−8	−20	−14
Eu-150	−33	−24	−18	−36	−30
Gd-148	−32	−23	−16	−35	−28
Tb-157	−32	−23	−17	−35	−28
Tb-158	−30	−21	−15	−33	−26
Re-186m	−8	−7	−6	−22	−16
C-14	−4	−5	−5	−5	−5
Tc-99	−8	−7	−6	−22	−16

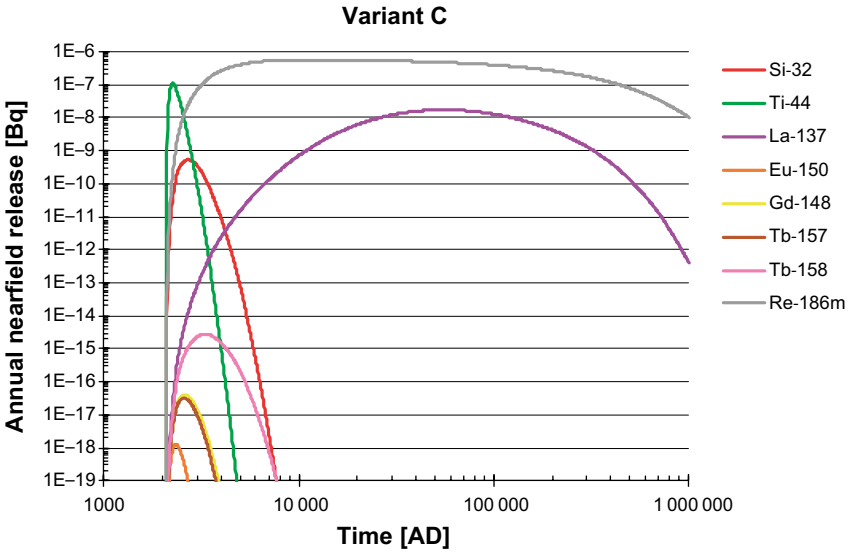

Figure 6-7. *Annual near-field release for variant C of the evaluation case concerning the placement of ESS radionuclides. This variant represents the placement in BHA with diffusion characteristics of cationic or neutral species and includes sorption reduction factors.*

The radiotoxicity varies significantly among the ESS-specific radionuclides. Re-186m radiotoxicity is seven times higher than the chemically analogous Tc-99, which is a main dose contributor in the base case. However, the high Tc-99 doses are mainly a consequence of its large inventory. Of the ESS-specific radionuclides, Gd-148 has the highest radiotoxicity, three orders of magnitude higher than Tb-157 which has the lowest.

6.5.3 Conclusions

- If it is assumed that there is no effect of complexing agents in the waste vault used for disposal of the ESS-specific radionuclides, this evaluation suggests that both barrier concepts are efficient in retarding the transport out of the repository for most ESS-specific radionuclides (variants A, D and E in Table 6-4). For the relatively short-lived and sorbing radionuclides Si-32, Eu-150, Gd-148, TB-158 and Tb-158, the maximum near-field activity release (per initial activity) is insignificant as compared with that of the main contributors (e.g. C-14) to the near-field activity release in the base case. However, for the long-lived La-137 and Re-186m, both barrier concepts are to some extent less efficient.
- The ESS-specific radionuclides show a broad distribution in radiotoxicity, which, along with the inventory data when established, will determine the final dose consequences of these radionuclides.
- In the presence of cellulose, the sorption capacity in BHA is assumed to be reduced for most of the ESS-specific radionuclides. The result is substantially higher near-field releases for these radionuclides.

Only ESS-specific radionuclides are evaluated here, and no account is taken of the complete radionuclide inventory from ESS since it is still uncertain. To decide which repository concept is most suitable for the ESS inventory, the total activity releases and doses must be assessed.

7 Sensitivity of the safety evaluation to site-specific conditions

7.1 Introduction

Site-specific conditions may influence the performance of the repository. In this chapter, six evaluation cases are presented that analyse the sensitivity of resulting doses to different aspects of the site. In addition, an evaluation case is presented that assesses the doses potentially occurring from a drilled well above the repository. The evaluation cases are presented in the following sections of the chapter.

- *Lower groundwater flow,* evaluating the effect of lower groundwater flow rates than at the chosen SE-SFL location in the Laxemar area. Laxemar shows a wide distribution of hydraulic conductivities and there are other sites investigated by SKB that show narrower distributions with smaller median values of groundwater flow (Section 7.2).
- *Initially submerged conditions,* illustrating the effect of siting the repository just off the coast, in a location with a relatively steep coast and slow shoreline displacement and evaluating the potential benefits associated with an initial, submerged period (Section 7.3).
- *Alternative geosphere retention properties,* illustrating the effect of applying bedrock retention parameters from previous safety assessments relating to Forsmark and Olkiluoto (Section 7.4).
- *Alternative realisations of stochastic bedrock fractures,* evaluating the effect of the choice of a specific stochastic realisation of the hydrogeological discrete fracture network, by assessing five different fracture network realisations (Section 7.5).
- *Alternative discharge area,* illustrating how the location, properties and development of the discharge area affects the calculated dose and thus assessing to what extent discharge-area properties should be included in the site-selection process (Section 7.6).
- *Alternative regional climate,* assessing the effects of temperature, annual precipitation rate and vegetation period on the dose rates (Section 7.7).
- *Drilled well,* assessing the dose from drilled water wells that are located within areas where particle tracks from the repository reach the surface (Section 7.8).

In this chapter, results are compared with the base case, i.e. the *present-day evaluation case*.

7.2 Lower groundwater flow

The *lower groundwater flow evaluation case* evaluates the effect of lower groundwater flows in the geosphere than those estimated for the SE-SFL location in Laxemar. The rationale behind the evaluation case is that the Laxemar area shows a wide distribution of hydraulic conductivities, so flow rates around the near-field could potentially be minimised by identifying a body of rock for the repository that has more favourable hydraulic characteristics. Furthermore, it is likely possible to find an entirely different site that has generally lower flow rates than Laxemar. Decreased flow influences the radionuclide transport both directly, and indirectly through slower degradation of the barriers. In the present case, only the direct effects on radionuclide transport are analysed.

7.2.1 Handling in the near-field and geosphere model

In the near-field model, the base-case flow rates in the waste compartments (Sections 2.6.3 and 2.6.4 in Shahkarami 2019) and in the backfill compartments (Sections 2.8.3 and 2.8.4 in Shahkarami 2019) are multiplied by a scaling factor. Three variants are included; variants A, B C with scaling factors of 0.1, 0.01, and 0.001, respectively (Section 4.2.1 in Shahkarami 2019). The equivalent flow rate, Q_{eq} (see Section 4.3.2), is multiplied by the square-root of the scaling factor for BHA, and for BHK during its intact-concrete and degraded-concrete periods. During the degraded-zone period in BHK, the total equivalent flow rate represents the groundwater flow in the degraded part of the backfill rather than the total groundwater flow in the bedrock fractures. Therefore, Q_{eq} is multiplied by the original (non-square-rooted) scaling factor.

In the geosphere model, the total advective travel time t_w [a] for a water particle, and the sum of the flow-related transport resistances F [a m^{-1}], are divided by the scaling factor. The trajectory lengths are assumed to be unaffected by changes in flow conditions.

7.2.2 Handling in the biosphere model

Radionuclides from the repository are discharged to the same biosphere object as in the base case, namely biosphere object 206. It is assumed that the groundwater discharge from the bedrock to the biosphere is primarily driven by recharge of meteoric water, and thus a reduction of groundwater flow at repository depth is not expected to have any significant effect on this flow. Thus, the hydrological and ecological conditions, as well as the exposed groups, from the present-day calculations are also used in this evaluation case.

7.2.3 Annual release from the near-field model

BHA

As discussed for the base case, radionuclide transport through the near-field of BHA occurs mainly through diffusion. Therefore, the reductions of the BHA near-field releases are modest in comparison with the decreases in the groundwater flow rate applied in this evaluation case (Figure 7-1). Further, the temporal-dynamics characteristics of the releases are retained. Diffusive transport within the bentonite backfill is influenced by the diffusive resistance, which is not affected by the decrease in the groundwater flow rate. The transport over the near-field-geosphere interface in the model is however also influenced by the equivalent flow in the rock fractures, Q_{eq} (Section 2.9.2 in Shahkarami 2019), which is decreased by the square root of the scaling factor. Since the diffusion transport resistance in the bentonite is lower for cations and neutral species than for anions (Section 2.8.1 in Shahkarami 2019), the release of cations and neutral species is more affected by a reduction in the equivalent flow than the release of anions. The maximum annual releases of the cations Tc-99, C-14 and Ag-108m are 41 % (variant A, left panel in Figure 7-1), 14 % (variant B) and 5 % (variant C) of the maximum annual releases in the base case. Corresponding values for the anions Mo-93 and Cl-36 are 66 % (variant A, left panel in Figure 7-1), 33 % (variant B), and 13 % (variant C).

BHK

As in the base case, the transport both within and out from the BHK near-field in variant A of the *lower groundwater flow evaluation case* is dominated by advective transport while the concrete backfill is initially intact. Therefore, the decrease in the advective flow rate through the concrete backfill leads to a significant reduction in releases compared with the base case (Figure 7-1, right panel). As the flow rate decreases further in variants B and C, diffusion becomes the dominant transport process, which diminishes the response of the annual releases to the even lower flow rate.

The lower advective transport in variant A compared with the base case retards the releases from the near-field, which allows for more decay within the near-field and influences the relative release of different radionuclides. For example, the maximum near-field release of the sorbing Mo-93 in variant A is only 2 % of the base-case release. The maximum near-field annual release of the non-sorbing C-14 occurs earlier than from Mo-93 and a smaller proportion decays in the near-field. Therefore, the maximum annual release of C-14 from the near-field is less reduced to 16 % of the base-case release. In general, radionuclides with a higher proportion of decay in the near-field due to strong sorption and/or rapid decay are more affected by a decreased advective flow through the repository than radionuclides with weaker sorption and/or longer half-life.

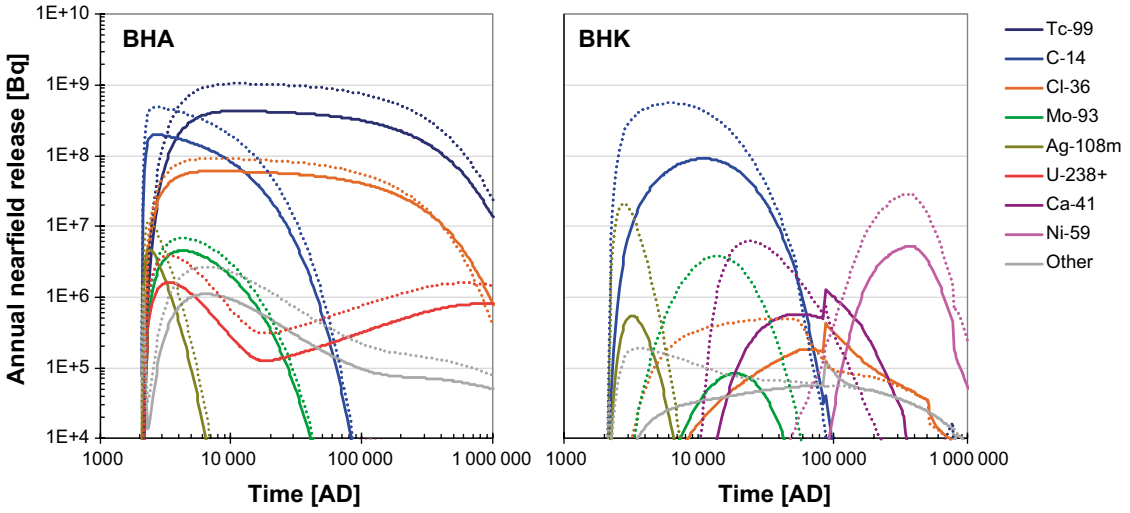

Figure 7-1. *Annual near-field releases from BHA (left panel) and BHK (right panel) for variant A of the lower groundwater flow evaluation case, i.e. with a reduction of the groundwater flows by a factor 10. The corresponding near-field releases for the base case are shown as dotted lines. The top three radionuclides for maximum near-field activity release and the top three radionuclides for maximum annual dose are included in the figure. The sum of the release from radionuclides in the U-238 decay chain (U-238, U-234, Th-230, Ra-226, Pb-210, Po-210) is also shown.*

7.2.4 Annual release from the geosphere model and annual doses

BHA

Lower groundwater flow rates retard radionuclides and increase their decay in the geosphere. In combination with lower near-field releases, this contributes to the reduction of the geosphere release into the biosphere and the resulting doses (Figure 7-2, left panel). With ten times lower groundwater flow rates (variant A), the increased geosphere retention is modest for most dose-contributing radionuclides from BHA. The maximum annual geosphere releases of Mo-93 and C-14 are about 30 % of the maximum annual near-field releases, compared with 80 % and 70 % respectively in the base case. Just as in the near-field, the effect of the lower groundwater flow in the geosphere is smaller for long-lived, non-sorbing radionuclides such as Cl-36, and larger for strongly sorbing radionuclides. For the long-lived Tc-99, the strong sorption results in a maximum annual geosphere release which is only 1 % of the maximum annual near-field release, compared with 20 % in the base case.

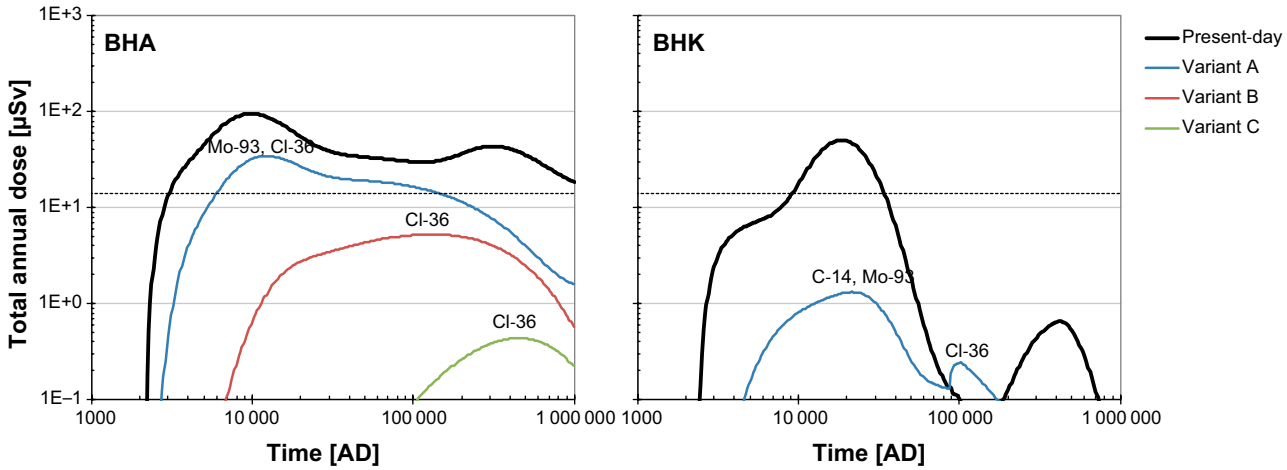

Figure 7-2. *Annual dose from BHA (left) and BHK (right) in the lower groundwater flow evaluation case. Blue, red and green lines correspond to the dose from calculations where the groundwater flow in the repository and the geosphere is reduced by a factor of 10, 100 and 1 000, respectively. The dose in the base case is shown for reference (black line). The dose corresponding to the regulatory risk limit is shown with a dashed line (14 µSv).*

With 100- and 1 000-fold lower groundwater flows (variants B and C), the importance of decay in the geosphere increases as the radionuclide retention times in the geosphere increasingly exceed their half-lives, and the radionuclide-specific responses are accentuated. The total maximum annual doses decrease to 36 %, 6 % and 0.5 % for variant A, B and C in relation to the base case. The dose contribution of Mo-93, C-14 and, in particular, Tc-99 decrease and the dose from Cl-36 becomes of greater relative importance as the groundwater flow rate decreases.

BHK

The radionuclide-specific effects on releases from BHK, lower groundwater flows and longer travel times through the geosphere, are similar to the effects on releases from BHA. However, since travel times through the geosphere are generally shorter from BHK than from BHA (Table 5.2), the response in terms of increasing geosphere decay is somewhat smaller for BHK releases.

Nevertheless, the significant decrease in near-field release of the dose-dominating radionuclides, in combination with the increased geosphere retention as compared with the base case, results in significantly lower geosphere releases and doses. With ten times lower groundwater flow rates, the total maximum annual dose is reduced to 3 % of that in the base case, and the dose contribution of Mo-93 decreases (Figure 7-2, right panel). With 100 times lower flow rates, the maximum annual dose decreases to 0.08 % of that in the base case. Since the effect of lower groundwater flow rates is smaller for long-lived, non-sorbing radionuclides, the relative contribution to the dose from Cl-36 increases with decreasing flow rate.

In the near-field, the transition from advection- to diffusion-dominated transport causes diminishing returns of lowered flow rates, and hence going from the base case to variant A has a larger impact than going from variant A to B or B to C. In the geosphere, conversely, variants B and C are increasingly impactful on the release because they entail retention times that start to rival the half-lives of many radionuclides, significantly increasing the decay in the geosphere.

Comparison between the lower groundwater flow and alternative concrete backfill in BHK evaluation cases

The BHK near-field releases and resulting total annual doses in variant A of the *lower groundwater flow evaluation case* are similar to the results for the *alternative concrete backfill in BHK evaluation case* (Section 6.4). The similarities are largely explained by the reduction in near-field advective flow by ten times in both evaluation cases. The responses of individual radionuclides, however, differ more between the evaluation cases than do the total doses. For radionuclides that sorb in the concrete backfill (e.g. Mo-93), the decrease in near-field release is larger in the *alternative concrete backfill in BHK evaluation case* than in the *lower groundwater flow evaluation cas*e (Figure 6-6 vs Figure 7-1). This is mainly explained by the 50 % decrease in porosity in the *alternative concrete backfill in BHK evaluation case* (Section 6.4.1) and the associated increase of sorption sites that increases retention and radioactive decay in the near-field in this evaluation case. For non-sorbing radionuclides (e.g. C-14), however, the near-field release is slightly larger in the *alternative concrete backfill in BHK evaluation case* than in the *lower groundwater flow evaluation cas*e. The reason is mainly that the decreased porosity in the alternative concrete results in higher porewater concentrations of non-sorbing radionuclides that partly counteract the effect of the lower flow rate through the near-field in the *alternative concrete backfill in BHK evaluation case*. Moreover, the geosphere retention increases in the *lower groundwater flow evaluation case* but not in the *alternative concrete backfill in BHK evaluation case*, influencing the geosphere release and resulting doses. With a tenfold lower groundwater flow, this effect is however limited compared with the effects on the BHK near-field releases. Altogether, the effects of higher C-14 doses and lower Mo-93 doses in the *lower flow evaluation case* than in the *alternative concrete backfill in BHK evaluation case* mostly counterbalance each other, resulting in similar total annual doses for the two evaluation cases, given the initial inventory used.

7.2.5 Conclusions

- Lower groundwater flow rates have a greater impact on the doses from BHK compared with BHA. 100 times lower groundwater flow rates are needed to decrease the annual maximal dose from BHA to 6 % of that in the base case, but ten times lower flow rates are enough to decrease the dose from BHK to 3 % of that in the base case. The explanation is mainly that transport within and out of the near-field in BHK is limited by advection in the base case, whereas transport in BHA is mainly limited by diffusion which is insensitive to groundwater flow rates.
- With ten times lower groundwater flow rates, the lower doses from BHK are mainly caused by increased retention and decay in the near-field, whereas retention and decay in the geosphere have a moderate effect. However, with even lower groundwater flow rates, the relative importance of decay in the geosphere increases as the radionuclides retention times in the geosphere increasingly exceed their half-lives. The near-field release, on the other hand, eventually becomes dominated by diffusion with increasingly lowered groundwater flow rates.
- Lower groundwater flow rate affects the releases more for radionuclides with a large relative activity decrease by decay, due to a high decay rate and/or strong sorption. Thus, the near-field release from BHK of the sorbing Mo-93 decreases more with lower flow rates than release of the non-sorbing C-14, and the geosphere release from BHA of the strongly sorbing Tc-99 decreases more than that of the non-sorbing Cl-36.
- The BHK near-field releases and doses in variant A of the *lower groundwater flow evaluation case* are similar to the results for the *alternative concrete backfill in BHK evaluation case.* The similarities are largely explained by the reduction in near-field advective flow by ten times in both evaluation cases. Geosphere retention and decay is however only affected in the *lower groundwater flow evaluation case*, and the decreased porosity in the *alternative concrete backfill in BHK evaluation case* influences sorbing and non-sorbing radionuclides in the near-field differently. Given the initial inventory in BHK, these effects almost cancel out, resulting in similar total annual doses in the two evaluation cases.

7.3 Initially submerged conditions

7.3.1 General description

The *initially submerged conditions evaluation case* analyses the effect of locating the SFL vaults below the seabed. The groundwater flow rate is assumed to be initially lower than at present, but shoreline displacement causes a transition to the present rate. Low groundwater flow leads to decreased near-field and geosphere releases, as demonstrated in Section 7.3.4. Three variants are included in this evaluation case, reflecting different durations between repository closure and when the area above the repository and the discharge area start to emerge from the sea. In the three variants, the groundwater flow starts to be influenced by the surface environment at the start of the simulations, after 5 000, and after 10 000 years, respectively.

As in the *simplified glacial cycle evaluation case* (Section 5.4), the reconstructed shoreline displacement is used to describe the development of the landscape in the *initially submerged conditions evaluation case*, and radionuclides from the repository are discharged into biosphere object 206. This area is presently located at an altitude of 12.3 m above the mean sea level. For these calculations it is assumed that the groundwater flows in the surface environment (i.e. basin 206) start to become influenced by the surrounding terrestrial landscape when the average water depth is 6 meters (Chapter 3 in Grolander and Jaeschke 2019), which occurred at 8400 BC according to the shoreline displacement reconstruction (Section 6.2.1 in the **Main report**). 4 300 years later, the basin became an isolated lake. Table 7-1 relates the time of events in the historic reconstruction to the simulation time points in this evaluation case.

Table 7-1. Assumed shoreline displacement according to the reconstruction of the actual development, as well as in the three variants of the *initially submerged conditions evaluation case*. The simulations of all three variants start in 2075 AD.

Reconstructed shoreline characteristic	Historic reconstruction	1) Submerged conditions end at the start of the simulation	2) Submerged conditions for 5 000 a	3) Submerged conditions for 10 000 a
Sea depth above biosphere object 206 is 6 m	8400 BC	2075 AD	7075 AD	12 075 AD
Biosphere object 206 is isolated as a lake	4100 BC	6375 AD	11 375 AD	16 375 AD

7.3.2 Handling in the near-field and geosphere models

In the near-field and geosphere models the groundwater flow pattern is assumed to be the same as in the base case. The changes in groundwater flow associated with the shoreline development are represented by a scaling factor, which modulates the magnitude of the groundwater flow relative to the present-day groundwater flow rate. As in the *simplified glacial cycle* (Section 5.4) and *lower groundwater flow evaluation cases* (Section 7.2), the groundwater flow rates are scaled uniformly in the geosphere and near-field models. All other near-field and geosphere parameters are the same as in the base case.

The scaling used is identical to that used for the transition from submerged to terrestrial temperate conditions in the *simplified glacial cycle evaluation case* (see Section 5.4.2). Thus, the groundwater flow rate is assumed to be 100 times lower than in the base case until the terrestrial influence starts (first row in Table 7-1). The groundwater flow rate is then assumed to increase linearly until biosphere object 206 has reached the stage of an isolated lake (second row in Table 7-1). The scaling factor for the groundwater flow rate is shown for the three variants in Figure 7-3. The equivalent flow (Q_{eq}) i.e. the capacity of the groundwater passing the backfill to transport radionuclides, is scaled by the square root of the scaling factor for BHA, and during the intact concrete period for BHK. However, when the BHK barrier is partially degraded (DZ), Q_{eq} is multiplied by the non-square-rooted scaling factor. Moreover, the total flow of water through the waste ($Q_{advective}$) is multiplied by the scaling factor, and similarly, the total advective travel time t_w [a] for a water particle, and the sum of the flow-related transport resistances F [a m^{-1}], were scaled by division with the factor in the geosphere model. For a discussion of the effects of such scaling see *the lower groundwater flow evaluation case* (Section 7.2).

7.3.3 Handling in the biosphere model

In this evaluation case, radionuclides are discharged to the same biosphere object as in the base case, namely biosphere object 206. During the submerged period, the discharge is restricted to the central area of the sea basin, which is later transformed into a lake-mire complex.

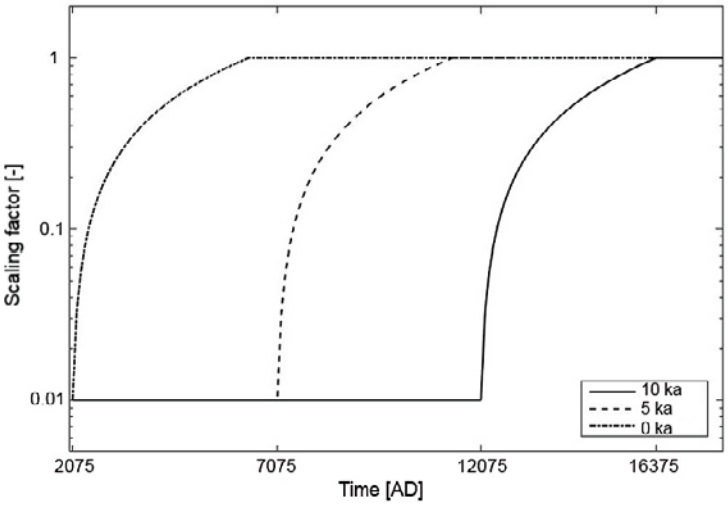

Figure 7-3. *Scaling factors applied to the groundwater flow rate in the base case near-field and geosphere models in the three variants of the initially submerged evaluation case.*

Object 206 starts as a sea basin in all variants of this evaluation case. The first variant starts with a groundwater flow that just starts to be influenced by the surrounding terrestrial environment, corresponding to an average water depth of 6 m. In the historical reconstruction of the site, this occurred at 8400 BC (see above). The two other variants entail later emergence from the sea. To model this, their shoreline regression evolution is parallel-shifted 5 000 and 10 000 years earlier in time, respectively. Consequently, the simulation for the second variant starts with conditions corresponding to 13 400 BC, and the third variant with 18 400-BC conditions. The historical reconstruction does not cover the period before 10 000 BC. Therefore, it is assumed that the conditions at 10 000 BC are representative of all times prior to 10 000 BC (i.e. the average water depth of the sea basin is 50 m and the water residence time is 4 days).

As land rises, the sea basin will develop into a bay, which finally gets isolated from the sea (4100 BC in the reconstruction, Table 7-1). The development of the object during the submerged period (i.e. the change in bathymetry and the accumulation of post-glacial sediments) is described with the coupled regolith-lake development model (Brydsten and Strömgren 2010). The original size of the lake was estimated from present conditions (area and regolith stratigraphy of object 206) and the development of the lake is described as a function of vegetation ingrowth and net sediment accumulation. According to the projected development, the mire ingrowth is complete 4 400 years after isolation. For details on the landscape development see Chapter 3 in Grolander and Jaeschke (2019).

Surface hydrology

None of the states that the discharge area goes through in this evaluation case can currently be observed in Laxemar for object 206. Thus, a conceptual water balance model in combination with empirically derived rules for percolation and discharge from the surrounding local catchment was used to calculate groundwater flows for object 206 for all stages (sea, lake, mire). Flows during the coastal stage, when the hydrology in the basin is influenced by the terrestrial landscape, were interpolated from those in the sea and lake stages. The procedure used is described in detail in Section 5.9 of Grolander and Jaeschke (2019) and is briefly outlined in *the simplified glacial cycle evaluation case* (Section 5.4).

Ecosystem parameters

Parameter values for the properties of aquatic ecosystems are the same as used in the *alternative discharge area evaluation case* (Section 7.6). Parameters for the mire ecosystems are the same as those used in the base case (Section 5.2).

Exposed population

All exposed groups for natural ecosystems (sea, lake and mire) were included in this evaluation case. Hunter-gatherers (HG) can forage the area at all times. A garden plot household (GP) can also be exposed during both submerged and terrestrial conditions (through fertilization by algae and later irrigation), whereas the infield–outland farming (IO) depends on hay from the terrestrial part of the object. When the biosphere object is sufficiently elevated above the sea level, the consequences of converting the lake-mire complex into an agricultural ecosystem (by draining, DM) were also evaluated in parallel with evaluating the potential exposure from the undisturbed natural ecosystem.

7.3.4 Annual release from the near-field and geosphere models

The effect of a 100 times lower groundwater flow rate on annual releases from the near-field and geosphere is described in detail for the *lower groundwater flow evaluation case* (see Section 7.2). The current evaluation case also entails lower flows, so in both cases, releases from BHK experience a greater reduction than releases from BHA, because advection is the dominant mass transport process in BHK (when the concrete is intact). Releases from the near-field of BHA are, on the other hand, diffusion-controlled. For both repository vaults, the effects of an initially submerged period diminish when the discharge area is above the sea level, and therefore no effects on the near-field and geosphere release are evident 20 000 years after the emergence of the discharge area (Figure 7-4).

The near-field and geosphere maximum annual releases of Cl-36, Mo-93 and C-14 are delayed by a time that approximately equals the length of the submerged period. However, the effect on the magnitude of the maximum release rate varies with the properties of the waste vaults (including the waste

form), the individual radionuclides and with the length of the submerged period (Figure 7-5). Thus, whereas the maximum near-field release rate of Cl-36 (BHA) is marginally affected by an initially submerged period, the maximum release rate of Mo-93 is reduced for both waste vaults. The near-field maximum release rate of C-14 from BHA is also reduced, but a submerged period has only a marginal effect on the maximum annual release of this radionuclide from BHK. These patterns are discussed in more detail below.

Decay of the Cl-36 activity (half-life = 3×10^5 a) is limited during the submerged period. Therefore, once the groundwater flow rate increases, the maximum near-field and geosphere release rates are similar to those in the base case (Figures 7-4 and 7-5). However, after 10 000 years of submerged conditions, the increased groundwater flow results in flushing out of the accumulated bedrock activity, and the release of Cl-36 from the geosphere is noticeably increased over a transient period of a few thousand years, even higher than the near-field release (left panel in Figure 7-4).

The inventory of Mo-93 decays during the submerged period and, consequently, the maximum release rate of Mo-93 is lower than in the base case. The reduction in the maximum release rate from BHA clearly reflects the length of the submerged period, i.e. it is reduced by ~50 % and ~80 % after 5 000 and 10 000 years of submerged conditions, respectively. In BHK, Mo-93 is released from the waste via corrosion and the accumulation in the waste vault during the period of submerged conditions partly compensates for the loss of activity from radioactive decay. Thus, the reduction in maximum near-field release rate of Mo-93 from BHK is 25 % and 50 % for the 5 000- and 10 000-year submerged periods, respectively (Figure 7-5). As for Cl-36, a transition after 10 000 years of submerged conditions, results in flushing out the bedrock inventory of Mo-93 from BHA (Figure 7-4). Despite this transient release from the bedrock, the maximum release rate of Mo-93 from BHA to the biosphere is still reduced to 40 % of the maximum release rate given constant terrestrial conditions (data not shown).

The inventory of C-14 also decreases over time due to decay, and 5 000 and 10 000 years of submerged conditions result in a reduction of maximum near-field release rate from BHA to 35 % and 20 %, respectively, of the maximum release rate in the base case (Figure 7-5). However, in BHK, dissolved C-14 from corrosion accumulates during the submerged period to such an extent that there is a higher activity of dissolved C-14 at the end of the submerged period than the maximum under constant terrestrial conditions. Consequently, the maximum release rate from BHK, which occurs at the end of the transition to terrestrial conditions, is slightly higher than the maximum release rate in the base case (Figures 7-4 and 7-5).

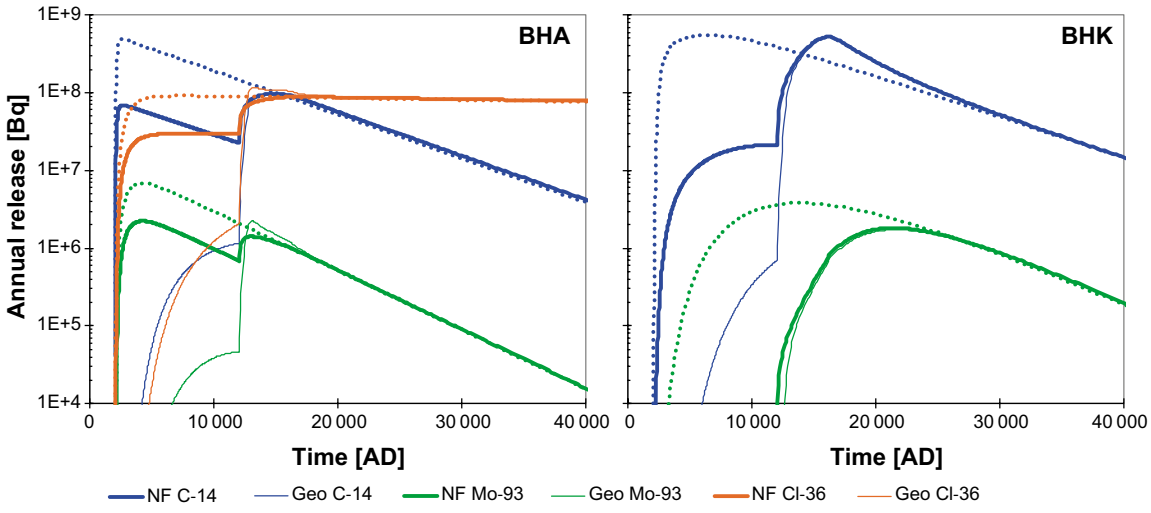

Figure 7-4. *Annual release from BHA (left) and BHK (right) for three radionuclides, given 10 000 years of initially submerged conditions. Bold lines represent near-field (NF) release whereas thin lines represent geosphere (Geo) release. The near-field release rates in the base case (dotted lines) are shown for reference. Note that the simulations start at 2075 AD.*

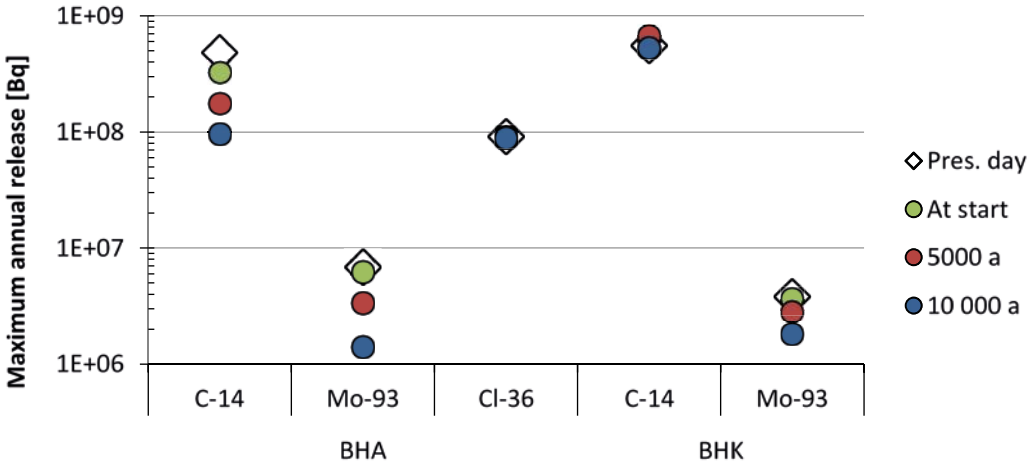

Figure 7-5. *Maximum annual near-field release of radionuclides from BHA (left) and BHK (right) for the three variants of the initially submerged conditions evaluation case. Colours indicate the length of the initially submerged period. The near-field release in the base case is shown for reference (white diamonds).*

7.3.5 Annual dose

The maximum annual doses in all three variants of the *initially submerged conditions evaluation case* are lower than in the base case, and the reduction in the dose is similar for the two waste vaults (BHA, BHK). Compared with the base case, the maximum dose is approximately halved when the repository is submerged for 10 000 years (47 %, 54 %), reduced by approximately one third (37 %, 29 %) when submerged for 5 000 years, and only reduced marginally (12 %, 6 %) when the discharge area is covered by 6 m water at the start of the simulations. The annual dose after 20 000 years is not noticeably affected by the length of the submerged period, and for BHA, the second maximum (at about 350 000 AD due to Tc-99) is almost as high as the first maximum in the 10 000 years submerged variant (data not shown). In the base case, the maximum dose from both waste vaults is caused to a large extent by exposure to Mo-93 (after ingestion of crops cultivated on the drained mire). This is also true for BHK in all variants of the *initially submerged conditions evaluation case*, and for BHA when submerged conditions end at repository closure. However, when BHA is submerged for 5 000 years or more, the largest dose is caused by exposure to Cl-36 in the drained mire (Figure 7-6). The variations in the maximum annual dose therefore primarily reflect the reduced release of Mo-93 and C-14 from the geosphere. In BHA, this relationship is partly masked by exposure to Cl-36.

The first maximum in the annual dose curves of all variants of the *initially submerged conditions evaluation case* (Figure 7-6) reflects release to a sea basin. For BHA, the maximum is low compared with the base case, reflecting a significant reduction in the Mo-93 and C-14 releases from the geosphere, and low exposure to Cl-36 and Mo-93 from aquatic foods (due to a relatively high rate of dilution and low productivity in sea ecosystems, as compared with terrestrial cultivated ecosystems). In comparison, the first maximum from BHK in the three variants is relatively high. This reflects that the early dose from BHK is dominated by exposure to C-14. The maximum BHK release of C-14 from the geosphere is slightly higher than in the base case (data not shown), and the uptake of C-14 is more effective in aquatic than terrestrial ecosystems. Thus, the doses resulting from a C-14 release from BHK during a transitional stage exceed the C-14 dose in the base case (Figure 7-6).

The influence of landscape development on the annual dose is evident in the shape of the dose curve. For BHA, the first maximum occurs just before lake isolation, when the water exchange rate is approaching that of the lake and the cover of mire vegetation is negligible. The decline in this initial dose maximum is primarily driven by the ingrowth of the mire. The annual dose increases by an order of magnitude when the mire can be drained. At this point, the mire area is only a few hectares, and therefore the dose continues to increase with mire ingrowth, until the mire is large enough to support the most exposed group (after a few hundred years). The influence of biosphere object development is discussed further in the *alternative discharge area evaluation case* (Section 7.6). Over the rest of the terrestrial phase, the dynamics in dose largely reflects the dynamics in the geosphere release.

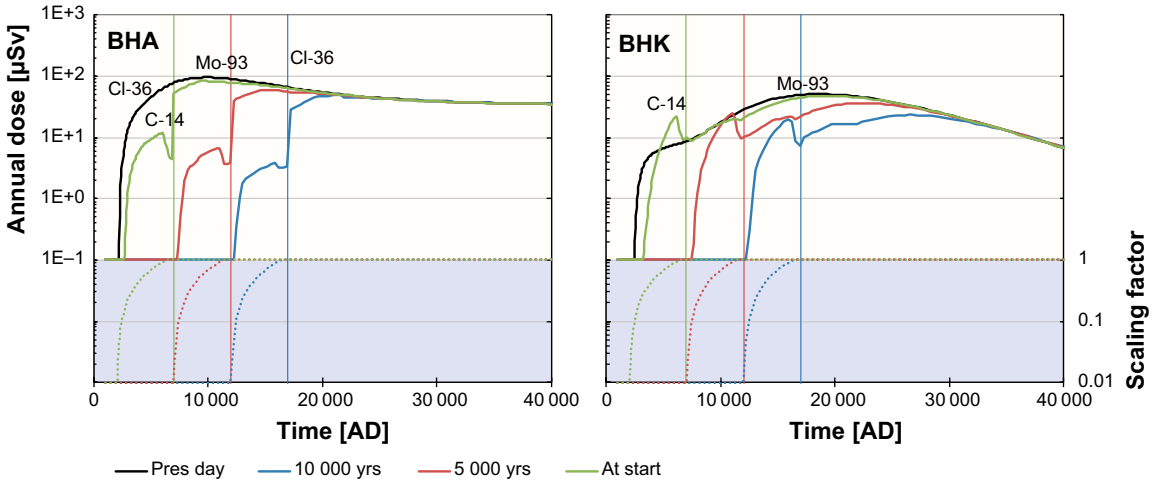

Figure 7-6. *Annual dose from BHA (left) and BHK (right) in the three variants of the initially submerged conditions evaluation case. The terrestrial landscape starts to influence flow-conditions in the waste vaults and the bedrock at the start of the simulation (green), after 5 000 years (red), or after 10 000 years (blue). The annual dose in the base case is shown for reference (black line). Dose-contributing radionuclides are indicated above the curves (early dose due to Cl-36 from BHA occurs in the base case only). Vertical line indicates when the biosphere object is 1 m above sea level, allowing cultivation of the drained mire. Lower panels show the hydrological scaling factor for the near-field and the geosphere release.*

7.3.6 Conclusions

The *initially submerged conditions evaluation case* analyses the effect of locating SFL at a position that is currently below the seabed. A prolonged period of submerged conditions is likely to retard the advective transport from the repository due to low groundwater flow. The evaluation shows that the maximum release rates to the biosphere may be delayed by the duration of the submerged period, and that radioactive decay may reduce the dose significantly in the terrestrial period following the sea period. As Mo-93 is a major dose-contributing radionuclide with a relatively short half-life, the maximum dose from SFL is reduced by an initially submerged period, and the size of the reduction increases with the length of the sea-covered period. However, the effect of an initially submerged period is not dramatic; the maximum dose from a repository that is submerged for 10 000 years is reduced by a factor two, as compared with release to a land location (described in the base case). It can also be noted that the reduction in dose from a near-coastal, submerged location (where the hydrology is influenced by the terrestrial landscape) is expected to be marginal (~10 % or less). Moreover, the C-14 dose resulting from such a repository position may even be significantly higher than from a land location, as the uptake of C-14 (per unit mass of stable carbon) is higher in aquatic plants (and food-webs) than in terrestrial ecosystems.

7.4 Alternative geosphere retention properties

The *alternative geosphere retention properties evaluation case* illustrates the sensitivity of the safety evaluation to the choice of geosphere retention properties. Alternative geosphere retention properties have been taken from SR-Site, the safety assessment for SKB's Spent Fuel Repository in Forsmark (SKB 2010f), and from TURVA-2012, the safety assessment for Posiva's repository for spent fuel in Olkiluoto, Finland (Posiva 2013). The differences between these data sets and the data used in the base case can be attributed to both site-specific conditions and differences in the reasoning behind the selection of sorption coefficients (K_d values).

The effect of geosphere retention on the release to the biosphere can be quantified as the proportion of the near-field release that decays in the geosphere (i.e. the relative geosphere release). The decay in the geosphere is a function of well-known radionuclide specific decay rates and more uncertain residence times of radionuclides in the geosphere. Part of the residence time uncertainty is linked to ground water flows that in turn is related to the modelling of the bedrock fracture network, i.e. the

relative flow wetted area (a_w) that influences the diffusion into the rock matrix, and the advective travel time (t_w). These two parameters are evaluated in the *alternative realisations of stochastic bedrock fractures evaluation case* (Section 7.5) and the effects of generally lower ground water flows are evaluated in the *lower groundwater flow evaluation case* (Section 7.2). In *the alternative geosphere retention properties evaluation case* the effect of sorption (K_d), matrix porosity, rock density, effective diffusivity and maximum penetration depth into the rock matrix are analysed and/or discussed.

7.4.1 Handling in the geosphere model

Sorption in the rock matrix is modelled based on element-specific values of the sorption coefficient (K_d). In this evaluation case, the modelling results based on K_d values adopted in the *base case* for Laxemar are compared with the results from using two alternative sets of K_d values, from Forsmark and from Olkilouto (Sections 3.3.5 and 4.3.1 in Shahkarami 2019). K_d values for the base case (Laxemar) are more similar to the corresponding values for Forsmark than to those for Olkiluoto (Table 7-2). K_d values in the Forsmark variant are about half of those used in the base case for Ag, Ni, Tc, U including some of its decay products, and some other less important radionuclides. The differences reflect the general site-specific differences between Forsmark and Laxemar in terms of groundwater chemistry (pH, redox potential, salinity) and mineral composition. In the Olkiluoto variant, on the other hand, the K_d values are higher than in the base case for Ni, Mo, Ra, Tc and some less important radionuclides and lower for Ag, U and a few more elements. The differences in K_d values between Olkiluoto and Forsmark largely result from site-specific measurements (or lack thereof in Forsmark for some elements), and some higher K_d values in Olkiluoto can be explained by a greater presence of micaceous minerals (i.e. biotite, chlorite, muscovite) that offers increased cation sorption.

Table 7-2. Sorption coefficients K_d for the base case (Laxemar) and the ratios between the respective Forsmark and Olkiluoto parameter values and the base case. For Be and Mo, which have K_d = 0 in the base case, the absolute value of the K_d value is shown in brackets. Only elements for which the K_d value differs from the base case are shown. The full set of K_d values is available in Section 4.3.1 in Shahkarami (2019). The last column contains the effective diffusivity ratios between Olkiluoto and the base case (7 for anions and 2 for cations and non-charged species). Effective diffusivities in the base case (and for Forsmark) are given in Table 7-3.

Element	Base case: Laxemar [m^3 kg^{-1}]	Forsmark variant (relative to base case)	Olkiluoto variant (relative to base case)	Olkilouto effective diffusivity (relative to base case)
Ag	0.0007	0.5	0	7
Am	0.01		10	2
Be	0		[0.006 m^3 kg^{-1}]	2
Cd	0.002	0.5	0.5	2
Cm	0.01		10	2
Cs	0.0007	0.5	80	2
Mo	0		[0.0003 m^3 kg^{-1}]	7
Nb	0.02		20	7
Ni	0.002	0.5	3	2
Np	0.1	0.5	4	2
Pa	0.06		0.4	2
Pd	0.05		0.1	2
Pu	0.03	0.5	5	2
Ra	0.0005	0.5	6	2
Se	0.0003		0	7
Sm	0.01		10	2
Sr	0.000006	0.5	5	2
Tc	0.1	0.5	4	7
Th	0.05		8	7
U	0.1	0.5	0.2	7
Zr	0.02		20	7

Differences in most other retardation-related parameters between the sites are relatively small (Table 7-3). The same rock density of 2 700 kg/m^3 as was originally applied in both SR-Site (Table 6-55 in SKB 2010g) and TURVA-2012 (Table 7-14 in Posiva 2013) is used in both the base case and the alternative parameter sets of this evaluation case. The only difference between the base case (Laxemar) and Forsmark is the slightly lower matrix porosity estimated in Forsmark (0.18 % instead of 0.19 %). For the base case as well as in Forsmark the effective diffusivity of anions is about three times larger than for cations and neutral species. In Olkiluoto, a common effective diffusivity that is seven times higher than for anions and twice as large as for cations in the base case is used. Laxemar and Forsmark have a maximum penetration depth for matrix diffusion of 4.5 m and Olkiluoto has 3.0 m.

Table 7-3. Bedrock density, matrix porosity, effective diffusivity and maximum penetration depth values applied in the base case and the *alternative geosphere retention properties evaluation case*.

	Laxemar	Forsmark	Olkiluoto
Rock density [kg m^{-3}]	2700	2700	2700
Matrix porosity [%]	0.19	0.18	0.5
Effective diffusivity for cations and non-charged species [m^2 a^{-1}]	8.5×10^{-7}	8.5×10^{-7}	1.9×10^{-6}
Effective diffusivity for anions [m^2 a^{-1}]	2.7×10^{-7}	2.7×10^{-7}	1.9×10^{-6}
Maximum penetration depth [m]	4.5	4.5	3.0

A decreased penetration depth from 4.5 m to 3.0 m will influence the geosphere release only marginally for sorbing radionuclides with a significant retention in the geosphere (see Appendix B). Mobile, long-lived radionuclides could potentially diffuse further into the matrix than three meters, but this will only affect the geosphere releases marginally due to their low decay rate.

7.4.2 Effects of porosity, diffusivity and sorption on relative geosphere releases

The analytical steady-state solution of the relative geosphere release N_{geo}/N_{NF} [Bq a^{-1}/(Bq a^{-1})] can be expressed as an exponential function of the effective decay rate for the flow pathway times the advective travel time (see Chapter 5.2.9)[6]:

$$N_{\text{geo}}/N_{NF} = e^{-\lambda^n_{\text{pathway}} t_w} \quad \text{7-1}$$

where

t_w : Total advective travel time [a].

$\lambda^n_{\text{pathway}}$: Is the effective decay rate for the flow pathway for radionuclide n [a^{-1}] defined as:

$$\lambda^n_{\text{pathway}} = \lambda^n + a_w \sqrt{\lambda^n D_e^n (\varepsilon_m + K^n_{d,m} \rho_m)} \quad \text{7-2}$$

where

a_w : Area of the flow-wetted surface per volume of water [m^2 m^{-3}].

λ^n : Decay rate for radionuclide n [a^{-1}].

D_e^n : Effective diffusivity of radionuclide n in the rock matrix [m^2 a^{-1}].

ε_m : Porosity of the rock matrix [-].

$K^n_{d,m}$: Sorption coefficient in rock matrix for radionuclide n [m^3 kg^{-1}].

ρ_m : Bulk density of the rock matrix [kg m^{-3}].

[6] The solution is for transport without longitudinal dispersion and an infinite penetration depth into the rock matrix.

The effective pathway decay rate ($\lambda^n_{\text{pathway}}$) is a function of decay rate in the fracture (λ^n, first term in right hand side of Equation 7-2) and decay rate in the rock matrix ($a_w\sqrt{\lambda^n D_e^n(\varepsilon_m + K_{d,m}^n \rho_m)}$, right term). Decay of short-lived non-sorbing radionuclides ($K_d = 0$) mainly occurs in fractures ($\lambda^n > a_w\sqrt{\lambda^n D_e^n \varepsilon_m}$) and is consequently not significantly affected by changes in the matrix porosity and effective diffusivity. Long-lived (i.e. small λ^n) non-sorbing radionuclides (e.g. Cl-36) may penetrate far into the rock matrix, and the decay in the matrix can be substantial ($\lambda^n < a_w\sqrt{\lambda^n D_e^n \varepsilon_m}$) . Thus, the higher porosity and effective diffusivity in the Olkiluoto parameter set results in a higher effective pathway decay rate than in the base case. However, since the pathway decay rate of mobile long-lived radionuclides is anyway very small, almost all the near-field release will cross the geosphere despite the increase in porosity (2.5 times) and effective diffusivity (2–7 times), and thus the relative geosphere release is not substantially influenced. Decay of sorbing radionuclides ($K_d > 0$ and $K^n_{d,m}\rho_m \gg \varepsilon_m$) mainly occurs in the rock matrix ($a_w\sqrt{\lambda^n D_e^n K_{d,m}^n \rho_m} \gg \lambda^n$), and the decay is thus positively related to changes in both effective diffusivity (D_e) and the sorption coefficient (K_d).

The diffusivity is identical between the Forsmark set and the base case and consequently the higher relative geosphere releases in the Forsmark variant of some radionuclides (Figure 7-7) are only caused by the lower sorption coefficients (K_d). Since the relative geosphere release is exponentially related to the pathway decay rate, a decrease of the K_d value (or diffusivity) by a factor of two has a larger effect on the geosphere release for radionuclides with high pathway decay rates (i.e. radionuclides with a low relative geosphere release in the first panel of Figure 7-7).

For the Olkiluoto parameter set, changes in relative geosphere release of sorbing radionuclides in relation to the base case are caused both by increased diffusivity (D_e) and changes in sorption (K_d). Relative changes in D_e and K_d have equal and multiplicative effects on the effective pathway decay rate. The increased effective diffusivity (by a factor of 2 or 7) results in lower relative geosphere releases and the relative change is stronger with lower relative geosphere releases (Figure 7-7, red squares in the mid panel). For radionuclides which have a higher K_d value in Olkiluoto than in the base case, the multiplicative effects of the increased diffusivity and increased sorption magnify the decay in the rock matrix and decrease geosphere releases further (e.g. Tc-99 and Mo-93). However, for radionuclides which have lower K_d values in Olkiluoto than in the base case, the increased diffusivity and the decreased sorption counteract each other. This can result in a negligible change in the relative release (e.g. U-238) or even higher relative releases than in the base case, when the relative decrease of the K_d value exceeds the relative increase in diffusivity (e.g. Ag-108m).

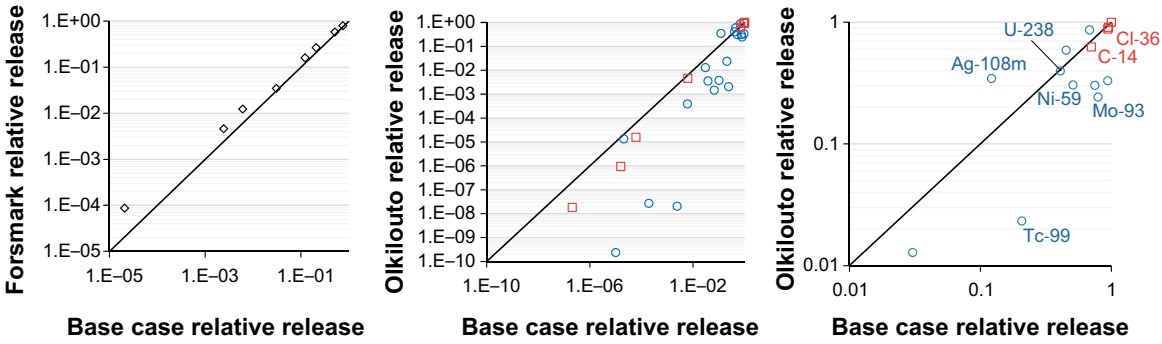

Figure 7-7. *The relative geosphere release of radionuclides from BHA (excluding decay products) with the Forsmark and Olkiluoto parameter sets as a function of the base case releases. The black lines show the 1:1 relationship between the alternative retention parameter sets and the base case. The lower K_d values in the Forsmark set result in higher relative releases and the effect is most pronounced for radionuclides with a low base case release (left panel). The red squares (mid and right panels, Olkiluoto parameters) are radionuclides with increased effective diffusivity but no change in K_d, and the blue circles represent radionuclides with increased diffusivity and changing K_d (increased or decreased, see Table 7-2). The right panel is a zoomed in version of the upper right corner of the mid panel.*

7.4.3 Release from the geosphere model and annual doses

For radionuclides that do not sorb in the geosphere (e.g. C-14 and Cl-36), the geosphere release is insensitive to changes in the retention properties of the geosphere (Figures 7-8 and 7-9). Thus, the combined effect of changes in matrix porosity, effective diffusivity and maximum penetration depth influence the radionuclide specific dose from C-14 and Cl-36 only marginally (< 12 % change). Moreover, a modest reduction in sorption (a factor of ~2 in the Forsmark data) also has a limited effect on the geosphere release of (Figure 7-8 and Figure 7-9) and on the annual dose from sorbing radionuclides (Ag-108m, Ni-59, Tc-99, U-238).

However, the combined effects of increased diffusivity and significant changes in K_d values (as it occurs in the Olkiluoto parameter set) may result in significant changes in the geosphere releases of sorbing radionuclides. For example, the maximum annual geosphere release of Tc-99 from BHA is reduced by a factor of ten, and the maximum release of Mo-93 is reduced to a third (BHA) or half (BHK) of the maximum release in the base case (Figure 7-8 and Figure 7-9). Changes in annual doses are proportional to the changes in the geosphere releases. The decreased geosphere release of Mo-93, makes Cl-36 dominate the maximum annual dose from BHA instead of Mo-93 as in the base case (Figure 7-10).

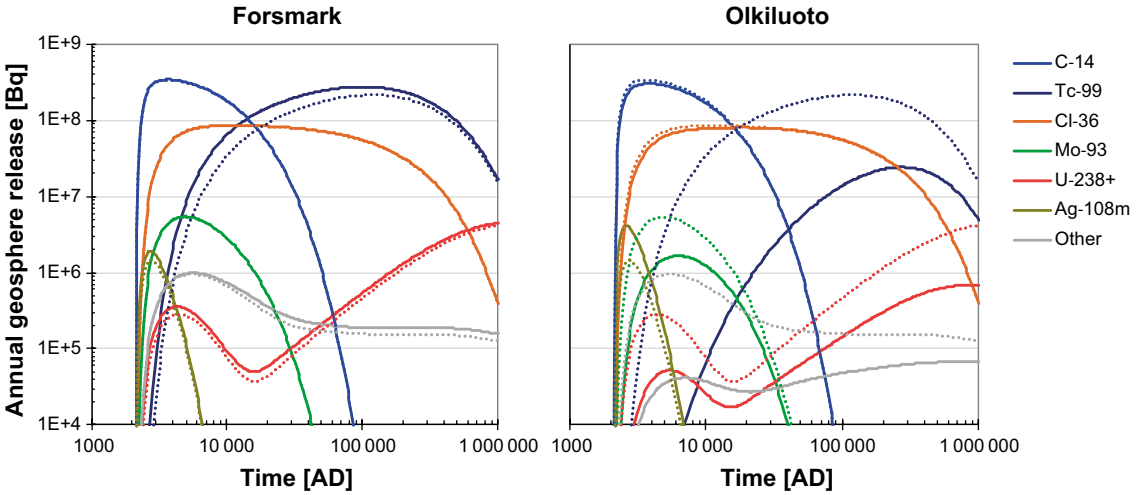

Figure 7-8. Radionuclide release from the geosphere for BHA in the Forsmark variant (left panel) and Olkiluoto variant (right panel) of the alternative geosphere retention evaluation case. Geosphere releases in the base case are shown as dotted lines for comparison.

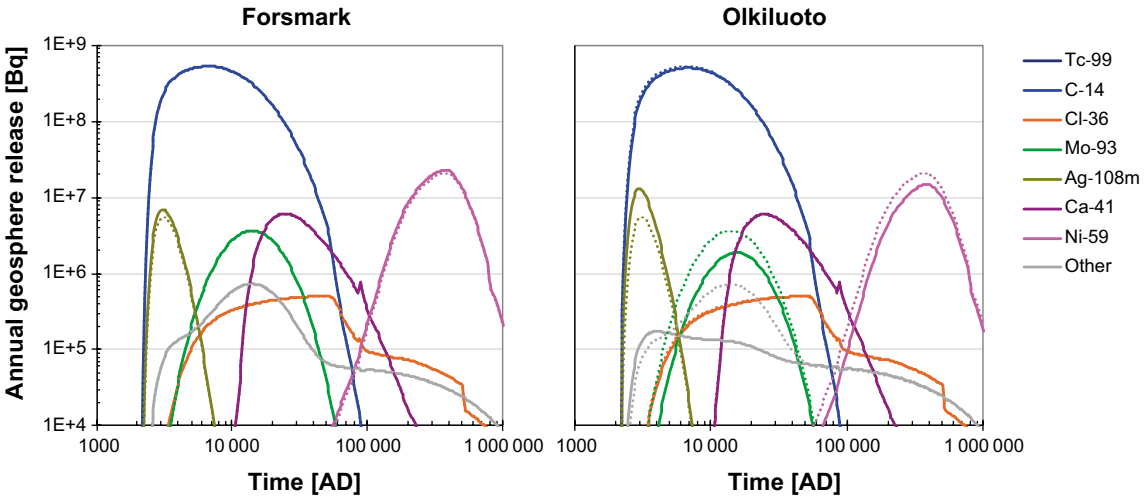

Figure 7-9. Radionuclide release from the geosphere for BHK in the Forsmark variant (left panel) and Olkiluoto variant (right panel) of the alternative geosphere retention evaluation case. Geosphere releases in the base case are shown as dotted lines for comparison.

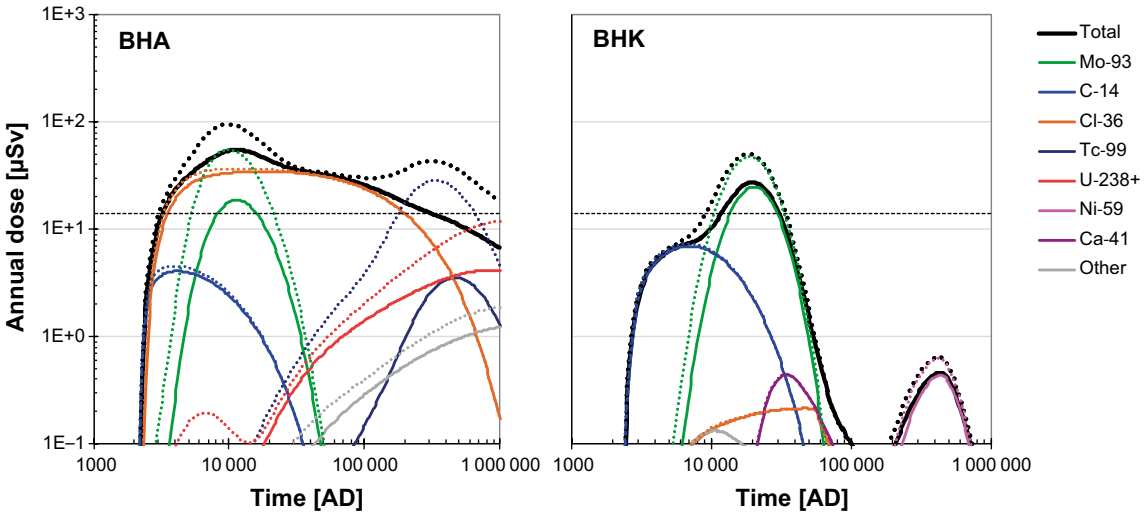

Figure 7-10. *Annual doses from BHA (left panel) and BHK (right) with the Olkiluoto retention parameter set (solid lines) and for the base case (dotted lines).*

The lower K_d value for U-238 in Olkiluoto almost cancels out the negative effect on relative releases by the increased diffusivity (Figure 7-7), but higher K_d values of some of its decay products (Th-230 and Ra-226) increase their decay in the geosphere. This results in lower geosphere releases and doses from the entire decay chain (U-238+ in Figure 7-8 and Figure 7-10). The effect of changing the K_d value for Ag-108m from 0.0007 kg m^{-3} in the base case to zero in Olkiluoto exceeds the effect of the increased diffusivity and increases maximum geosphere releases by 2–3 times. However, maximum doses from Ag-108m are still three orders of magnitude lower than total maximum doses (not shown). The significant decrease in the maximum annual release of unspecified radionuclides (called Other in Figures 7-8 and 7-9) in the Olkiluoto variant in both BHA and BHK is mainly caused by the decreased release of Nb-93m. This is explained by the 20 times increase in the K_d value in combination with the seven times increase in diffusivity, despite an increased ingrowth of Nb-93m from Mo-93 in the geosphere in Olkiluoto.

7.4.4 Conclusions

- Geosphere retention and decay of the mobile radionuclides in the SFL repository (e.g. Mo-93, Cl-36 and C-14) is small and the relatively limited changes in diffusivity, porosity and penetration depth in the Forsmark and Olkiluoto variants are not large enough to have any impact.
- Retention and decay of sorbing nuclides are positively related to the effective diffusivity (D_e), sorption (K_d) and rock density (although density is constant between retention cases), and the sensitivity of the relative geosphere release to relative changes in those parameters is larger for radionuclides with a high proportion of decay in the geosphere.
- The reduction by a factor two of K_d values in the Forsmark set has a limited effect on geosphere releases of sorbing nuclides and since the main dose contributors, Mo-93, Cl-36 and C-14, are non-sorbing in both the Forsmark data set and in the base case, the effects on total annual doses during the first 100 000 years is marginal.
- The increased diffusivity in combination with changing the K_d value for Mo-93 from zero in the base case to non-zero in the Olkiluoto set, decreases the Mo-93 release and its maximum dose from BHA by a factor three. This makes Cl-36 the main contributor to the maximum annual dose instead of Mo-93 (Figure 7-10) and the maximum total annual dose decreases by a factor of two. In addition, the second maximum in annual doses from BHA is significantly reduced due to the increased diffusivity and higher sorption of Tc-99 in Olkiluoto than in the base case. BHK releases display similar but smaller effects for Mo-93 and Ni-59 (instead of Tc-99).

- The sensitivity of the relative geosphere release to relative changes in diffusivity and K_d values is larger for radionuclides with a higher proportion of decay in the geosphere. Thus, the choice of retardation parameters is most important for relatively strongly retarded and dose-contributing radionuclides like Tc-99. Geosphere releases and annual doses from most high-retention radionuclides are very low due to decay in the near-field and the geosphere, and substantial K_d value reductions are needed for these radionuclides to become noticeable. Furthermore, a shift between non-sorbing ($K_d = 0$) and sorbing ($K_d > 0$) behaviour could also influence geosphere releases and doses substantially and should be carefully considered for some cases, particularly for Mo-93.

7.5 Alternative realisations of stochastic bedrock fractures

The groundwater flow through the bedrock is modelled using a discrete fracture network (DFN) approach (Joyce et al. 2019). The network contains deterministic fractures and also fractures generated stochastically from the derived fracture network statistics, assuming that the positions of the fractures are generated from a Poisson process, i.e. they are randomly distributed in space. The orientation of the stochastic fractures is assumed to follow a Fisher distribution, and the size of the fractures is described with a power-law distribution. Finally, the transmissivity of fractures is calculated assuming that it is semi-correlated with the fracture size (Tables 3-2 to 3-5 in Joyce et al. 2019).

The stochastically generated DFN realisations will differ both with respect to the number of fractures intersecting each vault and their properties near the repository, and with respect to the characteristics of the flow pathways from repository depth to the surface. In this evaluation case, the sensitivity of the performance of BHA (including the bedrock as a natural barrier) to variations in the discrete fracture network is examined.

7.5.1 Handling in the near-field and geosphere model

Five DFN realisations were performed and, for each realisation, the BHA repository was assumed to be located either at its original position (East) or at the BHK position (West). The first realisation (r1) uses a hydraulic conductor domain (HCD) with deterministic depth-dependent properties (Joyce et al. 2019). In this realisation, which was selected for the base case (Section 5.2.5), the repository is comparatively well connected to the geosphere. The other four realisations treat the hydraulic properties of the deformation zones stochastically, accounting for a depth dependency of the properties. Although the number of realisations may be insufficient to fully assess the variability that is associated with the stochastic properties of the DFN, they should still give a reasonable indication of the likely spread of effects on transport and dose that can be expected between individual realisations.

For the western position, the conditions at the outer geometry of the BHA vault are approximated with those outside BHK. Within the BHA waste vault, transport is dominated by diffusion, and therefore the advective flow through the near-field was not modified in the alternative DFN realisations. Thus, in total, ten DFN variants were studied, and each of these variants has its unique set of connectivity parameters (R_{plugtot} and Q_{eq}, Section 5.2.8) and a unique distribution of flow pathways (characterised by the two parameters t_w and a_w, Section 5.2.5 and Figure 7-11). In Figure 7-11, results for the East position are illustrated in terms of the connectivity parameter Q_{eq} and the flow pathway travel time t_w. All other near-field and geosphere parameters are the same as in the base case.

7.5.2 Annual release from the near-field model

The release from the BHA waste vault is controlled by diffusion in the proximity of the narrow bedrock fractures (that is characterised with the lumped plug resistance $R_{\text{plugtot,}}$) and by the capacity of the groundwater to transport radionuclides into the fractures in the bedrock (characterised by the equivalent flow rate Q_{eq}; see Section 5.2.8 for details). Both of these properties are affected by the fracture network (i.e. they are a function of the number of intersecting fractures, the length of the intersections, the flow and aperture in the first fractures), and the effective flow Q_{tot}, [m^3 $year^{-1}$] which transports radionuclides from the waste vault to the bedrock can be approximated as: $Q_{tot} \sim (R_{\text{plugtot}} + Q_{eq}^{-1})^{-1}$.

The range in the maximum near-field release between the ten examined DFN variants is limited to less than a factor three (Figure 7-12), and the variation is tightly linked to the DFN realisation

(p-value ≤ 0.01).[7] Thus, the release in realisation one is consistently higher than that in realisation two, and the releases from the other three realisations fall in between. There is also a tendency for a higher release from the East than from the West position. This difference is most likely related to the larger dimensions of the BHA waste vault, which will lead (on average) to a larger number of intersecting fractures.[8]

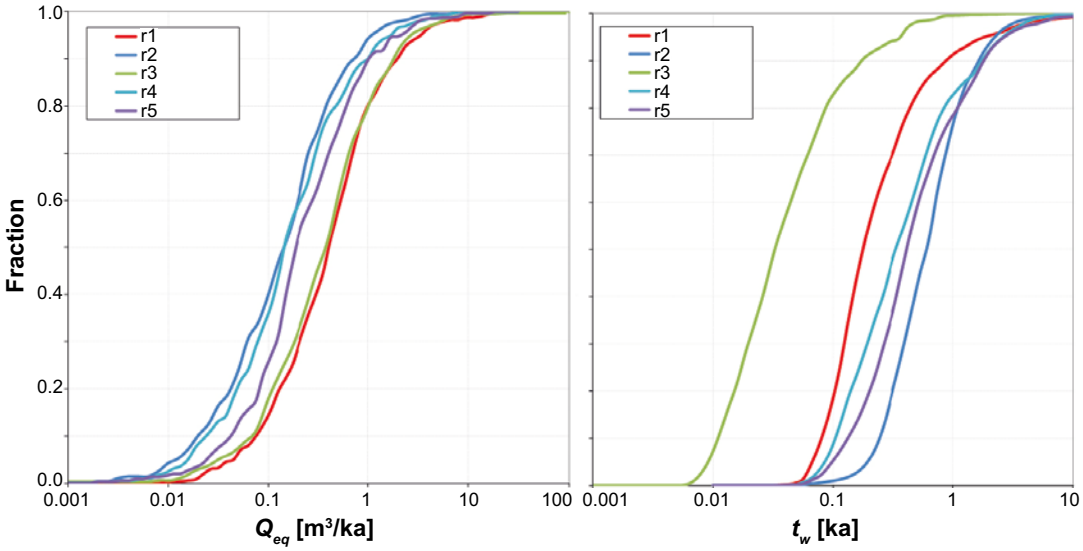

Figure 7-11. *Connectivity and flow pathway characteristics from BHA in the East position for the five different DFN realisations. The graphs show the cumulative distribution functions for Q_{eq} (left) and t_w (right) of particles reaching the surface. r1 (red curve) is the realisation used in the base case. In realisations 1 and 3, large sub-vertical fractures intersecting the vaults cause significantly higher Q_{eq} values and significantly lower t_w values. Figure adapted from Joyce et al. (2019).*

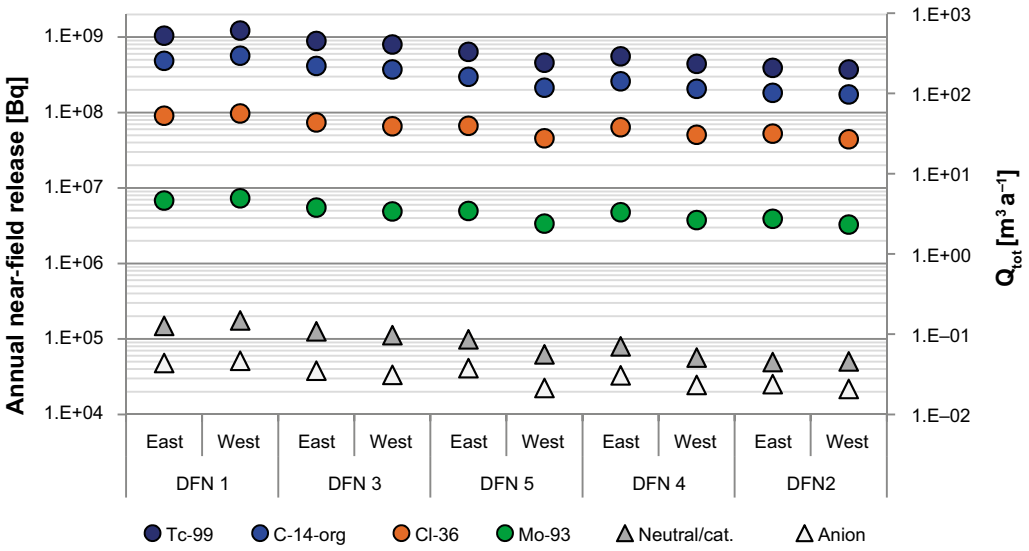

Figure 7-12. *Maximum annual release from the near-field of four radionuclides (coloured circles) as a function of DFN realisation and waste vault position. The variation in release rate is controlled by the plug resistance of the fractures in the repository-bedrock interface and the capacity of the flowing water in the rock to transport radionuclides, and the combined effect of these two factors is summarized in the effective transport flow (Q_{tot}, grey triangles).*

[7] P-values are from ANOVA with realisation and position as fixed factors.

[8] The external dimensions of the BHA waste vault (East) is 169 × 21 × 18 m, and the dimensions of the BHK waste vault (West) are 134 × 21 × 20 m.

7.5.3 Annual relative release from the geosphere model

A large number of flow pathways (~$1-2 \times 10^3$) are used to calculate transport (and decay) from the waste vault to the surface in each DFN realisation (Joyce et al. 2019). Each flow pathway is characterised by a travel time t_w [a] and an area of the flow-wetted surface per volume of water, a_w [m^2/m^3]. A large advective flow, corresponding to a short travel time, favours transport towards the surface, whereas a large flow-wetted surface increases diffusion into the rock matrix. The rate of diffusion into the rock matrix is typically much larger than the rate of advective flow, and thus the release from the geosphere to the biosphere will be delayed, and reduced by radioactive decay, in the rock matrix. The degree of delay and reduction strongly depends on the degree of sorption in the rock matrix and the radioactive half-life (Section 5.2.9).

To examine the effects of the different realisation of fracture network on the geosphere transport, the variation in the maximum geosphere release rate is expressed as a proportion to the maximum near-field release rate. The sensitivity of this relative release to variation in geosphere transport properties in different DFN realisations differs greatly between radionuclides (Figure 7-13). Thus, whereas the range of variation in the relative release of mobile radionuclides is limited (i.e. 20 % for Cl-36 and a factor of 2 for C-14 and Mo-93), the proportion of the near-field release that reaches the biosphere varies by almost an order of magnitude for Tc-99 (i.e. between 6.2 % and 60 %). The higher degree of reduction, and the higher sensitive to the fracture network of Tc-99 (as compared with mobile radionuclides) is primarily due to sorption in the rock matrix ($K_{d,\text{Tc-99}} = 9.9 \times 10^{-2}\ m^3\ kg^{-1}$). Most of the near-field release of the three mobile radionuclides reaches the surface, and differences in reduction between the mobile radionuclides primarily reflects differences in radioactive half-life, and to a lesser extent the dynamics of the near-field release (i.e. the period with a high release rate is relatively short for C-14 and relatively long for Cl-36).

The median flow wetted area (a_w) is 60 % higher in the eastern position than in the western position, and it varies by a factor of three between DFN realisations (p-values 0.003 and 0.002). Moreover, the median travel time (t_w) differs by more than an order of magnitude between DFN realisations, i.e. from less than 50 years in realisation three to more than 500 years in realisation two, p-value = 0.01. For Tc-99, practically all activity in the geosphere occurs as solid state (within the rock matrix), and consequently the relationship between the rate of diffusion into the rock matrix and the rate of advection towards the surface will be a key factor determining the retention and decay of the near-field release. The effects of diffusion increase with travel time and the flow-wetted surface, and thus there is a strong relationship between the median value of the product $t_w \times a_w$ (i.e. F_w) and the geosphere release of Tc-99 (Figure 7-13). For mobile radionuclides diffusion is also important. However, long travel time as a single parameter is more important for reduction of the near-field release of C-14 and Mo-93 (which have half-lives of a few thousand years). Moreover, the reduction of the release is only weakly linked to the median (or average) characteristics of the DFN, since the decay that is reducing the near-field release occurs in a minor fraction of flow pathways (those associated with a long travel times). Consequently, significantly less of the variation in the release of mobile radionuclides between DFN realisations can be explained by variation of the relationship between diffusion and advection, i.e. the median of the product $t_w \times a_w = F_w$.

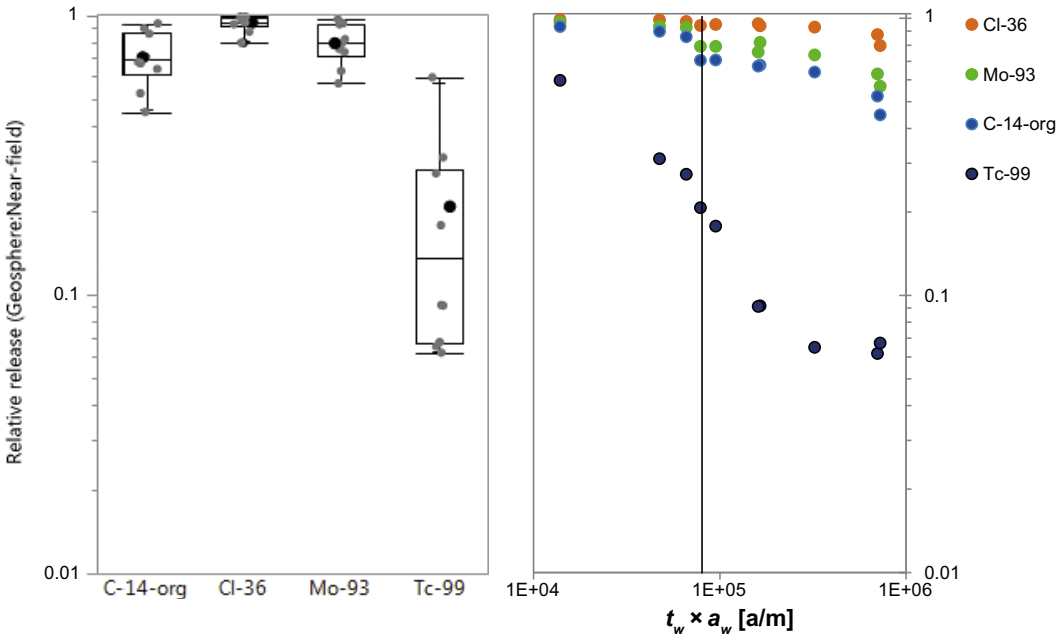

Figure 7-13. *Maximum geosphere release rates of four radionuclides, relative to maximum near-field release rates, and their dependence on flow-pathway properties for ten DFN variants. Left: Box-plot showing the distribution of geosphere release (25th, 50th and 75th) over the ten variant calculations. Whiskers indicate the range (max and min), and the values of individual variants are shown as filled circles. Right: Relative geosphere release as a function of the median value for the product of transport time (t_w) and volume specific flow wetted surface (a_w). The base case is shown in both panels for reference (large black circle in the left panel and dashed line in the right panel).*

7.5.4 Annual release from the geosphere model and annual doses

Stochastic variation in the discrete fracture network has a substantial effect on the geosphere release of mobile radionuclides, i.e. the releases span a factor of between 2 and 5 between variants, and an even larger effect on the release of Tc-99 (the corresponding factor is 20; Figure 7-14). As it is assumed that the biosphere object receiving the release is the same in all variants, and that the discharge of groundwater from the bedrock is unaffected by the fracture network, the response in annual doses primarily reflects variations in the geosphere release. Thus, the range in dose during the first maximum (~10 000 AD) spans a factor of 2.6, which is similar to that of the geosphere release of Mo-93 (Figure 7-14). In the base case, exposure to Tc-99 is underlying the second dose maximum. This is also true for the DFN variants that yield similar or higher doses. However, in variants where the pathways of the fracture network have a relatively long transport time, and/or a large flow-wetted area, the geosphere release of Tc-99 is significantly reduced. For these variants, it is instead release of Cl-36 that contributes most to the dose around 300 000 AD, and consequently the dose span at this time is considerably smaller than (~ one third of) the span in the geosphere release of Tc-99.

The fracture network affects both the connectivity between the waste vault and the geosphere, and the flow pathways to the surface. The relative importance of DFN effects on the near-field and the geosphere transport varies with radionuclide. Thus, for Cl-36, differences in the near-field connectivity are the primary source of variation in the geosphere release and the radionuclide-specific dose. On the other hand, differences in the flow pathways through the bedrock are by far the most important driver of the variation in geosphere release of, and dose from, Tc-99. For C-14 and Mo-93, both components contribute to release and dose variation, but the effects from the near-field connectivity are somewhat larger. There is a negative correlation between the capacity of the groundwater passing the BHA to transport radionuclides (Q_{eq}) and the advective travel times from repository depth to the surface (median t_w) ($r^2 = 0.5$). This suggests that DFN variants may modulate overall hydraulic characteristics in ways that influence the near-field and the geosphere transport in the same direction. This is reasonable as large fractures intersecting the vaults can provide connectivity from the vaults to other large flow-carrying fractures and provide direct pathways to the surface. Such overall influence will inflate the variation in the geosphere release (of C-14, Mo-93 and Tc-99), as compared with localized effects affecting transport properties in the near-field and the geosphere independently.

Although the properties of the fracture network have a noticeable effect on the dose from several important radionuclides, uncertainty with respect to the DFN realisations is not likely to have a significant influence on the results of this safety evaluation. This is partly because of the limited sensitivity of non-sorbing radionuclides to variations in the fracture network, and partly because the properties assigned to the DFN in the base case result in doses that are above the average for all ten variants (Figure 7-14). The fracture network also affects the position of the release on the surface, and dispersion between discharge areas. Both of these effects are also expected to have a limited effect on the resulting dose. This is because at least 40 % of the flow pathways in each realisation (from both repository locations) terminate in one discharge area (Joyce et al. 2019, **Biosphere synthesis**), and the potential effects of spatial dispersion are, therefore, limited. Moreover, the dose resulting from release to object 206 (used in the base case) is in between that resulting from a release into either of the other two potential biosphere objects that receive deep groundwater in the examined DFN realisations (i.e. the dose is 20 % lower than in 204 and 75 % higher than in 210) (see the *discharge area evaluation case* for details on the dose, Section 7.6). Thus, the effect of explicitly evaluating the dose in the areas that receive the release according to the specific DFN realisations is expected to be marginal compared with evaluating the dose in object 206 (as done in the base case).

7.5.5 Conclusions

Stochastic variation in the discrete fracture network has a notable effect of the geosphere release of mobile radionuclides such C-14, Cl-36 and Mo-93 and a significant effect on the release of Tc-99. The fracture network affects both the connectivity between the waste vault and the flow pathway to the surface and the characteristics of that flow pathway. For Cl-36, the difference in the connectivity is the primary source of variation in the geosphere release, whereas differences in the flow pathways through the bedrock is by far the most important source of the variation for release of Tc-99. Because Tc-99 sorbs in the rock matrix, the relationship between the rate of advection towards the surface and diffusion into the fracture is a key factor determining the activity reaching the biosphere. The geosphere transport of non-sorbing radionuclides with substantial near-field releases is also affected by the travel time and the volume-specific flow-wetted area, but they are far less sensitive to variations in DFN properties. The limited sensitivity of non-sorbing radionuclides and the selection of properties assigned to the DFN in the base case, together ensure that uncertainties with respect to the fracture network realisation are not likely to have a significant influence on the results of this safety evaluation. Nevertheless, large sub-vertical fractures intersecting a waste vault can influence both the connectivity of the vaults and provide direct pathways to the surface, and hence the occurrence and properties of such features is of key interest in a site characterisation.

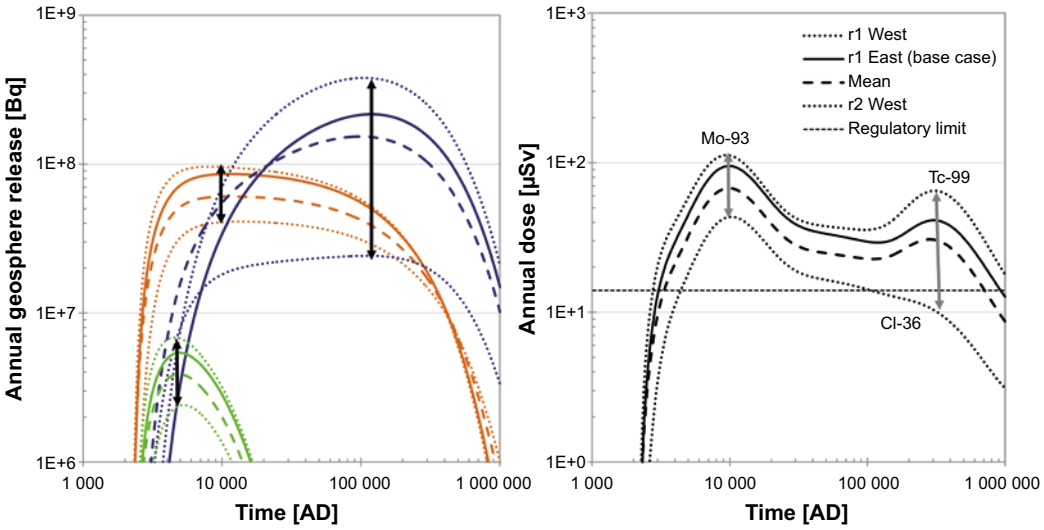

Figure 7-14. *Annual geosphere releases and annual doses from BHA in the alternative realisations of stochastic bedrock fractures evaluation case. The realisations with the largest and smallest values are indicated with dotted lines, the mean over ten DFN variants are shown with a dashed line, and the release and dose in the base case is shown with a solid line. Vertical arrows indicate the approximate range of maximum values. Left: Release of individual radionuclides; Cl-36 (brown), Mo-93(green) and Tc-99 (dark blue). Right: Annual dose; dominant dose-contributing radionuclide indicated with text.*

7.6 Alternative discharge area

7.6.1 General description

The *alternative discharge area evaluation case* simulates radionuclide releases from the geosphere into a range of sea basins, lakes, mires and agricultural fields. The main objective is to study how annual doses are affected by properties of the discharge area, and to what extent the simplifications made in the base case (i.e. terrestrial ecosystems in biosphere object 206) influence the projected doses. The representativeness of object 206, which is used in all other evaluation cases, is examined and discussed.

7.6.2 Handling in the near-field and geosphere models

All near-field and geosphere parameters are the same as in the base case. Thus, the size and temporal pattern of the release from the geosphere and repository into the lower regolith (till) of each biosphere object is the same as the release into object 206 in the base case (Section 5.2.9). This means that all radionuclides from BHA and BHK that reached the bedrock surface in the radionuclide transport model were respectively released into each of the biosphere objects used in the *alternative discharge area evaluation case*.

7.6.3 Handling in the biosphere model

Biosphere objects

The *alternative discharge area evaluation case* simulates releases into static biosphere objects in a permanent ecosystem state, i.e. sea bay, lake, mire or agricultural land. As in the base case, the ongoing shoreline displacement and landscape development is not considered. That is, the geometry and stratigraphy of the discharge area does not change, no biological succession is accounted for and present-day conditions are assumed for the entire assessment period of 1 million years (**Biosphere synthesis**). The effects of landscape development on annual doses are explored (**Biosphere synthesis**). The calculations of potential effects are limited to the primary discharge area, and exposure in down-stream objects is not evaluated.

Nine potential discharge areas of deep groundwater (i.e. biosphere objects) in Laxemar and six areas in Forsmark were used in the analysis. The selected biosphere objects vary with respect to geometrical properties (object and watershed surface area), the depths of water, the regolith stratigraphy, and associated groundwater flow.

The Laxemar objects (Figure 4-13) are five present agricultural ecosystems (object 204, 206, 210, 212 and 213), one mire (203), one lake (207), one sheltered (208) and one relatively open (201) coastal bay. The five agricultural objects and the three aquatic objects were also described as static mire ecosystems (that could have or will develop in the absence of human intervention). All Laxemar biosphere objects are likely discharge areas for deep groundwater, and thus the set illustrates the potential effect of alternative locations of a hypothetical SFL repository within the Laxemar area or of differences in transport pathways from the repository to the surface system.

The local and regional topography affects the geometry of ecosystems and the surface hydrology. With the Forsmark biosphere object set, the effects of a release to a landscape with a flatter topography are examined (Figure 3-13 in Grolander and Jaeschke 2019). The set consist of six presently submerged biosphere objects located above the SFR repository (SKB 2014e), but in this evaluation they are all assumed to be fully developed mires.

Landscape geometries and regolith properties

For the Laxemar objects, the regolith layer thicknesses from the present regolith depth model are used when available (Nyman et al. 2008). The regolith stratigraphy of mire ecosystems in present agricultural objects is set to reflect the mature mire state (for details see **Biosphere synthesis**). The object geometries and regolith layer thicknesses for the aquatic objects in Laxemar and mires in Forsmark are determined with the corresponding regolith lake development models (RLDM, Brydsten and Strömgren 2010, 2013; Grolander and Jaeschke 2019).

Object areas and regolith layer thicknesses of the fully developed static mires are used in the analysis of relationships between doses and object properties in Section 7.6.6. The object areas of the nine Laxemar and six Forsmark mire objects range between 8 and 150 ha, with object 206 being the smallest. Both large and small objects are represented in the Laxemar and Forsmark object sets (Figure 7-15). The total regolith thickness ranges between 3 and 15 m and the thickness of the till layer is less variable than that of the upper layers (Figure 7-15). The upper regolith layers are on average more variable and thinner in Forsmark than in Laxemar, with particularly thin peat (RegoPeat) and post-glacial sediments (RegoPG) in object 157_2 and 121_2. There is a positive correlation between the till and glacial clay layer thickness over objects as well as between the post-glacial sediment and the peat layer thickness, but no correlation between the lower and the upper layers (**Biosphere synthesis**). In relation to other biosphere objects, object 206 is a small object with intermediate regolith layer thicknesses.

Surface hydrology

The surface hydrology in biosphere objects is influenced by local topography, by regolith layer thicknesses and hydraulic properties, and by precipitation/evapotranspiration. The groundwater flows are the main driver of radionuclide transport. Groundwater flows in Forsmark and Laxemar have previously been simulated with the MIKE SHE software and the results summarized as water balances at the level of individual biosphere objects (Werner et al. 2013, Grolander and Jaeschke 2019). MIKE SHE water balances in *Laxemar* were available only for present conditions. Thus, to extrapolate ground- and surface-water flows to other ecosystems and successional stages, a stylised water balance model has been developed in SE-SFL (detailed description in Section 1.4 in Grolander and Jaeschke 2019). The model uses boundary conditions of net precipitation in the object, runoff from the catchment and discharge from the bedrock to calculate discharge within the object, accounting for the regolith stratigraphy and maintaining the water balance within each compartment. For consistency, all hydrological flows in Laxemar are calculated with this method.

For *Forsmark*, MIKE SHE water balances are available for a mature mire stage in all six biosphere objects (Werner et al. 2013), and consequently the parameters previously derived in SR-PSU for this stage (Grolander 2013, Werner et al. 2013) are used also in this evaluation.

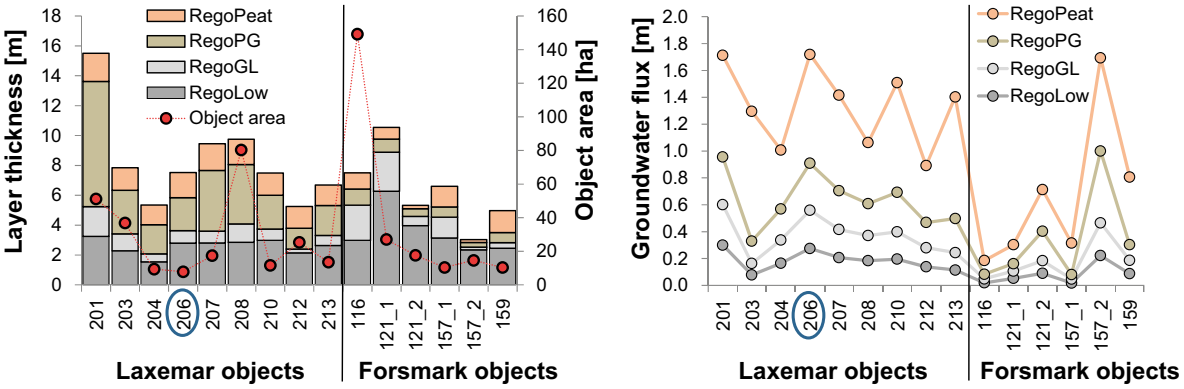

Figure 7-15. *Thicknesses of regolith layers (scale on left side) and areas of mire objects (scale on right side) in Laxemar and Forsmark (left panel) and upward groundwater flux (right panel) from the till (regoLow), glacial clay (RegoGL), post-glacial deposits (RegoPG) and peat (RegoPeat). The Forsmark objects are in general more variable than the Laxemar objects regarding upper regolith layer thicknesses and groundwater flows. Object 206 (blue circle) is a small object with intermediate regolith layer thicknesses and high groundwater flow.*

Upward groundwater flux (q) in the nine Laxemar and six Forsmark mire objects are used in the analysis of relationships between doses and object properties in Section 7.6.6. The groundwater flux increases towards the surface (Figure 7-15). The variation among objects ranges from a factor of 10 (upward flow from peat) to 20 (from till). Laxemar objects have in general higher groundwater flows than Forsmark objects, except for the relatively high flows in Forsmark object 157_2. Groundwater flows are positively correlated between regolith layers, so that objects with high flows from the till layer (RegoLow) also have high flows in the peat layer. Correlations between regolith thicknesses and groundwater flows are generally weak and so are correlations between object area and most other object properties, except that large objects tend to also have thick glacial clay layers (RegoPeat, **Biosphere synthesis**). Object 206 has a relatively high upward groundwater flux, in particular in comparison to most Forsmark objects.

Ecosystem parameters

In the *alternative discharge area evaluation case*, a main objective is to analyse how doses are influenced by object properties for possible biosphere objects at a coastal site in Sweden. Effects of site differences with respect to regional climate are evaluated in the *alternative regional climate evaluation case* (Section 7.7) and effects of uncertainties in chemical conditions and element sorption (K_d) are examined in separate sensitivity analyses (**Biosphere synthesis**). Thus, in this evaluation case, the same parameter values are used for element-related parameters, i.e. sorption coefficients K_d, and concentration ratios CR, in both Laxemar and Forsmark objects.

Since present-day conditions are assumed for the entire assessment period of 1 million years, the terrestrial parameter values (e.g. for biomass, productivity, and respiration) are identical to those used in the base case (Section 5.2.7; Grolander and Jaeschke 2019).

Exposed populations

The land-use variants from the base case are used also in this evaluation case. That is, a family farm is used to evaluate exposure from the continuously cultivated land (Agr), and the potential exposures from a mire ecosystem are evaluated for the exposed groups: hunter-gatherers (HG), infield–outland farmers (IO), a household with a garden-plot (GP), and a family farm cultivating the drained mire (DM). Doses from farming (Agr, DM, IO) include exposure through water from a dug well, but doses without the well contribution are estimated for comparison. Aquatic systems (sea bays and lakes) are evaluated for hunter-gatherers only.

7.6.4 Annual doses by ecosystem type and land use variant

Doses from draining and cultivating a mire always exceed doses from other mire land-use variants and doses from static agricultural systems (Figure 7-16) and these findings are consistent with the base case results (Section 5.2). This is explained by the additional contribution from the accumulated inventory of radionuclides in the upper mire layers that becomes available for plant uptake after draining. Due to the lower water turnover rate, the maximum annual doses from lakes are typically higher than the corresponding doses from the open sea stage, and aquatic doses are dominated by the C-14 contribution through fish consumption (Figure 7-16).

Since doses in terrestrial ecosystems are highest for drained mires, this land use was adopted to analyse the relationship between doses and object properties, as described in Section 7.6.6. In some cases, e.g. if releases of C-14 are substantial in large objects, like BHK releases into object 201 and 208 (Figure 7-16), doses could be higher for hunter-gatherers in aquatic objects with low water turnover times (e.g. lakes) than in the corresponding drained mire objects. However, doses from such objects are relatively stable between objects and an analysis of relationships between doses and object properties is, therefore, of limited interest.

7.6.5 Total and radionuclide-specific annual doses

The radionuclide composition of releases from the geosphere, in combination with biosphere object properties, determines the radionuclide contributions to the total doses. The drained mire doses, including the dug well contribution, from nine Laxemar and six Forsmark objects are included in the analysis of the relationship between doses and object properties (Section 7.6.6). Those are compared with doses from the five Laxemar objects evaluated as static agricultural systems, as well as the exposed sea basin, the sheltered sea bay and the three lakes in Laxemar (Figure 7-16).

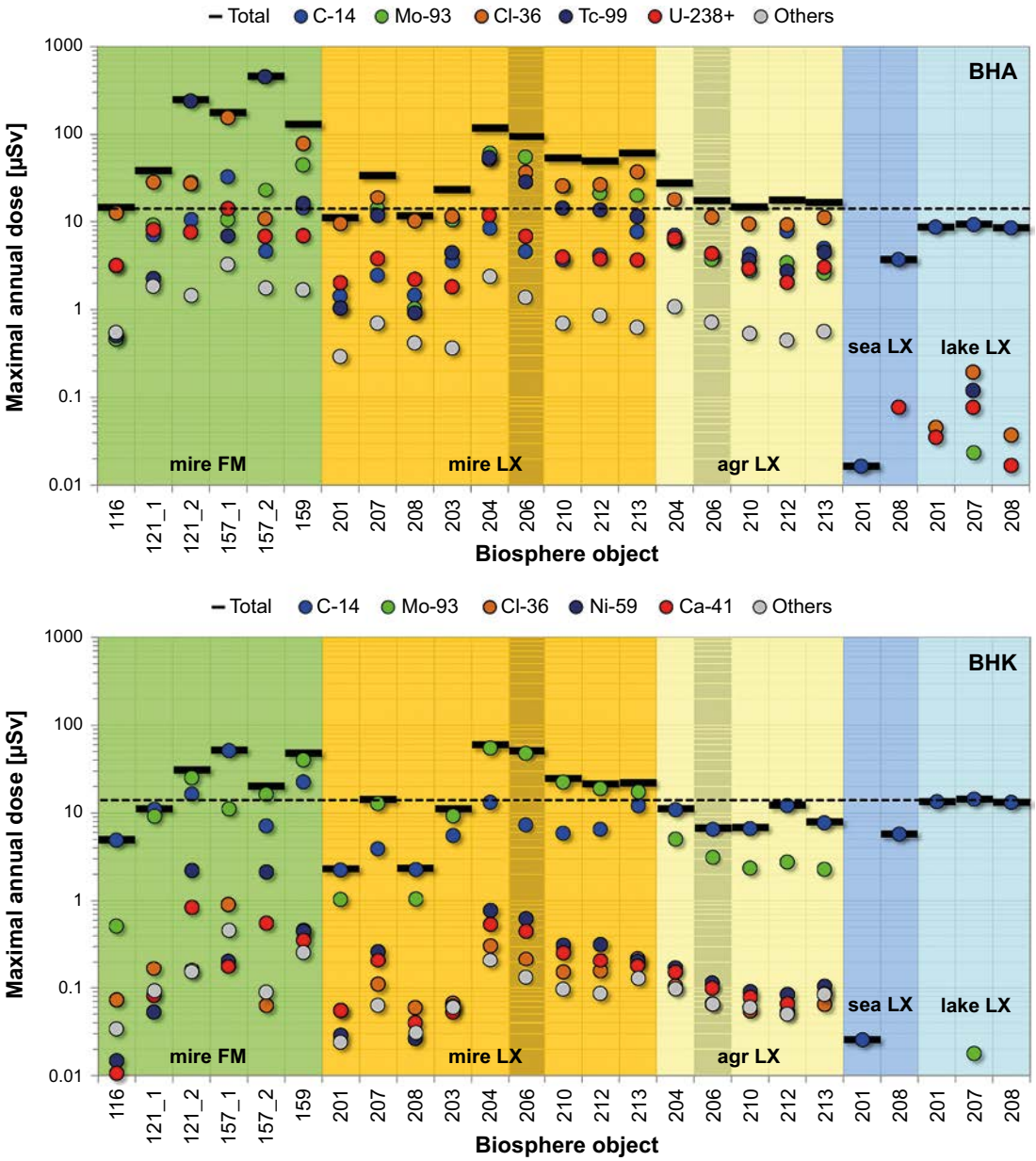

Figure 7-16. *Maximum annual doses from the most important radionuclides in objects from Forsmark (FM, green background) and Laxemar (LX, all other background colours) from BHA (upper panel) and BHK (lower panel). The base case object 206 is indicated in darker shade. Static mire objects in Forsmark (green background) and Laxemar (orange background) are represented by drained mire doses including exposure from a dug well. Static agricultural objects (yellow) include exposure from a dug well and static sea (blue) and lake (light blue) objects are represented by doses to hunter-gatherers. The dose corresponding to the regulatory risk limit is shown with a dashed horizontal black line (14 µSv). Note that the sum of the radionuclide-specific doses can be larger than the total dose, since the doses from individual radionuclides reach their maxima at different times.*

The maximum total mire dose (from BHA and BHK) in object 206 is, together with object 204, higher than the doses from other mire objects modelled in Laxemar. However, there is more variation in total doses from BHA releases among the Forsmark mire objects, with higher estimated doses in some objects (121_2, 157_1, 157_2 and 159) than in object 206. For BHK releases, doses in Forsmark objects were lower than in object 206.

The dose-dominating radionuclides from BHA releases were Cl-36, Mo-93, Tc-99, C-14 and radionuclides in the U-238 decay chain (Figure 7-16). Cl-36 dominated the dose in most drained mires and all stationary agricultural objects. In several Laxemar mire objects, the Mo-93 dose was almost as high as the Cl-36 dose and even slightly higher in objects 204 and 206. Tc-99 was the third most important radionuclide in several Laxemar mire objects, but clearly dominated in two Forsmark mire objects (121_2 and 157_2). In static agricultural objects, Cl-36 was generally more dominant than in the mires. In aquatic objects, the dose contribution from C-14 was more than one order of magnitude larger than that from the second next most important radionuclide. The explanation is that C-14 gives a high dose from fish consumption and this pattern is consistent with results from the SR-PSU safety assessment (SKB 2014e).

Drained mire doses from BHK-releases were dominated by Mo-93 and C-14, and the doses from the next most important radionuclides (Cl-36, Ni-59 or Ca-41) never contributed more than 10 % to the total dose. In static agricultural systems, C-14 was the most important dose contributor followed by Mo-93, and in aquatic systems C-14 totally dominated.

7.6.6 Relationship between doses and object properties

Radionuclides behave and respond differently to biosphere object properties due to their differences in decay rates and sorption properties. Non- and weakly sorbing (i.e. mobile) radionuclides with relatively slow decay rates are transported with the groundwater flow (e.g. C-14 and Cl-36), whereas sorbing radionuclides with relatively fast decay are retarded in and decay in the regolith (e.g. Ag-108m and Po-210). The lower decay rate, the higher sorption is needed for a radionuclide to decay in the regolith instead of being transported through the it. Several dose-contributing radionuclides, such as Mo-93, Tc-99 and U-234, are within an intermediate group that is regulated by transport or decay, depending on the properties of the biosphere objects.

Doses depend on radionuclide-specific environmental activity concentrations in different media. Doses from drinking and using well water are assumed proportional to the porewater concentration in the till layer. The doses from ingestion of food, obtained through plant uptake from the drained mire, are proportional to the activity concentration in the cultivated soil. The doses from well water and from the cultivated soil respectively, differ between radionuclides and are strongly influenced by their decay rates and sorption to specific regolith layers. To simplify understanding and interpretation of the relationships between doses and biosphere object properties, exposure from well water and cultivated soil respectively, are initially analysed separately for specific radionuclide groups below.

Well dose

A stylised model for a one-layer system (**Biosphere synthesis**, and Saetre and Ekström 2017) projects that doses from mobile radionuclides (e.g. Cl-36 and C-14) should be proportional to the inverse of the groundwater flow (volumetric flow Q [$m^3\ a^{-1}$]. There is a strong relationship between the inverse of the upward flow of groundwater [$m^3\ a^{-1}$] and the well dose from C-14 and Cl-36, explaining about 98 % of the variation (Figure 7-17). The model projects that strongly sorbing radionuclides will be retained and decay in the till. Thus, the activities and doses will instead be proportional to the inverse of the volume of the till layer. The variation in well doses of strongly sorbing and long-lived radionuclides such as Ra-226, Po-210 and Pb-210 between objects is almost completely explained by the inverse of the regolith volume (Figure 7-17).

The volumetric groundwater flow and the regolith volume are both functions of the object area. Thus, the dose from both non-sorbing and more strongly sorbing radionuclides is in fact related to the inverse of the object area $1/A$ [m^{-2}]. For mobile radionuclides the remaining effect of dilution is explained by the inverse of the groundwater flux $1/q$ [$a\ m^{-1}$] and for more strongly sorbing radionuclides the dose is related to the inverse of till thickness $1/z$ [m^{-1}] (Figure 7-17).

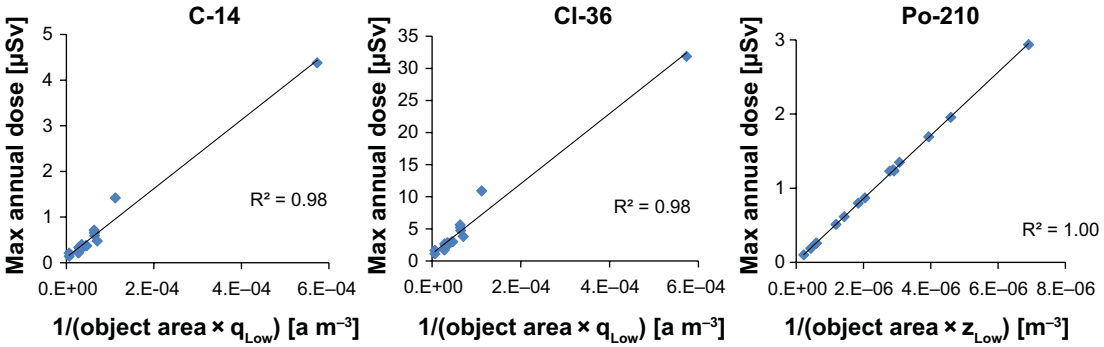

Figure 7-17. *Maximum annual doses from ingestion of well water as a function of object properties. The dose from mobile radionuclides (C-14 and Cl-36) is strongly related to the inverse of the product of the object area and the annual groundwater flux through the till (1/(object area × q_{Low})) which equals the inverse of the volumetric flow of water through till (1/Q_{Low}). Doses from strongly sorbing radionuclides (e.g. Po-210) are related to the inverse of the product of the object area and the till layer thickness (1/(object area × z_{Low})), which equals the inverse of the volume (or mass) of the till layer (1/V_{Low}).*

Doses from cultivated soil

Mobile and long-lived radionuclides are transported up through the regolith without significant losses by decay. Consequently, the activity concentrations in the upper regolith layers, from where the dose from cultivated soils originates, is regulated only by the diluting groundwater flow, similarly as for the well dose. C-14 is assumed not to accumulate by sorption ($K_d = 0$) in the upper regolith layers in the mire, and groundwater uptake from the saturated layer dominates the contribution to the activity concentration in the cultivated soil. There is a strong relationship between doses and the inverse of the upward flow from the layer from which the groundwater uptake occurs (Figure 7-18). Cl-36 displays a similar pattern, but in addition to the groundwater uptake from the saturated layer, the initial inventory in the drained soil also contributes to the activity in the cultivated soil ($K_d > 0$). The Cl-36 dose is thus regulated by a combination of the diluting flows in different layers so the correlation between doses and the flow in one specific layer is not as clear as for C-14 (Figure 7-18).

Strongly sorbing and short-lived radionuclides never reach the cultivated soil, except as decay products of more mobile parents in decay chains. However, radionuclides in the moderately sorbing group can contribute significantly to the total dose from cultivated soil. One example is Mo-93 and the proportion of the Mo-93 release from the geosphere that decays in the regolith varies from 22 % to 99 % among mire objects (**Biosphere synthesis**).

Faster transport through the regolith means that a lower proportion decays. The proportion of a radionuclide that reaches the next layer is positively related to the upward groundwater flux (q) and negatively related to the regolith layer thickness (z) and sorption (K_d) in the layer, and these relationships get stronger with higher decay rates. The proportion that reaches the uppermost layer is then the product of the proportions transported through each of the underlying layers, which makes it hard to find strong correlations between activity concentrations or doses and object properties in one particular layer. Once released into the upper regolith, the concentration of Mo-93 and other radionuclides in the moderately sorbing group should be regulated in agreement with the stylised model for one layer (**Biosphere synthesis** and Saetre and Ekström 2017). That is, the activity concentration of all radionuclides should be proportional to the inverse of the object area, while mobile radionuclides are diluted by a high groundwater flux in the upper layer (cf. regulation of Cl-36 in the till porewater) and the concentration of strongly sorbing radionuclides is correlated to the inverse of the regolith layer thickness (cf regulation of Po-210). This means that increased deeper upward groundwater flow has an increasing positive effect on doses, whereas increased groundwater flow in surface layers has a decreasing negative effect on doses. Since groundwater flow is correlated between layers, the effects of groundwater flow could, at least, partly cancel each other out. This could be the reason why doses are more strongly correlated to the inverse of the product between object area and thickness of e.g. the glacial clay layer (Figure 7-18) than to relationships that include groundwater flow.

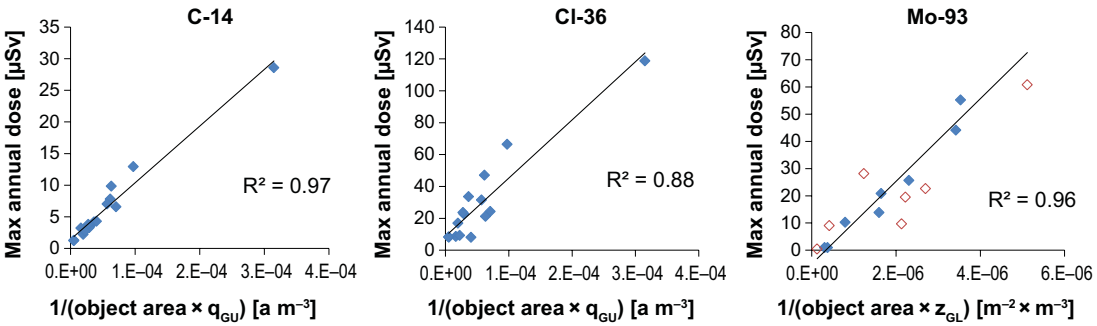

Figure 7-18. *Maximum annual doses from BHA for specific radionuclides as a linear function of object-specific properties. The doses from C-14 and Cl-36 are correlated with the inverse of the product between the object area and the annual groundwater flux in the undisturbed layer below cultivated soil (1/(object area × q_{GU}, where GU = layer of groundwater uptake), which equals the inverse of the volumetric flow through the layer (Q_{GU}). The maximum annual dose of Mo-93 is correlated with the inverse of the product between the object area and the thickness of the glacial clay layer (z_{GL}), which equals the inverse of the glacial clay layer volume ($1/V_{GL}$). The unfilled red squares represent objects where accumulation in regolith layers below the peat contributed to the activity of the cultivated soil (these observations were excluded from the estimated fit).*

The activity concentration in the cultivated soil is, in turn, a function of both the accumulated initial inventory in one or more of the uppermost regolith layers depending on their thicknesses and of the groundwater uptake from the saturated layer below the cultivated soil. Thin upper regolith layers means groundwater uptake from a deeper and generally less diluted regolith layer, but regolith layer thickness, in combination with radionuclide-specific sorption properties in different layers, has a potentially even more important effect on doses. Mo-93 sorbs strongly to peat and post-glacial sediments containing organic matter and less to minerogenic matter in deeper layers. Thin upper layers mean that the initial inventory of Mo-93 in the cultivated soil after draining could be both higher, if Mo-93 rich post-glacial sediments are included, or lower, if Mo-93 poor glacial clay also contributes to the cultivated soil. Therefore, the correlation is stronger between Mo-93 doses and properties in objects where only peat is included in the cultivated soils (Figure 7-18). Tc-99, on the other hand, is strongly sorbing to the glacial clay layer, and thin peat and post-glacial sediment layers mean cultivation of the glacial clay layer. This results in a high initial inventory in the cultivated soil after draining and high doses in e.g. objects 121_2 and 157_2 (Figure 7-15 and Figure 7-16).

To summarise, there are no simple relationships between doses from the cultivated soil and a few object properties for moderately sorbing radionuclides. This motivates the use of a mechanistic and relatively complex radionuclide transport model, and that becomes even more important when considering decay chains.

For total annual doses, no simple relationships between doses and object properties are expected either, since they are a sum of exposures from the well and cultivated soil for different radionuclides that all have different responses to biosphere object properties. Nevertheless, there are some general relationships. There is a relatively strong relationship between maximum annual doses and the inverse of the object area (Figure 7-19, $R^2 = 0.67$), except for the two objects with thin upper regolith layers (121_2 and 157_2). If groundwater fluxes are not highly negatively correlated with the object area, it makes sense and could even be argued as trivial, that releases into large biosphere objects result in lower average concentrations and doses from those objects. Perhaps more surprisingly, there is an even stronger relationship between total doses and the inverse of the total regolith depth (Figure 7-19, $R^2 = 0.77$). This relationship has at least two different possible mechanistic explanations. First, the thin layers in objects 121_2 and 157_2 result in high doses from Tc-99 due to cultivation of the glacial clay. Second, transport through thin layers is faster and concentrations and doses from the cultivated soil for radionuclides regulated by decay should therefore be higher. Although the upward groundwater flux influences the activity concentrations, the response is different for mobile and sorbing radionuclides respectively and the effect on total doses, therefore, is not obvious (Figure 7-19). In a multiple linear regression model of the logarithms of the total doses versus the logarithms of the object properties, object area and thickness of the glacial clay layer, but not groundwater flow, become highly significant predictors, and the model explains 86 % of the variation in total doses (91 % if objects 121_2 and 157_2 are excluded).

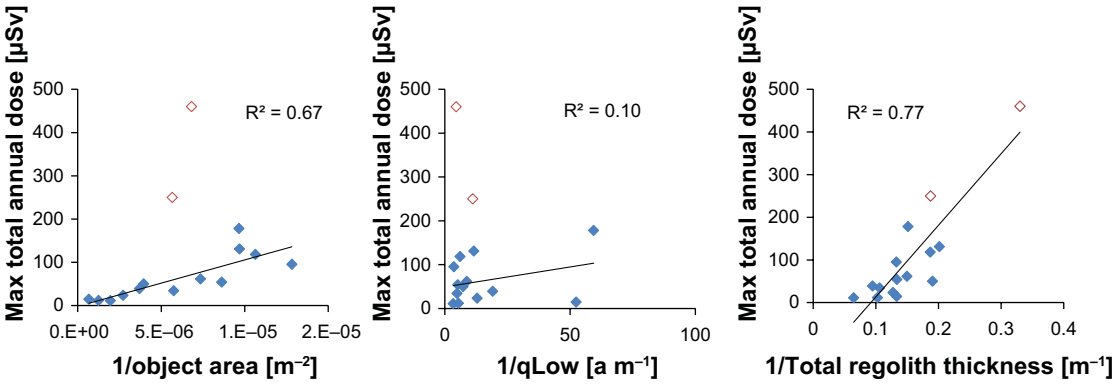

Figure 7-19. *Correlations between maximum total annual doses and the inverse of the object area, total regolith layer thickness and the upward annual groundwater flux from the till (q_{Low}). The red unfilled symbols are the total doses in object 121_2 and 157_2 with thin upper regolith layers and they are included only in the linear regression between doses and the inverse of total regolith thickness.*

Doses with landscape development

The potential effects of shore-line displacement and ecosystem succession on the projected dose were evaluated by comparing the results for ecosystems arising during the development of coastal basins into lakes and mires with results for static ecosystems (see **Biosphere synthesis**). With the radionuclide releases from the SFL-repository, the maximum doses from biosphere objects modelled with landscape development are in general close to the doses from static representations (mire or lake) of the same objects. The results indicate that using a static representation of the mire ecosystems (as is done in *the base case* and most *other evaluation cases*) is a reasonable and sound simplification for radionuclides for which accumulation in the mire is a primary source of exposure.

7.6.7 Site selection and correlation of object properties

Better characterisation of the waste, well-designed repository barriers and selecting a site for SFL are all possible measures to ensure the long-term safety of the future repository. Site-selection processes have earlier focussed on finding suitable bedrock with low groundwater flow through the repository and a geosphere that limit releases of radionuclides. At least three requirements should be met if the effects of site-surface characteristics on doses should be considered in a site selection process:

- The variation in doses between biosphere objects should be significant compared with other sources of variation that could be influenced by the site selection or design of the repository.
- The variation in in doses between objects should be linked to biosphere object properties and the underlying mechanisms should be understood.
- The object properties identified should be susceptible to influence by selecting a site, and object properties that can influence the dose from long-lived radionuclides with a significant late dose maximum should be sustained (or at least predictable) also for very long-time periods, including subsequent to passage of an ice sheet.

There is a considerable variation in doses among different types of ecosystems receiving a radionuclide release that could be considered in a site selection process (more than four orders of magnitude, Figure 7-16.). Releases into an open sea basin with a fast turnover of water will minimize doses. The highest doses will arise from mires that become drained and cultivated or from lakes if C-14 releases are important (e.g. BHK releases). If the position of the repository restricts the release of radionuclides to terrestrial systems, the dose variation among the objects in the Laxemar and Forsmark decreases to about 1.5 orders of magnitude, but the average dose increases. Most of this variation seems related to the areas of the biosphere objects, but regolith thickness should also be considered. Finding sites where terrestrial biosphere objects are and will be large, with thick deep regolith layers (e.g. till and glacial clay) could reduce doses.

Due to the large potential consequences that ecosystem and object properties have on doses, they should be treated with care in the subsequent steps of the SFL programme, i.e. site selection and safety analysis. Possible measures include ensuring doses with a substantial margin to the risk-regulatory dose limit, carefully studying current and potential future discharge objects to decrease the uncertainties, and/or actively pursuing areas with low dose consequences in the site-selection process.

7.6.8 Conclusions

In the biosphere assessment, the dose to the most exposed group of future human inhabitants is examined. Since the location of the repository and the areas where groundwater from the repository will reach the surface are unknown, the *alternative discharge area evaluation case* is designed to study how total and nuclide-specific annual doses are affected by properties of the discharge area.

There are several factors that affect the projected dose from a discharge area, including the type of ecosystem, the properties of the area, and the development of the area. The maximum annual doses typically result from accumulation of radionuclides in a mire, which are subsequently exposed and mobilised by drainage and cultivation, i.e. a scenario evaluated in the base case. On the other hand, release to an open sea basin can result in doses that are several orders of magnitude lower, partly due to a reduction of the activity during slower transport through the regolith (e.g. Tc-99 and Mo-93), and partly due to dilution in the open water (all radionuclides). The doses from lake ecosystems are also typically lower than from terrestrial ecosystems. However, for medium- and large-size discharge areas, the exposure from a lake (or a water reservoir) can yield higher dose from C-14 than the dose which results from draining a mire.

The total maximum annual dose from both BHA and from BHK varies by more than an order of magnitude among the mire systems. For BHK, the doses from C-14 and Mo-93 always contribute 90 % of the total dose or more. However, for releases from BHA, the relative contribution of individual radionuclides (e.g. Tc-99) may vary substantially. In general, doses from all radionuclides are lower in large objects (cf. object 116, 201, 208). This is because large objects typically have greater groundwater flows that result in dilution of all radionuclides, and this is especially evident for mobile radionuclides such as C-14 and Cl-36. The activity of sorbing radionuclides (e.g. Mo-93 and Tc-99) is also affected by radioactive decay, and parameters that decrease transport rates reduce the activity from the geosphere release along the upward flow pathway. Thus, there is a general trend of decreasing dose with the total depth of regolith deposits. As the area-specific discharge affects both transport rates and the volumetric dilution of radionuclides in the regolith, there is no uniform relationship between this rate and the total dose. That is, whereas an increase in the groundwater discharge from the bedrock may increase the activity of Mo-93 and Tc-99 that reaches regolith layers exposed by cultivation, it also dilutes radionuclides in these layers (and this is the only effect on mobile radionuclides). These general conclusions are largely in agreement with the results from the sensitivity analysis of the hydrological system, and the differences are mainly explained by correlations between properties of the objects included in the analysis that are not considered in the sensitivity analysis (**Biosphere synthesis**).

The terrestrial biosphere object (206) that is used in the base case is a mire that has developed in a small (but relatively deep) lake basin, which has a relatively high specific discharge of groundwater from the bedrock. This configuration results in a relatively high annual dose that is either due to exposure from Cl-36 and Mo-93 (first 100 000 years) or due to exposure from Tc-99 (BHA after 100 000) years. The dose from C-14 in this terrestrial object is considerably lower than in discharge areas with open lakes, but doses from lakes are still smaller than estimated total drained mire doses from object 206. Moreover, the doses in developing objects are similar to or lower than the doses from static representations (lakes or mires) of the same ecosystems (Section 9.3.11 in the **Biosphere synthesis**). Thus, the results indicate that using a stationary representation of the mire ecosystem in object 206 (as is done in the base case and most other evaluation cases) is a reasonable simplification of the biosphere for discharge areas in Laxemar. However, the thick layer of peat in the object prevents activity in the glacial clay from being exposed by drainage and cultivation. Thus, if the postulated release from BHA is discharged in an area with relatively thin layers of peat and post-glacial sediments overlying glacial clay, then the resulting dose from Tc-99 alone could be a factor of five larger than the total dose projected from object 206.

7.7 Alternative regional climate

7.7.1 General description

The *alternative regional climate evaluation case* illustrates to what extent the external conditions driven by the regional climate at the repository site may affect the calculated dose. External conditions are derived from temperature and precipitation regimes at three additional locations along the Swedish coast (Figure 7-20). The near-field and geosphere conditions are not expected to be affected by variations in regional climate within the temperate domain. However, groundwater recharge and discharge at the surface is expected to respond to changes in climate. Thus, post-closure safety for alternative regional climates is evaluated by adjusting the groundwater flow in biosphere object 206.

External conditions

The North and Central regional climate variants correspond to locations along the Baltic-sea coast, and the Southwest climate corresponds to a location facing the Swedish west coast (i.e. on the shores of Kattegatt/Skagerrak) (Table 7-4). As in the base case, the variant climatic conditions are assumed to prevail during the entire analysis period of 1 million years after repository closure.

Table 7-4. Present-day climate conditions for Laxemar and three other sites along the Swedish coast chosen to represent different regional coastal climate types in Sweden. The location of the sites is shown in Figure 7-20. All values are for the reference period 1961-1990 (Alexandersson and Eggertsson Karlström 2001), unless otherwise indicated. (Table modified from the Climate report).

Climate-related parameter	North	Central (Forsmark)	Laxemar	Southwest
Mean annual air temperature [°C]	2.6	5.0	6.4	7.3
Annual precipitation [mm]	654	606	553	738

7.7.2 Handling in the near-field and geosphere models

The properties of the engineered barriers are assumed to develop as described in the base case. Changes in regional climate are not expected to cause any additional chemical, thermal, or mechanical effects on the structural integrity of the waste vaults or affect the transport times in the near-field and the geosphere. Thus, the pattern and magnitude of groundwater flow in the bedrock and repository from the present-day calculations are used also in this evaluation case.

7.7.3 Handling in the biosphere model

In this evaluation case radionuclides from the repository are discharged to the same biosphere object as in the base case, namely biosphere object 206. The discharge of groundwater is assumed to increase in all examined regional climate variants (see *Surface Hydrology* below).

Landscape development

As in the base case, landscape development is not considered. That is, the geometry and stratigraphy of the discharge area does not change, and no biological succession is accounted for during the entire analysis period of 1 million years. Dose consequences are examined in two variants of the biosphere object, namely a continuously cultivated field and a mire filling the original lake basin.

Surface Hydrology

Groundwater flow for the alternative regional climate variants is derived by assuming that deep groundwater discharge and surface runoff follow a simple temperature and precipitation response previously predicted for the Äspö area (Losjö et al. 1999, Grolander and Jaeschke 2019). The response in runoff and bedrock discharge is then translated into groundwater flow rates through the regolith profile (Grolander and Jaeschke 2019). Thus, a high precipitation and cold Northern climate is expected to yield approximately 40 % more discharge from the bedrock and more than twice as much surface runoff as presently observed in Laxemar. Warm and high precipitation conditions (as in the Southwest) and slightly colder and higher precipitation conditions than in Laxemar (as in Central Sweden) are also expected to yield more discharge, but at levels that are intermediate between those in the North and the Laxemar region (Figure 7-20).

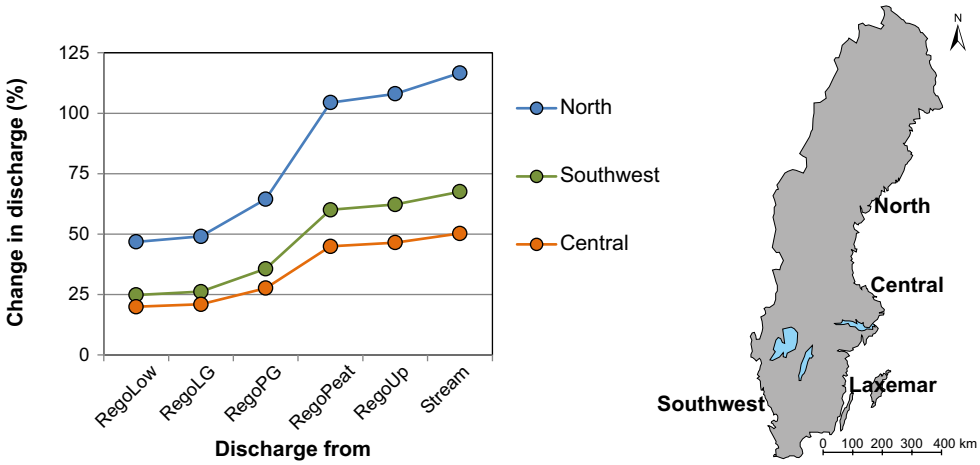

Figure 7-20. *Groundwater discharge pattern as a function of regolith layer and regional climate. The rates are calculated for a time-independent mire (object 206) and are expressed as the relative increase (change) compared to those in Laxemar. The regional climate variants are examples along the Swedish coast. Annual precipitation values and mean annual air temperatures for all locations are given in Table 7-4. Figure from Grolander and Jaeschke (2019).*

Ecosystem

Most properties of the mire and the agricultural ecosystems are expected to be marginally affected by the postulated change in the regional climate. However, precipitation and temperature are expected to affect the plant water deficit in cultivated soils during the growth season. Thus, the groundwater uptake in cultivated soil, and the amount of irrigation water required by a kitchen garden, are adjusted to lower rates in a Northern climate (~35 % reduction), somewhat lower rates in the Central climate, and somewhat higher rates in a Southwest climate. For detail see Grolander and Jaeschke (2019).

Exposed population

The land-use variants from the base case are used also in this evaluation case. That is, a family farm is used to evaluate exposure from the permanently cultivated land (Agr), and the potential exposure from a mire ecosystem is evaluated for the exposed groups: hunter-gatherers (HG), infield–outland farmers (IO), a household with a garden-plot (GP), and a family farm cultivating the drained mire (DM).

7.7.4 Annual doses

The *alternative regional climate evaluation case* shows that regional climate may have a limited effect on the annual dose, and that the conditions in Laxemar (low precipitation and fairly high temperature) result in slightly higher doses than wetter regional climate variants. A colder regional climate with higher precipitation is likely to result in more dilution and less accumulation of radionuclides and consequently a decrease of the maximum dose from both waste vaults is to be expected (~50 % reduction in dose from BHA and ~40 % reduction from BHK). A warmer and wetter climate (Southwest) and a somewhat colder and wetter climate (Central), are also likely to result in a reduction of the annual dose, but the reduction is more modest, i.e. approximately half of that in the Northern climate (Figure 7-21).

In all cases, the highest dose results from the land use where long-term accumulation in the mire is followed by cultivation (DM), and the primary cause of the reduction in dose is an increased discharge in the mire ecosystem (Figure 7-22), which dilutes radionuclide concentrations in all regolith layers. Surface runoff (and bedrock discharge) increase with precipitation and decrease with temperature. Thus, in the Northern and Central climate variants, the changes in precipitation and temperature work in the same direction, whereas in the Southwest climate a higher annual temperature increases the evapotranspiration, which cancels out part of the effect from the increased precipitation.

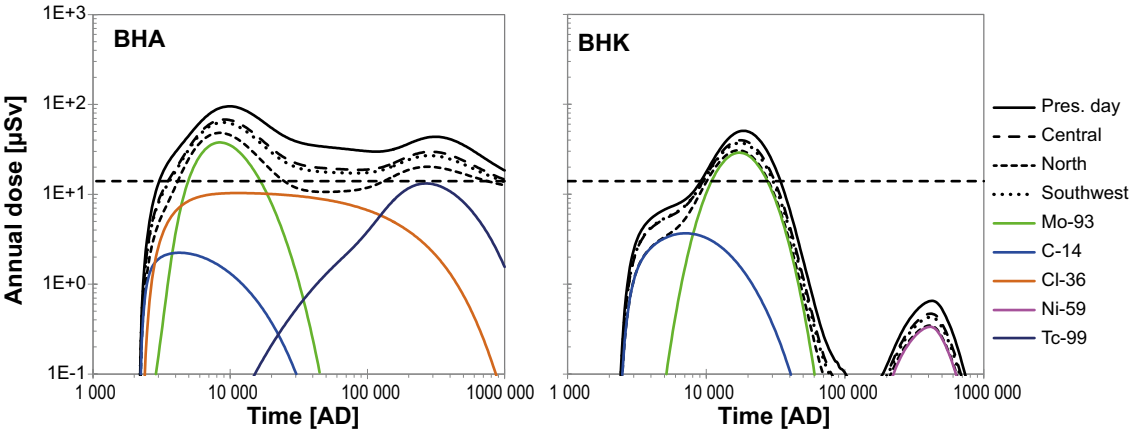

Figure 7-21. *Annual dose for release from BHA (left) and BHK (right) in the alternative regional climate evaluation case. Coloured lines represent the dose contribution from individual radionuclides for the North regional climate. The dose in the base case is shown for reference (black solid lines).*

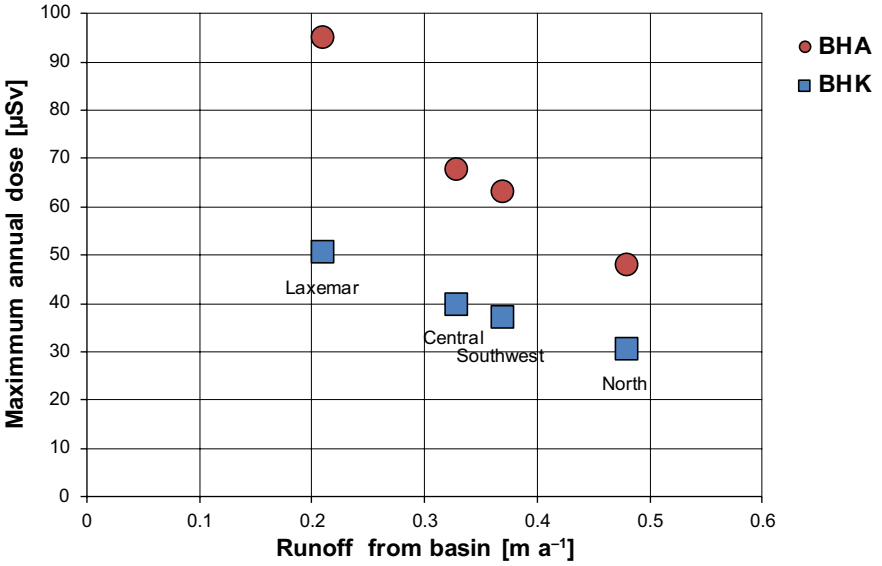

Figure 7-22. *Annual dose as a function of the runoff from the local basin for four regional climate variants. The runoff from the basin is the primary driver of the discharge in the upper part of the regolith profile (RegoPeat and RegoUp).*

Although, the relative importance of pathways and processes may vary among the climate variants, there is a tendency for a proportional reduction of the annual dose from both waste vaults with increasing discharge. Thus, on average, a doubling of the surface runoff corresponds to a 40 % reduction of the dose from BHA, and a 30 % reduction of the dose from BHK. The variation in response between the two waste vaults primarily reflects the difference in the composition of the release causing the maximum dose. The variation in response in the dose from BHA reflects the combined response of Cl-36 and Mo-93, whereas the response in dose from BHK primarily reflects variation in the accumulation of Mo-93 in peat. In the northern climate, Cl-36 doses are reduced by nearly 70 % (BHA), and both an increased dilution and a reduced groundwater uptake during cultivation contribute to the reduction. However, the reduction of the dose from Mo-93 to the northern climate is significantly weaker (30−40 %), as the effects of increased groundwater dilution are partly counterbalanced by an increased load of Mo-93 to the peat, as less activity is lost through radioactive decay when the transport rate is increased.

7.7.5 Conclusions

In this evaluation case, the extent to which variations in the regional climate has a potential to influence the annual dose from SFL has been examined. The results suggest that a climate associated with higher rates of groundwater recharge and discharge (i.e. a climate with higher precipitation and or lower annual temperature) is likely to result in a lower annual dose than in the base case. Thus, representing the climate of a future repository with the conditions in Laxemar is a cautious assumption for present conditions compared with sites not located in different parts of Sweden. However, the response to variations in regional climate is modest, and depends on the radionuclide composition of the release. Thus, it is unlikely that a location with a favourable climate within the borders of Sweden will reduce the annual dose from SFL by more than a factor two as compared with Laxemar (the base case). Moreover, if the release of Mo-93 from the repository remains at the postulated levels (that results in a major contribution to dose) a reduction of around 35 % is a more realistic upper estimate of what could be accomplished by selection of a site along the south and central Swedish coast.

7.8 Drilled well

In this evaluation case the effect of using drinking water from a well drilled into the bedrock is analysed. Five hypothetical, 60 m deep, wells are positioned in the areas north and east of the repository, where discharge from the repository occurs (Figure 7-23 and Joyce et al. 2019). With the postulated water withdrawal rate, only one of these five wells would receive particles from the repository at the example site. The properties from this single well are used to assess the potential dose in this evaluation case.

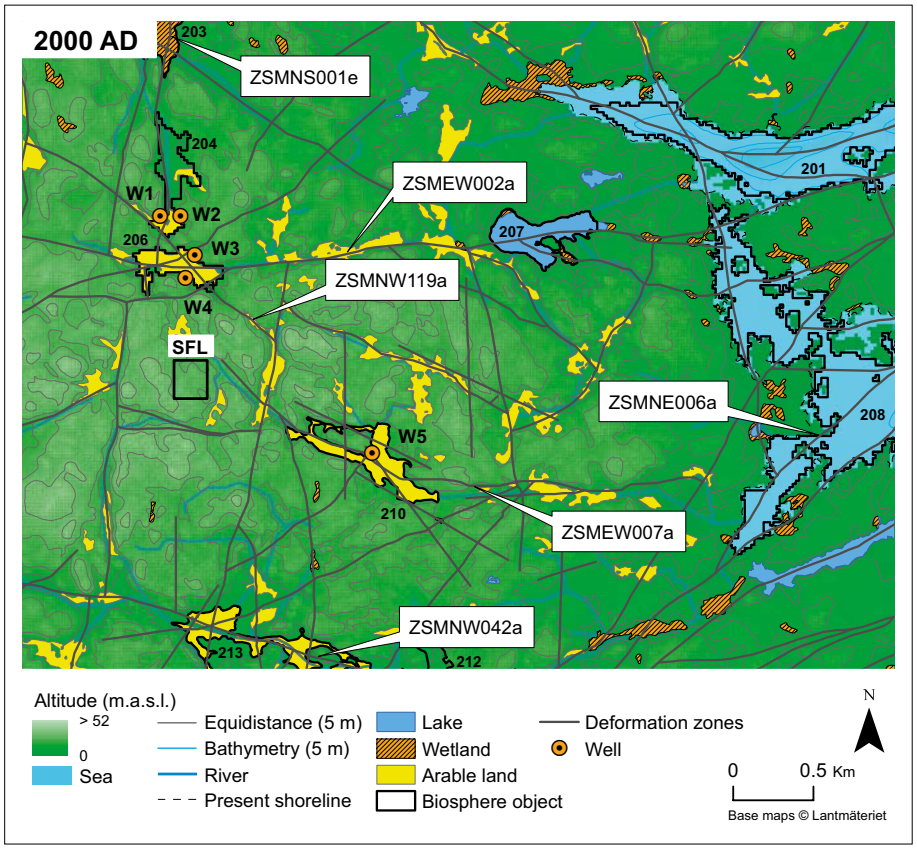

Figure 7-23. *Well locations (orange, labelled W1 to W5) in the present Laxemar landscape. Biosphere objects are marked with numbers (e.g. 204, 206 and 210) and the names of deformation zones are given in white squares (ZSM). The spatial location and extent of deformation zones is for a depth of 20 m below sea level. The assumed location of the SFL repository (black square) for this evaluation case is added for reference. Grey contour lines follow constant elevation, with a five meter difference between lines. Figure adapted from Joyce et al. (2019).*

7.8.1 Location of drilled wells

Five hypothetical drilled wells are positioned in the areas north and east of the repository (Figure 7-23), where discharge from the repository occurs. In five realisations of the stochastic fracture network, the discharge from the waste vaults primarily reaches biosphere objects 204 and 206 and, in one realisation, also biosphere object 210 (Section 4.7 in Joyce et al. 2019). Therefore, two wells are positioned close to each of objects 204 and 206, and one well is positioned close to object 210.

The exact position of the drilled well is determined accounting for three separate criteria: First, to ensure drinking water quality, a well needs to be protected from inflowing surface water and, therefore, low areas in the landscape, such as wetlands and agricultural land, are avoided. Second, to avoid an unnecessarily deep well, high points in the terrain are avoided. Third, to ensure a sufficient yield, the well needs to intersect at least one fracture in the flowing fracture network.

7.8.2 Handling in the near-field and geosphere models

The effect of the well on the hydrogeological performance measures was found to be small in the hydrogeological study (Joyce et al. 2019) and, therefore, the release from the geosphere to the well is calculated by multiplying the base case releases from the geosphere with the fraction of particle tracks that end up in well W3 (Figure 7-23), i.e. 3.1 % for BHA and 2.1 % for BHK. Thus, all near-field and geosphere parameters are the same as in the base case.

7.8.3 Handling in the biosphere model

The dose from exposure to radionuclides in well water is evaluated using a garden plot household of five individuals. The members of the group are exposed through drinking water, and by ingestion of vegetables and potatoes from an irrigated kitchen garden. There are no a *priori* assumptions on the physical location of the household.

The amount of water extracted from the well is assumed to be 700 L d^{-1} (255 m^3 a^{-1}), which is higher than the water use expected from a tap in a yard, and somewhat lower than present-day levels when connected to a public water works (either of these could correspond to a garden-plot household). The water concentration is calculated by dividing the geosphere release that reaches the well by the water extraction rate.

In accordance with the guidance in the regulations (SSM 2008a), the family household utilizing a well is viewed as a small group. Consequently, the calculated annual effective dose is evaluated against an annual dose criterion of 140 μSv (which corresponds to an annual risk criterion of 10^{-5}).

7.8.4 Annual doses

The maximum annual dose from a drilled well is above 100 μSv for release from BHA (Figure 7-24). This dose level is reached 200 000 years after the start of the assessment and the dose keeps rising continuously throughout the assessment period. Decay products from the U-238 decay chain are the main contributors to the dose from consumption of drinking water. Of these, Ra-226 (including its two short-lived decay products Pb-210 and Po-210) are especially important (Figure 7-25). After 200 000 years of the assessment there is no activity left of the initial inventory of Ra-226 in BHA (the half-life of Ra-226 is 1 600 years), and the primary source of Ra-226 is thus decay of uranium (238, 234) and thorium (230) isotopes in the bentonite backfill and the bedrock matrix. In the latter half of the assessment period, almost all Ra-226 originates from U-238 waste deposited in the repository. In addition, Cl-36 and Tc-99 give a significant dose contribution of 10 μSv after 5 000 and 100 000 years, respectively (Figure 7-24). However, as the number of people exposed to water extracted from a single drilled well is limited, the dose from Cl-36, Tc-99 and other radionuclides is more than an order of magnitude below the dose corresponding to the risk criterion for a small group (140 μSv), and the total dose from BHK is almost two orders of magnitude below this level at all times of the assessment (Figure 7-24).

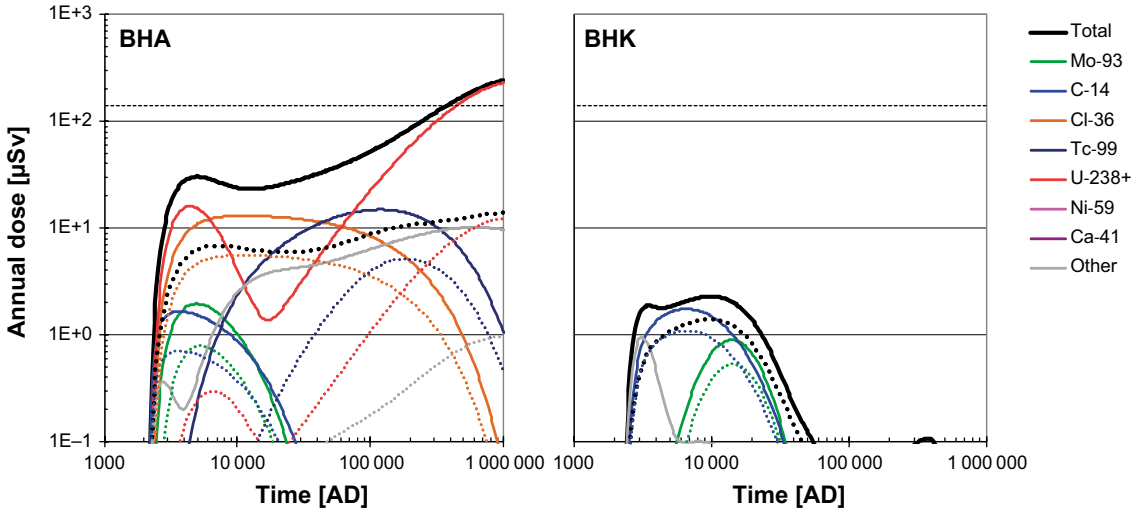

Figure 7-24. *Annual dose from BHA and BHK to a garden plot household in the drilled well evaluation case. Colours represent doses from individual radionuclides. Dotted lines represent the dose in the base case (for a garden plot house hold without exposure through fertilization with ash). The dose corresponding to the regulatory risk limit for a small group (140 µSv) is shown with a dashed line.*

Well water is the primary environmental media that contributes to dose in this evaluation case. Thus, a comparison of the concentrations in well water illustrates the processes that underlie the elevated dose in the drilled well, as compared with the water in a dug well used in the base cases. The dilution of the geosphere release in the drilled well, ~2−3 % of the daily release diluted in 700 L of water, is approximately half of the dilution that occurs by discharging groundwater in the till (~all geosphere release diluted in the groundwater discharge from the bedrock into biosphere object 206). Thus, for radionuclides that are marginally affected by radioactive decay when transported through the till, e.g. C-14, Cl-36, and Mo-93, the concentration in water from the drilled well is twice as great as that from a dug well (horizontal line in Figure 7-25). On the other hand, the dissolved concentration of radionuclides with a relatively short half-life is even more reduced in the till, especially when the transit time is relatively long due to sorption (sloping line in Figure 7-25). This is because the water in the regolith well is assumed to be extracted from the entire till layer, and short-lived radionuclides decay before they reach the upper sections of the well.

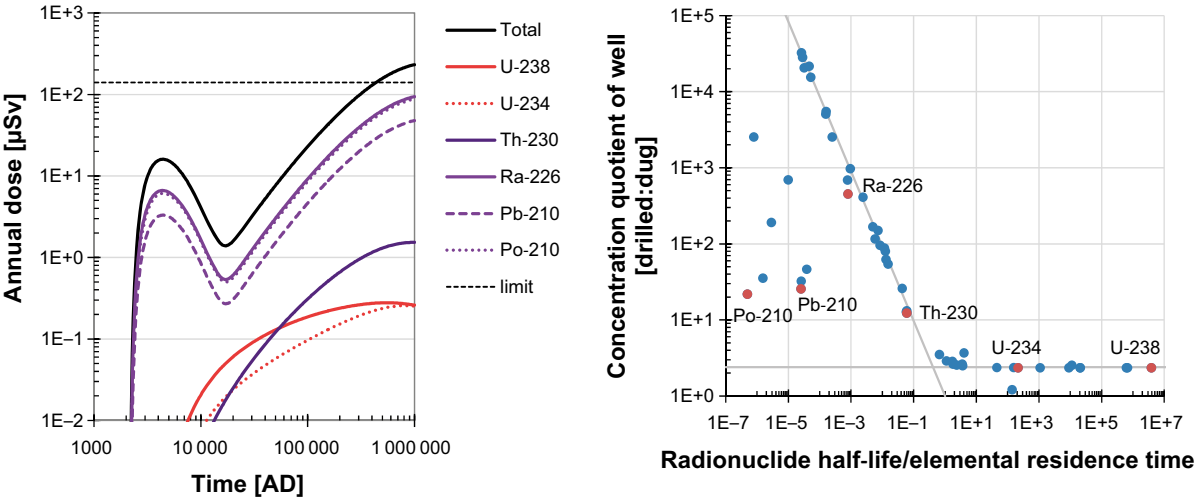

Figure 7-25. *Annual dose from and relative activity concentration of well water from BHA. Left: Dose from U-238 including decay products (black line), and contribution from individual radionuclides (coloured lines). Right: Quotient of activity concentration in well water extracted from a drilled (numerator) and dug (denominator) well, as a function of the ratio between half-life and transit time in till (regoLow). Orange symbols correspond to U-238 and its decay products. Note that the dose is calculated for a household utilizing the well for drinking water and irrigation (GP).*

Sorption properties (K_d values) in the regolith are typically two orders of magnitude larger than in the rock matrix, and accumulation of parent radionuclides may lead to an additional load of activity in the till. For example, Ra exhibits almost five orders of magnitude greater sorption in the regolith than in the rock matrix, and consequently the concentrations of decay products Pb-210 and Po-210 are considerably higher in the water from the dug well than expected from the geosphere release (radionuclides below the sloping line in Figure 7-25). However, despite the additional ingrowth of activity in the regolith, the water concentrations of decay products in the dug well are more than an order of magnitude below those in the drilled well. This is primarily due to stronger sorption in till than in bedrock of the daughter products (about two orders of magnitude) which limits the concentration in the lower section of the well and prevents the radionuclides from being transported to the upper sections of the well.

The dose from the drilled well is evaluated with a garden plot household of five members as the most exposed group. Since there are no a-priori assumptions on where the well is located apart from its feasibility to provide sufficient amounts of water, this land-use variant is not combined with exposure associated with the use of natural resources from the mire, e.g. through foraging on or draining and cultivating the mire. To assess mire land-use and drilled well doses separately is also a reasonable simplification from a radiation protection perspective. That is, if the dose assessed from the drilled well is close to the limit for a small group (140 μSv), then the additional contribution from potential mire land-use will be marginal (≤ 10 %) as long as dose from this land use meets the dose level corresponding to the regular risk criteria (14 μSv). Moreover, in the present assessment, ingestion of crops from the garden plot accounts for approximately 36 % of the dose when Ra-226 and its decay products dominate the dose. This means that the contribution from garden-plot crops to dose (~35 μSv) is close to or even above that from ingestion of food from the drained mire in the latter part of the assessment period. It would be double counting to assume that food requirements are obtained from both these sources, so only the larger contribution should be included if pathways from the two groups were to be combined.

7.8.5 Conclusions

The annual effective dose that results from extracting water from a drilled well is above 100 μSv for release from BHA after 200 000 years of the assessment period, and the annual dose keeps rising. Ra-226 and its decay products are the main contributors to dose, and the geosphere release of Ra-226 at times beyond 20 000 AD originates from U-238 in the waste (and accumulation of uranium and thorium isotopes in the near-field and the geosphere). The primary reason for a significantly higher activity of Ra-226 in the drilled well when compared to a dug well is reduction by radioactive decay along the transport pathway in the till (from where water from the dug well is extracted). Although the annual effective dose from the drilled well is significantly higher than that from a drained mire, the number of people exposed to water extracted from a single well is limited, and the dose from BHA is in the same order of magnitude as the dose corresponding to the risk criterion for a small group (140 μSv). The dose from BHK is almost two orders of magnitude below this level.

8 Discussion

This report documents the results from radionuclide transport and dose calculations performed for the post-closure safety evaluation SE-SFL. The report presents the methodology applied (Chapter 2) and the prioritisation and selection of radionuclides to consider in the safety evaluation of SFL (Chapter 3). Chapter 4 describes the modelling tools for calculation of the radionuclide releases from the repository (near-field), the transport from the repository to the surface system (geosphere), the transport and accumulation in the biosphere, and the resulting doses to members of the most exposed group (biosphere). The calculations are performed for a set of evaluation cases defined in SE-SFL to assess the potential for the proposed repository concept to meet applicable criteria on the maximum annual dose for humans after its closure. Firstly, three evaluation cases that are linked to the reference evolution (Chapter 5) are analysed. Secondly a set of evaluation cases that evaluate the sensitivity of the resulting release and dose to conditions in the repository (Chapter 6) and to site-specific conditions (Chapter 7) are analysed. Chapter 2 in the **Main report** elaborates on the selection and purpose of evaluation cases in SE-SFL.

This chapter summarizes the basis for the calculations (Section 8.1) and the results from the evaluation cases regarding the main features of the concepts for BHA and BHK. The function of the proposed repository concept at the example location, as inferred from the calculations, is described (Section 8.2). Further, simplifications in comparison to the reference evolution (Section 8.3), and cautious simplifications made in the modelling are discussed (Section 8.4). Finally, the results of the evaluation cases are discussed as a basis for the evaluation of under what conditions the proposed repository concept has potential to meet the regulatory requirements (Section 8.5). The implications of the results presented in this report for the objectives of SE-SFL are further discussed and summarized in Chapter 9-10 in the **Main report**.

8.1 SE-SFL

The safety evaluation SE-SFL is an initial analysis of post-closure safety for the SFL repository concept, and its purpose is to assess under what conditions in the repository and its environs that the proposed design concept for SFL has the potential to meet the regulatory requirements for post-closure safety. A one-million-year period is analysed, and Laxemar in south-eastern Sweden is used as an example area for the repository. The reference evolution (Chapter 6 in the **Main report**) describes the future evolution of the repository and its environs. Further, material properties for the repository components are taken from previous safety assessments. For instance, it is assumed that the BHA backfill is constructed with bentonite that is similar to that planned for the buffer in the Spent Fuel Repository, and the BHK backfill is constructed with concrete similar to the construction concrete employed in the existing SFR repository.

8.1.1 Post-closure safety

The safety principle for the proposed repository concept is *retardation* (Elfwing et al. 2013 and Chapter 5 in the **Main report**). The idea behind the proposed concept for SFL is thus to use a system of engineered and natural barriers to reduce the mobility and transport of radionuclides, resulting in retention and decay, primarily in the repository, but also in the bedrock surrounding the repository. In the waste domain, this is to be achieved by upholding the safety function *good retention* with beneficial conditions (e.g. high pH, low redox potential, low concentrations of complexing agents, high available surface area for sorption and low corrosion rate for metallic waste). For the bentonite barrier of BHA, the important safety functions are *low flow* in the waste vaults, and *good retention*. These safety functions are linked to a low hydraulic conductivity, low diffusivity, high available surface area for sorption, and high capacity to filter colloids. For the concrete barrier of BHK, retardation is to be achieved by ensuring the safety functions low flow in the waste vaults and good retention. For BHK good retention is related to low diffusivity, high available surface area for sorption, high pH, and low redox potential. For the bedrock, retardation is achieved by selecting a repository location that is characterised by a low flow of groundwater, which is defined as a safety function. Effective retardation ensures that annual

near-field releases are only small fractions of the total activity inventory at repository closure. This time-dilution via sustained release is crucial for post-closure safety and applies to all radionuclides. Additionally, the release and resulting dose is further decreased by retention and radioactive decay, which is most effective for radionuclides with short half-lives relative to their retention time in the near-field (or geosphere).

8.1.2 Radionuclide transport and dose modelling

The near-field radionuclide transport model in SE-SFL (Section 4.3) builds on the same principles as the corresponding SR-PSU model. For geosphere transport, the code FARFCOMP is used, which is a new implementation of the same conceptual model that underlies FARF31, used in SKB's previous safety assessments (Section 4.4 and Appendix B). The radionuclide transport model for the biosphere (Section 4.5) is essentially the same as the one used in the SR-PSU assessment. Thus, the level of detail applied in the geosphere and biosphere models is similar in SE-SFL as in SR-PSU and/or SR-Site. Since this is a first evaluation of a proposed repository concept with, for instance, a first estimate of the inventory of radionuclides and other materials in the waste, the near-field model is less detailed in some aspects than the corresponding SR-PSU model.

Most of the assumptions made in the radionuclide transport and dose modelling in SE-SFL are based on corresponding assumptions made in SR-PSU and/or SR-Site. These include several simplifying assumptions, including that all radionuclides are unaffected by solubility limitations, that no radionuclide is affected by the presence of others (except ingrowth from parent radionuclides), that waste containers provide no transport resistance, that dissolved radionuclides do not reprecipitate, and that all radionuclides that reach the biosphere are discharged into a geographically limited area. Some of these are discussed further in Section 8.3.

Further, the uncertainty in the initial inventory of radionuclides and other materials in BHA is larger than for BHK, and thus some near-field model assumptions are more simplified and pessimistic. For instance, no account is taken of the potential delayed release of radionuclides from the materials in BHA, even though part of the activity in BHA is likely to be contained in solid materials.

The calculations are performed for a set of evaluation cases that have been chosen based on the reference evolution or designed to evaluate the sensitivity of the results to different repository and site conditions. The *present-day evaluation case* (Section 5.2) constitutes the base case for the radionuclide transport and dose calculations in SE-SFL and assumes a constant present-day climate. The objective is to have a simplified base case that in a straightforward way can be compared with cases with alternative assumptions and different temporal evolutions. Thus, the base case is stylized and it is not intended to establish a main scenario as defined by the regulations. The *simplified glacial cycle* (Section 5.4) evaluation case allows a first evaluation of how the release and the dose resulting from the repository are affected by the large-scale landscape evolution coupled to the future climate development.

8.2 Function of the proposed repository concept at the example location

8.2.1 Near-field

The annual near-field activity release from BHA and BHK is dominated by the radionuclides that are most abundant in the initial inventory and have half-lives longer than a few thousand years, i.e. Tc-99, C-14 and Cl-36 from BHA (Figure 5-6) and C-14 and Ni-59 from BHK (Figure 5-9). Several radionuclides that contribute significantly to the initial inventories, e.g. Ni-63 and Co-60, do not contribute significantly to the release, due to their short half-lives and strong sorption onto cement and bentonite in the near-field. Further, the slow release by corrosion, assumed in the BHK near-field model, significantly reduces the annual near-field activity releases for non-sorbing radionuclides such as C-14.

The radionuclide retention in the near-fields of BHA and BHK is substantial. For the non-sorbing C-14, the fraction that decays while retained in the near-field is 93 % of the initial inventory in BHA, while corresponding value for BHK is 98 % (Figure 5-23). The total effect of retardation on C-14

is thus similar in the near-fields of BHA and BHK. However, the effect is achieved by different mechanisms, with retardation in bentonite backfill being the main factor in BHA and slow release by corrosion in BHK. Retention is even more efficient for Mo-93 with more than 99 % decaying in the near-field. This is because Mo-93 has a low but non-zero K_d for cement and a half-life that is somewhat shorter than that of C-14. Of the radionuclides that contribute significantly to the near-field release and resulting dose, decay of retained activity is least important for the long-lived and low-sorbing Cl-36; only about 40 % of the initial inventory in either waste vault decays in the near-field. However, retardation in the near-field is still important since it leads to distribution of the release in time, which reduces the annual release to a small fraction of the inventory. For Cl-36, the maximum annual near-field release is five orders of magnitude lower than the initial inventory. Cl-36 furthermore contributes significantly less to the near-field releases of BHK than of BHA (Figures 5-10 and 5-7), with a difference of about two orders of magnitude for the maximum release. This is mainly due to about two orders of magnitude lower initial inventory in BHK. For Tc-99, with a half-life similar to that of Cl-36, retention in the BHA and BHK near-fields is stronger than for Cl-36 due to sorption. Tc-99 retention in the backfill is significantly stronger in BHK than in BHA, since sorption of Tc-99 in BHA is assumed to be strongly reduced (by a factor of 10 000) due to formation of non-sorbing complexes with cellulose-degradation products.

8.2.2 Geosphere and biosphere

Retention and decay in the geosphere have a marginal effect on the release of non-sorbing radionuclides to the biosphere in the base case. Furthermore, the reduction of long-lived sorbing radionuclides is also limited (Figure 5-23). The groundwater flow that is used in the base case (and in most other evaluation cases) is taken from one out of five discrete fracture network realisations of the bedrock. In this realisation, the repository is comparatively well connected to the geosphere. The sensitivity of the performance of BHA (including the bedrock as a natural barrier) to variations in the discrete fracture network is examined in the *alternative realisations of stochastic bedrock fractures evaluation case* (Section 7.5). For each realisation, the BHA repository was assumed to be located either at its original position or at the BHK position. Although the number of realisations may be insufficient to fully assess the variability that is associated with the stochastic properties of the DFN, they should still give a reasonable indication of the likely spread of effects on transport and dose that can be expected between individual realisations. Stochastic variation in the discrete fracture network has a notable effect on the geosphere release of mobile radionuclides such as C-14, Cl-36 and Mo-93 and a significant effect on the release of Tc-99 (Figure 7-14). The limited sensitivity of non-sorbing radionuclides and the selection of properties assigned to the DFN in the base case, together ensure that uncertainties with respect to the fracture network realisation are not likely to have a significant influence on the results of this safety evaluation. Nevertheless, large sub-vertical fractures intersecting a waste vault can influence both the connectivity of the vaults and provide direct pathways to the surface, and hence the occurrence and properties of such features is of key interest in a site characterisation.

The fracture network also affects the position of the release on the surface, and dispersion between discharge areas. Both of these effects are also expected to have a limited effect on the resulting dose. This is because at least 40 % of the flow pathways in each realisation (from both repository locations) terminate in one discharge area (Joyce et al. 2019, **Biosphere synthesis**), and the potential effects of spatial dispersion are, therefore, limited. Moreover, the dose resulting from release to object 206 (used in the base case) is in between that resulting from a release into either of the other two potential biosphere objects that receive deep groundwater in the examined DFN realisations (i.e. the dose is 20 % lower than in 204 and 75 % higher than in 210) (see the *discharge area evaluation case* for details on the dose, Section 7.6). Thus, the effect of explicitly evaluating the dose in the areas that receive the release according to the specific DFN realisations is expected to be marginal compared with evaluating the dose in object 206 (as done in the base case).

The terrestrial area that is used to evaluate dose consequences in the base case (and most other evaluation cases) represents the most likely area for discharge of groundwater from the repository, as determined by particle tracking from the assumed repository position to the present surface landscape (given five different realisations of the discrete fracture network in the bedrock). The area was selected to achieve an internally consistent description of the transport of radionuclides from the repository to the surface. However, as the repository location is yet to be determined, the area as such is nothing but a relevant example. Thus, doses calculated for a release to this area need to

be interpreted in the context of the uncertainties associated with the properties of the potential discharge area. In the *alternative discharge area evaluation case* (Section 7.6) doses from object 206 were compared with those from other discharge areas. From this evaluation case, it was concluded that object 206 is a reasonable and sound simplification of a potential discharge area in Laxemar. This was because the dose from this object was judged to be reasonably representative for relatively small geographic areas in the Laxemar landscape. However, it was also noted that the response to object properties differs between radionuclides. Thus, whereas the estimated dose from Mo-93 and Ni-59 is on the high end even for small objects (~five and three times above the geometric mean) the opposite was true for C-14 (a factor two below the geometric mean of the Forsmark area, Figure 7.16). The comparatively high doses from moderately sorbing radionuclides are due to the properties of biosphere object 206 (i.e. a high rate of bedrock discharge resulting in fast transport to the upper soil layers). The relatively low C-14 dose is due systematic differences between the two sites. That is, the less pronounced topographical relief in Forsmark results in reduced groundwater discharge in several small objects. This leads to a lower degree of dilution in intermediate regolith layers (which are assumed to provide crops with water after drainage) and relatively high C-14 concentrations in cultivated soil and in crops. Thus, whereas a high rate of bedrock discharge may have increased the importance of Mo-93 in object 206, this effect is partly counter-balanced by a larger dilution of C-14 with the groundwater discharging from the bedrock. It was also noted that a release to a lake would result in somewhat elevated doses of C-14 (~ a factor two higher than in object 206). However, if the C-14 dose in the drained mire is not substantially higher than doses from other radionuclides, the exposure from an aquatic recipient is unlikely to yield higher total annual doses than exposure from a mire. This is because the dose from radionuclides other than C-14 is typically considerably lower (~ three orders of magnitude lower) from a lake than from a mire (Figure 7.16).

8.3 Simplifications in comparison with the reference evolution

In general, important aspects of the three variants of the reference evolution (Chapter 6 in the **Main report**) are extracted to the corresponding evaluation cases, and aspects that are judged to have minor importance are simplified in the calculations. For instance, the ongoing change in relative sea-level at Laxemar has for simplicity been neglected in the *present-day evaluation case*, since it has been judged not to have any significant implications for the performance of the repository at the example site under continued temperate conditions. This judgement considers the predicted changes in hydrogeology and hydrochemistry over the coming tens of thousands of years, as well as the influence on the ecosystems that receive radionuclide releases. The sensitivity to ecosystem changes of the *present-day evaluation case* are limited, since both the area above the repository and the associated discharge areas (biosphere object 206) are already above the sea level at repository closure. The *simplified glacial cycle evaluation case*, however, includes the effects of submerged conditions and shoreline displacement after the inland ice sheet has withdrawn. During this period, the change in relative sea-level at Laxemar is likely to affect the results. The effect of the temporal evolution of biosphere objects has been analysed in the *discharge area evaluation case*. The results show that the doses in objects subject to temporal development are about the same or lower than the doses from static representations of the same ecosystems (lakes or mires).

There are other aspects of the variants of the reference evolution that have been neglected in the evaluation cases, although they might influence the evolution of the barriers and repository performance as discussed in the following. In consequence, the set of evaluation cases representing the reference evolution will need to be further developed to reflect all aspects that must be included in a main scenario in a full safety analysis as described in the general guidance to SSM's regulations (SSM 2008b).

Potential effects of external conditions on the near-field on the barrier performance that have been neglected in the base case include: the change of salinity at repository depth, and changes in the redox conditions in the rock. As detailed in the description of the reference evolution for BHA, intrusion of dilute waters and glacial meltwaters might possibly lead to physical bentonite erosion (**Main report**, Section 6.4.9). If bentonite erosion is sustained over sufficiently long times it could impair the performance of the barrier functions. In contrast, the concrete barrier in BHK is unlikely to be affected by dilute waters reaching repository depth and thus the performance of the BHK should not be influenced significantly.

In addition, the chemical interactions of the concrete in the waste domain with the bentonite backfill leading to clay mineral transformations could potentially influence bentonite barrier performance (Section 6.2.9 in the **Main report**). The effects of clay mineral transformations on the near-field transport processes would need to be quantified to evaluate potential implications for repository performance. Thereby it needs, for instance, to be considered that the plug resistance at the interface between the bentonite and rock fractures is an important part of the total transport resistance, whereas the mineral transformations in the bentonite are developing from the inner concrete structure outwards. The effect of the selected bentonite thickness may also be an important factor to consider.

In the *simplified glacial cycle variant* of the reference evolution, mechanical, chemical, or thermal effects on the structural integrity of the waste vaults have been described (Section 6.3 in the **Main report**). Such effects are, however, neglected in the *simplified glacial cycle evaluation case*. This is a simplification, and, for instance, the ice-sheet load will have mechanical effects on the bedrock and possibly on the repository vaults. Simulations indicate that mechanical damage may occur due to increased rock stresses in the concrete backfill of BHK at the interface between the backfill and the rock (Idiart et al. 2019a). However, the effect of considering the mechanical damage in the near-field transport calculation may be limited, as the concrete is assumed to already have degraded considerably at the onset of the glacial period in the *simplified glacial cycle evaluation case*. Nevertheless, in a full safety assessment, the combined effects of degradation (due to chemical cement leaching) and increased rock stresses would need to be evaluated. The effect of changes in rock stress on the bentonite barrier of BHA has not been evaluated, but it is less likely to be affected by changes in the rock stresses due to its limited stiffness.

During periglacial conditions, the temperature will decrease around the repository. In SE-SFL it is assumed that the repository is situated deep enough not to be frozen during periods of permafrost. In general, the effect of decreased temperature on the barrier evolution is expected to be advantageous, since chemical processes acting to degrade the barriers should slow down. However, if the bentonite pore water freezes, requiring a pore water temperature below −4 °C for buffer bentonite in the Spent Fuel Repository (SKB 2011a), a degraded repository performance cannot be ruled out. The temperature at which the pore water in concrete freezes depends on the pore size. Thus, it will vary with time and within the concrete barrier due to chemical leaching. The potential for adverse effects of periglacial conditions for SFR due to freezing of concrete has been summarized by Näslund et al. (2017). Studies performed for SFR show that internal micro-fractures occur when the concrete pore water freezes, however the concrete retains its structural integrity. Näslund et al. (2017) conclude that freezing of aged (i.e. chemically degraded) concrete will not result in higher hydraulic conductivities than those assumed in the radionuclide transport calculations. It can be noted the maximum permafrost and frozen ground depth at Forsmark and Laxemar occurs prior to the first major glacial advance, at about 50 ka, in SKB's reconstruction of the last glacial–interglacial cycle (Section 4.2.3 in SKB 2006b). At this time the modelled permafrost depth reaches about 250 m at Forsmark and about 160 m at Laxemar. The frozen depth is, at the same time, a few tens of metres to a few meters shallower. More recent modelling of Forsmark (Hartikainen et al. 2010) confirms the maximum depth of about 250 meters for the reconstruction of the last glacial–interglacial cycle in Forsmark. Based on these results, together with results from cases with deeper permafrost studied at Forsmark (SKB 2010e), freezing of pore water in the waste vaults is judged to not occur in Laxemar at the 500 m repository depth evaluated in SE-SFL, during the coming 1 million years. Nevertheless, in a future safety assessment for a selected site, the potential for freezing of pore water in the repository needs to be analysed.

When the ice-sheet advances and retreats, high groundwater flows are expected to alter the redox conditions, which in turn may affect the radionuclide speciation in the rock (and K_d values). These effects have not been accounted for in the *simplified glacial cycle evaluation case*. In SR-Site, the effect of such K_d changes was analysed with the conclusion that the releases to the biosphere increased but that this was compensated by release reaching a coastal basin with decreased human exposure (Section 13.5.6 in SKB 2011a). As the inventory of C-14 is expected to have decayed to insignificant levels at the time of the ice-sheet advance, and as the dose from sorbing radionuclides like Ni-63 and Tc-99 is reduced by three orders of magnitude in aquatic ecosystems, this conclusion is also likely to hold also here.

8.4 Cautious simplifications used in the calculations

One way of managing uncertainties is to make cautious assumptions in the assessment. This is likely to lead to overestimation of calculated dose, all other factors being the same. In the radionuclide transport and dose calculations, several cautious assumptions have been made. Some of these are discussed in the following. In future safety analyses for SFL all these cautious assumptions may be reconsidered to assess whether more detailed studies would be merited by the potential gains with respect to the knowledge of the system behaviour, leading to a more realistic estimation of the releases and doses resulting from the analysis.

8.4.1 Effect of complexing agents in BHA

In the near-field of BHA it is assumed that complexing agents are present. The concentration of the complexing agent isosaccharinate (ISA) is assumed to be at the solubility limit for $Ca(ISA)_2$ throughout the whole assessment period, and sorption reduction factors are selected to reflect such conditions. The amount of cellulose in BHA, which degrades to ISA, is not well known. However, ISA sorbs to cement, and when this process was accounted for, the ISA concentrations in SFR vaults with known amounts of cellulose was estimated to be at least two orders of magnitude below the solubility limit for $Ca(ISA)_2$ (Keith-Roach et al. 2014). Therefore, the assumed ISA concentrations in BHA and the associated sorption reduction factors are likely to be overestimated. This should result in an overestimation of transport of radionuclides that are affected by the sorption reduction factors, such as Tc-99 (see also *no effect of complexing agents in BHA evaluation case*, Section 6.2).

Since ISA sorbs to cement it is expected to be retained in the near-field of BHA over long periods of time. For example, von Schenck and Källström (2013) estimated that 90 % of ISA was retained within a cementitious vault of SFR after 20 000 years. Although insignificant for a repository for short-lived waste such as SFR, the decrease with time of the ISA concentrations in the waste vault may be relevant for SFL.

The stability of complexing agents over long time-scales is also an important consideration. ISA was found to be chemically stable at high pH over a period of 12 years (Glaus and Van Loon 2008). It can be degraded by bacteria under alkaline conditions (e.g. Bassil et al. 2015, Bassil and Lloyd 2018), but the experimental data and general understanding of microbial processes suggest that this will not occur until the pH has decreased to pH ~11 (see for example Section 3.5.8 in Keith-Roach et al. 2014). In the base case, this pH is assumed to occur after a couple of hundred thousand years post-closure.

Overall, improved knowledge of amounts and longevity of complexing agents in BHA will not change the dose from non-sorbing radionuclides. However, less conservative assumptions may reduce the dose from Tc-99 and nuclides in the U-238 decay chain, which may reduce the total dose after about 100 000 AD.

8.4.2 Radionuclide availability for transport

A number of cautious assumptions that increase the amount of radioactivity available for transport are made in SE-SFL. Some of the most important are that all radionuclides are unaffected by solubility limitations, that no radionuclide is affected by the presence of others (except ingrowth from parent radionuclides), that waste containers provide no transport resistance, that metal with induced radioactivity in BHK starts corroding instantly at a constant rate, that radionuclides released by corrosion or otherwise dissolved do not re-precipitate, and that radionuclides do not sorb on, or co-precipitate with, corrosion products. More realistic assumptions may reduce the calculated doses. As illustrated by the *lower steel corrosion rate evaluation case* (Section 6.3), the effect of altered assumptions may not be proportional to the change. Thus, detailed investigations are needed in order to reduce the conservatism in these assumptions.

Further, the uncertainty in the initial inventory of radionuclides and other materials in BHA is larger than for BHK. Therefore, some near-field model assumptions are more simplified and pessimistic in BHA than in BHK. For instance, no account is taken of the potential delayed release of radionuclides from the materials in BHA, even though part of the activity in BHA is likely contained in solid materials such as metals (Section 2.3.1 in Shahkarami 2019). Better characterization of the physical form of the uranium inventory will likely lead to higher retention in the near-field thanks to delayed release.

8.4.3 Geosphere retention

In the geosphere transport calculations, no sorption in the fracture is considered, neither on its walls nor in possible fracture fill. Sorption inside the bedrock matrix is accounted for but the K_d values have been cautiously chosen (Section 3.3.1 in Shahkarami 2019). For instance, the K_d value of the dose-dominating radionuclide Mo-93 is set to zero. Site-specific data from Olikiluoto suggest that Mo-93 sorption does occur (see *alternative geosphere retention evaluation case*, Section 7.4). Moreover, pathways through the geosphere along which the particles do not reach the geosphere biosphere interface are neglected. One reason for particles not reaching the surface is that the flows are so low that numerical artefacts occur. Thus, neglecting such pathways disregards transport with high potential for retention.

8.4.4 Distributed release

In the dose calculations, it is assumed that all geosphere releases occur in a single biosphere object. This is cautious, since the hydrogeological analysis suggests that the geosphere releases will be dispersed among several objects (Section 4.6 in Joyce et al. 2019).

8.5 Potential to meet the regulatory requirements on the dose to humans

The total annual doses from each of the two waste vaults exceed the dose of 14 μSv in the *present-day evaluation case*, corresponding to the regulatory risk criterion (Figure 5-18). The annual doses from several individual radionuclides are within an order of magnitude of this limit: C-14 and Mo-93 for both vaults and Tc-99, Cl-36 and the uranium series for BHA. The doses resulting from the other two evaluation cases related to the reference evolution, i.e. the *increased greenhouse effect evaluation case* and the *simplified glacial cycle evaluation case* are similar to, or smaller, than predicted in the *present-day evaluation case*.

It should be noted that the base case does not correspond to a main scenario in a regulatory context and that the results for doses cannot be directly interpreted in relation to the risk criterion. Nevertheless, the evaluation cases presented below illustrate under what conditions the repository performance improves to yield doses that are well below 14 μSv. It should moreover be noted that the results for BHA rely on the inventory that is judged to be subject to substantial uncertainties, with changes in the inventory giving rise to proportional changes in the resulting doses.

8.5.1 BHA

Waste

The total annual activity release from the BHA near-field (Figure 5-8), and the annual doses (Figure 5-18), are dominated by the radionuclides that dominate the initial inventory and have half-lives longer than a few thousand years, i.e. Mo-93, Cl-36 and Tc-99 (Figure 5-7). Also, nuclides in the U-238 decay chain contribute significantly towards the end of the one-million-year analysis period. Reducing uncertainties in the initial inventory of these radionuclides is therefore important in order to perform a full safety analysis to assess if the regulatory requirements are met.

SE-SFL evaluates the potential for the proposed repository concept for the waste from Studsvik Nuclear AB, Cyclife Sweden AB and AB SVAFO based on a first estimated initial inventory of radionuclides and other materials. Further, as discussed in Section 8.4.2, radionuclides from the materials in BHA are assumed to dissolve and be available for transport immediately.

As discussed in Section 8.4.1, complexing agents are assumed to be present and strongly affect the sorption capacity for several radionuclides, e.g. Tc-99, throughout the whole assessment period of one million years. Improved knowledge of amounts of complexing agents in BHA will not change the maximum dose that is related to non-sorbing radionuclides, but more informed assumptions are likely to reduce the calculated impact of complexing agents on Tc-99 and the U-238 decay chain, and consequently reduce the dose after about 50 000 AD (Figure 6-2).

Groundwater flow rate

More favourable hydrological properties than those assumed in the base case could, according to preliminary data, be found at other locations in Laxemar (e.g. at greater depths) and elsewhere in Sweden. The location of the repository below the seabed could also reduce the groundwater flow in the rock at repository depth.

Lower groundwater flow at repository depth than that postulated in the base case leads to reduced releases and doses from BHA. Radionuclide transport through the near-field of BHA occurs mainly through diffusion. Therefore, the reductions of the BHA near-field releases are modest as response to a decrease in the groundwater flow rate. With 10 times lower flow rate, the maximum near-field releases of the cations Tc-99, C-14 and Ag-108m are 41 % of that in that in the base case (left panel in Figure 7-1). The corresponding maximum near-field releases of the anions Mo-93 and Cl-36 are 66 % of that in the base case.

However, with 100 times lower groundwater flow than in the base case, the importance of decay in the geosphere increases as the radionuclide retention times in the geosphere increasingly exceed their half-lives, and the radionuclide-specific responses are accentuated (Figure 8-1). For Tc-99, which sorbs in the geosphere, retention in the geosphere is more than seven orders of magnitude higher than in the base case. The maximum dose from BHA is reduced to 6 % of that in the base case (left panel of Figure 7-2). The dose contributions of Mo-93, C-14 and, in particular, Tc-99 decrease and the dose from Cl-36 becomes of greater relative importance as the groundwater flow rate decreases.

The *initially submerged conditions evaluation case* analyses the effect of locating SFL at a position that is currently below the seabed. A prolonged period of submerged conditions is likely to retard the advective transport from the repository due to low groundwater flow. This reduction is here assumed to be 100 times lower groundwater flow rates during an initial period after repository closure (e.g. 10 000 years).

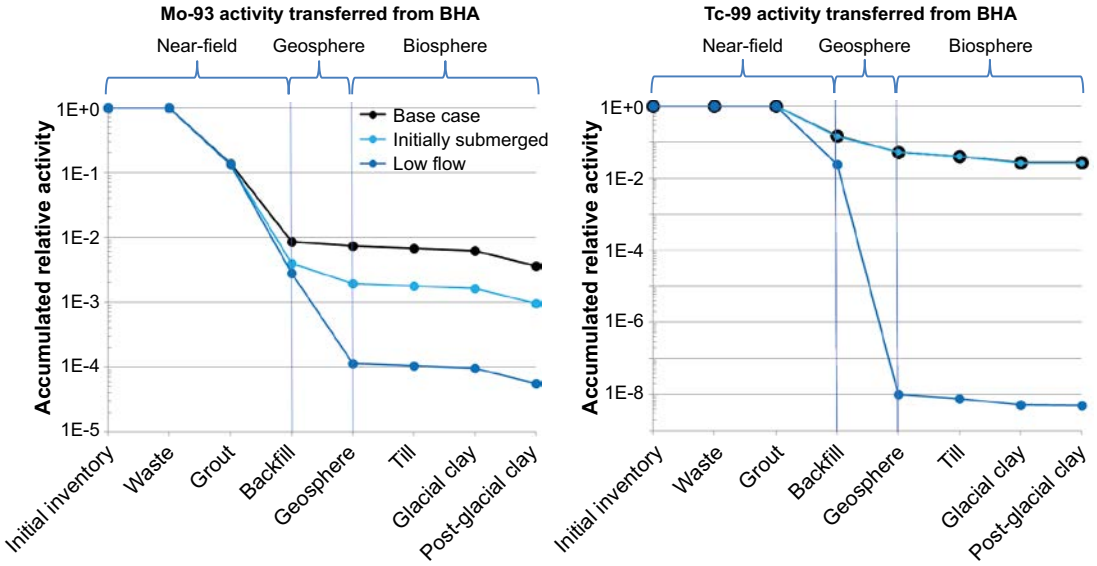

Figure 8-1. *Activity of Mo-93 (left panel) and Tc-99 (right panel) transferred along the way from the initial inventory in BHA to the biosphere, accumulated over the entire analysis period of one million years, and normalised by the initial inventory. The relative activity transferred is shown for the base case (black), the variant with 10 000 years of initially submerged conditions (light blue) and for the variant of the lower groundwater flow evaluation case with 100 times lower groundwater flow rate than in the base case (dark blue). Note that the base case and initially submerged data coincide throughout the right panel.*

The evaluation shows that the maximum release rates to the biosphere may be delayed by the duration of the submerged period, and that radioactive decay may reduce the dose substantially in the terrestrial period following the submerged period due to shoreline displacement. For Mo-93 and C-14, which decay moderately during the submerged period, the maximum near-field annual release rate is lower than in the base case (Figure 7-5, Figure 8-1). However, decay of Tc-99 and Cl-36 (half-life $> 2 \times 10^5$ a) is limited during the submerged period. Therefore, once the groundwater flow rate increases, the maximum near-field and geosphere release rates are similar to those in the base case (Figure 7-5, Figure 8-1). The resulting effect of an initially submerged period is not dramatic; the maximum annual dose from a repository that is submerged for 10 000 years is reduced by a factor two, as compared with release to a land location (described in the base case).

8.5.2 BHK

Release by corrosion of metallic waste

The waste planned for BHK is mostly in the form of scrap metal and most of the activity originates from neutron irradiation of the construction material of reactor components close to the core (Herschend 2014). The release of this induced radioactivity from the waste is assumed to be controlled by a constant corrosion rate. Since most of the waste planned for BHK is stainless steel, the corrosion rate of 0.01 μm/a used for stainless steel under alkaline anoxic conditions in SR-PSU (Table 5-3 in SKB 2014d) is applied also in the base case of SE-SFL. There are also fractions of the radionuclide inventory that are present in very thin metallic parts (< 1 mm, Table 6-1). Those fractions are assumed to be available for instant release. This is a pessimistic assumption as even very thin metal may give retention on timescales of 100 000 years.

The corrosion rate used in the base case is higher than recently reported long-term corrosion rates, such as 0.0004 μm/a for stainless steel in simulated repository conditions (Sakuragi et al. 2016), or 0.001 μm/a, which is the lower end of the range for stainless steel corrosion under alkaline anoxic conditions recommended for use in PSAR for SR-PSU. Reducing the corrosion rate to this lower end of the range (i.e. by a factor of ten as compared to the base case) reduces the maximum annual activity release from the near-field (Figure 8-2) and maximum annual doses (Figure 6-3) by a factor of four. This reduction is fully controlled by the response of Mo-93, which dominates the dose in the base case.

The effects of the corrosion rate on near-field releases and doses varies among radionuclides depending on the inventory in the instant-release fraction and in the thicker metal fractions that are influenced by corrosion, but retention and decay rates also influence the response. Consequently, the potential for reduced releases and doses from BHK associated with the uncertainty in corrosion rate needs to be evaluated in relation to the assumptions about, and uncertainty in, the initial distribution of the radionuclide inventory between the instant release and thicker metal fractions.

Concrete backfill

The quality of the concrete used as backfill material in BHK is a design consideration. A concrete composition with lower hydraulic conductivity, porosity and diffusivity can significantly improve the repository performance. In the *alternative concrete backfill in BHK evaluation case*, transport parameters are chosen based on modelling of concrete degradation for a new improved concrete formula (Idiart et al. 2019b). The resulting dose is only 3 % of that in the base case, primarily due to increased retention and decay in the near-field (left panel in Figure 8-2). The decrease in the near-field release of the sorbing Mo-93 is larger than for the non-sorbing C-14 (right panel in Figure 8-2), and the dose-dominating radionuclide switches from Mo-93 in the base case to C-14 in the *alternative concrete case* (Figure 6-6). In general, radionuclides with a high proportion of decay in the near-field (in the base case), i.e. due to high sorption and/or high decay rate, are most affected by a more favourable concrete composition.

The values of the transport parameters in the alternative concrete backfill in BHK are comparable with the properties of the concrete developed for 2BMA (Lagerblad et al. 2017, Mårtensson and Vogt 2019, Idiart et al. 2019b). In addition to the improved transport properties that are applied in the modelling, the concrete developed for 2BMA also has lower porosity and diffusivity, so cement leaching should be suppressed (Idiart et al. 2019b) compared with what is assumed in the *alternative concrete backfill in BHK evaluation case* (and in the base case). This implies that the degraded-zone period would occur later, if at all, within the time frame of the analysis. Consequently, the late time releases of Ca-41 and Ni-59 would decrease even further, although these radionuclides are not dose-dominating. Overall, this case results in an improved long-term performance of BHK.

Groundwater flow rates

Lower groundwater flow rates have a greater impact on the doses from BHK compared with BHA, and 10 times lower flow rates are enough to decrease the dose from BHK to 3 % of that in the base case (Figure 7-2). The explanation is mainly that transport within and out from the near-field in BHK is limited by advection in the base case, whereas transport in BHA is mainly limited by diffusion which is insensitive to groundwater flow rates.

With ten times lower groundwater flow rates, the lower doses from BHK are mainly thanks to increased retention and decay in the near-field, while retention and decay in the geosphere have a moderate effect (Figure 8-2). Lower groundwater flow rates affect the releases more for radionuclides strongly affected by decay, caused by a high decay rate and/or strong sorption. Thus, the near-field release from BHK of the sorbing radionuclide Mo-93 (left panel in Figure 8-2) decreases more with lower flow rates than release of the non-sorbing C-14 (right panel in Figure 8-2).

With even lower groundwater flow rates, the relative importance of decay in the geosphere increases as the radionuclide retention times in the geosphere increasingly exceed their half-lives (not shown). The BHK near-field release eventually becomes dominated by diffusion with increasingly lowered groundwater flow rates.

The BHK near-field releases and doses in the *lower groundwater flow evaluation case* are similar to the results for the *alternative concrete backfill in BHK evaluation case* (Figure 8-2). The similarities are largely explained by the reduction in near-field advective flow by ten times in both evaluation cases. Geosphere retention and decay is however only affected in the *lower groundwater flow evaluation case*, and the decreased porosity in the *alternative concrete backfill in BHK evaluation case* has a different near-field effect on sorbing and non-sorbing radionuclides. Given the initial inventory in BHK, these two effects are of similar magnitude, resulting in similar total annual doses in the two evaluation cases (Figures 6-6 and 7-2).

As described above, locating SFL at a position that is currently below the seabed is likely to retard the advective transport from the repository due to low groundwater flow. In the *initially submerged conditions evaluation case*, 100 times lower groundwater flow rates are assumed during a limited initial period after repository closure. Once the groundwater flow rate increases, the maximum near-field and geosphere release rates become similar to those in the base case (Figure 7-5). Nevertheless, the initial inventory for BHK contains significantly lower radioactivity from very long-lived (e.g. Cl-36), or uranium-series radionuclides. Therefore, a prolonged period of about 50 ka or more of initially submerged conditions (not included in the analysis which is limited to 10 ka) could potentially lead to a significant reduction of the maximum dose from BHK.

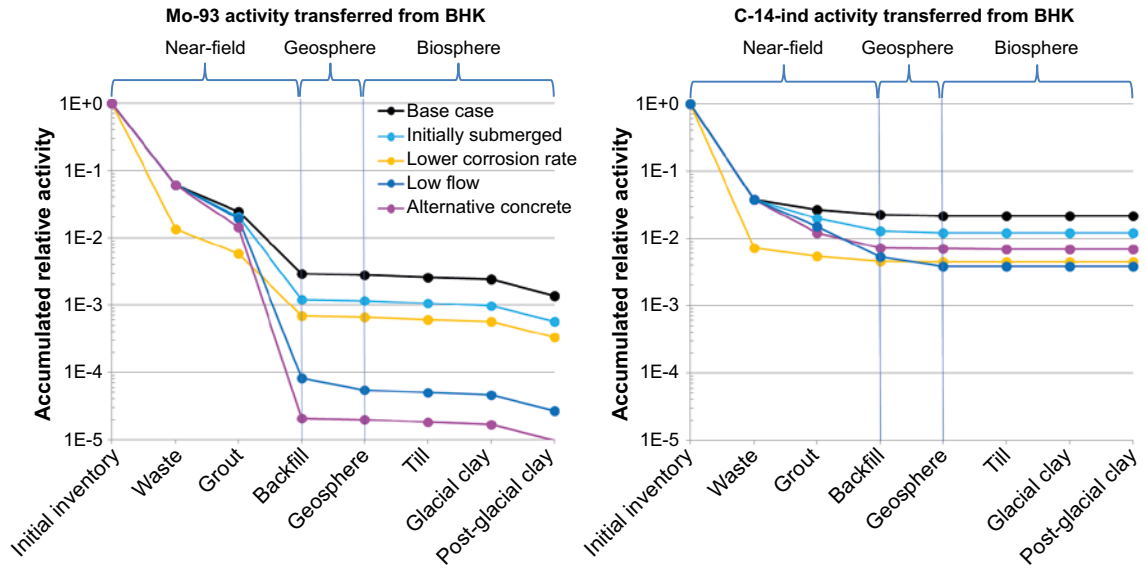

Figure 8-2. *Activity of Mo-93 (left panel) and C-14 (right panel) transferred along the way from the initial inventory in BHK to the biosphere, accumulated over the entire analysis period of one million years, and normalised by the initial inventory .The relative activity transferred is shown for the base case (black), the variant with 10 000 years of initially submerged conditions (light blue), for ten times lower corrosion rate (yellow), for the variant of the lower groundwater flow evaluation case with 10 times lower groundwater flow rate than in the base case (dark blue) and for the case with alternative concrete (magenta).*

References

SKB's (Svensk Kärnbränslehantering AB) publications can be found at www.skb.com/publications. SKBdoc documents will be submitted upon request to document@skb.se.

References with abbreviated names

Main report, 2019. Post-closure safety for a proposed repository concept for SFL. Main report for the safety evaluation SE-SFL. SKB TR-19-01, Svensk Kärnbränslehantering AB.

Biosphere synthesis, 2019. Biosphere synthesis for the safety evaluation SE-SFL. SKB TR-19-05, Svensk Kärnbränslehantering AB.

Climate report, 2019. Climate and climate-related issues for the safety evaluation SE-SFL. SKB TR-19-04, Svensk Kärnbränslehantering AB.

FEP report, 2019. Features, events and processes for the safety evaluation SE-SFL. SKB TR-19-02, Svensk Kärnbränslehantering AB.

Initial state report, 2019. Initial state for the repository for the safety evaluation SE-SFL. SKB TR-19-03, Svensk Kärnbränslehantering AB.

Other references

Abarca E, Sampietro D, Molinero J, von Schenck H, 2019. Modelling of the near-field hydrogeology-temperate climate conditions. Report for the safety evaluation SE-SFL. SKB R-19-03, Svensk Kärnbränslehantering AB.

Alexandersson, Eggertsson Karlström C, 2001. Temperaturen och nederbörden i Sverige 1961−1990: referensnormaler. 2nd ed. Norrköping: SMHI. (In Swedish.)

Andersson J, Hermansson J, Elert M, Gylling B, Moreno L, Selroos J-O, 1998. Derivation and treatment of the flow wetted surface and other geosphere parameters in the transport models FARF31 and COMP23 for use in safety assessment. SKB R-98-60, Svensk Kärnbränslehantering AB.

Bassil N M, Lloyd J R, 2018. *Anaerobacillus isosaccharinicus* sp. nov., an alkaliphilic bacterium which degrades isosaccharinic acid. International Journal of Systematic and Evolutionary Microbiology. doi:10.1099/ijsem.0.002721.

Bassil N M, Bryan N, Lloyd J R, 2015. Microbial degradation of isosaccharinic acid at high pH. The ISME Journal 9, 310−320.

Bodin L, Delay F, de Marsily G, 2003. Solute transport in a single fracture with negligible matrix permeability: 2. Mathematical formalism. Hydrology Journal 11, 434−454.

Brenner D J, Doll R, Goodhead D T, Hall E J, Land C E, Little J B, Lubin J H, Preston D L, Preston R J, Puskin J S, Ron E, Sach R K, Samet J M, Setlow R B, Zaider M, 2003. Cancer risks attributable to low doses of ionizing radiation: assessing what we really know. Proceedings of the National Academy of Sciences 100, 13761−13766.

Brydsten L, Strömgren M, 2010. A coupled regolith-lake development model applied to the Forsmark site. SKB TR-10-56, Svensk Kärnbränslehantering AB.

Brydsten L, Strömgren M, 2013. Landscape development in the Forsmark area from the past into the future (8500 BC − 40,000 AD). SKB R-13-27, Svensk Kärnbränslehantering AB.

Claesson Liljedahl L, Kontula A, Harper J, Näslund J-O, Selroos J-O, Pitkänen P, Puigdomenech I, Hobbs M, Follin S, Hirschorn S, Jansson P, Kennell L, Marcos N, Ruskeeniemi T, Tullborg E-L, Vidstrand P, 2016. The Greenland Analogue Project: Final report. SKB TR-14-13, Svensk Kärnbränslehantering AB.

Crawford J, 2018. Screening of radionuclides for radionuclide and dose calculations. Report for the safety evaluation SE-SFL. SKB P-16-09, Svensk Kärnbränslehantering AB.

Egan M, Little R, Walke R, 2012. Review of landscape models used in SR-Site. Technical Note 2012:46, Swedish Radiation Safety Authority.

Elfwing M, Evins L Z, Gontier M, Grahm P, Mårtensson P, Tunbrant S, 2013. SFL concept study. Main report. SKB TR-13-14, Svensk Kärnbränslehantering AB.

Fetter C W, 1999. Contaminant hydrogeology. 2nd ed. Upper Saddle River, NJ: Prentice Hall.

Glaus M A, Van Loon L R, 2008. Degradation of cellulose under alkaline conditions: new insights from a 12 years degradation study. Environmental Science & Technology 42, 2906−2911.

Grolander S, 2013. Biosphere parameters used in radionuclide transport modelling and dose calculations in SR-PSU. SKB R-13-18, Svensk Kärnbränslehantering AB.

Grolander S, Jaeschke B, 2019. Biosphere parameters used in radionuclide transport modelling and dose calculations in SE-SFL. SKB R-19-18, Svensk Kärnbränslehantering AB.

Gylling B, 1997. Development and applications of the channel network model for simulations of flow and solute transport in fractured rock. PhD thesis. Department of Chemical Engineering and Technology, Royal Institute of Technology, Stockholm, Sweden.

Hartikainen J, Kouhia R, Wallroth T, 2010. Permafrost simulations at Forsmark using a numerical 2D thermo-hydro-chemical model. SKB TR-09-17, Svensk Kärnbränslehantering AB.

Herschend B, 2014. Long-lived intermediate level waste from Swedish nuclear power plants. Reference inventory. SKB R-13-17, Svensk Kärnbränslehantering AB.

IAEA, 2007. IAEA safety glossary: terminology used in nuclear safety and radiation protection. 2007 edition. Vienna: International Atomic Energy Agency.

ICRP, 1998. Radiation protection recommendations as applied to the disposal of long-lived solid radioactive waste. Oxford: Pergamon. (ICRP Publication 81; Annals of the ICRP 28(4))

ICRP, 2006. Assessing dose of the representative person for the purpose of radiation protection of the public and the optimisation of radiological protection: broadening the process. Oxford: Pergamon. (ICRP Publication 101; Annals of the ICRP 36(3))

Idiart A, Laviña M, 2019. Modelling of concrete degradation in a one-million-year perspective – Hydro-chemical processes. Report for the safety evaluation SE-SFL. SKB R-19-13, Svensk Kärnbränslehantering AB.

Idiart A, Shafei B, 2019. Modelling of concrete degradation – Hydro-chemical processes. Report for the safety evaluation SE-SFL. SKB R-19-11, Svensk Kärnbränslehantering AB.

Idiart A, Laviña M, Coene E, 2019a. Modelling of concrete degradation – Hydro-chemo-mechanical processes. Report for the safety evaluation SE-SFL. SKB R-19-12, Svensk Kärnbränslehantering AB.

Idiart A, Olmeda J, Laviña M, 2019b. Modelling of concrete degradation – Influence of concrete mix design. Report for the safety evaluation SE-SFL. SKB R-19-14, Svensk Kärnbränslehantering AB.

Joyce S, Appleyard P, Hartley L, Tsitsopoulos V, Woollard H, Marsic N, Sidborn M, Crawford J, 2019. Groundwater flow and reactive transport modelling of temperate conditions. Report for the safety evaluation SE-SFL. SKB R-19-02, Svensk Kärnbränslehantering AB.

Keith-Roach M, Lindgren M, Källström K, 2014. Assessment of complexing agent concentrations in SFR. SKB R-14-03, Svensk Kärnbränslehantering AB.

Lagerblad B, Rogers P, Vogt C, Mårtensson P, 2017. Utveckling av konstruktionsbetong till kassunerna i 2BMA. SKB R-17-21, Svensk Kärnbränslehantering AB. (In Swedish.)

Lindborg T (ed), 2010. Landscape Forsmark – data, methodology and results for SR-Site. SKB TR-10-05, Svensk Kärnbränslehantering AB.

Lindgren M, Pettersson M, Karlsson S, Moreno L, 2001. Project SAFE. Radionuclide release and dose from the SFR repository. SKB R-01-18, Svensk Kärnbränslehantering AB.

Lindgren M, Gylling B, Elert M, 2002. FARF31 Version 1.2. User's guide. SKB TS-02-03, Svensk Kärnbränslehantering AB.

Losjö K, Johansson B, Bringefelt B, Oleskog I, Bergström S, 1999. Groundwater recharge – climatic and vegetation induced variations. Simulations in the Emån and Äspö areas in southern Sweden. SKB TR-99-01, Svensk Kärnbränslehantering AB.

Maul P R, Robinson P C, 2008. Radionuclide transport calculations in preparation for the review of SR-Site. Quintessa Report QRS-1097K-1, Quintessa Ltd, UK.

Mårtensson P, Vogt C, 2019. Concrete caissons for 2BMA. Large scale test of design and material. SKB TR-18-12, Svensk Kärnbränslehantering AB.

Neretnieks I, 1986. Stationary transport of dissolved species in the backfill surrounding a waste canister in fissured rock: some simple analytical solutions. Nuclear Technology 72, 194−200.

Norman S, Kjellbert N, 1990. FARF31 – A far field radionuclide migration code for use with the PROPER package. SKB TR 90-01, Svensk Kärnbränslehantering AB.

Nyman H, Sohlenius G, Strömgren M, Brydsten L, 2008. Depth and stratigraphy of regolith. Site descriptive modelling SDM-Site Laxemar. SKB R-08-06, Svensk Kärnbränslehantering AB.

Näslund J-O, Mårtensson P, Lindgren M, Åstrand P-G, 2017. Information om klimat och effekter på SFR till följd av frysning av betong. SKBdoc 1572377 ver 1.0, Svensk Kärnbränslehantering AB. (In Swedish.)

Odén M, Follin S, Öhman J, Vidstrand P, 2014. SR-PSU Bedrock hydrogeology Groundwater flow modelling methodology, setup and results. SKB R-13-25, Svensk Kärnbränslehantering AB.

Painter S, Mancillas J, 2009. MARFA version 3.2.2 user's manual: migration analysis of radionuclides in the far field. SKB R-09-56, Svensk Kärnbränslehantering AB.

Painter S, Mancillas J, 2013. MARFA user's manual: Migration analysis of radionuclides in the far field. Posiva Working Report 2013-01, Posiva Oy, Finland.

Posiva, 2013. Safety case for the disposal of spent nuclear fuel at Olkiluoto – Models and data for the repository system 2012. Posiva 2013-01, Posiva Oy, Finland.

Rhén I, Forsmark T, Hartley L, Jackson C P, Roberts D, Swan D, Gylling B, 2008. Hydrogeological conceptualisation and parameterisation. Site descriptive modelling, SDM-Site Laxemar. SKB R-08-78, Svensk Kärnbränslehantering AB.

Rhén I, Forsmark T, Hartley L, Joyce S, Roberts D, Gylling B, Marsic N, 2009. Bedrock hydrogeolology. Model testing and synthesis. Site descriptive modelling, SDM-Site Laxemar. SKB R-08-91, Svensk Kärnbränslehantering AB.

Sakuragi T, Yoshida S, Kato O, Tateishi T, 2016. Study of stainless steel corrosion by hydrogen measurement under deoxygenated, low-temperature and basic repository conditions. Progress in Nuclear Energy 87, 26−31.

Saetre P, Ekström P-A, 2017. Kompletterande beräkningar om biosfärsobjekt. SKBdoc 1571087 ver. 1.0, Svensk Kärnbränslehantering AB. (In Swedish.)

Saetre P, Nordén S, Keesmann S, Ekström P-A, 2013. The Biosphere model for radionuclide transport and dose assessment in SR-PSU. SKB R-13-46, Svensk Kärnbränslehantering AB.

Sassner M, Sabel U, Bosson E, Berglund S, 2011. Numerical modelling of present and future hydrology at Laxemar-Simpevarp. SKB R-11-05, Svensk Kärnbränslehantering AB.

Shahkarami P, 2019. Input data report for near-field and geosphere radionuclide transport modelling. Report for the safety evaluation SE-SFL. SKB R-19-09, Svensk Kärnbränslehantering AB.

Sidborn M, 2018. Metallic corrosion. SKBdoc 1622757 ver 1.0, Svensk Kärnbränslehantering AB.

Silva O, Coene E, Moliner J, Laviña M, Idiart A, 2019a. Gas release from the BHK vault – Multiphase flow modelling of the near-field. Report for the safety evaluation SE-SFL. SKB R-19-06, Svensk Kärnbränslehantering AB.

Silva O, Sáinz-García Á, Molinero J, 2019b. Gas release from the SFL repository and migration through the geosphere. Report for the safety evaluation SE-SFL. SKB R-19-07, Svensk Kärnbränslehantering AB.

SKB, 1999. Deep repository for long-lived low- and intermediate-level waste. Preliminary safety assessment. SKB TR-99-28, Svensk Kärnbränslehantering AB.

SKB, 2006a. Long-term safety for KBS-3 repositories at Forsmark and Laxemar – a first evaluation. Main report of the SR-Can project. SKB TR-06-09, Svensk Kärnbränslehantering AB.

SKB, 2006b. Climate and climate-related issues for the safety assessment SR-Can. SKB TR-06-23, Svensk Kärnbränslehantering AB.

SKB, 2009. Site description of Laxemar at completion of the site investigation phase. SDM-Site Laxemar. SKB TR-09-01, Svensk Kärnbränslehantering AB.

SKB, 2010a. Geosphere process report for the safety assessment SR-Site. SKB TR-10-48, Svensk Kärnbränslehantering AB.

SKB, 2010b. Radionuclide transport report for the safety assessment SR-Site. SKB TR-10-50, Svensk Kärnbränslehantering AB.

SKB, 2010c. Biosphere analyses for the safety assessment SR-Site – synthesis and summary of results. SKB TR-10-09, Svensk Kärnbränslehantering AB.

SKB, 2010d. Comparative analysis of safety related site characteristics. SKB TR-10-54, Svensk Kärnbränslehantering AB.

SKB, 2010e. Climate and climate-related issues for the safety assessment SR-Site. SKB TR-10-49, Svensk Kärnbränslehantering AB.

SKB, 2010f. Data report for the safety assessment SR-Site. SKB TR-10-52, Svensk Kärnbränslehantering AB.

SKB, 2010g. Model summary report for the safety assessment SR-Site. SKB TR-10-51, Svensk Kärnbränslehantering AB.

SKB, 2011a. Long-term safety for the final repository for spent fuel at Forsmark. Main report of the SR-Site project. SKB TR-11-01, Svensk Kärnbränslehantering AB.

SKB, 2011b. Site selection – siting of the final repository for spent nuclear fuel. SKB R-11-07, Svensk Kärnbränslehantering AB.

SKB, 2014a. Waste form and packaging process report for the safety assessment SR-PSU. SKB TR-14-03, Svensk Kärnbränslehantering AB.

SKB, 2014b. Engineered barrier process report for the safety assessment SR-PSU. SKB TR-14-04, Svensk Kärnbränslehantering AB.

SKB, 2014c. Geosphere process report for the safety assessment SR-PSU. SKB TR-14-05, Svensk Kärnbränslehantering AB.

SKB, 2014d. Data report for the safety assessment SR-PSU. SKB TR-14-10, Svensk Kärnbränslehantering AB.

SKB, 2014e. Biosphere synthesis report for the safety assessment SR-PSU. SKB TR-14-06, Svensk Kärnbränslehantering AB.

SKB, 2014f. Climate and climate-related issues for the safety assessment SR-PSU. SKB TR-13-05, Svensk Kärnbränslehantering AB.

SKB, 2015a. Safety analysis for SFR. Long-term safety. Main report for the safety assessment SR-PSU. Revised edition. SKB TR-14-01, Svensk Kärnbränslehantering AB.

SKB, 2015b. Radionuclide transport and dose calculations for the safety assessment SR-PSU. Revised edition. SKB TR-14-09, Svensk Kärnbränslehantering AB.

SSM, 2008a. The Swedish Radiation Safety Authority's regulations and general advice concerning the protection of human health and the environment in connection with the final management of spent nuclear fuel and nuclear waste. Stockholm: Swedish Radiation Safety Authority. (SSMFS 2008:37)

SSM, 2008b. The Swedish Radiation Safety Authority's regulations concerning safety in connection with the disposal of nuclear material and nuclear waste. Stockholm: Swedish Radiation Safety Authority. (SSMFS 2008:21)

SSM, 2018. Strålsäkerhet efter slutförvarets förslutning. Beredning inför regeringens prövning Slutförvaring av använt kärnbränsle. SSM Rapport 2018:07, Swedish Radiation Safety Authority.

SSM, 2019. Granskningsrapport – Utbyggnad och fortsatt drift av SFR. Del III Långsiktig strålsäkerhet. SSM Granskningsrapport SSM2017-5969-2, Swedish Radiation Safety Authority.

Sudicky E A, Frind E O, 1982. Contaminant transport in fractured porous media: analytical solutions for a system of parallel fractures. Water Resources Research 18, 1634−1642.

Tang D H, Frind E O, Sudicky E A, 1981. Containment transport in fractured porous media: analytical solution for a single fracture. Water Resources Research 17, 555−564.

Thomson G, Herben M, Lloyd P, Rose D, Smith C, Barraclough I, 2008. Implementation of project Safe in Amber Verification study for SFR 1 SAR-08. SKB R-08-13, Svensk Kärnbränslehantering AB.

Trinchero P, Ebrahimi H, Colas E, Fernández-Garcia D, 2018. Assessing nickel and molybdenum transport in the bedrock at SFL using a dynamic K_d approach. Report for the safety evaluation SE-SFL. SKB R-17-03, Svensk Kärnbränslehantering AB.

Tröjbom M, Grolander S, Rensfeldt V, Nordén S, 2013. K_d and CR used for transport calculations in the biosphere in SR-PSU. Updated 2016-10. SKB R-13-01, Svensk Kärnbränslehantering AB.

Vahlund F, Hermansson H, 2006. A direct numerical approach to solving the transport equations for radionuclide transport in fractured rock. SKB R-04-50, Svensk Kärnbränslehantering AB.

Vidstrand P, Rhén I, Zugec N, 2010a. Groundwater flow modelling of periods with periglacial and glacial climate conditions – Laxemar. SKB R-09-25, Svensk Kärnbränslehantering AB.

Vidstrand P, Follin S, Zugec N, 2010b. Groundwater flow modelling of periods with periglacial and glacial climate conditions – Forsmark. SKB R-09-21, Svensk Kärnbränslehantering AB.

Vidstrand P, Follin S, Selroos J-O, Näslund J-O, Rhén I, 2013. Modeling of groundwater flow at depth in crystalline rock beneath a moving ice-sheet margin, exemplified by the Fennoscandian Shield, Sweden. Hydrogeology Journal 21, 239−255.

Vidstrand P, Follin S, Selroos J-O, Näslund J-O, 2014a. Groundwater flow modeling of periods with periglacial and glacial climate conditions for the safety assessment of the proposed high-level nuclear waste repository site at Forsmark, Sweden. Hydrogeology Journal 22, 1251−1267.

Vidstrand P, Follin S, Öhman J, 2014b. SR-PSU Hydrogeological modelling. TD13 – Periglacial climate conditions. SKB P-14-06, Svensk Kärnbränslehantering AB.

von Schenck H, Källström K, 2014. Reactive transport modelling of organic complexing agents in cement stabilized low and intermediate level waste. Physics and Chemistry of the Earth, Parts A/B/C 70, 114−126.

Walke R, Limer L, Shaw G, 2017. In-depth review of key issues for the main review phase regarding biosphere models for specific radionuclides in SR-PSU. SSM2016-3262-3, Swedish Radiation Safety Authority.

Werner K, Bosson E, Berglund S, 2006. Description of climate, surface hydrology, and near-surface hydrogeology. Preliminary site description. Laxemar subarea – version 1.2. SKB R-05-61, Svensk Kärnbränslehantering AB.

Werner K, Sassner M, Johansson E, 2013. Hydrology and near-surface hydrogeology at Forsmark – synthesis for the SR-PSU project. SR-PSU Biosphere. SKB R-13-19, Svensk Kärnbränslehantering AB.

Wessely O, Shahkarami P, 2019. Development of radionuclide transport models for the near-field. Report for the safety evaluation SE-SFL. SKB R-19-05, Svensk Kärnbränslehantering AB.

Appendix A

Glossary

This appendix contains explanations of terms and abbreviations used in the report.

Table A-1. Terms and abbreviations used in the report.

Term/abbreviation	Description
Advection	Transport of a dissolved substance by the bulk flow of water.
Annual dose	Used in this report to denote yearly committed, effective dose to a representative member of an exposed group.
Biosphere object	A part of the landscape that potentially will receive radionuclides released from the repository.
BHA	Vault for legacy waste from the early research in the Swedish nuclear programmes, and smaller amounts of waste from medicine, industry and research.
BHK	Vault for reactor internals.
Calculation case	A calculation case provides a parameterised model chain for the quantitative assessment of an evaluation case.
Control volume	Entities of the 3D-domain of the hydrological near-field model used to derive the water balance of the specified volume, for which flows across surfaces of the control volume are determined. Compartments of the near-field radionuclide transport model correspond with control volumes of the hydrological model or with fractions of them.
DM	Drained-mire farmers. DM refers to a self-sustained industrial agriculture in which wetlands are drained and used for agriculture (both crop and fodder production). It is one of the land-use variants considered in SE-SFL for assessment of the most exposed group.
Ecolego	Compartmental modelling code used for radionuclide transport calculations undertaken in this assessment.
Effective dose	Effective dose or effective dose equivalent is a measure of dose designed to reflect the risk associated with the dose. It is calculated as the weighted sum of the dose equivalents in the different tissues of the body.
Exposed group	Different hypothetical communities that utilize the area in different ways have been used in this assessment (Agr, DM, IO, HG and GP). These groups are credible bounding cases for relevant exposure pathways and reflect land uses and habits that are reasonable and sustainable.
Evaluation case	Case designed to evaluate potential dose to humans given an initial state and future development of the conditions in the repository and its environs.
Glacial climate domain	Regions with an ice sheet.
GP	Garden-plot households. GP refers to a type of household that is self-sustained with respect to vegetables and root crops produced through small scale horticulture. It is one of four land use variants considered in SE-SFL for assessment of the most exposed group.
FARF31	Semi-analytic modelling code for modelling of radionuclide transport in the geosphere (far-field) based on a dual-porosity concept including advection, longitudinal hydrodynamic dispersion, matrix diffusion, sorption on microsurfaces in the interior of the rock and radioactive decay and ingrowth.
FARFCOMP	A numerical compartment model, built in Matlab, used for modelling transport in the geosphere based on the same conceptual model as FARF31.
HG	Hunter-gatherers. HG refers to a community that uses the undisturbed surface ecosystems as living space and to obtain food. It is one of four land-use variants considered in SE-SFL for assessment of the most exposed group.
IO	Infield–outland farmers. IO refers to a self-sustained agriculture in which infield farming of crops is dependent on nutrients from wetlands for haymaking (outland). It is one of four land-use variants considered in SE-SFL for assessment of the most exposed group.

Term/abbreviation	Description
ka	Kiloannum, one thousand years.
K_d	Partitioning coefficient for sorption [m^3/kg]. Partitioning coefficient is defined as the ratio between the element concentrations in the solid and liquid phases.
Matrix diffusion	Migration of solutes by molecular diffusion into the interior of the rock matrix.
Mean annual dose	The arithmetic mean value of the calculated annual dose (in a probabilistic assessment).
Most exposed group	In this report the term most exposed group is used to denote the one of the four, DM, IO, HG and GP that receives the largest dose in a certain calculation case (sometimes defined at a certain time point).
Periglacial climate domain	Regions that contain permafrost without the presence of an ice sheet.
SE-SFL	The safety evaluation of a proposed repository concept for SFL, of which this report forms part.
SFL	Final Repository for Long-lived Waste.
SFR	Final Repository for Short-lived Radioactive Waste, which is located in Forsmark.
SKB	Swedish Nuclear Fuel and Waste Management Company.
Spent Fuel Repository	Final Repository for Spent Nuclear Fuel.
Sorption	In this report, the term is used to designate all processes by which a dissolved species is retained at a solid surface.
SSM	Swedish Radiation Safety Authority.
SR-PSU	Safety Report – Project SFR Extension.
Temperate climate domain	Region without permafrost or the presence of ice sheets. It is dominated by a temperate climate in a broad sense, with cold winters and either cold or warm summers. Within the temperate domain, the site may also at times be submerged by the sea.
Waste form	The physical and chemical form of the waste after treatment and/or conditioning.
Waste package	The waste (form) and its packaging.
Waste type	Systematically classified waste category with a certain assigned code.
Waste vault (or vault)	Part of repository where waste is stored.

Appendix B

FARFCOMP – an implementation of a geosphere modelling tool in Matlab

This appendix documents the implementation and verification of a compartment model developed in Matlab for radionuclide migration calculations in the geosphere. The code is denoted FARFCOMP and is used for radionuclide transport calculations in fractured rock within the project SE-SFL.

In several previous safety assessments performed by SKB, radionuclide transport in the geosphere (far-field) has been modelled with FARF31, which is a (semi)analytic FORTRAN code (Norman and Kjellbert 1990, SKB 2006a, 2010b, Lindgren et al. 2001). In 2006, Vahlund and Hermansson presented a code in Matlab for solving the transport equations using a direct numerical approach with the additional capability of colloid-facilitated radionuclide transport in the fractured rock (Vahlund and Hermansson 2006). In the safety analysis for SFR submitted in 2008, SAR-08, the same FARF31 conceptual model was used, but the mathematical model was implemented as a compartment model with the modelling tool Amber (Thomson et al. 2008). In the safety assessment for the extension of SFR, SR-PSU (SKB 2015a), a model like the one used in SAR-08 was applied using the modelling tool Ecolego, with slight modifications in the discretisation and the number of compartments.

The main reason for developing the FARFCOMP code has been to get a clear, more flexible, faster and consistent solution method compared with existing codes, for solving the transport equation in one flow path. In terms of flexibility, FARFCOMP is designed to allow straightforward implementation of various features and processes that have not been considered in SKB's transport modelling code FARF31. These include sorption within a fracture, cylindrical rather than flat-slit fracture shapes with radial diffusion, colloid-facilitated transport, and variation in time of properties of flow paths or other parameters. However, to maintain direct comparability to, and continuity from, previous code results, the same parameter set used previously by SKB in FARF31 have been applied in SE-SFL's transport modelling.

The following sections in this document detail the steps from governing equations to model implementation and a set of code comparisons performed to verify model implementation, i.e. code comparisons implemented using analytical solutions as well as results from calculations with similar modelling codes, FARF31 and MARFA SP (Painter and Mancillas 2009, 2013), with input data from the SE-SFL project. A novel approach of selecting a small subset of flow-paths from a large set of flow-path trajectories to represent migration through all potential fractures in the fractured rock is also presented.

B1 Conceptual model

Radionuclides released from the barriers of a deep underground repository are carried into the local rock by advection of the flowing water and/or diffusion into open rock fractures. The retardation (and associated decay) of radionuclides before reaching the biosphere is dependent on the transport resistance of the rock, which itself is determined by groundwater flow rate, transfer distance and the rate of exchange of radionuclides between the flowing water and the rock.

Conceptually, the model uses one-dimensional transport in the direction of water flow in a trajectory of fractures (conceptualised as a stream tube) surrounded by porous rock and thus coupled with one-dimensional transport by diffusion into the immobile pore water in the rock matrix. The fracture is conceptually seen as a flat, vertical slit with parallel walls surrounded by porous rock (Gylling 1997). See Figure B-1 for an illustration of the conceptual fracture-matrix system, where a constant groundwater velocity v [m a^{-1}], fracture aperture $2b$ [m], and distance between fractures $2d_{max}$, [m] is applied. The transport equations use a so-called dual porosity description with advection–dispersion in the mobile phase (transport by flowing water along the rock fracture) and diffusion into immobile pore water in the rock matrix, where sorption is also considered.

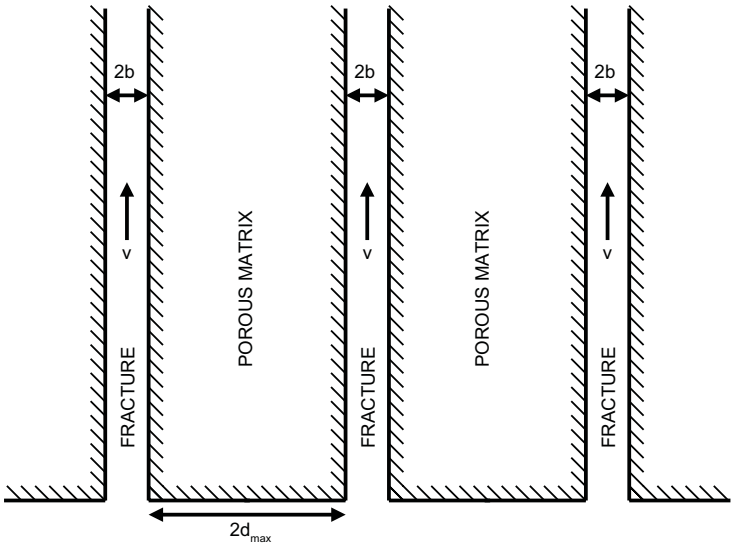

Figure B-1. *Conceptual fracture-matrix system (adapted from Tang et al. 1981).*

The migration rate of radionuclides in the geosphere is usually much lower than is implied by the advective travel time (travel time due to advective flow, without any retardation). The reason for this is due to two general retention mechanisms: first, radionuclides in the fracture network enter the internal porous network of the rock matrix by diffusion, and second, radionuclides are removed from the aqueous phase by sorption.

The transport processes in the system of Figure B-1 can be described by two coupled, one-dimensional equations, one for the fracture and one for the porous matrix. The coupling is provided by the continuity of fluxes and concentrations along the interface.

B2 Mathematical model description

A dual-porosity model for radionuclide transport in fractured rock is derived in Norman and Kjellbert (1990). Under the following assumptions

(i) Stationary flow conditions prevail.

(ii) Transverse dispersion may be neglected.

(iii) The longitudinal dispersion coefficient and the exchange terms between flow- and diffusional porosity may be replaced by averages over the stream tube cross section.

(iv) The density is constant, and the variation of porosity is small compared with the variation of concentration.

(v) The stream tube is sufficiently narrow to warrant the assumption that the pore velocity may be replaced by some average over the cross section.

The governing equations constituting the basic transport equation are:

$$\frac{\partial C_f^n}{\partial t} = -v\frac{\partial C_f^n}{\partial z} + D_L\frac{\partial^2 C_f^n}{\partial z^2} - \lambda^n C_f^n + \sum_{p\in P_n}\lambda^n C_f^p Br_p^n + \frac{D_e^n}{b}\frac{\partial C_m^n}{\partial x}\Big|_{x=0}$$

$$R_m^n\frac{\partial C_m^n}{\partial t} = D_e^n\frac{\partial^2 C_m^n}{\partial x^2} - R_m^n\lambda^n C_m^n + \sum_{p\in P_n}R_m^p\lambda^n C_m^p Br_p^n \qquad \text{B-1}$$

where

C_f^n : Flux-averaged concentration of radionuclide n in the flowing water of the fracture [Bq m^{-3}].
C_m^n : Surface and flux-averaged concentration of radionuclide n in rock matrix pore-water [Bq m^{-3}].
t : Time [a].
v : Mean water velocity in water bearing fracture [m a^{-1}].
z : Distance in the flow direction [m].
D_L : Longitudinal dispersion coefficient [m^2 a^{-1}].
b : Half-aperture of the fracture [m].
D_e^n : Effective diffusivity of radionuclide n in the rock matrix [m^2 a^{-1}].
x : Distance into the rock matrix [m].
λ^n : Decay rate for radionuclide n [a^{-1}].
P_n : Set of indices of parents of radionuclide n [-].
Br_p^n : Branching ratio from parent radionuclide p to radionuclide n [-].
R_m^n : Capacity factor for radionuclide n in rock matrix [-] defined as:

$$R_m^n = \varepsilon_m + K_{d,m}^n \rho_m \qquad \text{B-2}$$

where

ε_m : Porosity of the rock matrix [-].
$K_{d,m}^n$: Solid–liquid partitioning (distribution) coefficient in rock matrix for radionuclide n [kg m^{-3}].
ρ_m : Bulk density of the rock matrix [kg m^{-3}].

Note that the capacity factor $R^n{}_m$ for code-historical reasons is defined slightly differently from the conventionally used retardation coefficient, differing in that the latter is divided by the porosity. The solution to Equation B-1 is restricted to the following boundary conditions:

$$C_f^n\big|_{z\to\infty} = 0 \qquad \text{B-3}$$

$$Q_{\text{tube}}\left(C_f^n - \frac{D_L}{v}\frac{\partial C_f^n}{\partial z}\right)\bigg|_{z=0} = F_{\text{in}}^n \qquad \text{B-4}$$

$$C_m^n\big|_{x=0} = C_f^n \qquad \text{B-5}$$

$$\frac{\partial C_m^n}{\partial x}\bigg|_{x=d_{\max}} = 0 \qquad \text{B-6}$$

where

Q_{tube} : Volume flow of water in the stream tube [m^3 a^{-1}].
F_{in}^n : Input flux of radionuclide n to the stream tube [Bq a^{-1}].
$d_{\max}$: Maximum penetration depth into the rock matrix [m] (average half-space between fractures).

The desired quantity is the output flux for radionuclide n, denoted F_{out}^n, [Bq a^{-1}] at the end of the stream tube with length z_{tot} [m]:

$$F_{\text{out}}^n = Q_{\text{tube}}\left(C_f^n - \frac{D_L}{v}\frac{\partial C_f^n}{\partial z}\right)\bigg|_{z=z_{\text{tot}}} \qquad \text{B-7}$$

where

F_{out}^n : Output flux of radionuclide n from stream tube [Bq a^{-1}].
z_{tot} : Total length of stream tube [m].

B3 Theory behind the numerical implementation

The two coupled, one-dimensional equations (the dual-porosity model) defined in Equation B-1 are approximated using a compartment approach. A compartment model (also known as a box model) is a type of mathematical model used to describe the way materials are transferred between compartments of a system. Each compartment is assumed to be a homogeneous entity within which the entities being modelled are uniformly distributed and equally available for transfer to other compartments. The compartment model is defined as a system of ordinary differential equations with time as the independent variable and can therefore simply be solved using any ordinary differential equation solver. Hence, the partial differential equation described in Equation B-1 needs to be discretised in space (into homogenous compartments) such that a system of ordinary differential equations representing an approximation to the system can be obtained. The discretised equations are herein derived using the finite volume approach with second-order central differences for the dispersion/diffusion terms and a first-order *upwind* scheme for the advective term and the interface term between the fracture and the rock matrix. The same system of differential equations could also be derived using the finite difference method.

Finite volume methods are closely related to finite difference methods, and a finite volume method can often be interpreted directly as a finite difference approximation to the differential equation. However, finite volume methods are derived on the basis of the integral form of the conservation law and have a direct connection with the idea of compartments representing actual volumes in the real world.

Conservation law and integral form of the governing equations

V_f is defined as the domain of the fracture and V_m as the domain of the rock matrix. Their boundaries are ∂V_f and ∂V_m. The boundary between the fracture and the rock matrix is defined as $\Gamma = \partial V_f \cap \partial V_m$. Now, instead of looking at the differential form of the governing equations (Equation B-1), the integral form is used, that is

$$\int_{V_f} \frac{\partial C_f^n}{\partial t} = -v \int_{V_f} \frac{\partial C_f^n}{\partial z} + D_L \int_{V_f} \frac{\partial^2 C_f^n}{\partial z^2} - \int_{V_f} \lambda^n C_f^n + \sum_{p \in P_n} \int_{V_f} \lambda^n C_f^p B r_p^n + \int_{V_f} \frac{D_e^n}{b} \frac{\partial C_m^n}{\partial x}\bigg|_{x=0}$$

$$\int_{V_m} R_m^n \frac{\partial C_m^n}{\partial t} = \int_{V_m} D_e^n \frac{\partial^2 C_m^n}{\partial x^2} - \int_{V_m} R_m^n \lambda^n C_m^n + \sum_{p \in P_n} \int_{V_m} R_m^p \lambda^n C_f^p B r_p^n \qquad \text{B-8}$$

Considering a general conservation law problem, in differential form, it can be represented by

$$\frac{\partial C}{\partial t} + \nabla \cdot \mathbf{F}(C) = Q \qquad \text{B-9}$$

where C is a scalar unity, $\mathbf{F}$ is a flux function (or flux tensor) and Q is a source term. The problem is defined on a domain V with a smooth boundary S, see Figure B-2.

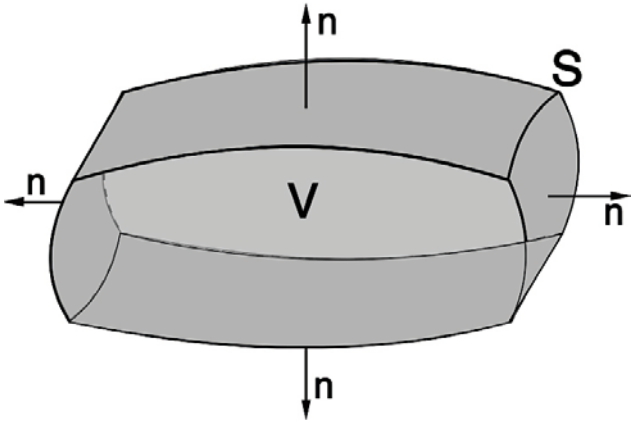

Figure B-2. *A domain V bounded by the surface* ***S = ∂V*** *with the surface normal n. Reproduced with permission from https://commons.wikimedia.org/wiki/File:Divergence_theorem.svg.*

By taking the integral over the domain one obtains the integral form of the problem,

$$\int_V \frac{\partial C}{\partial t}\mathrm{d}V + \int_V \nabla \cdot \mathbf{F}(C)\mathrm{d}V = \int_V Q\mathrm{d}V \qquad \text{B-10}$$

By Gauss' theorem (integration by parts) we get

$$\frac{\partial}{\partial t}\int_V C\mathrm{d}V + \oint_S \mathbf{F}(C)\cdot\mathbf{n}\mathrm{d}S = \int_V Q\mathrm{d}V \qquad \text{B-11}$$

where **n** being the outward pointing unit normal field in the boundary of *S*.

Consequently, **F***(C)* · **n** represents any fluxes over the boundaries, *S*, of the volume *V*, and *Q* represents volume sources (i.e. anything that is generated or destroyed within the volume).

Then we can discretize the whole domain *V* into sub-volumes V_i each with a boundary S_i. Subsequently, this should be true for all *i*,

$$\frac{\partial}{\partial t}\int_{V_i} C\mathrm{d}V + \oint_{S_i} \mathbf{F}(C)\cdot\mathrm{d}\mathbf{S} = \int_{V_i} Q\mathrm{d}V \qquad \text{B-12}$$

As a short hand for **n**d*S* we can write d**S**.

Discretisation

By using the integral form of Equation B-1 expressed in Equation B-8, and knowing that C_f^n is defined on the domain V_f (the total volume of the modelled fracture) and C_m^n is defined on the domain V_m (the volume of the modelled porous rock matrix).

$$\begin{aligned}\frac{\partial}{\partial t}\int_{\mathrm{V}_f} C_f^n\mathrm{d}V &= -v\int_{\mathrm{V}_f}\frac{\partial C_f^n}{\partial z}dV + D_L\int_{\mathrm{V}_f}\frac{\partial^2 C_f^n}{\partial z^2}\mathrm{d}V - \int_{\mathrm{V}_f}\lambda^n C_f^n\,dV + \sum_{p\in P_n}\int_{\mathrm{V}_f}\lambda^n C_f^p Br_p^n\,\mathrm{d}V \\ &\quad + \int_{\mathrm{V}_f}\frac{D_e^n}{b}\frac{\partial C_m^n}{\partial x}\bigg|_{x=0}\mathrm{d}V \\ \frac{\partial}{\partial t}\int_{\mathrm{V}_m} R_m^n C_m^n\mathrm{d}V &= \int_{\mathrm{V}_m} D_e^n\frac{\partial^2 C_m^n}{\partial x^2}\mathrm{d}V - \int_{\mathrm{V}_m} R_m^n\lambda^n C_m^n\mathrm{d}V \\ &\quad + \sum_{p\in P_n}\int_{\mathrm{V}_m} R_m^p\lambda^n C_f^p Br_p^n\,\mathrm{d}V\end{aligned} \qquad \text{B-13}$$

By Gauss' theorem we have

$$\begin{aligned}\frac{\partial}{\partial t}\int_{\mathrm{V}_f} C_f^n dV + \oint_{\mathrm{S}_f}\left(vC_f^n - D_L\frac{\partial C_f^n}{\partial z}\right)\cdot\mathrm{d}\mathbf{S} &= \int_{\mathrm{V}_f}\left(-\lambda^n C_f^n + \sum_{p\in P_n}\lambda^n C_f^p Br_p^n + \frac{D_e^n}{b}\frac{\partial C_m^n}{\partial x}\bigg|_{x=0}\right)\mathrm{d}V \\ \frac{\partial}{\partial t}\int_{\mathrm{V}_m} C_m^n\mathrm{d}V - \oint_{S_m}\frac{D_e^n}{R_m^n}\frac{\partial C_m^n}{\partial x}\cdot\mathrm{d}\mathbf{S} &= \int_{\mathrm{V}_m}\left(-\lambda^n C_m^n + \sum_{p\in P_n}\frac{R_m^p}{R_m^n}\lambda^n C_m^p Br_p^n\right)\mathrm{d}V\end{aligned} \qquad \text{B-14}$$

The interchange term between the fracture and the rock matrix (the transverse diffusive flux) is handled by a volume source term, since the fracture surface is assumed to be very irregular (Vahlund and Hermansson 2006).

N_f is the number of volumes the fracture is divided into (equispaced). So, if the total length of the fracture is z_{tot} then each fracture volume is of length $\Delta z = z_{\mathrm{tot}}/N_f$. The aperture of the fracture is 2b and the width along the y-axis is *W*. Consequently, the total cross-sectional surface area interfacing rock matrix of one fracture volume *i* (i.e. the common area of the volume representing the fracture and first rock volume representing the bedrock confining the fracture volume) is the two aperture sides and the two sides of the fracture plane and can be therefore be described and approximated as

$$A_{\chi,i} = 2\Delta z(W + 2b) \approx 2\Delta z W \qquad \text{B-15}$$

where

Δz : Length of fracture compartment i [m] ($\Delta z = z_{tot}/N_f$).

W : Average width of fracture [m].

$2b$: Average aperture of fracture [m].

The approximation above is reasonable since the aperture of a fracture is assumed to be much smaller than both the fracture length and width ($b << \Delta z$ and W). Conceptually this approximation leads to the conclusion that the interchanging areas between the fracture and the porous rock matrix only occurs at the plane sides.

The volume $V_{f,i}$ [m^3] of one fracture compartment i can therefore be written as:

$$V_{f,i} = A_{\chi,i} b \qquad \text{B-16}$$

Figure B-1 shows the conceptual fracture-matrix system, and the first column (A) in Figure B-3 expands this conceptual picture by adding dimensions of the modelled volumes of the system. The volume of the modelled porous rock is in this conceptualisation defined by the total length and depth of the fracture and by the total penetration depth d_{max}[m] into the matrix. It is assumed that there is no transport out from these bounding rock volumes in any direction except back into the fracture by diffusion. As described above, an assumption is that the aperture of the fracture $2b$ [m] is much smaller than the total fracture length z_{tot} [m] and fracture width W [m], and thus the total cross-sectional area between the fracture and the porous rock matrix A_χ [m^2] can be approximated by $A_\chi = 2z_{tot}W$ (representing the total area of the two sides of the fracture plane). The second column (B) in Figure B-3 illustrates the discretisation of the fracture (and corresponding rock-matrix blocks) into sub volumes and modelled fluxes between volumes shown as arrows. The length in z-direction of each sub-volume is the quotient of the total fracture length and the number of intervals in the discretisation of the fracture ($\Delta z = z_{tot}/N_f$ [m] where N_f is the number of discretisations of the fracture). As the fracture length of a discretised sub-volume is assumed to be much longer than the total penetration depth it is reasonable to assume no diffusive transport vertically between rock matrix sub-volumes for different fracture sections. Though it would be straightforward to implement these exchange terms as a 2D-diffusion model, there would be an overhead in increasing the number of exchange terms when solving the final differential equation as well as an increasing complexity in describing the system. The final column (C) in Figure B-3 shows how the fracture has been split in half and the two identical volumes have been put side by side, this step does not change the results in any way, but due to the symmetry of the system it is possible to reduce the total system size by almost half. Thus, only diffusive exchange terms are considered in the eastern direction from the fracture.

Discretisation of the fracture could, in theory, have varying lengths in the z-direction for the sub-volumes representing the fracture, accounting for varying requirements of the resolution of the concentration gradient. For example, closer to the interface with the biosphere, a higher resolution could be of interest, if, for instance, the water concentration in the fracture close to the surface was an important endpoint (e.g. in water abstracted from a drilled well). However, since it is assumed that only the final breakthrough is of importance from this code and average properties over flow paths are used, an equidistant grid of compartments with uniform size along the fracture is used for simplicity. Even though properties change in fracture segments over the flow path, the sums of the flow-related transport resistances (F-factors) and travel times in a series of segments, where properties are constant within each segment, can be used as effective F-factors and travel times for the entire migration path (Andersson et al. 1998).

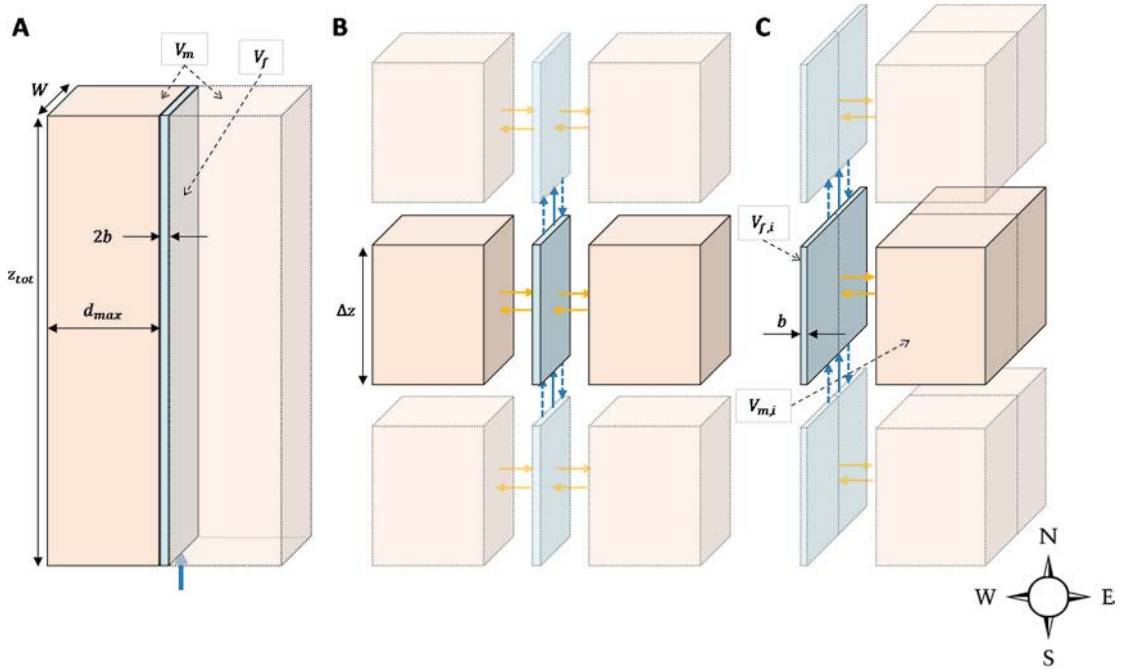

Figure B-3. *Conceptual picture of the simplified geometries modelling fracture and rock matrix as a thin plane with rock boxes around is shown in the left section (A). Discretising the simple volumes in (A) in sections along the fracture with arrows illustrating mass flow between volumes is shown in the middle section (B). Blue arrows represent advective (solid) and dispersive (dashed) transport along the fracture and yellow arrows represent diffusive transport with the rock matrix. The right section (C) illustrates a simplification of the volumes by rearranging them such that only one rock matrix volume needs to be considered per discretised fracture volume.*

For the rock-matrix, on the other hand, there will be a large concentration gradient when contaminated water is penetrating the matrix pores. This together with the original requirement (Equation B-5) that the border concentration between rock matrix and fracture (i.e. fracture wall) should have the same water concentration, an exponential increase of the thickness of the matrix volumes could capture the decreasing importance of modelling the transport correctly the deeper into the matrix one gets (with a reasonable number of matrix compartments). An incremental factor is chosen to represent the increasing thickness of the rock matrix compartments giving the possibility to use very thin interface compartments with the following equation:

$$\sum_{i=0}^{N_m-1} (inc)^i d_1 = d_1 \frac{(inc)^{N_m} - 1}{inc - 1} = d_{\max} \qquad \text{B-17}$$

where:

inc : Incremental factor [-].

d_1 : Depth of the first matrix compartment adjacent to the fracture compartment [m].

N_m : Number of rock-matrix compartments [-].

Figure B-4 illustrates the details of a discretised fracture compartment and corresponding matrix compartments with increasing thickness of matrix compartments with the distance from the fracture.

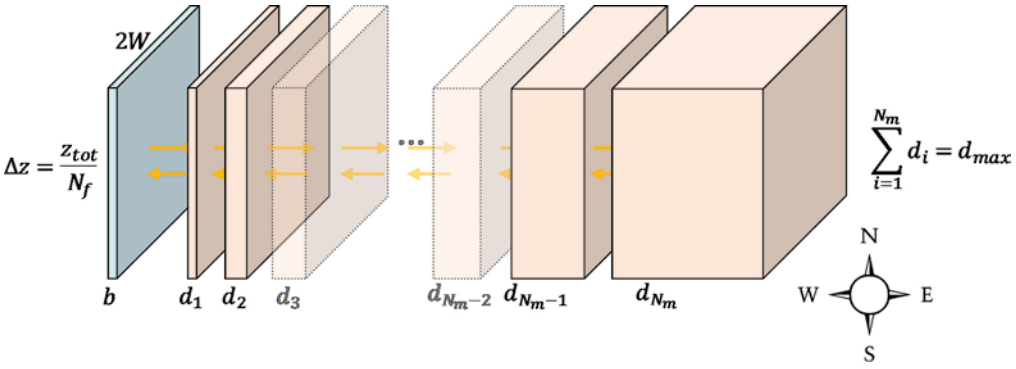

Figure B-4. *Conceptual illustration of the discretisation of one fracture section with rock matrix volumes discretised in the transversal direction perpendicular to the water flow.*

Discretisation of the fracture

Considering Equation B-13, and introducing the discretisation of the fracture, then the following must be true for all $i = 1 \ldots N_f$

$$\frac{\partial}{\partial t}\int_{V_{f,i}} C_f^n \mathrm{d}V + \oint_{S_{f,i}} \left(v C_f^n - D_L \frac{\partial C_f^n}{\partial z} \right) \cdot \mathrm{d}\mathbf{S} = \int_{V_{f,i}} \left(-\lambda^n C_f^n + \sum_{p \in P_n} \lambda^n C_f^p B r_p^n + \frac{D_e^n}{b} \frac{\partial C_m^n}{\partial x}\Big|_{x=0} \right) \mathrm{d}V \quad \text{B-18}$$

Now we will go through each component in Equation B-18. Since C_f^n is constant in each $V_{f,i}$ we have

$$\frac{\partial}{\partial t}\int_{V_{f,i}} C_f^n \mathrm{d}V = \mathrm{V}_{f,i} \frac{\partial C_{f,i}^n}{\partial t} \quad \text{B-19}$$

Continue to look at the advective term (the first part of the second component). By definition, the mean water velocity, v, is constant and in the positive z direction (upwards). If we denote the four sides of $V_{f,i}$ N, S, W and E (as shown in Figure B-3) the scalar product of the normal vector **n** and v will give us two boundaries per $V_{f,i}$ where the integral is non-zero

$$\oint_{\mathrm{S}_{f,i}} v C_f^n \cdot \mathbf{n} \mathrm{d}S = \oint_{S_{f,i}^N} v C_f^n \cdot \mathbf{n} \mathrm{d}S + \oint_{S_{f,i}^S} v C_f^n \cdot \mathbf{n} \mathrm{d}S \quad \text{B-20}$$

We know that the areas of the N and S boundaries are each $V_{f,i}/\Delta z$. Using the upwind flux, we will assign $C_{f,i}^n$ on the N boundary and $C_{f,i-1}^n$ on the S boundary. This is because v is the characteristic vector and water flows from bottom of fracture and upwards. Thus, since $\mathbf{n}_N \cdot \mathrm{v} > 0$ and $\mathbf{n}_S \cdot \mathrm{v} < 0$

$$\oint_{\mathrm{S}_{f,i}} v C_f^n \cdot \mathbf{n} \mathrm{d}S = \oint_{S_{f,i}^N} v C_f^n \cdot \mathbf{n} \mathrm{d}S + \oint_{S_{f,i}^S} v C_f^n \cdot \mathbf{n} \mathrm{d}S \approx v \frac{\mathrm{V}_{f,i}}{\Delta z} \left(C_{f,i}^n - C_{f,i-1}^n \right) \quad \text{B-21}$$

The same applies for the dispersion term (the second term), we know that $\partial C_f^n/\partial z$ is zero on the two boundaries E (since we have the boundary condition defined in Equation B-5, $C_{f,i}^n$ must be constant over the boundary) and W (also constant because of symmetry). Using *upwinding* to approximate the derivative fluxes in the fracture (by using the information upstream to calculate the flux) because D_L is directed upwards as v, a standard central difference scheme for the approximation of the surface integral appears,

$$\begin{aligned} -\oint_{S_{f,i}} D_L \frac{\partial C_f^n}{\partial z} \cdot \mathrm{d}\mathbf{S} &= -\oint_{S_{f,i}^N} D_L \frac{\partial C_f^n}{\partial z} \cdot \mathrm{d}\mathbf{S} - \oint_{S_{f,i}^S} D_L \frac{\partial C_f^n}{\partial z} \cdot \mathrm{d}\mathbf{S} \\ &\approx -D_L \frac{\mathrm{V}_{f,i}}{\Delta \mathrm{z}} \left(\frac{C_{f,i+1}^n - C_{f,i}^n}{\Delta \mathrm{z}} - \frac{C_{f,i}^n - C_{f,i-1}^n}{\Delta \mathrm{z}} \right) \\ &= -D_L \frac{\mathrm{V}_{f,i}}{\Delta \mathrm{z}} \left(\frac{C_{f,i+1}^n - 2C_{f,i}^n + C_{f,i-1}^n}{\Delta \mathrm{z}} \right) \end{aligned} \quad \text{B-22}$$

On the right-hand side of Equation B-18, the first two terms (decay and in-growth) in the integral can be evaluated straightforwardly by integration.

$$\int_{\mathrm{V}_{f,i}} \left(-\lambda^n C_f^n + \sum_{p \in P_n} \lambda^n C_f^p B r_p^n \right) \mathrm{d}V = \mathrm{V}_{f,i} \left(-\lambda^n C_{f,i}^n + \sum_{p \in P_n} \lambda^n C_{f,i}^p B r_p^n \right) \quad \text{B-23}$$

Thus, we only have one term left, and that is the interchange term between the fracture and the rock matrix. It can also be evaluated straightforwardly by integration. The derivative ($\partial C_m^n / \partial x|_{x=0}$) at the border ($\Gamma = \partial V_\mathrm{f} \cap \partial V_\mathrm{m}$) is approximated by a first-order *upwind* scheme between the border concentration (by definition $C_{f,i}^n$, see Equation B-13) that has of course no spatial extension in the x-direction (direction of the rock matrix) and the concentration in the first rock matrix volume

$$\int_{\mathrm{V}_{f,i}} \frac{D_e^n}{b} \frac{\partial C_{m,i}^n}{\partial x}\bigg|_{x=0} \mathrm{d}V = \mathrm{V}_{f,i} \frac{D_e^n}{b} \frac{\partial C_{m,i}^n}{\partial x}\bigg|_{x=0} \approx \mathrm{V}_{f,i} \frac{D_e^n}{b} \frac{C_{m,i,1}^n - C_{f,i}^n}{d_1/2} \quad \text{B-24}$$

In conclusion putting together Equation B-19 to Equation B-24 and dividing both sides by the fracture volume ($V_{f,i}$) we get

$$\begin{aligned} \frac{\partial C_{f,i}^n}{\partial t} + \frac{v}{\Delta z}\left(C_{f,i}^n - C_{f,i-1}^n\right) - \frac{D_L}{\Delta z}\left(\frac{C_{f,i+1}^n - 2C_{f,i}^n + C_{f,i-1}^n}{\Delta z}\right) \\ = -\lambda^n C_{f,i}^n + \sum_{p \in P_n} \lambda^n C_{f,i}^p B r_p^n + \frac{D_e^n}{b} \frac{C_{m,i,1}^n - C_{f,i}^n}{d_1/2} \end{aligned} \quad \text{B-25}$$

Discretisation of the rock matrix

Similarly, we introduce our discretisation for the rock matrix. Then the following must be true for all $i = 1 \ldots N_f$ and $j = 1 \ldots N_m$:

$$\begin{aligned} \frac{\partial}{\partial t} \int_{\mathrm{V}_{m,i,j}} C_m^n \mathrm{d}V - \oint_{S_{m,i,j}} \frac{D_e^n}{R_m^n} \frac{\partial C_m^n}{\partial x} \cdot \mathrm{d}\mathbf{S} \\ = \int_{\mathrm{V}_{m,i,j}} \left(-\lambda^n C_m^n + \sum_{p \in P_n} \frac{R_m^p}{R_m^n} \lambda^n C_m^p B r_p^n \right) \mathrm{d}V \end{aligned} \quad \text{B-26}$$

As for the fracture we go through each component in Equation B-26. Since C_m^n is constant in each $V_{m,i,j}$ we have

$$\frac{\partial}{\partial t} \int_{\mathrm{V}_{m,i,j}} C_m^n \mathrm{d}V = \mathrm{V}_{m,i,j} \frac{\partial C_{m,i,j}^n}{\partial t} \quad \text{B-27}$$

Continue to look at the diffusion term (the second component). $\partial C_m^n / \partial x$ is only non-zero in the E and W directions and therefore

$$-\oint_{S_{m,i,j}} \frac{D_e^n}{R_m^n} \frac{\partial C_m^n}{\partial x} \cdot \mathrm{d}\mathbf{S} = -\oint_{S_{m,i,j}^E} \frac{D_e^n}{R_m^n} \frac{\partial C_m^n}{\partial x} \cdot \mathrm{d}\mathbf{S} - \oint_{S_{m,i,j}^W} \frac{D_e^n}{R_m^n} \frac{\partial C_m^n}{\partial x} \cdot \mathrm{d}\mathbf{S} \quad \text{B-28}$$

We approximate the derivative $\partial C^n{}_m / \partial x$ by $(C^n{}_{m,i,j+1} - C^n{}_{m,i,j}) / ((d_j + d_{j+1})/2$ on the E direction and $(C^n{}_{m,i,j+1} - C^n{}_{m,i,j}) / ((d_j + d_{j-1})/2$ on the W direction. We then have, knowing that the cross-sectional area of E or W can be written as the quotient of the volume $V_{m,i,j}$ and thickness d_j of the current volume

$$-\oint_{S_{m,i,j}} \frac{D_e^n}{R_m^n} \frac{\partial C_m^n}{\partial x} \cdot \mathrm{d}\mathbf{S} \approx -\frac{D_e^n}{R_m^n} \frac{V_{m,i,j}}{d_j} \left(\frac{C_{m,i,j+1}^n - C_{m,i,j}^n}{(d_j + d_{j+1})/2} + \frac{C_{m,i,j-1}^n - C_{m,i,j}^n}{(d_j + d_{j-1})/2} \right) \quad \text{B-29}$$

On the right-hand side of Equation B-26 the two terms (decay and in-growth) in the integral can be evaluated straightforwardly by integration.

$$\int_{V_{m,i,j}} \left(-\lambda^n C_m^n + \sum_{p \in P_n} \frac{R_m^p}{R_m^n} \lambda^n C_m^p B r_p^n \right) \mathrm{d}V = V_{m,i,j} \left(-\lambda^n C_{m,i,j}^n + \sum_{p \in P_n} \frac{R_m^p}{R_m^n} \lambda^n C_{m,i,j}^p B r_p^n \right) \quad \text{B-30}$$

In conclusion putting together Equation B-27 to Equation B-30 and dividing both sides with the volume ($V_{m,i,j}$) we get

$$\frac{\partial C^n_{m,i,j}}{\partial t} - \frac{D^n_e}{R^n_m d_j}\left(\frac{C^n_{m,i,j+1} - C^n_{m,i,j}}{(d_j + d_{j+1})/2} + \frac{C^n_{m,i,j-1} - C^n_{m,i,j}}{(d_j + d_{j-1})/2}\right) = -\lambda^n C^n_{m,i,j} + \sum_{p\in P_n} \frac{R^p_m}{R^n_m}\lambda^n C^p_{m,i,j} Br^n_p \qquad \text{B-31}$$

Combining equations for the fracture and the rock matrix

Combining and rearranging the full set of equations after discretising the following system is obtained:

$$\begin{aligned}
\frac{\partial C^n_{f,i}}{\partial t} &= C^n_{f,i}\left(-\frac{2D_L}{\Delta z^2} - \frac{v}{\Delta z} - \frac{D^n_e}{b\, d_1/2} - \lambda^n\right) + C^n_{f,i-1}\left(\frac{D_L}{\Delta z^2} + \frac{v}{\Delta z}\right) + C^n_{f,i+1}\left(\frac{D_L}{\Delta z^2}\right) + C^n_{m,i,1}\left(\frac{D^n_e}{b\, d_1/2}\right) \\
&\quad + \sum_{p\in P_n} C^p_{f,i}(\lambda^n Br^n_p) \\
\frac{\partial C^n_{m,i,j}}{\partial t} &= C^n_{m,i,j}\left(\frac{-D^n_e}{R^n_m d_j\,(d_j + d_{j+1})/2} + \frac{-D^n_e}{R^n_m d_j\,(d_j + d_{j-1})/2} - \lambda^n\right) + C^n_{m,i,j+1}\left(\frac{D^n_e}{R^n_m d_j\,(d_j + d_{j+1})/2}\right) \\
&\quad + C^n_{m,i,j-1}\left(\frac{D^n_e}{R^n_m d_j\,(d_j + d_{j-1})/2}\right) + \sum_{p\in P_n} C^p_{m,i,j}\left(\frac{R^p_m}{R^n_m}\lambda^n Br^n_p\right)
\end{aligned} \qquad \text{B-32}$$

In the finite volume approach (as well as in the compartment approach), it is usual to consider the total inventory *I* in each volume (compartment) rather than the water concentration *C*. The relationship between the total inventory and water concentration is:

$$C^n_{f,i} = \frac{I^n_{f,i}}{V_{f,i}}, \qquad C^n_{m,i,j} = \frac{I^n_{m,i,j}}{V_{m,i,j}R^n_m} \qquad \text{B-33}$$

for the fracture and the matrix respectively. After converting the concentration components to inventories Equation B-32 becomes:

$$\begin{aligned}
\frac{1}{V_{f,i}}\frac{\partial I^n_{f,i}}{\partial t} &= \frac{I^n_{f,i}}{V_{f,i}}\left(-\frac{2D_L}{\Delta z^2} - \frac{v}{\Delta z} - \frac{D^n_e}{b\, d_1/2} - \lambda^n\right) + \frac{I^n_{f,i-1}}{V_{f,i-1}}\left(\frac{D_L}{\Delta z^2} + \frac{v}{\Delta z}\right) + \frac{I^n_{f,i+1}}{V_{f,i+1}}\left(\frac{D_L}{\Delta z^2}\right) \\
&\quad + \frac{I^n_{m,1}}{V_{m,1}R^n_m}\left(\frac{D^n_e}{b\,(b + d_1)/2}\right) + \sum_{p\in P_n}\frac{I^p_{f,i}}{V_{f,i}}(\lambda^n Br^n_p) \\
\frac{1}{V_{m,i,j}R^n_m}\frac{\partial I^n_{m,i,j}}{\partial t} &= \frac{I^n_{m,i,j}}{V_{m,i,j}R^n_m}\left(\frac{-D^n_e}{R^n_m d_j\,(d_j + d_{j+1})/2} + \frac{-D^n_e}{R^n_m d_j\,(d_j + d_{j-1})/2} - \lambda^n\right) \\
&\quad + \frac{I^n_{m,i,j+1}}{V_{m,i,j+1}R^n_m}\left(\frac{D^n_e}{R^n_m d_j\,(d_j + d_{j+1})/2}\right) + \frac{I^n_{m,i,j-1}}{V_{m,i,j-1}R^n_m}\left(\frac{D^n_e}{R^n_m d_j\,(d_j + d_{j-1})/2}\right) \\
&\quad + \sum_{p\in P_n}\frac{I^p_{m,i,j}}{V_{m,i,j}R^p_m}\left(\frac{R^p_m}{R^n_m}\lambda^n Br^n_p\right)
\end{aligned} \qquad \text{B-34}$$

Uniform volumes are assumed in each fracture component; Equation B-34 can therefore, after multiplication with the volume, *V*, and the retardation factor, *R*, finally be rearranged and simplified to:

$$\begin{aligned}
\frac{\partial I^n_{f,i}}{\partial t} &= I^n_{f,i}\left(-\frac{2D_L}{\Delta z^2} - \frac{v}{\Delta z} - \frac{2D^n_e}{bd_1} - \lambda^n\right) + I^n_{f,i-1}\left(\frac{D_L}{\Delta z^2} + \frac{v}{\Delta z}\right) + I^n_{f,i+1}\left(\frac{D_L}{\Delta z^2}\right) + I^n_{m,1}\left(\frac{2D^n_e}{R^n_m d_1(b + d_1)}\right) \\
&\quad + \sum_{p\in P_n} I^p_{f,i}(\lambda^n Br^n_p) \\
\frac{\partial I^n_{m,i,j}}{\partial t} &= I^n_{m,i,j}\left(\frac{-2D^n_e}{R^n_m d_j(d_j + d_{j+1})} + \frac{-2D^n_e}{R^n_m d_j(d_j + d_{j-1})} - \lambda^n\right) + I^n_{m,i,j+1}\left(\frac{2D^n_e}{R^n_m d_{j+1}(d_j + d_{j+1})}\right) \\
&\quad + I^n_{m,i,j-1}\left(\frac{2D^n_e}{R^n_m \mathrm{d}_{j-1}(\mathrm{d}_j + \mathrm{d}_{j-1})}\right) + \sum_{p\in P_n} I^p_{m,i,j}(\lambda^n Br^n_p)
\end{aligned} \qquad \text{B-35}$$

$$\frac{\partial I_{f,1}^n}{\partial t} = I_{f,1}^n\left(-\frac{D_L}{\Delta z^2}-\frac{v}{\Delta z}-\frac{2D_e^n}{bd_1}-\lambda^n\right)+I_{f,2}^n\left(\frac{D_L}{\Delta z^2}\right)+I_{m,i,1}^n\left(\frac{2D_e^n}{R_m^n {d_1}^2}\right)+F_{in}^n+\sum_{p\in P_n} I_{f,1}^p\left(\lambda^n Br_p^n\right)$$

$$\frac{\partial I_{f,N_f}^n}{\partial t} = I_{f,N_f}^n\left(-\frac{D_L}{\Delta z^2}-\frac{v}{\Delta z}-\frac{2D_e^n}{b(b+d_1)}-\lambda^n\right)+I_{f,N_f-1}^n\left(\frac{D_L}{\Delta z^2}+\frac{v}{\Delta z}\right)+I_{m,i,1}^n\left(\frac{2D_e^n}{R_m^n {d_1}^2}\right)$$
$$+\sum_{p\in P_n} I_{f,N_f}^p\left(\lambda^n Br_p^n\right)$$

$$\frac{\partial I_{m,i,1}^n}{\partial t} = I_{m,i,1}^n\left(\frac{-2D_e^n}{R_m^n d_1(d_1+d_2)}+\frac{-2D_e^n}{R_m^n {d_1}^2}-\lambda^n\right)+I_{m,i,2}^n\left(\frac{2D_e^n}{R_m^n d_2(d_1+d_2)}\right)+I_{f,i}^n\left(\frac{2D_e^n}{bd_1}\right) \qquad \text{B-36}$$
$$+\sum_{p\in P_n} I_{m,i,1}^p\left(\lambda^n Br_p^n\right)$$

$$\frac{\partial I_{m,i,N_m}^n}{\partial t} = I_{m,i,N_m}^n\left(\frac{-2D_e^n}{R_m^n d_{N_m}\left(d_{N_m}+d_{N_m-1}\right)}-\lambda^n\right)+I_{m,i,N_m-1}^n\left(\frac{2D_e^n}{R_m^n \mathrm{d}_{N_m-1}\left(\mathrm{d}_{N_m}+\mathrm{d}_{N_m-1}\right)}\right)$$
$$+\sum_{p\in P_n} I_{m,i,N_m}^p\left(\lambda^n Br_p^n\right)$$

As can be seen in the system of differential equations above, fluxes of radionuclides [Bq a^{-1}] between compartments are defined as inventory in [Bq] multiplied by transfer rates in [a^{-1}]; to the first fracture volume we also have the source term F_{in}^n [Bq a^{-1}]. Subsequent sections list the resulting transfer rates between discretised compartments as well as addressing the internal changes due to decay and ingrowth.

Radioactive decay and ingrowth

Handling of decay and ingrowth is straightforward and is described in terms of volume sources in Equation B-35, and Equation B-36 and corresponds to the rate of change within each compartment. The decay rate for a specific radionuclide *n* for all compartments is given by:

$$\lambda^n = \frac{\ln 2}{t_{1/2}^n} \qquad \text{B-37}$$

where:

ln 2 : Natural logarithm of 2 [-].

$t_{½}^n$: Half-life of radionuclide *n* [a].

The corresponding ingrowth rate (production rate) in each compartment derived from decaying parent radionuclide *p* to its decay product *n* is defined by:

$$\lambda_p^n = \lambda^n Br_p^n \qquad \text{B-38}$$

where

Br_p^n : Branching ratio from parent radionuclide *p* to daughter radionuclide *n* [-].

Advection in the fracture

From Equation B-35 and Equation B-36 it is clear that the advective rate between two adjacent fracture compartments *i* and *j* is given by the following equation:

$$\lambda_{ij}^{\mathrm{adv}} = \frac{v}{\Delta z} \qquad \text{B-39}$$

where

v : Average groundwater velocity in the water bearing fracture [m a^{-1}].

Δz : Distance along stream direction in one fracture compartment [m].

The groundwater velocity in the water-bearing fracture v [m a^{-1}], can be defined as the quotient of the total fracture length, z_{tot} [m] and the total advective travel time, t_w [a], and the length of one fracture compartment (for an equidistant grid) can be written as the total fracture length divided by the number of discretisations of the fracture, N_f [-], therefore Equation B-39 can be rewritten as:

$$\lambda_{ij}^{\text{adv}} = \frac{v}{\Delta z} = \frac{z_{\text{tot}}/t_w}{z_{\text{tot}}/N_f} = \frac{N_f}{t_w} \qquad \text{B-40}$$

Dispersion in the fracture

From Equation B-35 and Equation B-36 the dispersive rate coefficients from fracture compartment i to j and in the opposite direction, from fracture compartment j to i is shown to be:

$$\lambda_{ij}^{\text{disp}} = \lambda_{ji}^{\text{disp}} = \frac{D_L}{\Delta z^2} \qquad \text{B-41}$$

The Péclet number P_e is the quotient of the advective transport rate and the diffusive (dispersive) transport rate for non-sorbing solutes. In this context it is defined as:

$$P_e = \frac{z_{\text{tot}} v}{D_L} \qquad \text{B-42}$$

where

P_e : Péclet number for the fracture [-].
v : Average advective velocity [m a^{-1}] of water in the fracture.
z_{tot} : Total length [m] of the geosphere flow-path.
D_L : Longitudinal dispersion coefficient [m^2 a^{-1}].

Consequently, the dispersive rate in Equation B-41 can be rewritten without the longitudinal dispersion coefficient as:

$$\lambda_{ij}^{\text{disp}} = \lambda_{ji}^{\text{disp}} = \frac{v\left(\frac{z_{\text{tot}}}{P_e}\right)}{\Delta z^2} \qquad \text{B-43}$$

Pure advection cannot be modelled when solving a partial differential equation (PDE) using a first-order *upwinding* approximation since numerical dispersion will be introduced due to the approximation of the spatial derivative. To approximate the introduced numerical dispersion, we can examine the Taylor series expansion for u_{i+1}:

$$u_{i+1} = u_i + \left.\frac{\partial u}{\partial x}\right|_{x_i} \Delta x + \frac{1}{2}\left.\frac{\partial^2 u}{\partial x^2}\right|_{x_i} (\Delta x)^2 + (\text{Higher order terms}) \qquad \text{B-44}$$

Consequently, the first derivative can be written as

$$\frac{\partial u}{\partial x} = \frac{u_{i+1} - u_i}{\Delta x} - \frac{1}{2}\frac{\partial^2 u}{\partial x^2}(\Delta x) + \frac{1}{\Delta x}(\text{Higher order terms})$$

The PDE for pure advection in the fracture for radionuclide n (from Equation B-1) is given by

$$\frac{\partial C_f^n}{\partial t} = -v\frac{\partial C_f^n}{\partial z} \qquad \text{B-45}$$

and can therefore be written as

$$\frac{\partial C}{\partial t} = v\frac{C_{i+1} - C_i}{\Delta z} - v\frac{\Delta z}{2}\frac{\partial^2 C}{\partial z^2} + v\frac{1}{\Delta z}(\text{Higher order terms})$$

where the first term is our *upwind* approximation. Since the higher order terms are much smaller than the second derivative, these can be ignored. So, the magnitude of the introduced numerical dispersion is approximately $v\,\Delta z/2$. To get a more correct solution this numerically introduced dispersion term should be removed from the modelled dispersion, and therefore we end up with the following equation for the dispersion rate:

$$\lambda_{ij}^{\text{disp}} = \lambda_{ji}^{\text{disp}} = \frac{v\left(\frac{z_{\text{tot}}}{P_e}\right) - v\left(\frac{\Delta z}{2}\right)}{\Delta z^2} \qquad \text{B-46}$$

As with the advective rate, the expression for dispersion can be written independently of the advective velocity v, the total flow-path length z_{tot}, and fracture compartment length Δz:

$$\lambda_{ij}^{\text{disp}} = \lambda_{ji}^{\text{disp}} = \frac{v\left(\frac{z_{\text{tot}}}{P_e} - \frac{\Delta z}{2}\right)}{\Delta z^2} = \frac{z_{\text{tot}}/t_w\left(\frac{z_{\text{tot}}}{P_e} - \frac{z_{\text{tot}}/N_f}{2}\right)}{\left(z_{\text{tot}}/N_f\right)^2} = \frac{N_f^2}{P_e t_w} - \frac{N_f}{2t_w} \qquad \text{B-47}$$

As can be noted from Equation B-47, when the Péclet number equals twice the number of compartments in the fracture, the numerical dispersion equals the desired dispersion and the two terms cancel each other out. To account for a correct handling of the dispersion; a requirement of the implementation is therefore that the number of compartments in the fracture is large enough ($N_f \geq P_e/2$), otherwise the numerical dispersion will be larger than the desired dispersion.

Matrix diffusion

The diffusive rate from the fracture to the first rock-matrix compartment can be obtained from Equation B-35 and Equation B-36 by:

$$\lambda_{f\rightarrow m}^{\text{diff}} = \frac{2D_e^n}{bd_1} \qquad \text{B-48}$$

where:

D_e^n : Rock matrix diffusion coefficient for radionuclide n [$m^2\ a^{-1}$].

b : Half-aperture of the fracture [m].

d_1 : Thickness of first rock matrix compartment [m].

The (volumetric) flow-wetted surface area, a_w, of the rock matrix in contact with flowing water per unit volume of water [$m^2\ m^{-3}$] can be expressed in terms of flow-related transport resistance, F, and travel time, t_w, or with the flow-wetted surface, $A_{\chi,i}$, and the fracture volume, $V_{f,i}$, or the inverse of the half-fracture aperture, b:

$$a_w = \frac{F}{t_w} = \frac{A_{\chi,i}}{V_{f,i}} = \frac{1}{b} \qquad \text{B-49}$$

where:

F : Flow-related transport resistance [$a\ m^{-1}$].

t_w : Total advective travel time [a].

a_w : Area of the flow-wetted surface per volume of water [$m^2\ m^{-3}$].

$A_{\chi,i}$: Cross-sectional area in fracture compartment i in contact with rock matrix [m^2].

$V_{f,i}$: Volume of fracture compartment i [m^3].

Thus, the exchange rate from the fracture to the first matrix compartment can be expressed in terms of the volumetric flow-wetted surface area instead of the inverse of the half aperture as:

$$\lambda_{f\rightarrow m}^{\text{diff}} = \frac{1}{b}\frac{2D_e^n}{d_1} = a_w\frac{2D_e^n}{d_1} \qquad \text{B-50}$$

The diffusive transfer rate from the first rock matrix compartment back to the fracture can also be obtained from Equation B-35 and Equation B-36 by:

$$\lambda_{f\leftarrow m}^{\text{diff}} = \frac{2D_e^n}{R_m^n {d_1}^2} \qquad \text{B-51}$$

where:

R_m^n : Rock-matrix retardation factor [-].

Finally, from Equation B-35 and Equation B-36 the diffusive rate from matrix compartment k to matrix compartment l and in the opposite direction from matrix compartment l to matrix compartment k can be expressed as:

$$\lambda_{k\rightarrow l}^{\text{diff}} = \frac{2D_e^n}{R_m^n d_k(d_k + d_l)}, \qquad \lambda_{k\leftarrow l}^{\text{diff}} = \frac{2D_e^n}{R_m^n d_l(d_k + d_l)} \qquad \text{B-52}$$

B4 List of parameters

Parameterisation of the compartment model follows the historical heritage of previous model codes (Norman and Kjellbert 1990). Parameters presented in Table B-1 are required input data.

Table B-1. Parameters and data required to run the implemented compartment model.

Parameter	Symbol	Unit	Comment
Total advective travel time	t_w	a	
Flow-related transport resistance factor	F	a m^{-1}	The relation to flow-wetted surface area is: $F = a_w t_w$
Matrix porosity	ε_m	-	Either a constant value or a defined porosity for each radionuclide
Bulk density of the rock matrix	ρ_m	kg m^{-3}	
Radionuclide half-life	$t_{½}$	a	One value for each radioisotope
Branching ratio	Br_p^n	-	One fraction per decay-pair
Rock matrix distribution coefficient (sorption coefficient) in rock matrix	$K_{d,m}^n$	m^3 kg^{-1}	One value for each radionuclide
Effective matrix diffusion coefficient	D_e	m^2 a^{-1}	One value for each radionuclide
Péclet number	P_e	-	Ratio between the advective and dispersive components of the transport over the length scale of interest. Default value: 10
Number of discretisations of the fracture	N_f	-	Default value is 20
Number of discretisations of the rock matrix	N_m	-	Default value is 20
Thickness of first rock matrix compartment	d_1	m	Default value is 0.1 mm
Maximum penetration depth of rock matrix for any radionuclide	$d_{\max}$	m	Default value is 4.5 meters

B5 Matlab implementation

The Matlab implementation of the dual-porosity model FARFCOMP is listed in Appendix B8. In this section the code structure is described as well as additional developed codes. The implementation only contains three Matlab functions: the main function, a helping function to get the sparse Jacobian matrix for a specific radionuclide and a helping function to get default values for optional parameters.

Following is a list of the required input arguments to the code:

1. **time** [a] vector of data points in time to evaluate, first data point is the start of possible release.
2. **Fin** [Bq a^{-1}] function handle or a matrix with radionuclide releases. If this argument is a function handle the input arguments to this function handle are time and radionuclide index and it is assumed to return the radionuclide source term at the specified time point and radionuclide at position index. If the argument is instead a matrix, the size of the first dimension must be the same as the length of the time-vector and the size of the second dimension must be the same as the number of modelled radionuclides. Data in the matrix are assumed to be the source term.
3. **Tw** [a] total advective travel time for the modelled trajectory.
4. **F** [a m^{-1}] flow-related transport resistance for the modelled trajectory.
5. **epsil** [-] porosity of the rock matrix (may be a vector, one for each radionuclide).
6. **rhob** [kg m^{-3}] bulk density of the rock matrix.
7. **halflife** [a] radionuclide half-life (vector, one for each radionuclide).
8. **Kd** [m^3 kg^{-1}] partition coefficient in the rock matrix (vector, one for each radionuclide).
9. **De** [m^2 a^{-1}] effective diffusivity in the rock matrix (vector, one for each radionuclide).

The rest of the list is optional arguments to the code with default values defined in parentheses:

10. **Pe** [-] Péclet number (10).
11. **Nf** [#] number of discretisations of the fracture (20).
12. **Nm** [#] number of discretisations of the rock matrix (20).
13. **d1** [m] depth of first matrix compartment (0.0001).
14. **dmax** [m] maximum penetration depth into rock matrix (4.5).
15. **singleRnInd** [index vector] indices of single radionuclides (all radionuclides). This vector is filled with the indices of the radionuclides that are not incorporated in any decay chain.
16. **decayGroups** [cell structure] cell array with decay group matrices ({}). For each decay chain a decay group matrix is defined in a cell. A decay group matrix is built up using the decay pairs as rows [parent radionuclide index, daughter radionuclide index, branching ratio; next parent radionuclide index, etc].
17. **RelTol** [-] relative tolerance (10^{-3}). Relative tolerance passed through to the built-in ordinary differential equation solver.
18. **AbsTol** [Bq] absolute tolerance (10^{-6}). Absolute tolerance passed through to the built-in ordinary differential equation solver.

If the second argument is a matrix with releases, the code converts these data together with the time vector to a function that handles the interpolation of the release data internally.

A minimisation routine is used to calculate the optimal incremental value to define each rock matrix layer depth based on the first rock matrix depth, the maximum penetration depth and the number of discretisations.

The code contains two main loops, the first is used to calculate the solution for radionuclides not contained in any decay chains, and the other to calculate the solution for radionuclides involved in decay chains. In both loops the sparse Jacobian matrix for each involved radionuclide is obtained from the aiding Jacobian function. For the first loop, the Jacobian matrix is directly used in the solution of the differential equation by matrix vector multiplication. For the second loop, a block diagonal Jacobian matrix is constructed based on the Jacobian matrix for each individual radionuclide. By using the defined decay pair branching ratios between parent and daughter radionuclides, the individual Jacobian blocks are then connected within the big block diagonal Jacobian matrix for the whole system. Finally, this big Jacobian matrix is used in the solution of the differential equation by matrix vector multiplication.

An extended version of the code has been developed giving the possibility to use time-varying parameters. In this code, several Jacobian matrices for each unique parameter set are computed and interpolated over time.

To harmonise the workflow and simplify the handling of FARF31 another code has been implemented as an interface to the FARF31 executable with the same argument and result structure as FARFCOMP.

For comparison and quality assurance (QA), two codes with the same argument and result structure as FARFCOMP were implemented and compared with the analytic solution given a unit release (and no radionuclide ingrowth) for a given longitudinal dispersion and for no longitudinal dispersion respectively.

Aiding functions and scripts for QA-supported handling of parameters, simulations and storage of results has also been developed. For calculating multiple flow paths representing the possible pathways in the fractured rock, parallelisation is implemented (if the required Matlab toolbox is installed) to utilize the full potential of multicore computers.

B6 Code comparison

For verification of the compartment model, a series of comparisons have been performed with the developed codes, the analytical solutions, FARF31 as well as with MARFA SP version 4.3. The code comparisons utilize parameter data from the SE-SFL-project. In this chapter, the parameters used for the comparisons are first described, followed by comparison results and sensitivity analyses.

The first types of comparisons were performed using a unit release source term for a chosen set of radionuclides of importance for the safety evaluation SE-SFL. The chosen radionuclides for the comparison also have different transport characteristics (i.e. half-lives, decay chains and potential for retention etc). The selected radionuclides for these comparisons are organic C-14, Cl-36, Mo-93 and its decay products Nb-93m and the U-238 chain (U-238, U-234, Th-230, Ra-226, Pb-210 and Po-210). The same set of radionuclides has also been analysed with actual calculated releases from the BHA repository waste vault for the *present-day evaluation case* in the SE-SFL project. The unit release comparisons have been performed on a single pathway from the SE-SFL project as well as a full set of potential flow paths calculated for the investigation of the deep underground vault BHA in SFL; see Figure B-5 for an illustration of the modelled trajectories.

Also, simulations using a greatly reduced set (10) of approximations of trajectories from the ConnectFlow realisation used in the SE-SFL *present-day evaluation case* have been performed. This set can be run very fast in either FARFCOMP or FARF31 producing similar results to when using MARFA SP, FARFCOMP or FARF31 considering the original full trajectory set from the ConnectFlow realisation.

Present-day evaluation case realisation data

The input data used in the comparison are the same as used in used in the SE-SFL *present-day evaluation case*. Radionuclide-specific data used in the comparison are listed in Table B-2. The comparison was performed with the following constant properties: a rock-matrix porosity ε_m of 0.0019 for each radionuclide, a bulk density in the rock-matrix ρ_m = 2 700 kg m^{-3}, a maximum penetration depth $d_{\max}$ = 4.5 meter and for longitudinal dispersion a Péclet number P_e = 10 was chosen. For other model-specific parameters required for the compartment model, default values were chosen.

Table B-2. Radionuclide-specific data used in the code comparisons.

Radionuclide	Element	Half-life [a]	Source term [Bq a^{-1}]	D_e [m^2 a^{-1}]	K_d [m^3 kg^{-1}]	Branching percentage to decay product
(organic) C-14	C-org	5 730	1	8.5E−7	0	
Cl-36	Cl	301 000	1	2.7E−7	0	
Ni-59	Ni	76 000	1	8.5E−7	2.1E−3	
Mo-93	Mo	4 000	1	2.7E−7	0	88 % → Nb-93m
Nb-93m	Nb	16.13	0	2.7E−7	2.0E−2	
U-238	U	4 468 000 000	1	2.7E−7	2.0E−4	100 % → U-234
U-234	U	245 500	0	2.7E−7	2.0E−4	100 % → Th-230
Th-230	Th	75 386	0	2.7E−7	5.3E−2	100 % → Ra-226
Ra-226	Ra	1 600	0	8.5E−7	4.5E−4	100 % → Pb-210
Pb-210	Pb	22.3	0	8.5E−7	2.5E−2	100 % → Po-210
Po-210	Po	0.379	0	2.7E−7	2.5E−2	

The simulation time was set to one million years, comparable with the assessment time required in the SE-SFL project.

For the comparison each MARFA SP run was performed with 10 million (10^7) starting particles. Due to the stochastic nature of MARFA SPs Monte Carlo sampling, it is necessary to average over several runs to obtain reliable results for unit releases. Therefore, each radionuclide unit release run was performed five times. Since MARFA SP handles longitudinal dispersion in a different way, instead of a Péclet number, a dispersion length (longitudinal dispersivity) of one tenth of the path length was used for the single trajectory runs and 50 meters was used in the simulation with all trajectories.

As mentioned above, the analytical codes were not applicable in dealing with decay chains, and MARFA SP also had problems dealing with ingrowth of decay products so only FARFCOMP and FARF31 were available for comparison of radionuclide decay products. An updated version of MARFA SP which handles decay products with more stable and correct results was under development, but it was not released before this comparison was made. Neither MARFA SP nor FARF31 handles ingrowth with branching ratios that are lower than 100 %; therefore, resulting data presented from FARF31 in this comparison for Nb-93m was scaled by 88 % (this is a built-in feature of the interface code to FARF31).

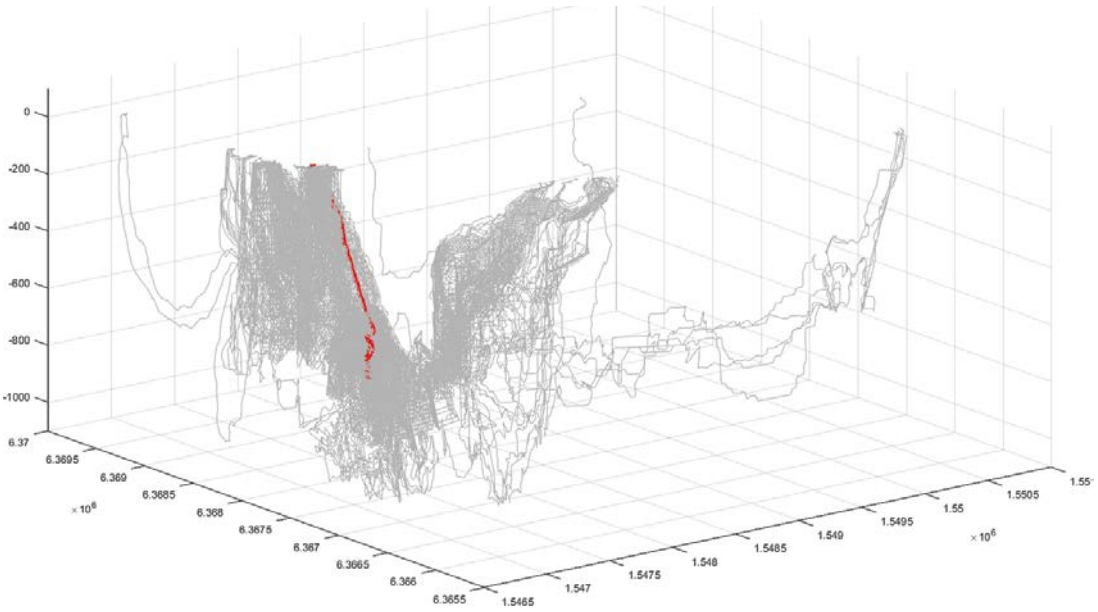

Figure B-5. *All 2 424 trajectories defined for BHA (grey), and modelled trajectory with ID 5216 (red).*

Representative particle trajectory

To make relevant unit release comparisons, a "representative particle trajectory" was selected from the waste vault BHA (particle trajectory ID 5216 from ConnectFlow realisation "sfl_elaborated_r1_hrd_site_nochem_pline_surfaces_2000" that was the realisation used in the SE-SFL *present-day evaluation case*). The trajectory was selected based on all of its properties: F-factor, travel time and total length all being as close as possible to the median of each parameter's range. The selected particle trajectory had a total length of 2 237 meters; a total travel time t_w of 235.2 years and the sum of the flow-related transport resistance F was 80 090 years per meter. The selected trajectory is illustrated in relation to the swarm of all accepted particle trajectories from the realisation with an X in Figure B-6 below.

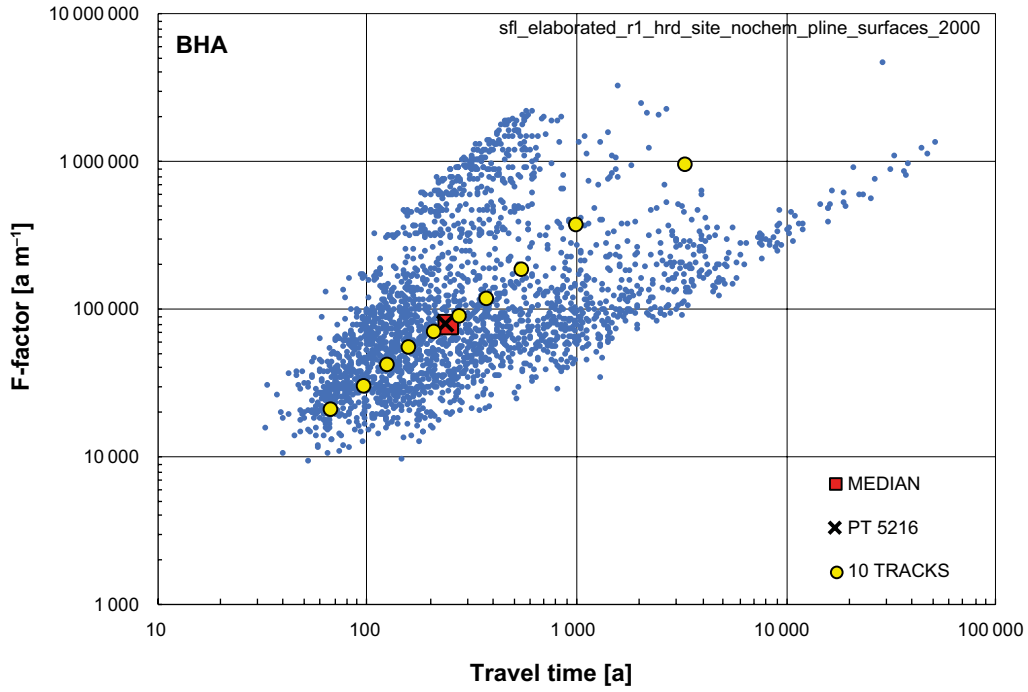

Figure B-6. *Scatter diagram of travel time versus F-factor for all accepted particle trajectories from BHA in the SE-SFL present-day evaluation case. Median value is marked with a red circle and the representative particle trajectory (ID 5216) is marked with a black X. The approximated set of trajectories is illustrated with yellow circles.*

Representative subset of trajectories

To make it possible to consider the full potential of all flow paths in the fractured rock in a probabilistic simulation, an approach for approximating the full set of trajectories with a small set of trajectories was developed. Using a similar methodology to the one tested in the safety assessment SR-Site (SKB 2011a), a small set of particle trajectories was created by combining, in order, the F-factors corresponding to the 10 percentile F-factor values spanning the full successful trajectory set (i.e. 5 %, 15 %, …, 95 %) with the travel times corresponding to the 10 percentile travel time values spanning the full successful trajectory set. Figure B-6 illustrates the set of approximated particle trajectories in relation to all accepted particle trajectories in the realisation.

Based on the methodology developed in Wessely and Shahkarami (2019) for assigning a fraction of the near-field release to each particle trajectory, each particle trajectory in the smaller set was assigned the total near-field release scaled to the sum of fractions assigned to the trajectories corresponding to the percentile interval for the F-factor. The resulting smaller set of particle trajectories and the fraction of the near-field release from BHA assigned to each trajectory are given in Table B-3.

Table B-3. Selected BHA particle trajectories and their assigned percentage of the source term in the SE-SFL present-day evaluation case.

Percentile			Source term percentages		
	F-factor [a m^{-1}]	Travel time [a]	F-factor interval	Anions[1)]	Cations/neutral[2)]
5 %	20 824	67	0–10 %	11.8 %	12.0 %
15 %	30 042	98	10–20 %	10.9 %	12.4 %
25 %	41 650	125	20–30 %	9.8 %	10.1 %
35 %	55 739	159	30–40 %	10.6 %	10.3 %
45 %	70 245	210	40–50 %	10.2 %	10.1 %
55 %	88 719	279	50–60 %	9.1 %	8.3 %
65 %	118 010	378	60–70 %	9.6 %	8.9 %
75 %	184 650	555	70–80 %	10.0 %	9.4 %
85 %	365 920	1 002	80–90 %	9.2 %	9.6 %
95 %	934 260	3 286	90–100 %	8.8 %	9.0 %

[1)] Cl-36, Mo-93, Nb-93m
[2)] organic C-14, Ni-59, U-238 chain

Unit release analysis for a single trajectory

To understand the potential breakthrough of different radionuclides given a unit release source term, analytical solutions of possible penetration length along fractures at steady state are of interest. According to Sudicky and Frind (1982) the penetration length at steady state into the fracture (with parameters defined in this Appendix) can be expressed as:

$$d_\delta = \frac{z_{\text{tot}} \ln \delta}{\frac{P_e}{2}\left(1 - \sqrt{1 + \frac{4T_w\lambda^n}{P_e}(1+\beta)}\right)}, \qquad \delta = \frac{C_f^n\big|_{z=d_\delta}}{C_f^n\big|_{z=0}},$$

$$\beta = \frac{a_w\sqrt{D_e^n R_m^n}}{\sqrt{\lambda^n}}\tanh\left[\sigma\sqrt{\lambda^n}\right], \qquad \sigma = \sqrt{\frac{R_m^n}{D_e^n}}\,d_{\max} \qquad \text{B-53}$$

Figure B-7 illustrates, for a single radionuclides and the given parameter values, the relative concentration at steady-state given a constant radionuclide concentration at the initial boundary for an infinitely long fracture. The figure gives information about how far into the fracture radionuclides penetrate before decaying (at steady-state). Radionuclide-specific processes such as radioactive decay, sorption and diffusivity will affect the shape. The total trajectory length of 2 237 meters is shown as a dashed line; the intersection with the radionuclide curves corresponds to the steady-state level at the end of the trajectory (bedrock-surface interface) for each radionuclide. Thus, almost all Cl-36 and U-238 are assumed to pass through the trajectory without any reduction by decay, because of the long half-life and low sorption of Cl-36 and very long half-life of U-238. For Ni-59, on the other hand, about 40 % of released radionuclides will decay during migration through the geosphere. Similarly, about 6 % of the released organic C-14 and Mo-93 will decay during the geosphere transport.

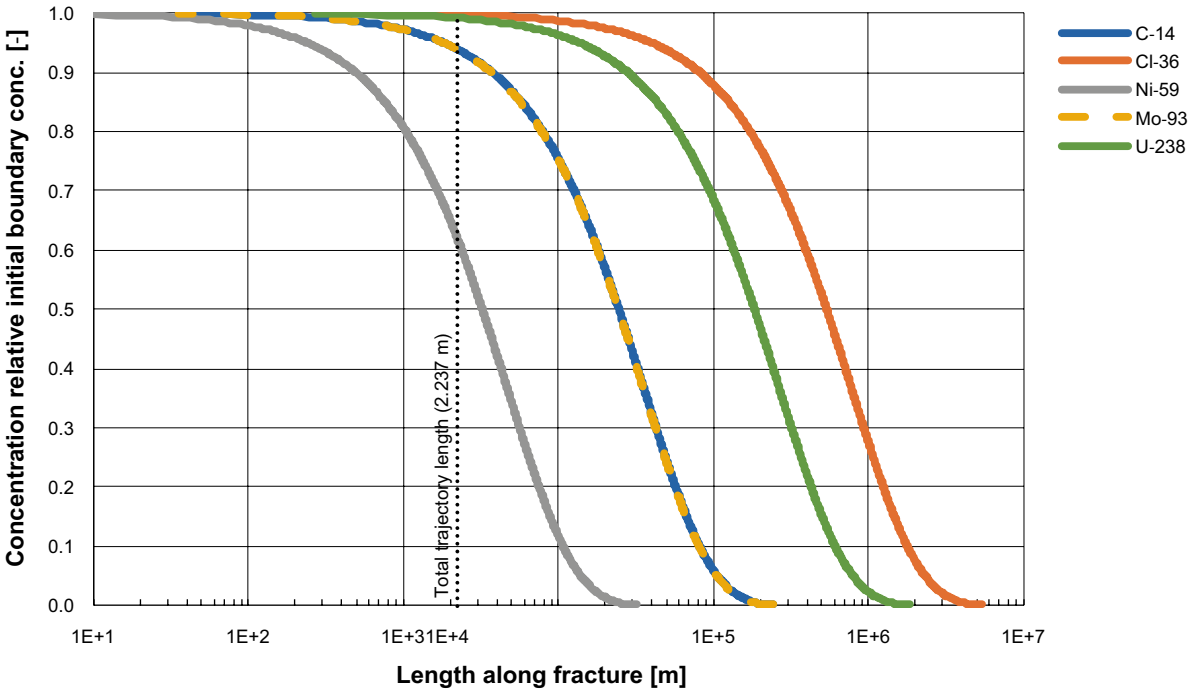

Figure B-7. *Relative concentrations of organic C-14, Cl-36, N-59, Mo-93 and U-238 which correspond to a certain travel length in an infinitely long fracture at steady state.*

Another interesting parameter affecting the potential breakthrough of different radionuclides is the penetration depth into the rock matrix by diffusion. According to Sudicky and Frind (1982), the penetration depth into porous rock matrix (rewritten with parameters defined in this Appendix) can be expressed as:

$$d_\delta = d_{\max} - \cosh^{-1}\left[\delta / e^{\frac{P_e}{2}\left(1-\sqrt{1+\frac{4T_w\lambda^n}{P_e}(1+\beta)}\right)}\cosh\left[\sigma\sqrt{\lambda^n}\right]\right] \Big/ \sqrt{\frac{\lambda^n R_m^n}{D_e^n}}, \qquad \text{B-54}$$

$$\delta = \frac{C_m^n|_{x=d_\delta}}{C_m^n|_{x=0}}$$

As a step in verifying the solutions produced by the FARFCOMP code, the penetration depth corresponding to a certain border concentration was extracted from the numerical simulation using the default 20 compartments of the rock matrix and where the fracture interfacing compartment has a thickness of 0.1 mm. An extra numerical simulation was also performed using an increased number of discretisations in which 1 000 compartments represented the rock matrix with a fracture interface compartment thickness of 0.001 mm. Figure B-8 illustrates the potential penetration depth at steady-state into the rock-matrix calculated for all radionuclides numerically (solid coloured lines for default discretisation and semi-transparent for the increased discretisation case) together with the analytical solution for the single radionuclides using Equation B-54 (black dotted lines). The results show that at maximum penetration depth (4.5 meters) there will be approximately half the pore water activity concentration of long-lived/non-sorbing Cl-36 compared with the boundary concentration (fracture concentration). For organic C-14, the concentration will be 9 times lower 4.5 meters into the matrix and for Mo-93 (with less effective diffusivity) the concentration decrease will be about 90 times. Ni-59 (which sorbs strongly onto the rock matrix) will not really penetrate the full rock matrix even at steady state (the analytical solution shows that a relative concentration at maximum penetration depth for Ni-59 is less than 15 orders of magnitude). For U-238, almost the same pore water activity concentration at steady state can be seen in the first ten centimetres of the rock matrix and at the maximum penetration depth the activity concentration is still within one order of magnitude of the fracture concentration. For all the decay product radionuclides, the results calculated are more complex since they are affected both by the source term at the fracture as well as the source term from the parent radionuclide within the rock matrix.

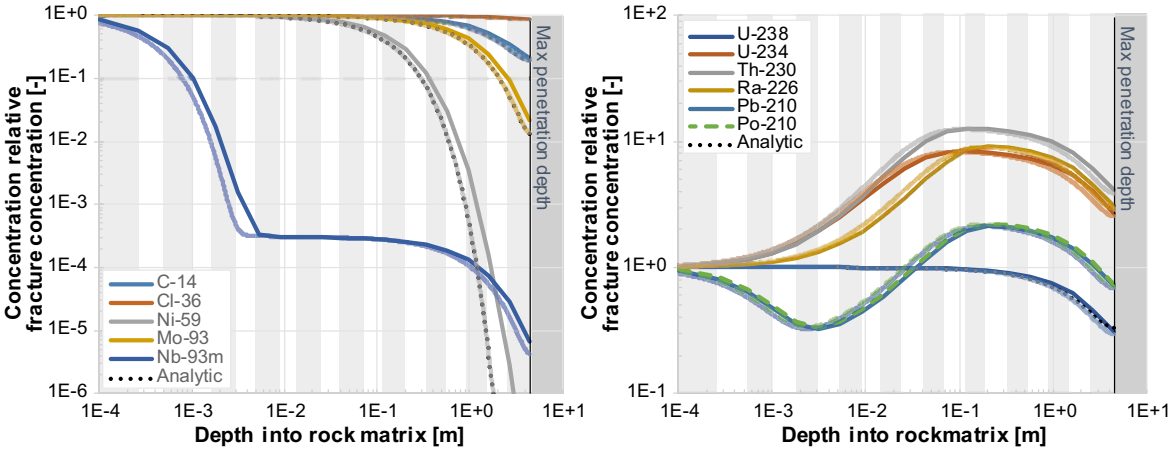

Figure B-8. *Penetration depth into the rock matrix at steady state. Coloured lines are calculated results using default discretisation values, semi-transparent colours are calculated results using an increased number of discretisations (1 000 compartments compared to default 20 compartments) and black dotted lines are corresponding analytical results for radionuclides with a source term. Background shades represent the actual rock matrix compartment thicknesses used for the numerical calculation with the default number of compartments.*

The discretisation coarseness has clear implications for the numerical results using default discretisation (solid coloured lines in Figure B-8) and the lower resolution is creating numerical dispersion in the numerical solution and thus produces a somewhat higher relative concentration within the rock compared with the analytical solution. The higher discretisation case reduces the effect of the undesired numerical dispersion and produces concentration gradients within the rock matrix that are visibly indistinguishable from the analytical solutions on a logarithmic scale (solid semi-transparent coloured lines in Figure B-8), giving some confidence in the solution method.

Sensitivity on breakthrough by varying solution codes

FARFCOMP, FARF31, MARFA SP, and analytical solutions are compared for the case defined by using unit release of single nuclides in a single trajectory, i.e. trajectory with ID 5216 described above. Figure B-9 and Figure B-10 show the release of radionuclides at the end of the geosphere calculated with the different geosphere transport codes for Cl-36, Ni-59, Mo-93, Nb-93m and U-238 chain. Breakthrough for organic C-14 is very similar to Mo-93, since both radionuclides are effectively non-sorbing in the geosphere and have similar, long half-lives.

An analytical breakthrough solution is defined in Tang et al. (1981) and can be written (with parameters defined in this document and an infinite penetration depth into the rock matrix) as:

$$F^n_{\text{out}}(t) = \frac{e^{\frac{P_e}{2}}}{\sqrt{\pi}} \int_{\sqrt{\frac{T_w P_e}{4t}}}^{\infty} e^{-x^2-\left(\frac{P_e}{4x}\right)^2} e^{\frac{-\lambda^n T_w P_e}{4x^2}} \left(e^{-\sqrt{\lambda^n} Y(x)} erfc\left(\frac{Y(x)}{2T} - \sqrt{\lambda^n} T(x,t)\right) + e^{\sqrt{\lambda^n} Y(x)} erfc\left(\frac{Y(x)}{2T} + \sqrt{\lambda^n} T(x,t)\right)\right) dx \qquad \text{B-55}$$

$$Y(x) = \frac{a_w T_w P_e \sqrt{D_e^n R_m^n}}{4x^2}, \qquad T(x,t) = t - \frac{T_w P_e}{4x^2}$$

For the case with no dispersion the analytical solution simplifies to:

$$F_{\text{out}}^{n*}(t) = \frac{1}{2} e^{-\lambda^n T_w} \left(e^{-\sqrt{\lambda^n} Y'} erfc\left(\frac{Y'}{2T'(t)} - \sqrt{\lambda^n} T'(t) \right) + e^{\sqrt{\lambda^n} Y'} erfc\left(\frac{Y'}{2T'(t)} + \sqrt{\lambda^n} T'(t) \right) \right) \quad \text{B-56}$$

$$Y' = a_w T_w \sqrt{D_e^n R_m^n}, \qquad T'(t) = \sqrt{t - T_w}$$

An analytical breakthrough steady-state solution for radionuclides that do not belong to a decay chain is defined in Tang et al. (1981) and can be written (with parameters defined in this document and an infinite penetration depth into the rock matrix) as:

$$F_{\text{out}}^{n}(t = \infty) = e^{\frac{P_e}{2} - \sqrt{\left(\frac{P_e}{2}\right)^2 + T_w P_e \left(\lambda^n + a_w \sqrt{\lambda^n D_e^n R_m^n}\right)}} \quad \text{B-57}$$

For the case with no dispersion the analytical steady-state solution simplifies to:

$$F_{\text{out}}^{n*}(t = \infty) = e^{-\lambda^n T_w - a_w T_w \sqrt{\lambda^n D_e^n R_m^n}} \quad \text{B-58}$$

Analytical solutions for the case with restriction on penetration depth are presented in Sudicky and Frind (1982). Since the analytical solutions for the breakthrough curves are complex only the steady state solutions are presented here as

$$F_{\text{out}}^{n}(t = \infty) = e^{\frac{P_e}{2}\left(1 - \sqrt{1 + \frac{4\lambda^n T_w}{P_e}(1+\beta)}\right)} \quad \text{B-59}$$

For the case with no dispersion the analytical steady-state solution simplifies to:

$$F_{\text{out}}^{n*}(t = \infty) = e^{-\lambda^n T_w (1+\beta)} \quad \text{B-60}$$

Results for the single radionuclides using FARFCOMP, FARF31, and the corresponding analytical solution all coincide in the charts below, giving confidence in the dynamic evolution of their respective solution methods. At end of the simulation, which is the steady-state solution for all radionuclides with a source term except for U-238, the largest error in release over tested radionuclides is 0.21 % for FARFCOMP and 0.41 % for FARF31. The errors from the code are thus several orders of magnitude smaller than many parameter uncertainties relating to the geosphere transport.

In MARFA SP, non-sorbing radionuclides from the repository reach the end of the geosphere earlier than in the other models, implying higher dispersion. Further, an oscillating effect is noted before reaching steady state. For Nb-93m and other decay product radionuclides, the results from MARFA SP (not shown) gave high amplitude oscillations and sometimes "converged" to solutions that differ very much from the other models. Such oscillations can occur if too few particles are assigned to a specific species. After this comparison was made, a new version of MARFA SP has been developed, resulting in decreased oscillations and a better handling of decay chains.

The breakthrough curves for the uranium series (Figure B-10) uses a log-log scale for the axes due to the large difference in the magnitude of the breakthrough curves for the released U-238 and its decay products. The coloured lines are the results from the FARFCOMP code and the overlapping black dashed lines are the results using the FARF31 code. At the end of the simulation, the difference between the normalised annual geosphere releases produced by the two codes are 0.17 %, 0.87 %, 1.00 %, 0.88 %, 1.38 % and 0.74 % for the U-238 series, in decay-chain order. Both codes give results in good agreement with the analytical solution for U-238 (not shown, a maximum error of 0.12 % at end of simulation). The result gives confidence that FARFCOMP discretised with 420 compartments generates similar results as the (semi)analytic FARF31 code for decay chains.

For decay products such as Nb-93m and those in the uranium series; results from MARFA SP never converged in this analysis and are therefore not presented in this comparison.

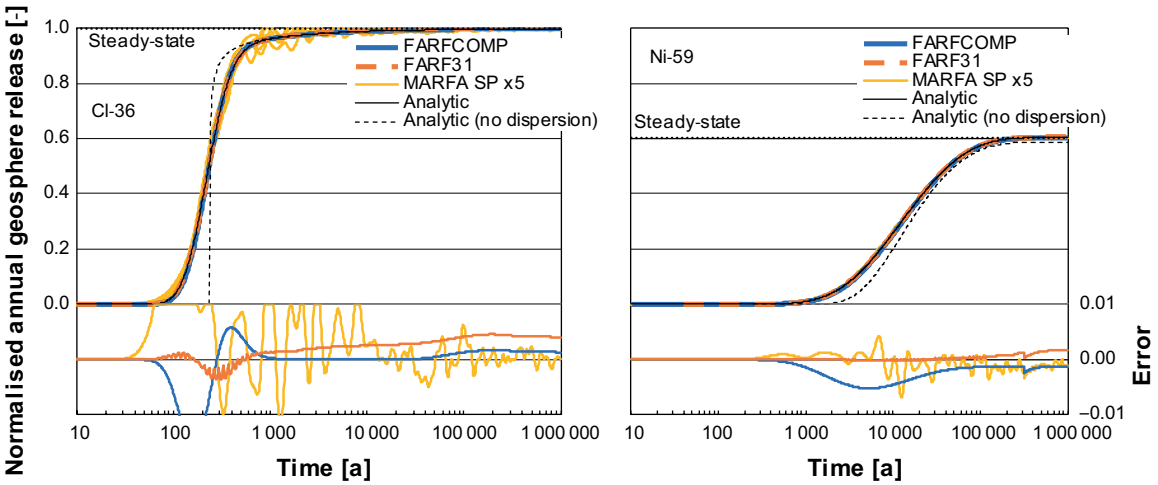

Figure B-9. *Normalised annual release (-) of Cl-36 (left) and Ni-59 (right) at the top the geosphere calculated using five different geosphere-transport codes. Comparisons between FARFCOMP, FARF31, MARFA SP and analytic solutions with and without dispersion. Lower panel shows the resulting error compared to the analytic solution of the numerical codes, where the average over five simulations is used for MARFA SP.*

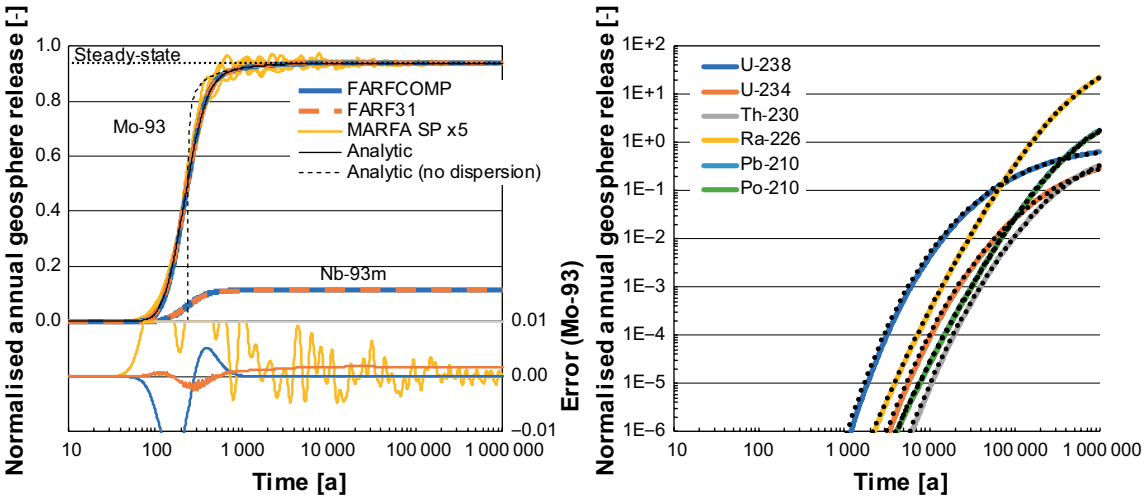

Figure B-10. *Normalised annual release of Mo-93 and its decay product Nb-93m (left) at the top of the geosphere calculated using five different geosphere-transport codes for Mo-93 and FARFCOMP and FARF31 for Nb-93m. Corresponding releases of the U-238-decay chain (right) illustrated with coloured lines for FARFCOMP and black dots for FARF31 (note the logarithmic y-axis). Lower panel shows the resulting error for Mo-93 of the numerical codes compared to the analytic solution, where the average over five simulations is used for MARFA SP.*

Table B-4 lists the annual geosphere release [Bq a^{-1}] at different times, assuming a constant near-field release of 1 Bq a^{-1}, and the accuracy comparison between different codes. The table shows the analytic solution to the unit release [Bq a^{-1}] at various points in time after closure (grey rows), and in coloured sections the unitless relative errors from FARF31, FARFCOMP with default discretisation and tolerance levels and with refined accuracy settings (denoted FARFCOMP* in Table B-4). Evidently, the early times and small unit releases (below assigned tolerance levels) are generally associated with large calculation errors from both codes; note also that the advective travel time along the trajectory is 235.2 years, so for the first two recorded time points (10 and 100 years), releases occur only by dispersion. After 10 years of release, none of the codes produced results within 100 % of the analytical results, though for mobile radionuclides (C-14, Cl-36, and Mo-93 with $K_d = 0$), the highly discretised FARFCOMP* produced results in the same order of magnitude whilst the other simulations produced clearly non-relevant results. The actual error over time illustrated in Figure B-9 and B-10 for Cl-36, Ni-59 and Mo-93 indicates that FARF31 is more robust in the early breakthrough phase, and as the

breakthrough curve approaches steady-state, FARFCOMP produces more accurate results. This trend can also be seen in Table B-4 where FARF31 produces the most accurate results for highly mobile radionuclides after 100 years of releases (early breakthrough phase). For the rest of the recorded time points, the breakthrough curves for the highly mobile radionuclides are either close to or at steady-state (Figure B-9 and B-10). For the sorbing radionuclide Ni-59, FARF31 has the most accurate results for all except the last recorded time point when it finally has reached steady-state (Figure B-9). U-238 is both sorbing and very long-lived and never reaches steady-state within one million years and thus FARF31 has the best accuracy for all relevant time points. In general, the errors in relevant time perspectives (longer for sorbing radionuclides) are less than 1 % for both mobile and sorbing radionuclides for both codes. It is clear that increasing the discretisation and the tolerance constraints is helpful to increase the accuracy for radionuclides in the late breakthrough phase (compare FARFCOMP and FARFCOMP* for C-14, Cl-36 and Mo-93 from 1 000 years and Ni-59 from 100 000 years in Table B-4). However, the increased numerical error due to the required shorter time-steps of FARFCOMP* actually seems to decreases the accuracy in the early breakthrough phase compared to FARFCOMP, see earlier time points for Ni-59 and U-238.

Note that without an analytic solution for decay products available, Table B-4 only presents the solution and relative error for radionuclides in the comparison with a source term. Comparing the calculated results from FARF31 and FARFCOMP for decay products yields relative differences smaller than 10 % after 10 000 years (not shown), and for most radionuclides and time points, the relative difference between the two codes are less than 1 %. For earlier recorded times (less or equal to 1 000 years) and for radionuclides where FARF31 converges, the relative difference is less than 80 % (for Nb-93m less than 10 %).

Table B-4. Analytic solution to the unit release [Bq a^{-1}] of various radionuclides at different times after closure, and the unitless relative error (|computed−analytic|/analytic) from FARF31 and FARFCOMP with default settings (described in Section B-5), as well as with more accurate settings denoted FARFCOMP* with RelTol = 10^{-10}, AbsTol = 10^{-15} Bq, and $N_f = N_m = 100$ compartments. Cell backgrounds are colour-coded by error size < 10 % (green), 10−100 % (yellow), and ≥ 100 % (red). The smallest error for each radionuclide and time-point is bolded.

Time [a]	Code	C-14	Cl-36	Ni-59	Mo-93	U-238
10	Analytic [Bq a^{-1}]	2.03E−25	2.35E−25	1.40E−32	2.35E−25	5.98E−50
	FARF31	9.4E+13	4.2E+13	No convergence		
	FARFCOMP	1.7E+11	1.7E+11	1.3E+15	1.7E+11	5.9E+29
	FARFCOMP*	**2.7E+01**	**2.7E+01**	**4.1E+02**	**2.7E+01**	**6.2E+18**
100	Analytic [Bq a^{-1}]	2.59E−02	2.99E−02	2.14E−07	2.95E−02	9.18E−17
	FARF31	**3.3E−02**	**3.4E−02**	**2.4E−01**	**1.1E−02**	No conv.
	FARFCOMP	1.2E−01	1.2E−01	1.7E+00	1.2E−01	8.4E+03
	FARFCOMP*	2.1E−01	2.0E−01	4.3E−01	2.0E−01	**1.2E+01**
1 000	Analytic [Bq a^{-1}]	9.01E−01	9.61E−01	1.01E−02	9.19E−01	5.38E−07
	FARF31	1.0E−03	1.4E−03	**1.9E−03**	1.0E−03	**1.4E−01**
	FARFCOMP	1.7E−03	9.5E−04	2.4E−02	9.4E−04	1.2E+00
	FARFCOMP*	**3.6E−04**	**2.9E−04**	1.4E−01	**2.0E−04**	3.4E−01
10 000	Analytic [Bq a^{-1}]	9.37E−01	9.89E−01	2.58E−01	9.38E−01	5.08E−03
	FARF31	2.6E−03	2.6E−03	**4.5E−04**	1.9E−03	**5.5E−03**
	FARFCOMP	5.9E−04	1.8E−04	8.0E−03	3.5E−04	6.9E−03
	FARFCOMP*	**2.3E−05**	**6.2E−06**	1.8E−02	**3.1E−05**	1.6E−01
100 000	Analytic [Bq a^{-1}]	9.39E−01	9.97E−01	5.74E−01	9.38E−01	1.97E−01
	FARF31	2.7E−03	2.8E−03	**7.8E−04**	1.9E−03	**7.4E−04**
	FARFCOMP	5.2E−04	1.7E−05	6.7E−03	3.4E−04	6.5E−03
	FARFCOMP*	**2.5E−05**	**2.4E−06**	2.4E−03	**3.5E−05**	2.6E−02
1 000 000	Analytic [Bq a^{-1}]	9.39E−01	9.98E−01	6.04E−01	9.38E−01	6.40E−01
	FARF31	2.7E−03	2.8E−03	2.7E−03	1.9E−03	**5.4E−04**
	FARFCOMP	5.2E−04	3.9E−06	5.8E−03	3.4E−04	6.9E−03
	FARFCOMP*	**2.5E−05**	**1.2E−06**	**2.1E−03**	**3.4E−05**	1.2E−03

Sensitivity on breakthrough by varying longitudinal dispersion

For radionuclides that are not modelled as decay products, the analytical models can give insights in how the breakthrough varies when varying the longitudinal dispersion. Figure B-11 illustrates the effect on the breakthrough for the representative trajectory (ID 5216) by varying the Péclet number from an unreasonably high longitudinal dispersion using a Péclet number of 1 to a very small longitudinal dispersion using a Péclet number of 100 as well as with no longitudinal dispersion at all (corresponding to an infinite Péclet number) for Mo-93 and Ni-59. Other non-sorbing radionuclides are affected in a similar way as Mo-93. The results show that dispersion in this single trajectory does not affect radionuclide migration very much for a longitudinal dispersion corresponding to a Péclet number of at least 10, as is the default choice.

Sensitivity on breakthrough by varying maximum penetration depth

For radionuclides that are not modelled as decay products, the analytical models can also give insights in how the breakthrough varies when varying the maximum possible penetration depth into the rock matrix. Figure B-12 illustrates the effect on the breakthrough for the representative trajectory (ID 5216) by varying the maximum penetration depth from 5 mm to 4.5 m as well as no maximum penetration depth at all for Mo-93 and Ni-59. Other non-sorbing radionuclides are affected in a similar way as Mo-93. The results show that for this trajectory the choice of 4.5 meters as maximum penetration depth does not affect the solution at all compared with having no restriction on the penetration depth, both for non-sorbing and sorbing radionuclides. Only a penetration depth restriction that is much smaller would affect the resulting breakthrough curves.

Sensitivity on breakthrough by varying size of discretisation

As noted in the previous comparison, using a default number of 20 compartments both to discretise the fracture as well as the rock matrix in the model (hence in total 420 compartments), is sufficient to reproduce analytical results and the results calculated by FARF31 for the specific analysed radionuclides. This study illustrates the effect of reducing the number of discretisations in both directions.

Calculations for each combination between 1 and 20 compartments in the fracture direction and 3 to 20 compartments in the matrix direction have been performed. It should be noted that by using less than 5 compartments in the fracture direction a numerical dispersion is introduced that is higher than the desired dispersion in the fracture defined by the Péclet number (10). A too small number of discretisations in any direction will underestimate the retardation for sorbing radionuclides. In Figure B-13, chosen simulations are presented to illustrate the effect of reducing the number of compartments in both directions. Black thin lines show the results of reducing the number of fracture

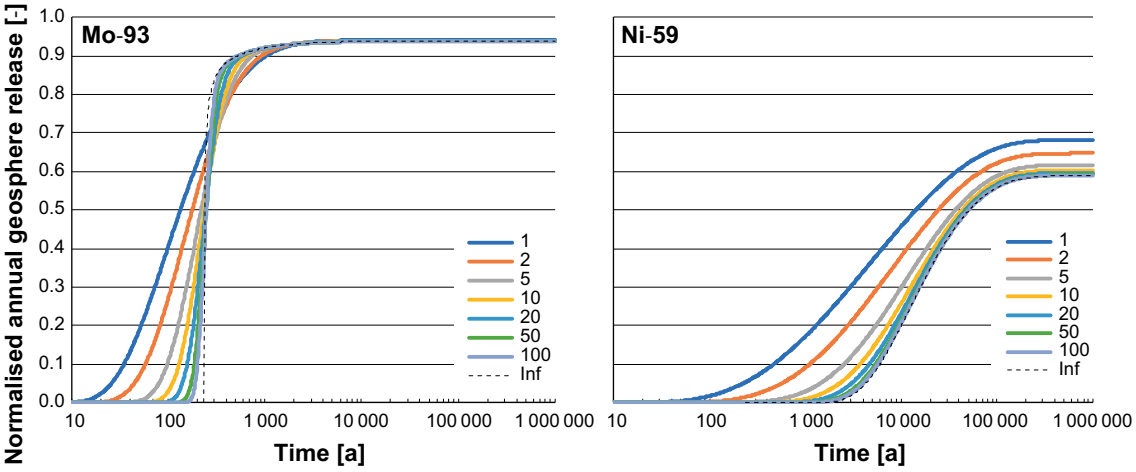

Figure B-11. *Normalised annual release of radionuclides using a unit source term for radionuclides out from the end of the geosphere calculated using one particle track (ID 5216). The effect on the breakthrough curve varying longitudinal dispersion (the Péclet number) for Mo-93 (left) and Ni-59 (right).*

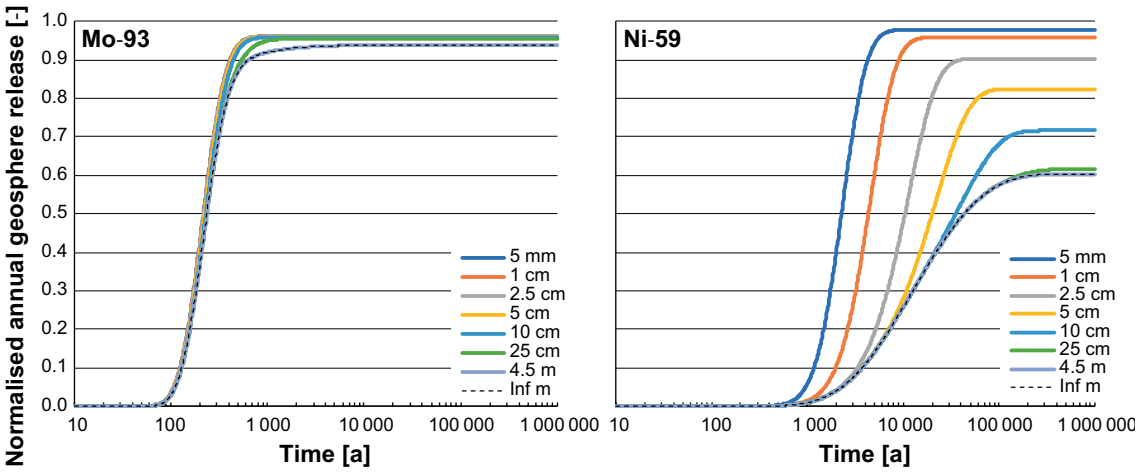

Figure B-12. *Normalised annual release of radionuclides using a unit source term for radionuclides out from the end of the geosphere calculated using one particle track (ID 5216). The effect on the breakthrough curve varying the maximum possible penetration depth into the rock matrix for Mo-93 (left) and Ni-59 (right).*

compartments keeping the number of rock matrix compartments at 20. The lowest number of fracture compartments shown is 5 and each black line represents a simulation increasing this number by one up until 20 compartments is used in each direction. By decreasing the number of fracture compartments, an earlier breakthrough is manifested, though the effect is hardly visible on a linear scale. At later times, the results are generally much more accurate, largely because the steepness of concentration profiles declines with time and therefore the necessity for smaller grid cells is reduced (see Maul and Robinson 2008). Similarly, thin lines with cyan colour represent a similar simulation with a fixed fracture discretisation of 20 compartments and varying the number of rock matrix compartments from 10 to 20. The effect of this variation is hardly visible in the figures but a small marginal increase in the steady-state results for Ni-59 and Nb-93m can be noted. Dotted and dashed red lines represent simulations with 10 and 15 compartments in both directions respectively. The presented results show that reducing the number of compartments to 10 in both directions (thus in total 110 compartments) does not significantly change the calculated results from the results obtained with 20 compartments in both directions.

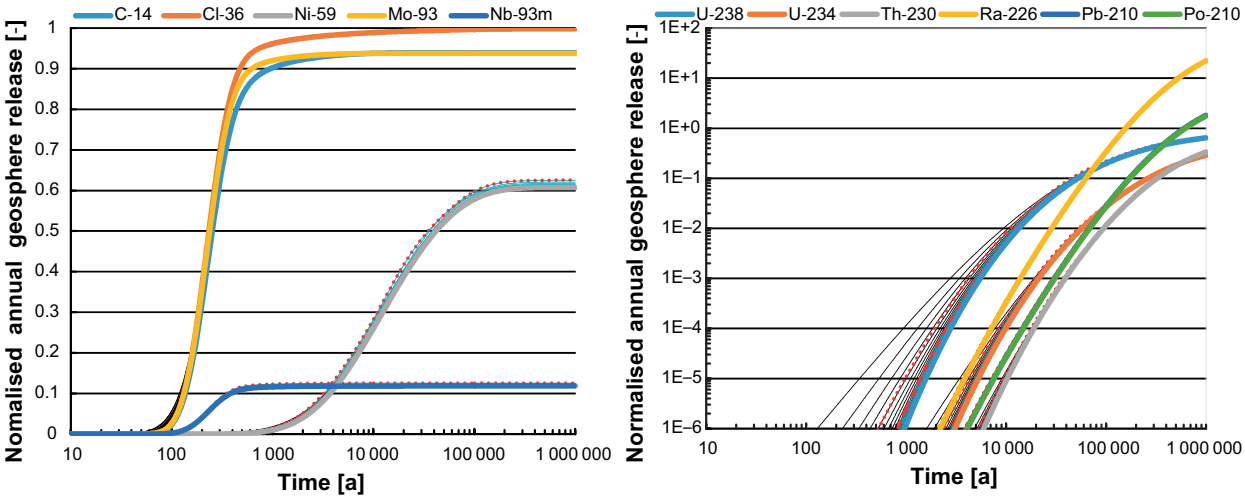

Figure B-13. *Normalised annual release of radionuclides using a unit source term for parent radionuclides out from the end of the geosphere calculated using one particle track (ID 5216) presented with thick coloured lines for default discretisation (20 compartments representing the fracture and 20 compartments per fracture compartment representing the rock matrix) Black thin lines represent a fixed matrix discretisation of 20 compartments and varying fracture compartments from 5 to 19. Cyan coloured thin lines represent a fixed fracture discretisation of 20 compartments and varying rock matrix compartments from 10 to 19. Dotted red line represents a discretisation by 10 and dashed red line represents a discretisation by 15 compartments in both directions.*

Unit release analysis with all trajectories

In this analysis a unit release is weighted over the full set of particle tracks from the BHA repository for the *present-day evaluation case* in the SE-SFL project. The calculations were performed with both the FARFCOMP code as well as FARF31 both producing similar results so only results from FARFCOMP are shown. The objective of this analysis is to illustrate the effect of macro-dispersion obtained from averaging radionuclide migration over multiple flow paths. Also, a simplified model using only 10 selected particle trajectories is tested and compared with the full set of particle trajectories.

Figure B-14 shows breakthrough curves for the tested radionuclides, the solid lines represent the weighted breakthrough curves over all valid (2 424) particle trajectories used in *present-day evaluation case* calculation from the BHA repository and the dotted lines represent the results using the same single particle trajectory as used in previous comparisons (ID 5216). Apart from having the effect that particle trajectory with ID 5216 has a shorter travel time than the weighted solution (lowering the steady state solution for the weighted calculation for radionuclides with shorter half-lives); the main effect of weighting over multiple flow-paths is the increased dispersion.

Figure B-15 compares the weighted breakthrough curve over all (2 424) particle tracks as in the previous comparison with the set of 10 approximated particle tracks chosen to capture the full range of the F-factor and the travel time. Differences in the solutions are of course noted, though both the dispersion as well as the steady-state solution seems to be well captured.

A note about simulation time: to simulate and create resulting breakthrough curves for the above-mentioned radionuclides and default discretisations for all trajectories took only half the time using FARFCOMP compared with FARF31. The difference in simulation time between the two codes becomes significant when accounting for parallelisation and also the possibility to heavily reduce the numerical problem by decreasing the number of discretisations both in the direction of the fracture and the direction of the rock matrix. In addition, the simulation time for the 10 representative particle tracks was about 0.4 % of that of the full trajectory set (approximately the required 10 trajectory runs compared with the 2 424 trajectories of the full set), reducing the total required simulation time even more.

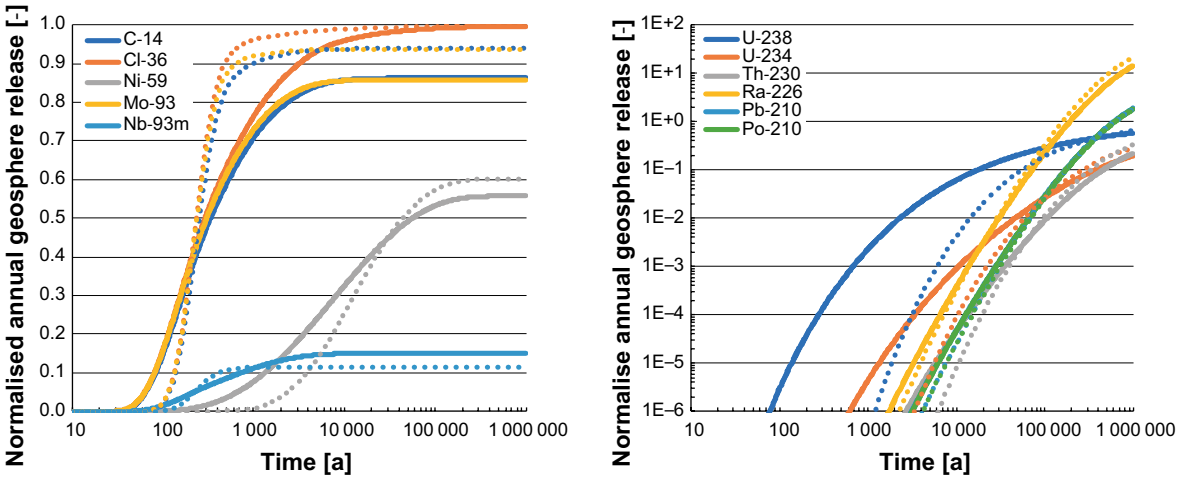

Figure B-14. *Normalised annual release of radionuclides using a unit source term for parent radionuclides at the end of the geosphere calculated using one particle track (ID 5216) presented with coloured dotted lines and weighted over all 2 424 particle tracks defined for radionuclide releases from BHA presented with coloured solid lines.*

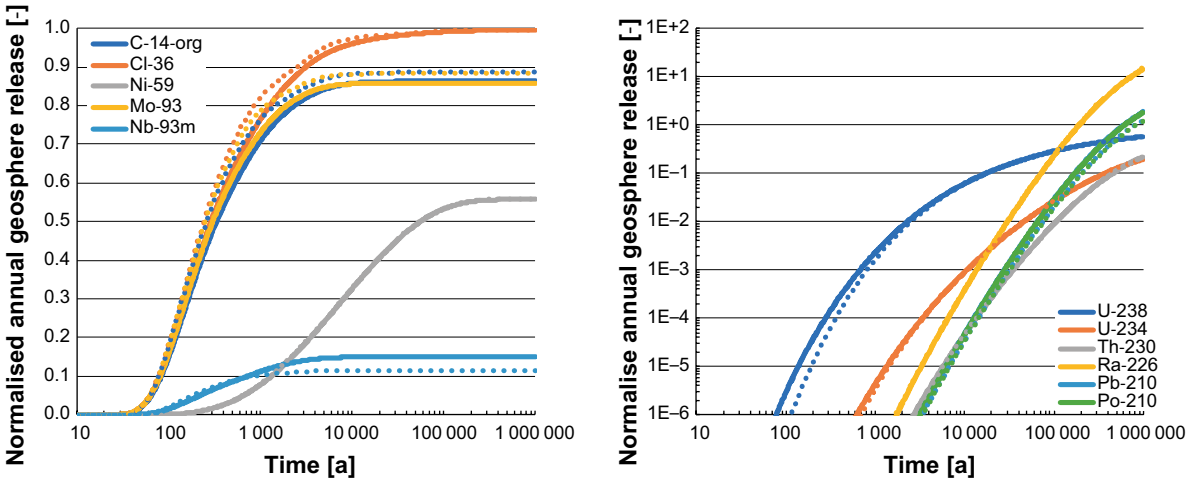

Figure B-15. *Normalised annual release of radionuclides using a unit source term for parent radionuclides at the top of the geosphere calculated using 10 chosen particle tracks and presented with coloured dotted lines and weighted over all 2 424 particle tracks defined for radionuclide releases from BHA presented with solid coloured lines.*

Comparison using actual release term from BHA and all trajectories

In this comparison the deterministic radionuclide release from the BHA vault for the *present-day evaluation case* in the SE-SFL project was used with the full set of particle trajectories (2 424) in which the radionuclide release is distributed to the particle trajectories according to weights in the same way as described above. The resulting breakthrough curves are the sum of all breakthrough curves of the full set of particle tracks calculated with FARFCOMP, FARF31 and MARFA SP. Also, a simplified variant using only 10 selected particle tracks is tested with FARFCOMP. Figure B-16 to Figure B-18 present the resulting geosphere release for each of the modelled radionuclides from the different codes, together with the total near-field radionuclide source term. As was suspected, after examination of the results of previous comparisons, breakthrough curves from FARFCOMP and FARF31 give almost identical results. The results from MARFA SP are also very close to those of FARFCOMP and FARF31 for non-decay-product radionuclides giving confidence in the results. For radionuclide decay products with short half-lives relative to their parent radionuclide, MARFA SP produced oscillating results and did not converge very well (mainly for Nb-93m, U-234, Ra-226, Pb-210 and Po-210), probably due to a too low resolution of particles to handle the ingrowth and transport correctly. Therefore, only MARFA SP-results from four single radionuclides (organic C-14, Cl-36, Mo-93 and Ni-59) are presented in the resulting figures.

For the weighted breakthrough curves of the ten-selected particle tracks a slight difference in results can be seen, a slightly higher and earlier breakthrough for non-sorbing radionuclides is noted, though only a difference in peak releases of up to ~15 % is seen. For decay-product radionuclides with breakthrough curves depending mainly on the source term from parent radionuclides within the geosphere the results are either an almost perfect match or somewhat lower for the very short-lived radionuclides (Nb-93m, Pb-210 and Po-210 all have a half-life shorter than 25 years), up to a 30 % lower peak breakthrough for these radionuclides is noted.

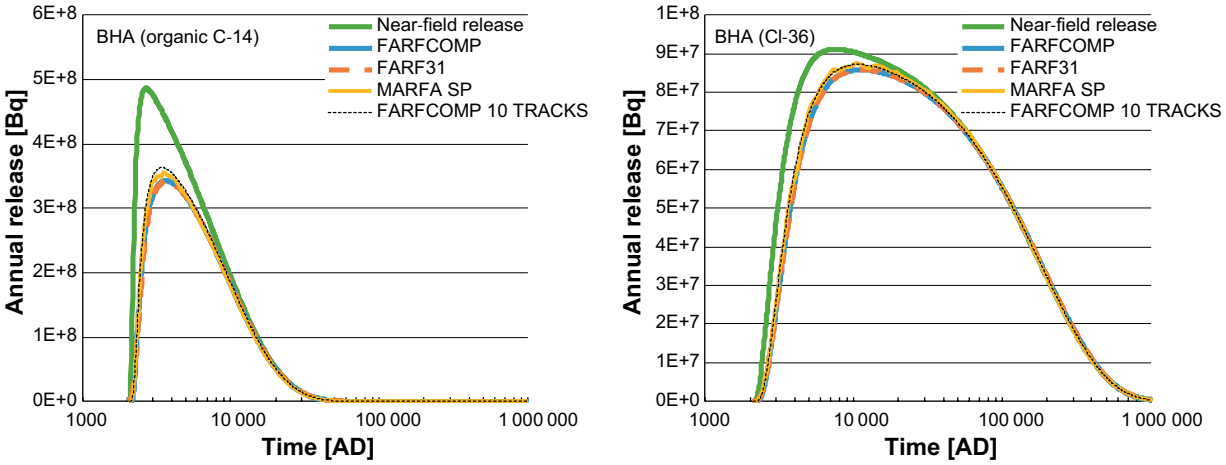

Figure B-16. *Annual activity release of organic C-14 (left) and Cl-36 (right) out from the near-field (green solid line) into the geosphere. Resulting release at the top of the geosphere calculated and weighted over 2 424 flow paths using FARFCOMP (solid blue line), FARF31 (dashed orange line) and MARFA SP (golden line). Black thin dashed line illustrates the resulting weighted geosphere release using ten approximated particle tracks.*

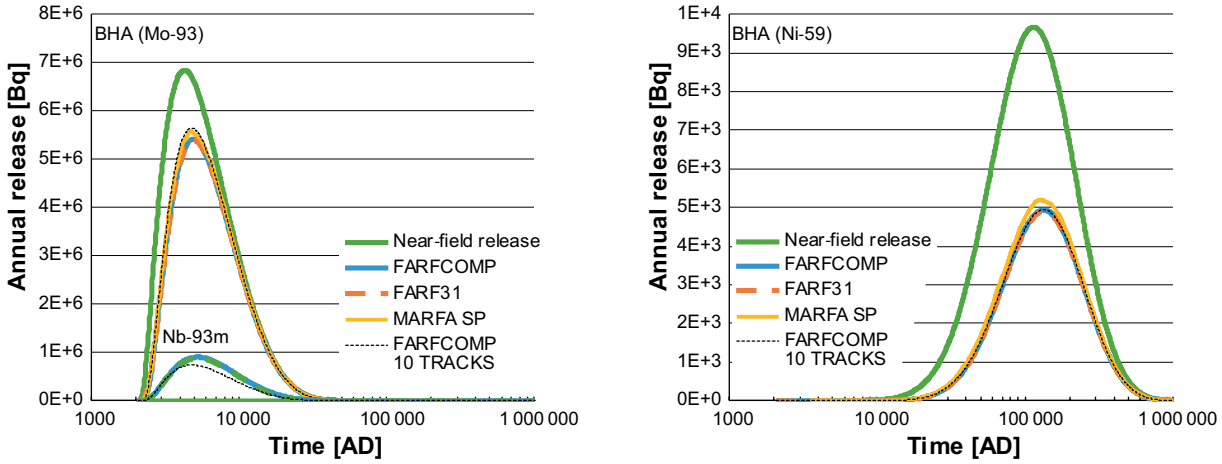

Figure B-17. *Annual activity release of Mo-93 → Nb-93 (left) and Ni-59 (right) out from the near-field (green solid line) into the geosphere. Resulting release at the top of the geosphere calculated and weighted over 2 424 flow paths using FARFCOMP (solid blue line), FARF31 (dashed orange line) and MARFA SP (golden line). Black thin dashed line illustrates the resulting weighted geosphere release using ten approximated particle tracks.*

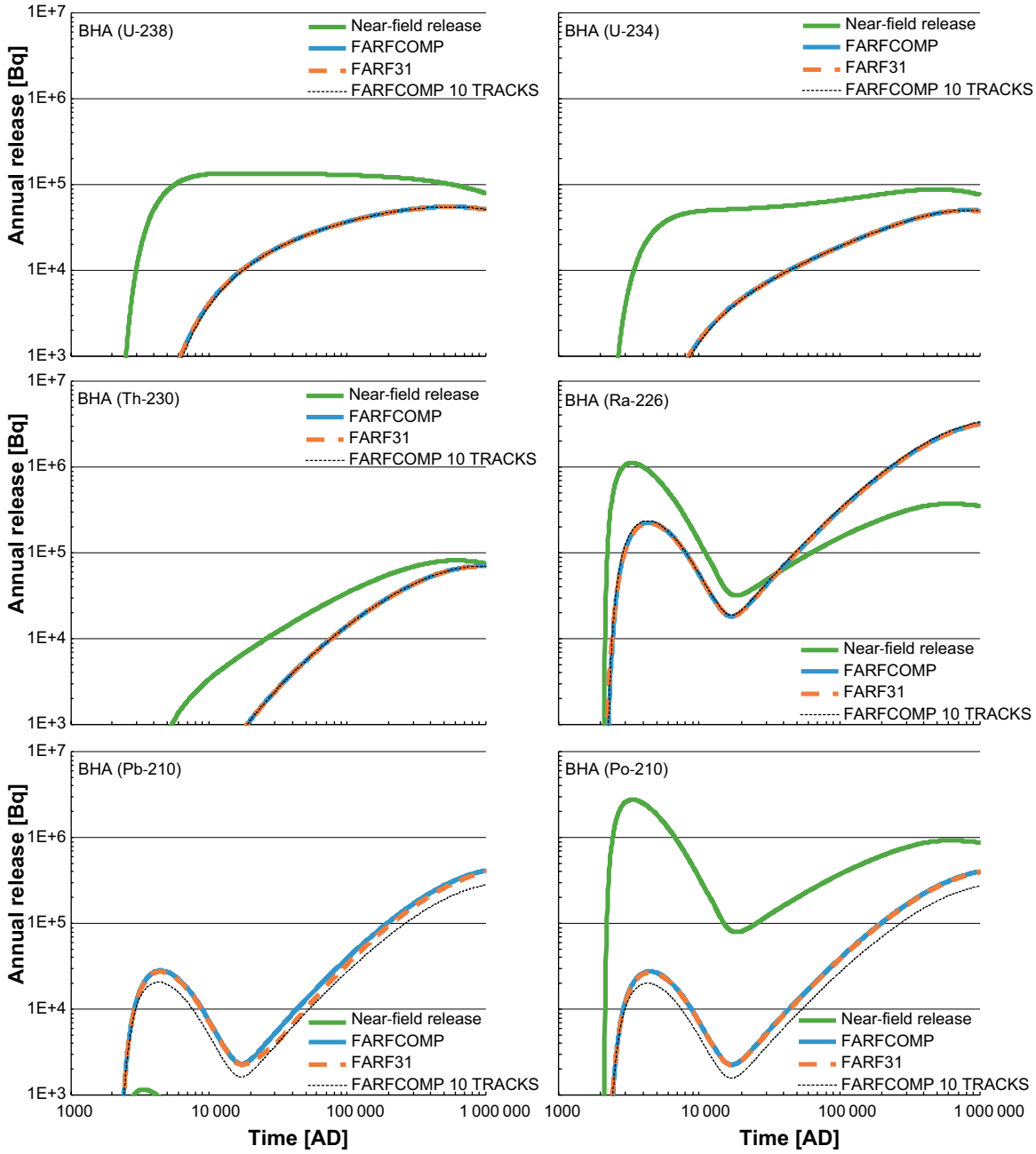

Figure B-18. *Annual activity release of uranium series: U-238 → U-234 → Th-230 → Ra-226 → Pb-210 → Po-210 out from the near-field (green solid line) into the geosphere. Resulting release at the top of the geosphere calculated and weighted over 2 424 flow paths using FARFCOMP (solid blue line) and FARF31 (dashed orange line). Black thin dashed line illustrates the resulting weighted geosphere release using ten approximated particle tracks.*

B7 Discussion

This appendix documents the implementation of a so-called compartment model in Matlab for geosphere transport of radionuclides released into sparsely fractured rock. The new tool for transport simulations is denoted FARFCOMP and the goal has been to solve the same governing equations and mimic the result calculated by the (semi)analytic code FARF31 as well as produced by analytical solutions. The underlying conceptual model can be seen as a porous medium model or fractured medium model, the same governing equations are used for both conceptualisations.

The main reason for developing the code has been to get a clear, more flexible, faster and consistent solution method for solving the transport equation in one flow path compared with existing codes such as FARF31. The code makes it possible to calculate consistent and accurate weighted solutions over multiple flow paths within reasonable computer time. Due to the direct numerical solution method, there is no problem handling any size or complexity of radionuclide decay chains, including diverging decay chains.

The current model assumes a conceptualisation of the fracture as a flat slit with parallel walls; it would be straightforward to implement radial diffusion instead using the same compartment approach.

It would also be straightforward to implement diffusion including the aperture sides of the fracture as well as implementing 2D diffusion and therefore considering the diffusion terms between each fracture segment. However, the simplifying approximations adopted in the present model are not thought to affect breakthrough curves noticeably.

A large number of physical and chemical processes affect retardation of radionuclides in fractured rock; however, a few of them have been thought to affect the migration more than others and are therefore relevant to include in this kind of simplified radionuclide transport modelling. The main radionuclide transport-related processes for modelling radionuclide migration in fractured rock are: radioactive decay and, consequently, chain decay, advection and dispersion in the fracture and diffusion and sorption in the rock matrix. As the numerical implementation of the conceptual model is performed by a compartment approach, the inclusion of other features and processes, for example retention (by sorption) within the fracture, colloid-facilitated transport and spatial and temporal variability in flow path properties or other processes, are all straight-forward to implement.

In order to keep the code as simple as possible and also to maintain compatibility with existing codes such as FARF31 and MARFA SP, and with implemented analytical solutions for comparison, only the main processes affecting radionuclide migration have been implemented. To help this, a similar parameterisation to that used in FARF31 and other assessment codes used in previous safety assessments by SKB has been chosen.

In the radionuclide transport calculations, interpolation between the values from several steady state calculations could be used to simulate, for example, time-dependent water fluxes in the geosphere. An expanded version of the model code gives the possibility to change transport properties over time.

Dispersion along individual flow paths (hydrodynamic dispersion) is modelled by means of a dispersion term, which is expressed through the dimensionless Péclet number that quantifies the ratio between advective and dispersive transport for non-sorbing solutes. Due to the modelling approach, a numerical dispersion term is introduced and is adjusted such that it matches the desired longitudinal dispersion. Therefore, a consequence is that there will be a restriction on the possible lower magnitude of hydrodynamic dispersion that can be modelled which is correlated with the chosen number of discretisations along the fracture. This should not be a problem since the dispersion in the whole system of independent channels will depend mainly on the difference in transport characteristics (travel times and transport resistances) among the channels (macro dispersion) and the dispersion in an individual channel should therefore have a small impact.

A finite penetration depth for radionuclides is assumed in the model (based on fracture half-spacing). In the matrix, the radionuclides are subject to sorption described using the linear equilibrium approach (based on element-specific K_d values). Matrix diffusion is caused by random movement of radionuclides, which, in the presence of concentration gradients, causes a net movement of solute. It is assumed here that the pore space of the matrix is connected over distances of possible penetration depth into the matrix, i.e. the matrix is modelled as a continuous porous medium. Thus, it is the fracture spacing (strictly half-spacing) that governs the penetration depth. Diffusion of a few centimetres into the rock matrix leads to a relevant retardation of radionuclide release into the near surface environment. After entering the pore system of the rock matrix, the solutes may sorb on the extensive pore surfaces. It is also important to note that matrix diffusion extends the residence time in the rock also for non-sorbing species.

Sorption in the rock matrix is included in the model; however, retardation due to sorption in the fractures (on e.g. fracture minerals) is neglected in the model to mimic historical codes. This is considered to be a pessimistic assumption, though as mentioned above it would be straightforward to implement sorption in the fractures within this framework.

The code comparison presented within this document gives confidence that the implementation and approximation of the governing equations using a compartment approach returns valid solutions. A resolution of 10 compartments in both the fracture direction and matrix direction has been shown to return reliable breakthrough curves for modelled radionuclides. Solving the transport problem using this compartment implementation is very much faster, provides more robust results and is easier to work with than the other compared codes (FARF31 and MARFA SP).

The novel approach of approximating a small set of trajectories representing all potential transport pathways through the rock reduces the total simulation time even more, while still replicating the total output flux using all possible trajectories for sorbing radionuclides and being within 30 % accurate for decay-product and non-sorbing radionuclides. This deviation is smaller than typically observed between different runs in the MARFA SP software. The approach permits the inclusion of all flow paths in a probabilistic simulation. Since the choice of representative trajectories is both based on covering the full range of the transport resistances as well as the travel times, both the early breakthrough governed by dispersion and the final breakthrough levels are considered.

B8 Source code

```
% ========================================================================
%  Dual porosity model for radionuclide transport in fractured rock
% ========================================================================
function Fout = FARFCOMP(time,Fin,Tw,F,epsil,rhob,halflife,Kd,De,varargin)
if nargin<9
    error('Required parameters: t,in,Tw,F,epsil,rhob,halflife,Kd and De')
end
% Get default values for non-required parameters
[Pe,Nf,Nm,d1,dmax,singleRnInd,decayGroups,RelTol,AbsTol] = ...
    default(length(halflife),varargin{:});

% If source term is not a function handle, assume matrix with radionuclide
% release, convert to function handle using linear interpolation
if ~isa(Fin,'function_handle')
    Fin = @(t,ind)interp1(time,Fin(:,ind),t);
end

Fout = zeros(length(time),length(halflife)); % Initialize output variable [Bq year-1]
Ntot = Nf*(Nm+1);                            % Total number of compartments [-]
lambda = log(2)./halflife;                   % Decay coefficient [y-1]
Rm = epsil+rhob*Kd;                            % Retardation in Matrix [-]
Aw = F/Tw;                                   % Flow-wetted surface area [m2 m-3]
adv = Nf/Tw;                                 % Rate of advection in fracture [y-1]
disp = max(0,Nf^2/(Tw*Pe)-Nf/(Tw*2));        % Rate of dispersion in fracture [y-1]

% Rock matrix layer diffusion depth [m]
inc = abs(fzero(@(x)sum(d1*x.^(0:Nm-1))-dmax,1.1));
d = d1*inc.^(0:Nm-1);

% Initialize option structure
options = odeset('Vectorized',1,'RelTol',RelTol,'AbsTol',AbsTol);

% Loop single radionuclides
for i=1:length(singleRnInd)
    ind = singleRnInd(i);
    Jac = getJac(Aw,Rm(ind),De(ind),lambda(ind),Ntot,Nm,d,adv,disp);
    [~,y] = ode15s(... Solve the differential equation
        @(t,y)Jac*y+sparse(1,1,Fin(t,ind),Ntot,1),... odefcn
        time,... time
        sparse(Ntot,1),... initial condition is zero
        odeset(options,'Jacobian',Jac,'NonNegative',1:Ntot));
    % Store advective flux from last fracture compartment
    Fout(:,ind) = y(:,end-Nm)*adv;
end

% Loop decay groups
for i=1:length(decayGroups)
    ind = unique([decayGroups{i}(:,1);decayGroups{i}(:,2)]);
    Ngroup = length(ind);
    JacChain = getJac(Aw,Rm(ind(1)),De(ind(1)),lambda(ind(1)),Ntot,Nm,d,adv,disp);
    for j=2:Ngroup
        JacChain =
blkdiag(JacChain,getJac(Aw,Rm(ind(j)),De(ind(j)),lambda(ind(j)),Ntot,Nm,d,adv,disp));
    end
    for j=1:size(decayGroups{i},1)
        ingrowth = log(2)/halflife(decayGroups{i}(j,2))*decayGroups{i}(j,3);
        indp = find(decayGroups{i}(j,1)==ind); % Parent index
        indd = find(decayGroups{i}(j,2)==ind); % Daughter index
        for k=1:Ntot
            JacChain(k+Ntot*(indd-1),k+Ntot*(indp-1)) = ingrowth;
        end
    end
    [~,y] = ode15s(... Solve the differential equation
```

```
        @(t,y)JacChain*y+sum(sparse((0:Ngroup-
1)*Ntot+1,1:Ngroup,Fin(t,ind),Ntot*Ngroup,Ngroup),2),... odefcn
        time,... time
        sparse(Ntot*Ngroup,1),... initial condition is zero
        odeset(options,'Jacobian',JacChain,'NonNegative',1:Ntot*Ngroup));
    % Store advective flux from last fracture compartment
    Fout(:,ind) = y(:,Ntot-Nm:Ntot:end-Nm)*adv;
end
% ========================================================================
%  Construct sparse Jacobian matrix for a specific radionuclide
% ========================================================================
function Jac = getJac(Aw,R,De,lambda,N_tot,N_m,d,adv,disp)
% Index of all fracture compartments
fInd = 1:(N_tot)*(N_m+1)+N_m+1:(N_tot)^2-(N_tot*N_m);

% Decay terms
Jac = -lambda*speye(N_tot);

% Forward terms in fracture (Advection and Dispersion)
Jac(fInd) = Jac(fInd)-adv;
Jac(fInd(1:end-1)) = Jac(fInd(1:end-1))-disp;
Jac(fInd(end)) = Jac(fInd(end));
Jac(fInd(1:end-1)+N_m+1) = adv+disp;

% Backward terms in fracture (Dispersion)
Jac(fInd(2:end)) = Jac(fInd(2:end))-disp;
Jac(fInd(2:end)-(N_m+1)) = disp;

% Fracture-compartment to first matrix compartment (Matrix diffusion)
diff = 2*Aw*De/d(1);
Jac(fInd) = Jac(fInd)-diff;
Jac(fInd+1) = diff;

% First matrix compartment to fracture-compartment (Matrix diffusion)
diff = 2.0*De/(R*d(1)^2);
Jac(fInd+N_tot+1) = Jac(fInd+N_tot+1)-diff;
Jac(fInd+N_tot) = diff;

% Diffusion in the rest of matrix compartments
for i=1:N_m-1
    % Forward diffusion terms (Matrix diffusion)
    diff = 2*De/(R*d(i)*(d(i)+d(i+1)));
    Jac(fInd+i*(N_tot+1)) = Jac(fInd+i*(N_tot+1))-diff;
    Jac(fInd+i*(N_tot+1)+1) = diff;
    % Backward diffusion terms (Matrix diffusion)
    diff = 2*De/(R*d(i+1)*(d(i)+d(i+1)));
    Jac(fInd+(i+1)*(N_tot+1)) = Jac(fInd+(i+1)*(N_tot+1))-diff;
    Jac(fInd+(i+1)*(N_tot+1)-1) = diff;
end

% ========================================================================
%  Get default values
% ========================================================================
function varargout=default(nrn,varargin)
% Pe,N_f,N_m,d_1,d_max,singleRnInd,decayGroups,RelTol,AbsTol
varargout = {10,20,20,0.0001,4.5,1:nrn,{},1e-3,1e-6};
varargout(1:nargin-1) = varargin;
```

Appendix C

Groundwater flow scaling factors for the near-field and geosphere in the simplified glacial cycle evaluation case

The groundwater flow magnitudes under temperate conditions at 2000 AD are assumed to be the baseline for scaling the groundwater flows under other climate phases. Thus, the scaling factor for the temperate period of the climate evolution equals 1 by definition. The results of Joyce et al. (2019) show little change in the performance measures, i.e. travel time, F-factors, Q_{eq}, particle track length, for the period after 2000 AD (Section 4.6.3 in Joyce et al. 2019) and the assumption of 2000-AD conditions for the entire temperate period is thus judged appropriate.

During the two permafrost periods that are presumed to start at 17 500 AD and 52 000 AD, the scaling factor is assumed to be 1. The effect of permafrost at the Laxemar and Forsmark sites was modelled by Vidstrand et al. (2010a, 2014b) under the assumption that the permafrost did not reach repository depth and that taliks are present in the landscape. In the study connected to the extension of the SFR facility, the results show small increases in groundwater flow at the repository for some vaults and cases, whereas for the other vaults and cases the flow decreased. A median value for the scaling factor of approximately 3 is reported in Vidstrand et al. (2010a) for the Laxemar site. The median value for the scaling factor calculated by Vidstrand et al. (2010b) for Forsmark in the SR-Site calculations is about 0.4. Based on these results a factor of 1 is judged reasonable.

At 56 200 AD, when the ice sheet advances towards the Laxemar site, the hydraulic gradient successively increases due to the ice-sheet profile. The ice-sheet advance occurs when permafrost conditions prevail and thus the groundwater flow near the rock surface is hindered compared with a situation without permafrost. Based on the detailed modelling show in Figure G-12 in Vidstrand et al. (2010b) for SR-Site, the scaling factor is assumed to linearly increase from 1 to 33 at 57 000 AD when the ice-sheet front is located over the repository. The linear increase then continues until a maximum value of 35 is reached 50 years after the ice front has passed over the repository. The factor 35 is judged to be a relevant example, given that the factors range from 10 to 100 for different measurement locations used in the modelling of Vidstrand et al. (2010b). The selection of a value smaller than the maximum value is judged adequate, since the scaling factor applies to the entire hydrogeological modelling domain and thus particle tracks used in the geosphere transport calculations. Assigning the maximum factor would likely overestimate the increase in flow in general, since it is tied to a specific location with a limited volume around the measurement point. The selected factor of 35 can be compared with the median values of about 20 that are reported both in SR-Site and in the corresponding study for Laxemar (Figure 6-18 in Vidstrand et al. 2010b, Figure 6-16 in Vidstrand et al. 2010a).

At 57 050 AD the ice sheet is located over the site and then advances further until the topographical gradients associated with the ice-sheet surface are small. At the same time, the base of the ice sheet starts to thaw, and warm-based conditions are assumed from 100 years after the ice-sheet front is located over the repository. By the year 58 200 AD the combined effect of the ice-sheet advance and basal thawing is that the flow decreases and can be assumed to have the same magnitude as predicted for temperate conditions. The results of the detailed modelling shown in Figure 6-5 in Vidstrand et al. (2010a) show a range of values that are close to 1 for the glacial maximum, and this factor is used in the radionuclide transport calculations for SR-PSU (SKB 2015b).Therefore, a linear decrease of the factor from 35 to 1 is applied during the period 57 050 AD to 58 200 AD.

From 58 200 AD to 68 800 AD, the ice sheet resides over the site and a factor of 1 is applied due to the small topographical gradients associated with the ice-sheet surface.

At 68 800 AD the deglaciation begins to affect the Laxemar site. The ice-sheet profile during deglaciation implies increased ice-surface gradients and the groundwater flow thus increases until 70 000 AD when the ice-sheet front passes over the site during its retreat. The scaling factor is assumed to linearly increase from 1 to 3. This reflects that the ice-sheet profile is considerably less steep during ice-sheet retreat compared to its advance (Section 4.5 in the **Climate report**). This assumption is in line with the values selected in the radionuclide transport calculations for SR-PSU (SKB 2015b) and can be compared with the results of Vidstrand et al. (2013) that report a range of the scaling factor from 3 to 20. A value at the low end of the range is here conservatively chosen so as to avoid overestimating the amounts of radionuclides that are flushed out of the area in the submerged period (when dose consequences are expected to be very small).

When the ice sheet has withdrawn from the site at 70 000 AD, the repository will be submerged and these conditions imply that the hydraulic gradient above the repository becomes very small and therefore also the groundwater flow become small. Results presented in Section 6.4.4 in Vidstand et al. (2010a) indicate that the flow magnitudes under submerged conditions are about 1 percent of the total flow during temperate conditions. During a transition period from glacial to submerged conditions, a linear decrease of the scaling factor from 3 to 0.01 in year 70 800 AD is therefore applied.

Based on the shoreline displacement curve, it is deduced that the site starts to be affected by land rebound at 74 400 AD. At that time, the most important biosphere object 206 starts its transition from coastal sea to isolated lake. Simulations of bedrock hydrology in Forsmark suggest that the groundwater flow at repository depth increases approximately linearly from present sea-covered conditions until times when the landscape has emerged out of the sea (Odén et al. 2014). The scaling factor thus starts to increase from 0.01 to reach the factor for temperate conditions at 78 700 AD, which is, by definition, 1. After that, and until 100 000 AD, it is assumed that temperate conditions identical to the initial period prevail and that the shore-level develops in the same way (Figure 5-28). After 100 000 AD the climate sequence repeats itself until the year one million AD.

The different sequences of events that influence the hydrogeology at the site are defined with rather high temporal accuracy regarding the effects of shoreline displacement. This should not be seen as a high level of confidence in the prediction of the timing of these events, rather this is an effect of assuming that the shoreline displacement that is currently ongoing will repeat itself after the glaciation included in the climate sequence in the simplified glacial cycle variant.

Table C-1. Summary of the development in the first cycle of the *simplified glacial cycle evaluation case*. Submerged conditions refer to the duration of sea water-covered conditions for biosphere object 206. Groundwater flow rates are relative those in temperate terrestrial conditions. Note that the conditions are assumed to be unfrozen at repository depth throughout the analysis period.

Time [AD]	Climate domain	State of discharge area	Conditions in bedrock above repository	Groundwater flow in repository and bedrock
2075−17 500	Temperate	Mire	Unfrozen	1
17 500−17 600	Periglacial	Mire freezes, start of discharge to lake talik	Frozen	1
17 600− 20 400	Periglacial	Mire frozen. All release to lake talik	Frozen	1
20 400−20 500	Periglacial	Mire thaws, discharge in lake talik ends	Frozen	1
20 500–52 000	Temperate	Mire	Unfrozen	1
52 000−52 100	Periglacial	Mire freezes, start of discharge to lake talik	Frozen	1
52 100− 56 200	Periglacial	Mire frozen. All release to lake talik	Frozen	1
56 200−57 000	Periglacial. Ice-sheet advancing towards Laxemar	Mire frozen. All release to lake talik	Frozen	Transition from 1 to 33
57 000−57 050	Glacial. Continued ice-sheet advance beyond Laxemar	Site ice-covered. All release to sea basin at ice margin	Frozen	Transition from 33 to 35
57 050−58 200	Glacial. Continued ice-sheet advance beyond Laxemar	Site ice-covered	Frozen during the first 50 years, then unfrozen	Transition 35 to 1
58 200− 68 800	Glacial. Thawed bedrock conditions	Site ice-covered	Unfrozen	1
68 800− 70 000	Glacial. Deglaciation of the Laxemar site	Site ice-covered	Unfrozen	Transition from 1 to 3
70 000−70 800	Submerged	Sea water depth above object ≥ 6 m	Unfrozen	Transition from 3 to 0.01
70 800−74 400	Submerged	Sea water depth above object ≥ 6 m	Unfrozen	0.01
74 400− 78 700	Submerged	Transition from coastal sea to isolated lake	Unfrozen	Transition from 0.01 to 1
78 700− 83 100	Temperate	Transition from lake to mire	Unfrozen	1
83 100− 102 000	Temperate	Mire	Unfrozen	1

Arkitektkopia AB, Bromma, 2019

SKB is responsible for managing spent nuclear fuel and radioactive waste produced by the Swedish nuclear power plants such that man and the environment are protected in the near and distant future.

skb.se